



University of
Nottingham

UK | CHINA | MALAYSIA

Aeroelastic Modelling and Analyses of a Short Wing-Propeller Configuration

Zi Wang

Supervised by Prof. Atanas A. Popov & Dr. Alessandro Anobile

A thesis presented for the degree of Doctor of Philosophy

October 2020

Abstract

Rotorcraft designs with the ability to fly as an aircraft but take off and land vertically as helicopters were first introduced in the early 1950s. However, the development of such concept stopped after a few failed attempts. Similar configurations, in which wings are equipped with additional propulsive propellers, has re-emerged in the past ten years for the compound helicopter and tilt-rotor aircraft. Those designs are aimed at introducing a new way of providing propulsive thrust, increasing the cruise speed, while retaining hovering advantages. However, the still open issue of high level of vibration resulting from fluid-structure interaction is exacerbated in the case of those rotorcrafts, with even more critical effects on the fatigue life, maintenance costs, on-board instrumental efficiency and comfort. Being able to model and predict the complex aeroelastic behaviour associated with the wing-propeller system is extremely important for achieving an optimised design. This project is an initial attempt to apply comprehensive analysis onto such compound aerostuctures. Aiming at providing sufficient information of dynamic responses in the time-domain for the preliminary design stages, low-fidelity aeroelastic models are reviewed and basic structural and aerodynamic theories are introduced as basic building blocks.

With this intention, a numerical computational approach is developed for characterising aeroelastic behaviour of a short-wing/propeller configuration on small rotorcrafts. The computational tool consists of many components and the integration of them. Firstly, a two-dimensional aerodynamic model is developed based on thin aerofoil theories, including Wagner's, Küssner's, Theodorsen's and Sears' unsteady models. The combinations of those theories are investigated for different output. The Wagner's and Küssner's theories are found to be the most suitable approach for obtain-

ing time-domain dynamic responses, which is one of the main objective outcomes for this thesis. Theodorsen's model, formulated in the frequency domain, is better suited for instability analyses and Sears' model is ideal for dynamic steady-state response solutions. At the same time, propeller inflow is simplified as several velocity components in its axial and vertical directions based on the general characteristic of propeller slipstream. Hence, the propeller effects on the wing structure can be taken into account by the two-dimensional aerodynamic model.

As for the mathematical representation of a short wing structure, beam theories are reviewed. Considering flapping, torsion and lead-lag motion, governing equations based on different beam theories are derived. In order to evaluate different structural effects and form a simple, yet realistic, representation, modal analyses based on different theories are compared. To perform efficient modal analyses, a numerical tool based on the transfer matrix method is introduced and validated. Structural coupling between flapping and torsion is examined and coupled modes are introduced. With the aid of modal analyses results, structural coupling, rotary inertia and shear deformation are found to contribute the most towards the structural modal behaviour. Hence, coupled flapping-torsion motion characterised by Euler-Bernoulli beam theory and separate lead-lag motion defined as a Timoshenko beam are found to be the most appropriate.

The integration of aerodynamic and structural models allows further investigation of aeroelastic stability boundary and time-domain dynamic responses under forced conditions. A numerical procedure is developed, featuring coupled modes, which has been proved to be accurate enough when validated against experimental results. Instability, both statically and dynamically, is then studied and flight condition defined. To obtain solutions of aeroelastic response under a defined flight condition, solution strategy and procedures for convergence analyses are specified. A case study on the short wing under propeller inflow is presented and time-domain dynamic responses are obtained. Collecting all modular solvers developed for the aeroelastic model, the tool was further exploited to demonstrate its capability in analysing phenomena involving different structural, flight and propeller conditions in preliminary design stages. It was found that, apart from the aeroelastic instability, the wingspan and propeller operational speed needs to be designed carefully in order to

keep deformation at a minimal level.

Acknowledgement

Firstly, I would like to thank my supervisors, Atanas Popov and Alessandro Anobile. This thesis would not have come together without their guidance and support over the past few years. Atanas, thank you for always being there and making this dream a reality for me. Alessandro, thank you for all the knowledge and patience you've shown, and I wish we could have worked together for longer.

In addition, I would like to acknowledge the CleanSky 2 Joint Undertaking ASTRAL project for the funding, which made my study here possible.

I am also extremely grateful for my family, especially my parents. Thank you for always standing by my side and supporting me emotionally and financially for whatever I decide to do. Thank you for everything.

Finally, there are so many people that I've worked with, connected to and encountered during these four years of my study, they made me the person that I am today. A special thank you for my friends and colleagues in ITRC and Sherwood Hall, Antonino La Rocca, Violetta Di Napoli, Tengtuo Zhu, Felix Biertümpfel, Hamid-Reza Danesh-Azari and Pigu. There are just too many names to mention, you made this journey an unforgettable one, thank you all.

Contents

| | | |
|----------|---|-----------|
| 1 | Introduction and Literature Review | 24 |
| 1.1 | Literature review on simulation and analysis approaches for wing aeroelasticity . . . | 26 |
| 1.1.1 | Aerodynamic theories for aeroelastic analyses | 29 |
| 1.1.2 | Application of low-fidelity models in aeroelasticity studies | 33 |
| 1.2 | Aim and objectives of thesis | 39 |
| 1.3 | Methodology and thesis outline | 41 |
| 2 | Representation of Aerodynamic Loadings | 44 |
| 2.1 | Aerodynamic effects in propeller-wing configuration | 45 |
| 2.2 | Steady aerodynamic theory | 47 |
| 2.3 | Quasi-steady aerodynamic theory | 50 |
| 2.4 | Unsteady aerodynamic theories | 52 |
| 2.4.1 | Time-domain indicial response: Wagner’s model | 53 |
| 2.4.2 | Frequency-domain unsteady response: Theodorsen’s model | 57 |
| 2.4.3 | Time-domain arbitrary gust field response: Küssner’s model | 59 |
| 2.4.4 | Frequency-domain sinusoidal gust response: Sears’ model | 63 |
| 2.5 | Model integration and optimisation | 65 |
| 2.5.1 | Plunging response under sharpe-edged gust | 68 |
| 2.5.2 | Recursive algorithm for the convolution integral | 71 |
| 2.5.3 | Plunging and pitching response under sharp-edged gust | 73 |

| | | |
|----------|--|------------|
| 2.6 | Conclusion | 76 |
| 3 | Wing Structural Representation | 79 |
| 3.1 | Euler-Bernoulli beam model | 80 |
| 3.2 | Timoshenko beam model | 83 |
| 3.3 | Modal Analysis | 85 |
| 3.3.1 | Numerical transfer matrix method | 89 |
| 3.3.2 | Validation | 92 |
| 3.4 | Modal study of compound helicopter wings | 99 |
| 3.4.1 | Flapping-torsion modal study | 101 |
| 3.4.2 | Lead-lag motion modal study | 104 |
| 3.4.3 | Coupled flapping-lead-lag-torsion modal study | 107 |
| 3.5 | Conclusion | 110 |
| 4 | Aeroelastic Instability and Numerical Application | 111 |
| 4.1 | Instabilities on aerofoil model | 112 |
| 4.1.1 | Static aeroelasticity - Divergence analysis | 112 |
| 4.1.2 | Unsteady aeroelasticity - Flutter analysis | 115 |
| 4.2 | Instabilities on wings | 122 |
| 4.2.1 | Coupled modes in aeroelastic stability analysis | 126 |
| 4.3 | Conclusion | 130 |
| 5 | Dynamic Response Solution | 131 |
| 5.1 | Aeroelastic model integration and solution strategy | 132 |
| 5.2 | Convergence study strategy | 136 |
| 5.3 | Aeroelastic response solution verification | 137 |
| 5.4 | Aeroelastic response for short-wing under propeller inflow | 143 |
| 5.4.1 | Convergence study | 144 |

| | | |
|----------|--|------------|
| 5.4.2 | Dynamic response using coupled modes | 148 |
| 5.4.3 | Uncoupled solver results and comparisons | 150 |
| 5.5 | Conclusion | 154 |
| 6 | Aeroelastic Model Exploitation and Further Analyses | 156 |
| 6.1 | Parameter set definition | 158 |
| 6.1.1 | Wingspan effect | 160 |
| 6.1.2 | Aircraft advancing velocity effect | 165 |
| 6.1.3 | Altitude effect | 169 |
| 6.1.4 | Propeller size effect | 174 |
| 6.1.5 | Propeller speed effect | 178 |
| 6.2 | Dynamic response under different disturbance | 180 |
| 6.2.1 | 1-cosine gust | 181 |
| 6.2.2 | Continuous turbulence | 184 |
| 6.3 | Conclusion | 190 |
| 7 | Conclusions and Future Work | 193 |
| 7.1 | Review of initial aims and objectives | 193 |
| 7.2 | Conclusions | 196 |
| 7.3 | Contributions | 197 |
| 7.4 | Future work suggestions | 200 |
| A | Recursive Algorithm Derivation | 214 |
| B | EoMs Derivation Based on Timoshenko Beam | 215 |
| C | Parameter Definition and Validation | 219 |
| D | Numerical Modal Analysis Process | 221 |
| D.1 | Lead-lag Motion | 221 |

D.2 Coupled Euler-Bernoulli beam flapping and torsion 222
D.3 Coupled Timoshenko beam flapping and torsion 224

E Matrices Definition 226

List of Figures

| | | |
|------|---|----|
| 1.1 | The short-wing/propeller configuration demonstrations | 25 |
| 1.2 | Structural models for characterising a wing, with green shading indicating applicable theories for the proposed problem | 27 |
| 1.3 | Aerodynamic theories and models suited for different flowfield conditions, with green shading indicating applicable theories for the proposed problem | 28 |
| 1.4 | Aerodynamic Models for Incompressible Inviscid Flow, with green shading indicating applicable theories for the proposed problem | 29 |
| 1.5 | Thin aerofoil theory with vortex distribution along camber line [10] | 30 |
| 2.1 | Main rotor wake under: (a) low speed forward flight (b) high speed forward flight [82] | 46 |
| 2.2 | Parabolic axial and vertical velocity components added by presence of a propeller . | 47 |
| 2.3 | An aerofoil in steady flow | 48 |
| 2.4 | Linear increment for (a) lift and (b) pitching moment due to the AoA before stalling | 50 |
| 2.5 | Aerofoil in quasi-steady aerodynamics | 51 |
| 2.6 | Aerofoil Model with Pitching and Plunging | 54 |
| 2.7 | Wagner's function $\phi(\tau)$ against dimensionless time describing transition to steady state | 55 |
| 2.8 | Theodorsen's function $C(k)$ against $1/k$ describing transition of lift and phase lag . | 58 |
| 2.9 | Uniform step-gust $w_0(\tau)$ along span | 60 |
| 2.10 | Step velocity profile $w_p(\tau)$ along span | 60 |

| | | |
|------|--|-----|
| 2.11 | Sinusoidal Gust | 61 |
| 2.12 | Küssner's function $\psi(\tau)$ against dimensionless time τ describing transition to- wards steady state | 62 |
| 2.13 | Real and imaginary part of the original Sears' function $S(k_p)$ describing lift and phase lag transitions | 64 |
| 2.14 | Aerofoil Model with Pitching and Plunging | 66 |
| 2.15 | Newmark-beta solver results aligned with results presented [42] | 69 |
| 2.16 | Results obtained by Wagner's unsteady and quasi-steady aerodynamics | 70 |
| 2.17 | Verification results showing alignment in comparison with [49] (a) Case 1 (b) Case 2 (c) Case 3 (d) Case 4 | 75 |
| 2.18 | Wing tip plunging and pitching behaviour | 76 |
| 2.19 | Wing tip plunging and pitching behaviour obtained by quasi-steady aerodynamics | 77 |
| 3.1 | Beam Model - Cantilever wing with flapping, lead-lag and torsion modes | 81 |
| 3.2 | Cantilever beam section coordinates note | 81 |
| 3.3 | Timoshenko beam and shear deformation flexibility | 83 |
| 3.4 | Segments to represent non-uniform beam cross-sections | 91 |
| 3.5 | Mode shape validation between analytical and numerical approaches | 93 |
| 3.6 | Coupled mode shape functions (Bending —; Torsion - - -; Results by [96] \times) | 94 |
| 3.7 | First five mode shapes derived for configuration in [101] via the transfer matrix method (Flap — ; Bending slope - - - ; Torsion - - - - -) | 96 |
| 3.8 | Mode shapes snapshot for the first five modes from case study demonstrated in [101] | 97 |
| 3.9 | Mode shapes based on transfer matrix method and analytical method for configu- ration in [90](Flap - - - - -; Lead-lag - - - ; Torsion —) | 99 |
| 3.10 | Modal analysis strategy | 101 |
| 3.11 | Coupled flap-torsion mode shapes comparison between Euler-Bernoulli and Tim- oshenko beam theory (ξ — ; α - - -) | 105 |

| | | |
|------|---|-----|
| 3.12 | Lead-lag 1st and 2nd mode shapes derived by Euler-Bernoulli beam and Timoshenko beam theories | 106 |
| 3.13 | Coupled flap-torsion-lead-lag motion mode shape derived by developed tool based on transfer matrix method (Flap - - - - ; Lead-lag - - - ; Torsion —) | 109 |
| 4.1 | Aerofoil under aerodynamic forces | 113 |
| 4.2 | Solution pattern when $\lambda < 0$ (- - -), $\lambda = 0$ (—) and $\lambda > 0$ (·-·-·) | 117 |
| 4.3 | Damping and reduced frequency against dimensionless velocity based on case studied in [52] | 121 |
| 4.4 | Flutter analysis on wing-tip sectional model for the short wing configuration given in Table3.5 | 121 |
| 4.5 | Divergence velocity on wing-tip sectional model for the short wing configuration given in Table3.5 | 122 |
| 4.6 | Wing flutter analysis based on uncoupled bending and torsional modes for the Goland wing | 125 |
| 4.7 | Wing flutter analysis based on coupled bending-torsion modes for Goland wing | 128 |
| 4.8 | Wing flutter analysis based on coupled bending-torsion modes for the short wing | 129 |
| 4.9 | Divergence boundary for the short wing | 130 |
| 5.1 | Solution strategy for aerodynamic and structural model iterations | 135 |
| 5.2 | Convergence study strategy | 137 |
| 5.3 | Agreement in aeroelastic responses derived from present model and results from [57] | 139 |
| 5.4 | Coupled mode shapes based on parameters from [57] (Bending —; Torsion - - - -) | 140 |
| 5.5 | Agreement in aeroelastic response results between uncoupled model and [57] | 141 |
| 5.6 | Aeroelastic response comparison with initial condition assumption on 1st coupled mode | 142 |
| 5.7 | Aeroelastic response comparison with initial condition assumed as step loads | 142 |
| 5.8 | Propeller parabolic addition velocity profile in (a) axial and (b) vertical directions | 143 |

| | | |
|------|--|-----|
| 5.9 | \bar{u}_f distribution | 144 |
| 5.10 | Steady-state amplitude comparison with fixed N_q (Dashed red line: lead-lag vibration amplitude; Solid blue line: percentage of changes) | 145 |
| 5.11 | Steady-state amplitude comparison with fixed N_p (Dashed red line: lead-lag vibration amplitude; Solid blue line: percentage of changes) | 146 |
| 5.12 | Confirmation on convergence with $N_q = 5$ (Dashed red line: lead-lag vibration amplitude; Solid blue line: percentage of changes) | 146 |
| 5.13 | Convergence study on iterative time step (Dashed red line: lead-lag vibration amplitude; Solid blue line: percentage of changes) | 147 |
| 5.14 | Final Confirmation for convergence parameters $N_q, N_p, \delta\tau, \beta$ | 148 |
| 5.15 | Flapping transient response of a short wing configuration under propeller inflow (Solved by coupled modes) | 149 |
| 5.16 | Torsional transient response of a short wing configuration under propeller inflow (Solved by coupled modes) | 149 |
| 5.17 | Lead-lag transient response of a short wing configuration under propeller inflow (Solved by coupled modes) | 150 |
| 5.18 | Steady-state response of a short wing configuration under propeller inflow for all three motions (Solved by coupled modes) | 151 |
| 5.19 | Flapping transient response of a short wing configuration under propeller inflow (Solved by uncoupled modes) | 152 |
| 5.20 | Torsional transient response of a short wing configuration under propeller inflow (Solved by uncoupled modes) | 152 |
| 5.21 | Lead-lag transient response of a short wing configuration under propeller inflow (Solved by uncoupled modes) | 153 |
| 5.22 | Steady-state response of a short wing configuration under propeller inflow for all three motions (Solved by uncoupled modes) | 154 |

| | | |
|------|---|-----|
| 6.1 | Aeroelastic Model Framework | 157 |
| 6.2 | Steady-state mean displacement against wingspan: (a) flapping motion; (b) lead-lag motion; (c) torsional motion | 163 |
| 6.3 | Amplitude comparison against wingspan: (a) flapping motion; (b) lead-lag motion; (c) torsional motion | 164 |
| 6.4 | Initial transient displacement comparison against airspeed | 166 |
| 6.5 | Mean displacement comparison against airspeed: (a) flapping motion; (b) lead-lag motion; (c) torsional motion | 167 |
| 6.6 | Amplitude comparison against airspeed: (a) flapping motion; (b) lead-lag motion; (c) torsional motion | 169 |
| 6.7 | Air density changes with variation of altitude from 0 to 4000m | 170 |
| 6.8 | Initial transient displacement at different altitudes: (a) flapping motion; (b) lead-lag motion; (c) torsional motion | 171 |
| 6.9 | Linear variation of mean displacements against altitude: (a) flapping motion; (b) lead-lag motion; (c) torsional motion | 172 |
| 6.10 | Variation of amplitudes against altitude: (a) flapping motion; (b) lead-lag motion; (c) torsional motion | 173 |
| 6.11 | Mean displacement comparison against propeller size: (a) flapping motion; (b) lead-lag motion; (c) torsional motion | 176 |
| 6.12 | Amplitude comparison against propeller size: (a) flapping motion; (b) lead-lag motion; (c) torsional motion | 177 |
| 6.13 | Mean displacement comparison against propeller speed: (a) flapping motion; (b) lead-lag motion; (c) torsional motion | 179 |
| 6.14 | Amplitude comparison against propeller speed: (a) flapping motion; (b) lead-lag motion; (c) torsional motion | 180 |
| 6.15 | 1-cosine gust schematic | 181 |
| 6.16 | Flapping transient response against 1-cosine gust length | 183 |

| | | |
|------|--|-----|
| 6.17 | Torsion transient response against 1-cosine gust length | 184 |
| 6.18 | von Kármán turbulence model defining PSD at each frequency | 186 |
| 6.19 | Frequency response function for coupled flapping-torsion motion: (a) flapping motion; (b) torsional motion | 188 |
| 6.20 | the PSD of displacements response in continuous gust: (a) flapping motion; (b) torsional motion | 189 |
| 6.21 | RMS displacement along wingspan: (a) flapping motion; (b) torsional motion . . . | 190 |
| C.1 | Wing-box cross-section | 219 |
| C.2 | Abaqus visualisation for rotational displacement in z direction | 220 |

List of Tables

| | | |
|------|--|-----|
| 2.1 | Computational time comparison for convolution integral and its recursive formulation | 73 |
| 2.2 | Combination of aerodynamic theories and their functionalities | 77 |
| 3.1 | Mode Shape Function Coefficients | 87 |
| 3.2 | Comparison of theoretical and transfer matrix derived natural frequencies | 92 |
| 3.3 | Comparison with [101] by derived natural frequencies of transfer matrix | 96 |
| 3.4 | Comparison of [90] and transfer matrix derived natural frequencies | 98 |
| 3.5 | Estimated wing structural parameters | 100 |
| 3.6 | Flapping modal frequencies based on two beam theories | 102 |
| 3.7 | Torsion modal frequencies and shapes | 103 |
| 3.8 | Coupled flapping torsion modal frequencies based on two beam theories | 104 |
| 3.9 | Lead-lag motion modal frequency based on two beam theories | 106 |
| 3.10 | Uncoupled and coupled lead-lag modal frequencies comparisons | 108 |
| 4.1 | Types of motion based on λ and k values [52] | 117 |
| 5.1 | Uncoupled natural frequencies from [57] | 140 |
| 5.2 | Coupled natural frequencies derived from the example parameters in [57] | 140 |
| 5.3 | Steady-state response comparison for coupled and uncoupled solver | 155 |
| 6.1 | Parameters and their range of studies | 159 |
| 6.2 | Coupled bending-torsional natural frequencies for wingspans from 2.0 m to 2.5 m . | 162 |

| | | |
|------|---|-----|
| 6.3 | Steady-state mean displacement comparison | 163 |
| 6.4 | Steady-state amplitude comparison | 164 |
| 6.5 | Steady-state mean displacement comparison | 167 |
| 6.6 | Steady-state amplitude comparison | 168 |
| 6.7 | Altitude vs. air density | 170 |
| 6.8 | Steady-state mean displacement comparison at different altitude | 171 |
| 6.9 | Steady-state amplitude comparison at different altitude | 173 |
| 6.10 | Steady-state mean displacement comparison | 175 |
| 6.11 | Steady-state amplitude comparison | 177 |
| 6.12 | Steady-state mean displacement comparison | 178 |
| 6.13 | Steady-state amplitude comparison | 179 |
| C.1 | Cross-sectional properties output from NASTRAN | 220 |

Nomenclature

- α Pitch/torsional displacement
- α_0 Initial condition for torsional/pitching displacement
- α_{AoA}^{eff} The effective angle of attack
- α_{AoA} The angle of attack
- $\bar{\omega}$ Plunging-pitching frequency ratio ω_h/ω_α
- \bar{u}_f The ratio between the flow approaching velocity and the aircraft advancing velocity
- $\bar{L}_{in}, \bar{M}_{in}$ Aerodynamic lift and moment caused by unit gust input
- κ_y, κ_z The shear coefficient in y- and z- directions
- $\lambda, \lambda_1, \lambda_2$ The damping factors for the instability study
- λ_j, σ_j Coefficients for analytical beam bending mode shapes
- $\mathbf{A}, \mathbf{A}_1, \mathbf{A}_2, \mathbf{A}_3, \mathbf{A}_4, \mathbf{A}_5, \mathbf{D}$ Transfer matrix in numerical modal analysis
- $\mathbf{M}_a, \mathbf{C}_a, \mathbf{K}_a$ The aerodynamically induced mass, damping and stiffness matrices
- $\mathbf{M}_s, \mathbf{C}_s, \mathbf{K}_s$ The dimensionless mass, damping and stiffness matrices
- $\mathbf{M}_{NC}, \mathbf{K}_{NC}$ The non-circulatory induced mass and stiffness matrices

M, C, K The mass, damping and stiffness matrices

T, R Boundary condition matrices in transfer matrix method

\mathcal{L} Lagrangian function

μ Mass parameter $\mu = m/\pi\rho b^2$

Ω The scaled frequency ω/U_∞

ω Harmonic frequency

$\omega_h, \omega_v, \omega_\alpha$ Natural frequencies in plunging, lead-lag and pitching

ω_p, k_p Propeller blade passing frequency and its dimensionless form $k_p = \omega_p b/U_\infty$

ω_{max} The maximum frequency considered in continuous turbulence model

$\phi(\tau)$ The Wagner's function

Φ_g Power spectral density for aeroelastic response

ϕ_p Phase change regarding the Sear's theory

Φ_r Power spectral density for aeroelastic response

$\psi(\tau)$ The Küssner's function

ρ Density of surrounding fluid

ρ_w Density of wing material, taken as 2720 kg/m^3 for aluminum

σ_g The root-mean-square gust velocity intensity

σ_r The root-mean-square of wing displacement

τ Dimensionless time, $U_\infty t/b$

- τ_0 Dummy time variable for convolution integral
- $\mathbf{A}(ik)$ Aerodynamic matrix for frequency domain stability study
- \mathbf{F} The loading vector
- \mathbf{F}_{aero} The aerodynamic loading vector
- \mathbf{F}_{in} The unit gust input for continuous turbulence
- \mathbf{u} The solution vector
- $\mathbf{z}(x)$ State space vector for transfer matrix method derivation
- θ Pre-twist angle along the wing-span
- $\Theta(x), \Theta_h(x), \Theta_v(x), Z(x)$ Mode shape functions
- $\theta_j(x), \eta_j(x), \zeta_j(x), \phi_j^z(x)$ The mode shape functions
- φ_y, φ_z The cross-sectional rotation angle in y- and z- directions
- A Stiffness parameter $A = k_h b^2 / m U_\infty^2$ in Chapter 2 and cross-sectional area in Chapter 3, 4 and 5
- a Dimensionless position measuring elastic axis from mid-chord, positive when mid-chord is in front of elastic axis
- A_1, A_2, b_1, b_2 Coefficients for the Wagner's function
- A_3, A_4, b_3, b_4 Coefficients for the Küssner's function
- A_p The disk area of propeller
- $C(k)$ The Theodorsen's function
- c, b The chord length and the half chord length, $c = 2b$

C_L Lift gradient between lift coefficient and the angle of attack, taken as 2π
 C_M Moment coefficient
 D_p Propeller diameter
 E, G The Young's and shear modules
 $f_j(\tau), p_j(\tau), z_j(\tau), q_j(\tau)$ The time-dependent functions for dynamic response solutions
 $F_{tip}, F_{thrust}, M_{tip}$ The propeller weight, thrust and induced moment
 $FRF(\omega)$ Frequency response function for the aeroelastic system
 h, ξ Plunging/bending/flapping displacement and its dimensionless expression, h/b
 h_0, ξ_0 Initial condition for bending/plunging displacement
 $H_n^{(2)}(k)$ Hankel functions of the second kind
 I_α Mass moment of inertia per unit span regarding the shear centre
 I_ω The warping constant
 I_y, I_z The second moment of area in the y- and z- directions
 I_{GC} Mass moment of inertia per unit span regarding the gravitational centre
 J The torsion constant
 j Imaginary unit for complex number in frequency-domain theories
 $J_n(k), Y_n(k)$ Bessel functions of the first and second kind
 k, k_1, k_2 The reduced frequency
 k_h, k_α Discrete spring stiffness coefficient in plunging and pitching

k_T Thrust coefficient

KE, PE The kinetic and potential energy

L Wing semi-span length in Chapter 3, 4, and 5

l The beam length, wing semi-span length

L, M_{ac} Aerodynamic lift and moment at the aerodynamic centre in Chapter 2

L_C, l_C Unsteady circulatory lift and its dimensionless form

L_g, l_g Lift generated by gust per unit span and its dimensionless expression

L_S, M_S Unsteady lift and moment derived from the Sears' theory

L_t The characteristic wavelength of turbulence

L_{cos} Length of 1-cosine gust

L_h, l_h Total in-plane lift per unit span and its dimensionless form

L_{NC}, l_{NC} Unsteady noncirculatory lift and its dimensionless form

L_v, l_v Total out-of-plane force per unit span and its dimensionless form

m Mass per unit span

$M(x), S(x)$ Moment and shear force state in beam

m, n, j Integer mode number in Chapter 3

M_C, m_C Unsteady circulatory moment and its dimensionless form

M_g, m_g Pitching moment generated by gust per unit span and its dimensionless expression

M_α, m_α Total pitching moment per unit span at shear centre and its dimensionless form

M_{NC}, m_{NC} Unsteady noncirculatory moment and its dimensionless form

n_p Propeller speed

N_q, N_p The number of modes taken into consideration

p, p_0, p_c, p_{static} Pressure in deriving propeller thrust

Q_i The generalised loads

q_i The generalised displacement coordinate

r_α Dimensionless radius of gyration, $(I_\alpha/m b^2)^{\frac{1}{2}}$

$S(k_p), S'(k_p)$ The Sears' function and the modified Sears' function

s, p, p_1, p_2 General frequency-domain solution

S_α, χ_α Static unbalance about elastic axis and its dimensionless form, $S_\alpha/m b$, positive when mass centre is in the front of elastic axis

t Time in seconds

U_∞ Aircraft advancing speed

U_a Flow approaching speed

U_D The divergence velocity

V Dimensionless advancing velocity, $V = U_\infty/b\omega_\alpha$

v, ν Lead-lag displacement and its dimensionless expression, h/b

v_0, ν_0 Initial condition for lead-lag displacement

v_0, v_e Entry and exit velocity of air in propeller thrust formulation

| | |
|--------------------|---|
| W | Virtual work of the system |
| w_0 | Uniform step-gust for the pretwist effect |
| w_G | Gust function, sharpened-edged gust in this case |
| w_i | Sinusoidal velocity variation function due to propeller inflow |
| w_i^a | Sinusoidal velocity variation amplitude |
| w_p | Velocity profile caused by propeller in the span-wise direction |
| $w_{3/4}$ | Downwash velocity at the 3/4 chord length |
| w_{add} | Additional velocity component due to aerofoil dynamics |
| w_{cos} | 1-cosine gust |
| w_{cos}^{max} | 1-cosine gust peak velocity |
| w_{in} | Unit input gust amplitude 1m/s |
| $X(\tau), Y(\tau)$ | Recursive term for convolution integral simplification |
| x_{ref} | Location of the reference point from the leading edge |
| x_{cos} | Aircraft location in 1-cosine gust |

Chapter 1

Introduction and Literature Review

Compound helicopters, being able to fly as an aircraft but take off and land vertically, were first introduced in the early 1950s. However, the concept received limited attention after several failure cases [1]. In the past ten years, the concept of a compound helicopter has re-emerged in rotorcraft design. Having the capability to take-off and land vertically using a main rotor like a helicopter, compound helicopters are also equipped with auxiliary systems for improved performance in fast forward flight. An implementation of such configuration has been demonstrated by the Eurocopter (now Airbus Helicopters) X3, as shown in Figure 1.1a. Besides the conventional helicopter fuselage, two short wings are added with tip-mounted propellers. Inheriting most characteristics from conventional helicopters, its propeller-wing configuration allows achieving much higher cruising speeds, going beyond the typical limitations of conventional helicopters.

One of the main limitations of conventional helicopters is the cruise speed. Indeed, their lifting and propulsive capability decrease with the forward speed due to the reduced performance of the main rotor, a single source of thrust and lift, in high-speed flight conditions. This is due to the asymmetry of lift on two sides of the helicopter. On the side where rotor blades are travelling in the same direction as the aircraft (advancing blades), as the aircraft speed gets higher, the blade travelling speed may approach the speed of sound causing a significant increase of drag, with a reduction of the rotor performance. On the retreating side, where the blades are travelling opposite



(a) Eurocopter (Airbus helicopter) X3



(b) Leonardo AW609

Figure 1.1: The short-wing/propeller configuration demonstrations

to the cruising direction, the blades experience stall conditions where lift decreases significantly. This is limiting the helicopter cruise speed.

With similar initiatives, the concept of tilt-rotors was brought in the late 1940s to overcome the helicopter's limitation in forward flight. A tilt-rotor aircraft is equipped also with a short wing and tip-mounted propellers, but, without the main rotor. The aircraft would rotate its propellers to alter between a helicopter-like and an aeroplane-like configuration. During taking off and landing, the propellers would act like helicopter rotors, providing lift together with the wing and maintaining the vertical take-off and landing ability of a helicopter. During its cruising condition, the tip-mounted propellers tilt by 90 degrees providing propulsive thrust in forward flights. The most recent model is the AW609 developed by Leonardo (formerly AgustaWestland) as shown in Figure 1.1b.

The designs of those rotorcrafts are aimed at introducing a new way of providing propulsive thrust, increasing the cruise speed while retaining the hover advantage. With this configuration, they can travel much faster than conventional helicopters, exceeding 250 mph for X3 and 300 mph for AW609 against the 150 mph, as typical speed for a conventional configuration. Furthermore, the ability of vertical take-off and landing eliminates the need for runway improvements and expansion. For these reasons, they are well suited for public services such as air ambulance, search and rescue, coast guard and passenger transport.

However, the still open issue of the high level of vibration resulting from fluid-structure interaction is exacerbated in the case of those rotorcrafts, with even more critical effects on the fatigue life of structures, maintenance costs, on-board instrumental efficiency and comfort. Therefore, being able to model and predict the complex aeroelastic behaviour associated with the wing-propeller system becomes extremely important to achieve an optimised design of such aircraft configurations. This project is inspired by the propeller-wing configuration of the compound helicopter Eurocopter X3. The study of such configuration, however, is not limited to the compound helicopter. Short aircraft wing with tip-mounted propulsive propellers is also exhibited on tilt-rotor aircraft. Having a similar propeller feature with regional aircraft, similar analysis approaches can be adapted to the short-wing and propeller configuration on small rotorcrafts. This project is an attempt of applying comprehensive analysis onto such compound aero-structures.

1.1 Literature review on simulation and analysis approaches for wing aeroelasticity

The subject of aeroelasticity emerges with the invention of aircraft. As the flight speed increases, the mutual interaction of structural elastic and inertia forces, and aerodynamics needs to be investigated, and a stiffness criteria must be specified in the design stage to prevent any catastrophic aeroelastic phenomena. Concerning the modelling and experimental efforts in the topic of aeroelasticity, several review papers were published in the past decades summarising some common aeroelasticity applications [2, 3], specifically in the area of fixed-wing aeroelasticity [4, 5], rotary-wing applications [6], instability phenomenon of flutter [7] and nonlinearity [8,9]. As aeroelasticity studies the interaction of structures with the surrounding flow, to analyse aeroelastic behaviour of a wing experiencing aerodynamic effects, there are two essential parts in the problem. Both parts need to include consideration of their interaction. The first part is characterising and mathematically modelling a solid structure for the wing, and the other part is to estimate and predict

external loadings introduced by aerodynamics of the surrounding flow. The choice of principles and theories for the structural and aerodynamic models would naturally depend on the structural configuration and operating environment associated with the flight condition. Besides, computational cost, accuracy requirement, project stages and development costs are equally important [9].

For the structural part, a short wing can be modelled in many ways, as listed in Figure 1.2. Ranging from the most simplified to the most sophisticated, they are applicable and suited for

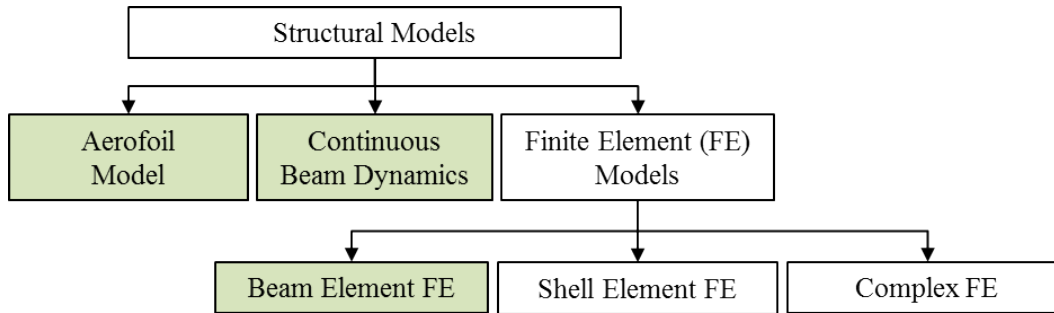


Figure 1.2: Structural models for characterising a wing, with green shading indicating applicable theories for the proposed problem

different situations. The aerofoil model, also known as the typical sectional model, takes the wing as its aerofoil cross-section, with discrete springs. This is often applied for wind tunnel wing models in which both sides are mounted on the walls. To represent a section of a finite wing, the discrete springs play the role of the elastic resistance in the degrees of freedom studied. However, the aerofoil is not representative for the elastic behaviour of the whole wingspan. In this case, a beam-like model is introduced. Having the wing root built-in and the wing tip free, classical beam theories with clamped-free boundary condition are another common mathematical representation. With simple loadings, a beam-like model can be used and solved analytically with static and dynamic loadings. Furthermore, as the loading condition becomes more complicated, a numerical model would be more suitable, hence, finite element (FE) models are incorporated based on beam theories. Depending on the structural complexity, different FE models can be applied, such as shell element models or with 3D solid elements, which contain more nodes and

require more computational efforts. For the configuration of this project, a short, unswept and uniform wing is considered. Due to the simple nature of such wings, an aerofoil model or beam-like model, as highlighted in Figure 1.2, would be the most suitable and efficient, also providing an easy coupling process for aerodynamic loadings. The models' application and mathematical backgrounds will be introduced in later chapters.

Considering the aerodynamics, there are many established theories relating to the flow condition and effects that one is interested in studying. As illustrated in Figure 1.3, from Laplace's equations, which assumes steadiness, linearity, incompressibility, inviscidity, irrotationality, to the Navier-Stokes equations which are far more versatile and proven to be accurate to real-world observations. For the task in this project, a short-wing-propeller configuration on small rotorcrafts,

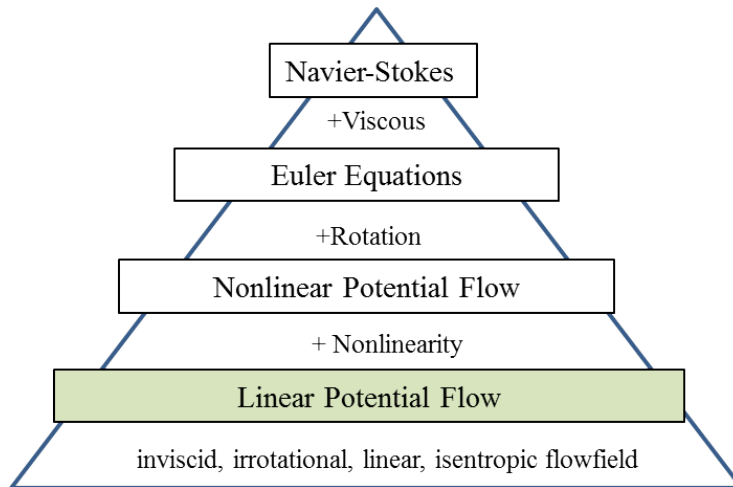


Figure 1.3: Aerodynamic theories and models suited for different flowfield conditions, with green shading indicating applicable theories for the proposed problem

like compound helicopters and tilt-rotor aircraft, is to be modelled and analysed. The short wing is designed for propeller attachment and maintains compatibility of existing vertical take off and landing (VTOL) facilities, hence, is relatively stiffer than most fixed-wings and can be considered to have only small perturbations. It operates in a subsonic regime with velocity not exceeding Mach number of 0.3, hence, an incompressible condition can be assumed. Besides, the assumptions for inviscid and irrotational flow are also valid and sufficient for the flight condition. A linear

potential flow condition is appropriate and assumed for this study.

Within the scope of this condition, Figure 1.4 shows different aerodynamic theories that can be used to model aerofoils or finite wings in incompressible inviscid flow. Various numerical solution schemes for those aerodynamic theories were developed in the past literature targeted at the flight conditions of interests. Here, however, only the original theory concept is introduced, with some references to works of other authors on the different topics.

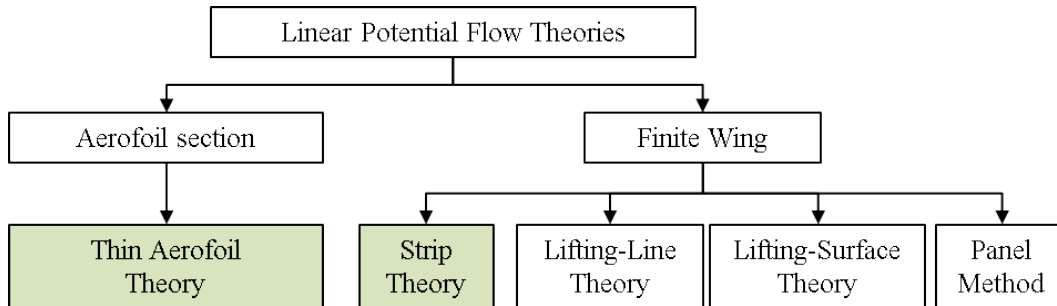


Figure 1.4: Aerodynamic Models for Incompressible Inviscid Flow, with green shading indicating applicable theories for the proposed problem

1.1.1 Aerodynamic theories for aeroelastic analyses

Thin aerofoil theories

The simplest approximation to study wing aerodynamic behaviour can be obtained referring to a thin two-dimensional aerofoil operating in inviscid, incompressible flows. In the classical development of linear potential flow theories, the velocity is written as $v = \nabla\phi$, and the Laplace equation $\nabla^2\phi = 0$ is solved to obtain the potential field around the body, imposing impermeability condition on its solid surface. The aerofoil, with a small angle of attack and camber, is modelled as a vortex sheet distributed along its camber line as shown in Figure 1.5. The strength of each vortex filament is a function defined in chord-wise direction and obtained imposing the flow tangency condition at the camber line, which represents the considered zero-thickness aerofoil.

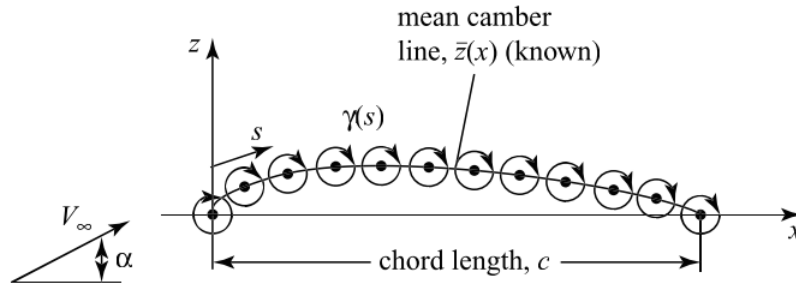


Figure 1.5: Thin aerofoil theory with vortex distribution along camber line [10]

Thin aerofoil theory gives a very well-established model with detailed features and formulations found in [10–13]. A sectional (2D) model can be also used to model quasi-steady and unsteady flow condition using Theodorsen’s and Wagner’s theory. In those models, lift and pitching moments are characterised by time-differentials of displacements, which can be directly coupled and integrated with a multi-degree of freedom aerofoil structural model.

Strip theory

Since thin aerofoil theory is only applicable in a two-dimensional space, strip theory can be applied to integrate the sectional model along the span, making the coupling with a beam-like structural model easy and straightforward. Since each aerofoil section is considered separately, an important assumption for the application of strip theory is that each chord-wise section is independent of other chord-wise sections for aerodynamic loads. However, this means that from the wing root to wing tip, the flow conditions are similar throughout. This neglects any tip effect that a finite wing would have. To incorporate a three-dimensional effect, aerodynamicists extended the theory involving a different setup in the form of a horseshoe vortex [10]. Those horseshoe vortex based theories are introduced in the following sections.

Even though there are many aerodynamics approaches taking into account various complex effects with versatile applications and close-to-reality results, thin aerofoil theory still has its place in aerodynamics simulation as it forms a preliminary understanding of lift generation. Strip theory is able to give an insight into more complex three-dimensional models.

Lifting-line theory

In the lifting-line model, a finite wing is replaced by a bound vortex and two free vortices of the same strength trailing downstream. According to the unique shape of the vortex, it is also called a horseshoe vortex. The superposition of several horseshoe vortices along the span is used to model the lift distribution on a finite wing. The circulation along the wing span can be solved when knowing the wing geometry and by imposing a flow tangency condition. Similarly, during design processes, if the desired lift distribution is known, the wing geometry can be determined. For detailed formulations of lifting-line theory, see [10–12, 14]. Many works can be found in the literature where lifting-line theory is used in modelling aerodynamic wing behaviour. For example, Loth and Loth studied the effect of tip-mounted propellers induced drag reduction using the elliptical loading distribution over the wing [15]. Similarly, Miranda and Brennan used the same elliptical loaded lifting-line theory to investigate this effect by developing also a numerical approach for the calculation of the optimum span-load distribution [16]. Concerning the limitations of the model, the lifting-line theory does not give reliable results for wings of low aspect ratios, nor it has the capability of modelling unsteady flow.

Lifting-surface theory

As the wing gets a larger chord length, the uniformity along the aerofoil chord is no longer valid in the lifting-line theory, therefore, the lifting-surface theory is introduced. In the lifting-surface theory, the wing is also represented by its camber mean surface in the chord-wise direction by ignoring the thickness effect. Instead of replacing the wing with vortex filaments only along its span, horseshoe vortices are also distributed along the chord of the wing forming a grid. The vortex strength becomes, in this model, a function of chord-wise and span-wise coordinates. This also means that a shell element FE model would be required to incorporate this chord-wise variation. For further reading of the detailed formulation, the reader can refer to fundamental aerodynamics books, e.g. books by Anderson [11] and Flandro et al. [10].

The lifting-surface theory is very well established for fixed-wings aerodynamic modelling. It can also be applied to rotary blades, especially for studying unsteady behaviour [17–19]. Williams and Hwang extended the theory for compressible flow in the prediction of unsteady and steady aeroelastic behaviour for advanced turboprops [19]. Also, it is worth mentioning the work of Cho et al., who presented the same numerical scheme in the frequency domain for modelling lift distribution under multiple harmonics [17, 18].

Related with the lifting-surface theory, the vortex lattice method is based on a representation of the wing as a superposition of a grid of horseshoe vortices. The wing is divided into panels and each panel corresponds to a horseshoe vortex. The vortex lattice method is widely used nowadays for modelling wings and propeller blades because of its simplicity and reliability. In terms of analysing the flutter effect on fixed-wing aircraft, the vortex lattice method is commonly used in conjunction with the finite element method [20–23]. An important study of the propeller-wing aerodynamic interaction by using the vortex lattice method representing the wing can be found in [24]. Dimchev used the same method to model a low aspect ratio wing for unmanned aerial vehicle designs [25]. As for its use on propeller blades, the vortex lattice method gives information about the propeller slipstream. Cho and Cho conducted a steady vortex lattice method in modelling propeller blades to investigate its effect on aircraft cruising [17]. As the vortex lattice method can be applied on both propeller blades and wings, a combination was made by Witkowski et al. and Lee, modelling both propeller and wing using the vortex lattice method [26, 27].

Panel method

When the wing section is no longer thin enough to neglect the thickness effect, the variation of flow characteristics along the chord direction needs to be considered. This can be done using the panel methods. The general idea behind all such panel methods is to cover the three-dimensional body with panels over which there is a distribution of singularities (such as point sources, doublets, or vortices). These singularities are solved through a system of simultaneous linear algebraic equations generated by calculating the induced velocity at control points on the panels and applying

the flow-tangency condition. When coupled with finite element analysis, the panel grid will need to be transformed to a corresponding mesh in order to solve the aeroelastic equations.

As for all the possible models and theories listed above, there are many available combinations for aeroelastic modelling. At different levels of computational complexity for these aeroelastic models, they serve different purposes along the lifespan of a project. Low to medium fidelity modelling tools featuring simplified structural and aerodynamic models, such as a sectional aerofoil or beam-like model, are often used in a preliminary design stage. In this way, an insight is given into a complex problem within a short period of time and information is collected to support high-level decisions [9].

Due to the lack of experimental results in the early predesign stage, the developed design tools can be validated against open literature results. There are a few established validation wings, such as results reported by Tang and Dowell in [28], Goland wing [29], Blisplinghoff, Ashley and Halfman (BAH) wing [14, 30, 31], AGARD 445.6 wing [32], BACT wing [33] and MAVRIC wing [34]. Amongst those listed, the Goland wing, unswept and uniform, is ideal for the validation tasks in this project.

As the project progresses and more detailed physical effects need to be taken into consideration, high fidelity modelling can be invested to identify test conditions, to optimise based on test data and to eliminate uncertainties. For the scope of this project, the configuration is a generic one, hence, the simulation analysis is aimed at efficiency in the pre-design stage. Low-fidelity aeroelastic simulation approaches hence are reviewed in this chapter.

1.1.2 Application of low-fidelity models in aeroelasticity studies

Aerofoil model

For wings to generate lift, they are often shaped as aerofoil for cross-sections along the length. The simplest approach would be to analyse a wing as an aerofoil section attached to springs in the motion directions. The wing structure is hence treated as a spring-mass system with multi-degrees

of freedom. This representation is often used when a rigid and span-wise uniform wing is mounted in a wind tunnel with elastic supports, or this can also correspond to a typical aerofoil section along a finite wing span with discrete springs reflecting motion resistance given structurally. This idealised and simplified configuration gives an insight into the scientific background of aeroelastic stability and dynamic response. An aerofoil model is often used for studying a certain numerical formulation or solution algorithms and the mathematical background of any structural or aerodynamic effects. Accordingly, analytical aerodynamic theories characterising airloads based on aerofoil angle of attack and other dynamic effects are available and compatible with the mass-spring aerofoil model. They are developed from linear potential theories and fitted to the subsonic flight environment of compound helicopters, tilt-rotor aircraft and other small rotorcraft with a short-wing/propeller configuration. On the topic of unsteady aerodynamic theories, comparisons and discussion of differences in methodologies and solutions are discussed in [35,36]. Commonly featured are Wagner's indicial response function, Küssner's gust response theory, Theodorsen's unsteady aerodynamic theory and Sears' sinusoidal gust response theory [37–41].

For example, Sears and Sparks used an aerofoil model with flexible plunging degree of freedom to study the non-stationary (unsteady) effect on structural deflection under sharp-edged and graded gusts [42] and, with linearity assumption, Wagner's and Küssner's functions were applied on 1 DoF mass-spring aerofoil system. Focusing on the validity of Jones' approximation for Theodorsen's theory, dynamic aeroelastic instability was studied by Kargarnovin and Mamandi [43]. Similar unsteady effect involving structural hardening nonlinearity were studied on a plunging-pitching aerofoil with Theodorsen's theory and verified by experimental data by Fichera et al. [44]. An aerofoil model was also used for investigation of nonlinear aerodynamic effects associated with static angles of attack by Strganac and Mook [45] featuring the unsteady vortex lattice method, which takes into account effects of wingtip vortex for a finite wing and implemented onto an aerofoil model by modifying the lift and pitch coefficients. On the topic of structural nonlinearity, O'Neil et al. studied the effect of nonlinear structure stiffness together within a linear flowfield using an aerofoil model [46]. The linear flow field featured was characterised by Wagner's indi-

cial response formulation. Marzocca et al. validated CFD code derived on the base of linear and nonlinear indicial response functions against an unsteady Euler equation based tool on an aerofoil model [47]. Due to the simplicity of the aerofoil model, the derivation of analytical solutions becomes possible. Marzocca et al. developed a linear aeroelastic model by integrating an aerofoil model with analytical theories for unsteady aerodynamics in the Laplace domain and studied aeroelastic responses of highly flexible wings under explosive types of loadings [48]. In the time domain, Shams et al. derived a pure analytical aeroelastic model for flutter analysis and dynamic responses featuring an aerofoil in plunging and pitching motion [49]. With a semi-analytical approach, Berci et al. applied a sectional aerofoil model to represent a quasi-slender Rayleigh beam. The effect of parabolic camber on the stability boundary was investigated analytically and aerofoil's dynamic gust response was presented [50]. The combination of aerofoil sectional model and 2D aerodynamic theories was proven sufficiently accurate in state space representing spring supported aerofoil in wing tunnel by Kurniawan and a difference of only 6.3% was observed comparing to experimental data [51].

Beam-like model

When it comes to representing a finite wing structure, however, in order to make practical and more realistic analyses, taking into account flexibility of the lifting surface is also crucial [52]. A wing can also be considered as a cantilever beam, with one end (wing root) clamped into the fuselage and the other end (wing tip) being free. 3D Finite element method (FEM) can also be an option, which is especially good for representing the wing's properties in detail. However, it drastically increases the number of degrees of freedom in consideration. For an efficient multidisciplinary optimisation tool, a beam-like model is much more suitable. In the research of aeroelasticity, the elastic axis of the beam is often featured and assumed to be straight along the span, denoting as the coordinate axis and reference point. This is simply because, at the elastic axis, torsional and bending displacements are statically uncoupled for isotropic beams. In other words, the application of a transverse force at any point along the elastic axis will result in a pure bending motion and a

moment about the elastic axis will result in a pure torsion. However, employing a beam-like model requires the cross-section being relatively uniform along the span. Also, a beam being continuous has an infinite number of degrees of freedom. Modal analysis of the beam structure is necessary for any aeroelastic behaviour to be investigated. Analytical aerodynamic theories derived on aerofoil can be implemented across the span by ignoring three-dimensional tip effects. Especially with tip-mounted propellers, propeller wake inflow can be taken into account as additional velocity components while also wing-tip vortices are less dominating. When a cantilever wing is divided into infinitely small aerofoil segments, the aerodynamic loads at a given spanwise location do not depend on those at any other location. This theory is commonly known as the strip theory.

The integration of structural and aerodynamic models to form a coupled aeroelastic system is the rationale of many studies. Depending on the aircraft and flight conditions, the structural and aerodynamic models can be matched with reasonable assumptions. One very common application is on the topic of flexible wings. Slender wings tend to be very flexible and the prediction their dynamic behaviour is of extreme importance in the preliminary design phase in prediction deformations and any possible instabilities. Flexibility, however, may bring in nonlinearity in the structure and aerodynamic formulations, hence research on nonlinear phenomena, such as Limit Cycle Oscillation (LCO) and dynamic stall in High Altitude Long Endurance (HALE) applications. Those studies are commonly carried out by a clamped-free beam model and unsteady aerodynamic theories featuring established theories and models discussed above. Application of nonlinear structural modelling methods to aeroelastic problems was discussed by Howcroft et al. [53, 54]. Including structural nonlinearity, Stodieck et al. developed a model reduction method that simplifies a 3D FE model into a Timoshenko beam-like model for rapid aeroelastic optimisation processes [55]. A linear flow field, however, is sometimes assumed for studying pre-flutter responses when small perturbations are exhibited. Employing a nonlinear structural model with a linear aerodynamic model, Frulla et al. investigated the effect of main design parameters on the onset of critical flutter velocity for flexible wings under small perturbation conditions. Experiments were also performed in pre-flutter nonlinear static equilibrium conditions, where good agreement was observed regard-

ing the numerical results [56]. A similar framework was also used by Shams et al.. They focused on the numerical time-marching scheme application and investigated the effects of coupling (using coupled mode shapes) between bending and torsional motion on nonlinear flutter prediction. The approach of obtaining coupled mode shapes, however, was not reported in the paper. By comparison with previous studies, Shams et al. also proved that linear aerodynamic approximation is reasonably accurate in predicting flutter boundaries [57]. As well as the work by Ghadiri and Razi, beam-like model containing stiffness cubic nonlinearity, typical of composite material wings, was used to study nonlinear aeroelastic behaviours combining a linear analytical theory by Wagner's indicial response model [58]. Extending from [50], Berci and Cavallaro implemented a linear beam-like model featuring Rayleigh beam theory with a modified linear strip theory corrected by doublet lattice method considering three-dimensional effects [59].

Within the same framework, aeroelastic behaviour of flexible rotor blades was also studied based on a coupled nonlinear beam-like model with quasi-steady or unsteady aerodynamic model [60–62]. Modifications on the linear beam model to include warping effect, shear deformation, rotary inertia and anisotropic materials for composite wings is also a common feature in the attempt of studying aeroelastic behaviour of thin-walled and composite wings [63, 64]. Further development on the linear aerodynamic model to include effects, such as dynamic stall, large angle of attack and compressible flow, together with structural nonlinearity, can also be found in [65–67].

Other studies were also carried out featuring attached mass on the wing [68–70]. The flutter of cantilever wing with tip mass and a transverse follower force was studied based on linear Euler-Bernoulli beam theory and Theodorsen's theory by Feldt and Herrmann [69]. Implementing a similar quasi-steady state, aerodynamic model, Gern and Librescu investigated the effect of attached mass on instability boundary with composite sweep wings [70]. Having a mounted store with plunge-pitch flexibility, the store position and dynamics would affect its stability boundary and dynamic behaviour under gust and thrust. With the added flexibility of the mounted store, the structural model can be modified. Featuring Theodorsen's theory, Fazelzadeh et al. [71] modelled a cantilever wing subjected to a tip mass and a follower force. The structural model is combined with

Wagner's indicial response model to predict the dynamic response of a wing-store system [72]. In most cases, those wings are considered slender and a Euler-Bernoulli beam theory was used. However, nonlinear aeroelastic phenomena are not eliminated, especially accounting for the deflection introduced by the attached mass. The aeroelastic model has been further developed to incorporate nonlinearity in aerodynamics [73–75].

There is limited research specifically focusing on a short wing configuration. In special cases of low-aspect-ratio wings such as a Delta wing, the chord-wise coordinate is as crucial as the span-wise coordinate and plate theories are commonly used [76,77]. Consequently, a more complex 3D aerodynamic model needs to be applied to incorporate the structural mesh. For the configuration of interest in this project, due to the aspect ratio for a short wing being comparatively low, the aerofoil cross-section along the span is uniform. Plate theories consider elasticity across the length and width of the structure. However, in wing designs, ribs are inserted to maintain rigidity in the chord direction. The structural behaviour in the chord direction is much less significant compared to that of the span-wise direction. Hence plate theories are not considered. Expanding further, a 3D finite element model also has the capability of analysing a short wing structure. It offers generality, versatility and reliability. However, in the preliminary design stage, not only is it computationally expensive and requires extra time and effort to ensure the correct physics being reproduced, but also it contains a large amount of data for pre- and post-processing. It is therefore much more suited for design refinements in later stages, where also the computational effort required can be afforded. Thus high-fidelity approaches such as 3D finite element model, computational structural or fluid dynamics (CSD-CFD) are not considered here.

However, a short and relatively stiff wing having small deflection fits within the linearity assumption given in the structural and aerodynamic theories. At the same time, propellers on the advanced rotorcraft can be integrated through a cradle on the wings, hence, making it a rigid attachment to the cantilever structure. The closest work of such application would be the research of Gennaretti et al. [78]. The attention was focused on the aerodynamic modelling of propeller wake flow and the prediction of the vibratory loads on a short tilt-rotor wing by capturing the

three-dimensional unsteady flow and the shape of wakes. The structural model based on Euler-Bernoulli beam theory is simple and takes into account flapping and torsional motions. There is clearly a gap for simple and numerically efficient analytical aeroelastic formulations on short-wing/propeller configuration in advanced rotorcrafts. The formulation would be based on aerofoil or beam-like model combined with sectional linear aerodynamic theories serving as a preliminary method to give an insight into the causes of aeroelastic instability and the prediction of time-domain responses.

1.2 Aim and objectives of thesis

As the aeroelastic properties directly affect the structure deformation and stress behaviours, the aeroelastic study of propeller-wing configuration is crucial for the development of rotorcraft technology concepts. In addition, as discussed earlier, the propeller-wing configuration studies were almost exclusively focused on flexible structures in the past literature. The development of a numerically efficient aeroelastic model can be important to the design engineers for preliminary evaluation typical of the early stages of a design for a better understanding of the short-wing/propeller interaction.

Therefore, the main aim of the project can be formulated as follow:

Model and investigate the complex aeroelastic behaviour of the short-wing/propeller configuration similar to a compound helicopter and/or a tilt-rotor configurations in order to obtain accurate and reliable predictions of structural vibration.

To achieve the main aim, it is broken down into step-by-step objectives in each chapter as listed below.

Chapter 2

- Develop a numerically efficient aerodynamic model that is compatible with 2D and 3D wing models for aeroelastic analysis.
- Investigate and simplify the propeller-wing interaction that can be easily modified and considered in the model developed.
- Validate/verify the aerodynamic model through benchmark results.

Chapter 3

- Develop a selection of structural models that are able to capture the significant effects, such as shear deformation, for a wing structure.
- Develop a versatile modal analysis tool that can be applied to all the structural model variations and validate the tool developed.

Chapter 4

- Link the aerodynamic and structural models for studying the aeroelastic behaviour of a propeller-wing configuration.
- Demonstrate the validity of the integrated model for aeroelastic analyses.
- Study the static and dynamic stability of the aeroelastic system.

Chapter 5

- Build up a series of numerical algorithms for obtaining aeroelastic response under the defined flight conditions.
- Verify different capabilities of the aeroelastic model against literature results.

- Demonstrate the capability of the combined model presented through a case study on a small propeller-wing under cruising condition.
- Discuss the different structural effects and analyse the main contributors towards the final results.

Chapter 6

- Establish core framework integrating modular structural and aerodynamic models developed
- Analyse dynamic behaviour involving different wing configuration, propeller configuration and flight conditions
- Further exploitation of flight condition types and wing's dynamic responses

1.3 Methodology and thesis outline

In order to achieve the final purpose of the project, the work can be broken down into several phases. The descriptions of each stage relating to the structure of this thesis are listed below:

1. Chapter 1: Introduction and Literature Review
 - (a) Project background study
 - (b) Literature review on aeroelastic approaches
 - (c) Set research aims and objectives
2. Chapter 2: Development of aerodynamic model
 - (a) Simplified propeller inflow effect
 - (b) Unsteady aerodynamic theories
 - (c) Application on aerofoil model and validation/verification

3. Chapter 3: Development of structure model

- (a) Derivation of beam-like wing model
- (b) Modal analysis and selection of beam theory

4. Aeroelastic model integration

- (a) Chapter 4: Aeroelastic instability analyses
- (b) Chapter 5: Solution to dynamic response

5. Chapter 6: Aeroelastic model exploitation

- (a) Parameter study regarding structure, propeller and flight configurations
- (b) Dynamic response under 1-cosine gust and continuous turbulence

In the aeroelastic model, the structural dynamics of the fixed-wing structure is modelled as a cantilever beam with a deformable elastic axis under flapping, torsional and lead-lag motion. Aerodynamic loads, such as lifting force and pitching moment, are considered and derived by unsteady 2D thin aerofoil sectional model based on Theodorsen's, Wagner's, Küssner's and Sears' theories.

Two-dimensional space is considered first and the aerodynamic model is developed incorporating effects introduced by propeller inflow. Thin aerofoil theories are investigated and different combinations of the time- and frequency domain theories are studied for the prediction of aerodynamic loads under different conditions. The propeller inflow is simplified and taken into account as several velocity components along the propeller axial and vertical directions in compatible with the aerodynamic model. The developed aerodynamic model is applied on a sectional aerofoil model with discrete springs attached for the degrees of freedom of interest and verified under disturbance and sharp-edged gust against literature results.

The structure model developed based on a cantilever beam takes into consideration of motion coupling, rotary inertia and shear deformation. A numerical efficient approach based on the trans-

fer matrix is developed for performing modal analyses. The significances of different structural effects are evaluated through natural frequencies and mode shapes obtained from the modal analyses. A certain combination of the beam theories is confirmed for representing the short wing in the compound configuration.

The developed aerodynamic and structural models are to be integrated to form the aeroelastic model. In performing aeroelastic analyses, a numerical model for studying aeroelastic stability is also built and validated. Subsequently, the time-domain dynamic response can be obtained. Verification of the solution process is carried out against similar cases in the literature. With the completion of verification, it can be implemented onto the short wing configuration for predicting its aeroelastic behaviour.

Following the completion of the aeroelastic model and the case study, further exploitation of the model are to be carried out by varying dimensional parameters and flight conditions. A core framework is developed integrating different modular solvers, regarding structure configuration, propeller design and flight conditions, into a strategy diagram. Through the core framework, parameter variations in structural configuration, propeller design and flight conditions are studied for their effects on the overall dynamic behaviour. Furthermore, two different types of flight condition, namely 1-cosine gust and continuous turbulence, are considered. Utilising the same framework and the modular models developed, the responses can be obtained and analysed.

Chapter 2

Representation of Aerodynamic Loadings

In the quest to study the aerodynamics of a propeller-wing system, an aerodynamic model is developed to understand the external loading generation and characterisation in the aeroelastic system. The aerodynamic model needs to be simple and numerically efficient, hence, it is derived from 2D aerofoil theories. This chapter describes the development of an aerodynamic model for characterisation of airloads generated in the propeller-wing system. For understanding the generation of lift and the contribution of a propeller, aerodynamic phenomena are studied for the integrated system.

Many propeller-wing configurations, including applications in compound helicopters, small commuter aircraft and tilt-rotors, are differentiated and discussed. For the main interest of this thesis, a short and relatively stiff wing with tip mounted propeller is the focus. With a tip-mounted propeller, the flow condition around the wing is simplified into different airflow velocity components. Next, in order to find suitable aerodynamic theories, established analytical theories for airload predictions are investigated. To start with, the steady aerodynamic theory is introduced as it can give a preliminary insight into the loading magnitude at different sections of the wing. However, it is not sufficient for predicting the dynamic response. In order to consider dynamic airload behaviour, quasi-steady and unsteady aerodynamic theories are also discussed. Theories both in time and frequency domains are covered, namely Wagner's, Theodorsen's, Küssner's and Sears' aerodynamic theories. Due to the different theoretical background, these theories are selectively

combined and applied on an aerofoil section model to verify and demonstrate their practical application to literature case studies. During these studies, an optimisation algorithm is proposed and tested with time-domain unsteady aerodynamic theories. At the same time, differences between quasi-steady and unsteady aerodynamic theories are discussed and analysed in specific case study examples.

In this chapter, the effects of a tip-mounted propeller on the wing will be specified into velocity components based on the general characteristics of a propeller in Section 2.1. Aerodynamic theories, from steady, quasi-steady to unsteady aerodynamics, will be reviewed in Section 2.2, 2.3 and 2.4 to suit the application of the specified flow condition. Lastly, the aerodynamic model will be integrated with an aerofoil model and verified based on literature examples in Section 2.5.

2.1 Aerodynamic effects in propeller-wing configuration

Before looking into the specifics in propeller and wing interaction, a crucial aspect is to discuss the contribution of main rotor wake on the propeller/wing system. In the layout of a compound helicopter, the wing and main rotor share the total lift that the aircraft requires under different flight conditions. In fact, the optimum performance of the auxiliary system (propeller/wing) relies on the size of that auxiliary system. While having the ability to offload the main rotor at high speeds, at a low aspect ratio, the wing does not extend into the higher-velocity region of the rotor wake [79,80]. The flow field around a sample compound helicopter was presented with no interference of main rotor wake onto the wing in [81]. In [82], the aerodynamic interaction between rotor wake and airframe is discussed for conventional helicopters. As illustrated in Figure 2.1, it is clear that, under hovering and low-speed flight conditions, the main rotor wake is expected to envelop more of the fuselage front than during high-speed flights.

For compound helicopters, the fact that the wing offloads the main rotor at high speeds results in a high advance ratio and consequently makes the rotor wake less dominating to the wing structure than the propeller slipstream. Hence, the main rotor effect is not considered under cruising

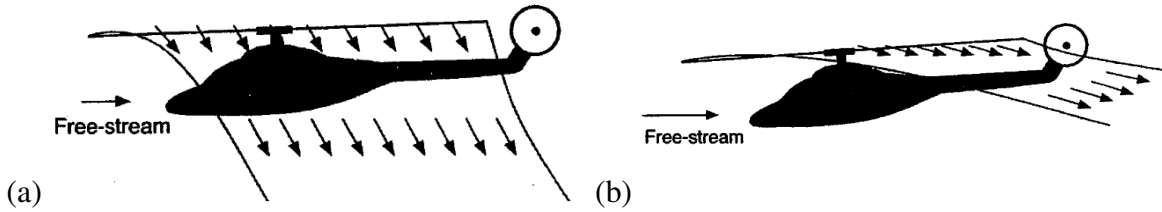


Figure 2.1: Main rotor wake under: (a) low speed forward flight (b) high speed forward flight [82]

condition in the present study. Although there is a very limited amount of work done in documenting the main rotor effect on a wing in forward flight, as it is highly dependent on flight conditions and design of the aircraft, studies into understanding the interaction between rotors, wings and propellers will be very beneficial for the further development of such rotorcraft.

Many small commuter aircraft feature turboprop engines, however, considering bending that would be introduced to the wing as a beam-like structure, turboprop engines are mostly mounted near to the wing centre and the fuselage. For wing-propeller configurations in this project, propellers are mounted at the wing tip, which requires a much stiffer wing design and results in less interaction of propeller wake into the wing structure. Another similar application of the propeller-wing configuration is tiltrotors. Tiltrotors change the angle of the propeller front to maintain a balance between lift and propulsion. Under hovering, also known as helicopter mode, propellers turn into vertical rotors providing lift to the rotorcraft. During cruising, known as its aeroplane mode, propellers are aligned in advancing direction giving propulsion. The aeroplane mode of tiltrotor is a similar application to the compound helicopter wing-propeller system. Hence, the aerodynamic model can also represent tiltrotors' wing-propeller system under aeroplane mode.

For the aerodynamic effects, there are two categories of airflow components involved, one is the advancing flow present for the whole span, similar to the case of a fixed wing, and the other is introduced due to the presence of a tip-mounted tractor propeller. Under cruising condition, each segment of the wing span is moving forward at a constant speed. In most cases, wings are not built horizontally. The angle between the chord and the advancing direction is an important parameter in generating lift. Hence in some cases the chord is built at an angle relatively to the aircraft

horizontal axis and this angle is termed as the pretwist angle in this thesis. If a pretwist angle is present, it can be considered as an angle itself or as an equivalent step gust which reproduces the relative angle between the chord and the advancing direction, hence it creates the same effect.

Propellers, however, pull air streams through and contribute to flow-approaching velocity near the propeller-covered areas. As illustrated in Figure 2.2, along the aircraft advancing direction, the airflow approaching profile U_a starts with a uniform cruising speed and sees a gradual addition due to propeller inflow. At the same time, propellers affect the vertical velocity profile. As each rotating blade passes the wing, a vertical velocity component is introduced. After some time, air streams are formed in a sinusoidal fashion.

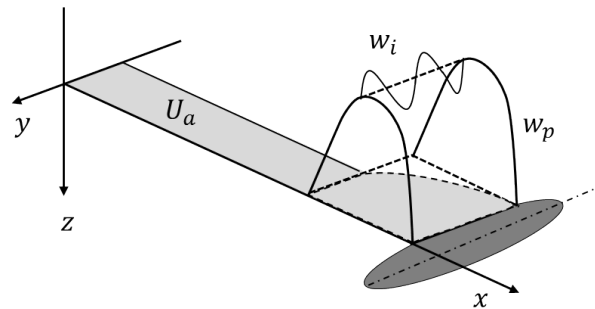


Figure 2.2: Parabolic axial and vertical velocity components added by presence of a propeller

These airflow components all contribute to the whole system dynamics in the form of forces and moments. In the following sections, aerodynamic theories that translate different airflow components into aerodynamic loadings are explained and applied in a numerical aerofoil model. Finally, verification of the aerodynamic model is studied through similar research work in literature.

2.2 Steady aerodynamic theory

In order to characterise aerodynamically-induced loads, namely lift and aerodynamic moments, some properties of the flow and aerofoil need to be clarified, as they play crucial roles in the generation of those loads. Starting with static parameters, the steady lift and moment can be

defined independently of the rate and acceleration of the lifting surface. First of all, the surrounding conditions are to be taken into account. This includes air density of the flow ρ , which is commonly linked with flight altitudes. The relative velocity between airflow and aerofoil U_a is another key factor, as well as its relative angle with respect to the aerofoil which is known as the angle of attack (AoA). Doubtlessly, the area of the lifting surface should also be considered. A larger wing would result in a greater lift under the same circumstance. On an aerofoil section, the chord length c is the representation of the lifting surface. In Figure 2.3, an aerofoil section is illustrated accordingly with those properties. Taking a unit length of the wing, the steady lift and aerodynamic moment, acting upon the aerodynamic centre, can be defined theoretically as

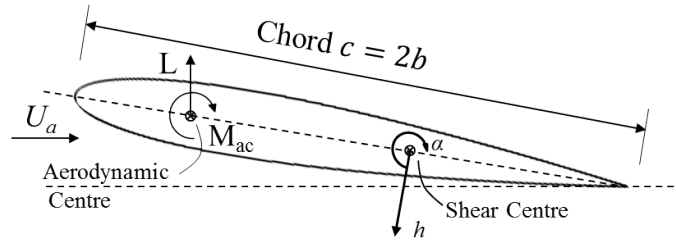


Figure 2.3: An aerofoil in steady flow

$$L = -\frac{1}{2}\rho U_a^2 c C_L \alpha_{AoA} \quad M_{ac} = \frac{1}{2}\rho U_a^2 c^2 C_M. \quad (2.1)$$

Having plunging h and pitching α degrees of freedom defined at the aerofoil shear centre, the AoA is only contributed by the pitching displacement α in steady flow. Also within the defined expression, C_L is the gradient between lift coefficient and the angle of attack and C_M is the moment coefficient. Both are dependent on the aerofoil shape. For the case of symmetric aerofoil as in Figure 2.3, C_M is zero. As for C_L , it is considered as a constant for linear aerodynamic theories, and as equal to 2π for thin aerofoil theory. However, when computational simulation or experimental data is available, the simplification should be removed, and results from those studies should be used.

As for the thesis objectives, one of them is to develop a numerically efficient model for the consideration of different aerodynamic effects in 2D and 3D wing models. Experimental data or extensive numerical flow field simulation do not fall into the objective outline. Instead, thin aerofoil theory provides a preliminary understanding of lift generation and gives an insight into more complex three-dimensional models, hence it is being implemented. With thin aerofoil theory, the aerodynamic centre is assumed to be at one quarter chord behind the leading edge, where aerodynamic loads are acting upon. Therefore, M_{ac} equals to zero. Meanwhile, Equation (2.1) can be simplified as

$$L = -2\pi\rho bU_a^2\alpha \quad M_{ac} = 0, \quad (2.2)$$

in which b is the half chord length. In this thesis, the shear centre is used as the reference point, hence the aerodynamic moment is introduced by the offset distance between the aerodynamic centre (quarter chord) and the shear centre. A simple case is demonstrated here with parameters listed as

$$b = 0.3 \text{ m} \quad U_a = 128 \text{ m/s} \quad a = -0.277 \quad \rho = 1.225 \text{ kg/m}^3,$$

where ab is the distance between aerodynamic centre and half chord, hence, the aerodynamic moment at the shear centre M_α can be written as $M_\alpha = b(1/2 + a)L$. Referencing to the shear centre, the lift (L_h) and pitching moment (M_α) would be proportional to the AoA before reaching stalling as illustrated in Figure 2.4.

Thin aerofoil theory does not account for stalling, which is a critical point of flow separation. Since during the operation of the wing-propeller configuration, the incident angle of the wing would not go near the critical stalling point (typically 10 deg to 15 deg), thin aerofoil theory is sufficient for this thesis.

Steady aerodynamics is the simplest theory for describing the loading condition of an aerofoil in steady flow. It is also the key to an important static aeroelastic instability named divergence. However, in terms of studying the aeroelastic response of a system, steady aerodynamics has its limitations. As time is not factored into the whole picture, transient or oscillatory steady-state

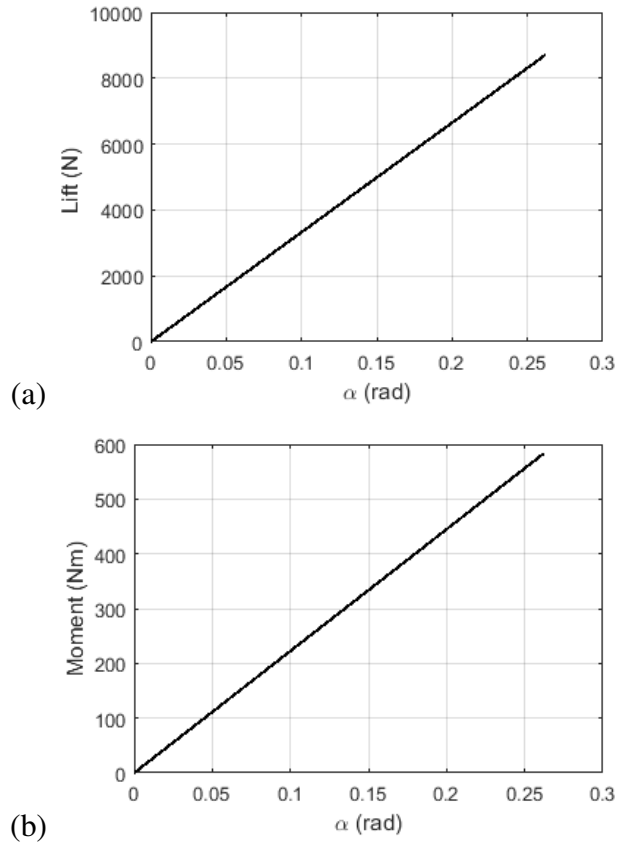


Figure 2.4: Linear increment for (a) lift and (b) pitching moment due to the AoA before stalling

response cannot be taken into account. Therefore, in order to predict aeroelastic response under oscillatory input, such as the one in propeller-wing configurations, unsteady effects have to be taken into consideration.

2.3 Quasi-steady aerodynamic theory

Between pure steady and unsteady aerodynamic theories, quasi-steady aerodynamic theory is a simplified approximation for quantifying unsteady aerodynamic loadings. It implies that the aerodynamics loads are dependent only on the instantaneous motion of the lifting surface. This is again a very convenient and efficient way to consider unsteady behaviour of an aeroelastic system, hence it was widely used in the pre-design stages. Following the basic format of lift generation, the lift is

defined by air density ρ , airflow velocity U_a , lifting surface area (defined by the chord length c) and AoA. Inheriting from the static aerodynamics, naturally the pitching displacement α is contributing towards the AoA. Since quasi-steady aerodynamic theory considers velocities and acceleration of the aerofoil, the relative angle between aerofoil chord and aerofoil resultant velocity needs to be modified, as well as the AoA.

In quasi-steady aerodynamic theory, the instantaneous AoA is measured at the three-quarter chord of the aerofoil. As shown in Figure 2.5, with defined motions at the shear centre, the changing rate of motion creates an additional velocity component in the plunging direction at the three-quarter chord point.

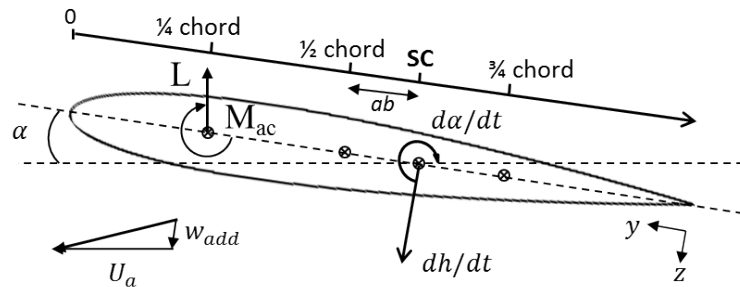


Figure 2.5: Aerofoil in quasi-steady aerodynamics

The shear centre is located behind the mid-chord point by length ab . The additional velocity component w_{add} then can be written as $w_{add} = \frac{dh}{dt} + b(0.5 - a)\frac{d\alpha}{dt}$. Overall, the angle between aerofoil chord and aerofoil resultant velocity, also the instantaneous AoA, can be written as $\alpha_{AoA} = \alpha + w_{add}/U_a$. With thin aerofoil theory, the quasi-steady lift and moment can be obtained by substitution of the instantaneous AoA as

$$L = -2\pi\rho bU_a^2\left(\alpha + \frac{dh}{dt} + b(0.5 - a)\frac{d\alpha}{dt}\right) \quad M_{ac} = 0 \quad (2.3)$$

Despite the simplicity and common usage of quasi-steady aerodynamic theory, limitations of the method need to be pointed out before any application. As stated by Haddadpour and Firouz-Abadi, the validity of quasi-steady approximation is accepted for flutter analysis in the special

supersonic flow regime. However, for usage in general in the subsonic flow regime, the same approximation is not reliable except for a few special cases [83]. Instead, the unsteady aerodynamic theory is much better suited for the analyses under incompressible subsonic flow.

2.4 Unsteady aerodynamic theories

For thin and rigid aerofoils undergoing small plunge and pitch motions in inviscid incompressible flow, analytical theories are available for characterising aerodynamic loadings in a simple and efficient way. However, as discussed, neither steady aerodynamic theory nor quasi-steady aerodynamic theory is sufficient for the application in this thesis. Unsteady aerodynamic theories are investigated in this section.

One of the differences between quasi-steady and unsteady aerodynamic theory is the consideration of transient behaviour. Lift, in general, is directly linked with advancing velocity of the aerofoil, density of the surrounding flow, aerofoil chord length and the AoA. When studying the dynamics of an aerofoil, changing of the AoA is of initial interest. Lift changes as the AoA changes. However, the transition is not instantaneous. In fact, the aerofoil needs to travel several chord length before reaching its steady state. This delay is caused by vortices formed at the trailing edge. Unsteady aerodynamic theories take into account the changes of lift at each time interval and its transition towards the steady state. Another difference is that unsteady aerodynamic theories introduce non-circulatory effects. Non-circulatory loadings, stemming from apparent-mass/inertia effects, are generated by the acceleration of fluid particles surrounding the oscillating body.

In this section, four main theories, namely Wagner's, Theodorsen's, Küssner's and Sears' models, are introduced, compared and applied to an estimated short wing configuration. Wagner's and Theodorsen's models both consider the advancing flow properties and the simultaneous motion of the lifting surface. Wagner's model features a convolution integral of the Wagner's function in the time domain, while Theodorsen's model involves a combination of Bessel functions giving a prediction of unsteady airloads in the frequency domain. On the other hand, a vertical velocity

profile along the span may be referred to as gust and can be taken into account via the Küssner model and the Sears' models. In the time domain, Küssner's model is able to predict resultant loads when the aerofoil enters an arbitrary gust field. Also, due to the nature of propeller inflow, steady-state lift and moment, induced by sinusoidal velocity field, can be obtained by Sears' model in the frequency domain.

All these four theories come from linear potential flow theory, however, the choice of time-domain or frequency-domain approach depends on the primary interest of the problem. When studying the transient response of an aerofoil under disturbance, time-domain theories are the most suitable and applicable. While, for stability analysis or obtaining steady-state responses, simple harmonic motions are assumed for all degrees of freedom analysed. Therefore, critical velocities or harmonic frequencies are the main interests. In this case, frequency-domain theories are preferred.

For all unsteady aerodynamic theories in the time domain, dimensionless time $\tau = U_\infty t/b$ is used, which considers a dimensionless unit as how long the aircraft needs to travel half a chord distance b at an advancing velocity U_∞ . On the other hand, in the frequency domain another dimensionless parameter, reduced frequency $k = \omega b/U_\infty$, is often featured. It is a parameter that defines the steadiness of the system. When $k = 0$, this indicates the steady state. While for k ranging between 0 to 0.05, the system can be treated as quasi-steady. As k goes beyond 0.05, unsteady aerodynamic theories need to be applied.

2.4.1 Time-domain indicial response: Wagner's model

Consider an aerofoil with plunging h (positive downwards) and pitching α (positive nose up) degrees of freedom, as shown in Figure 2.6. Its unsteady aerodynamic behaviour can be modelled by the Wagner's function with lift L_a and pitching moment M_a , where L_a is referenced to L_C and L_{NC} as $L_a = L_C \cos \alpha + L_{NC}$.

As lift is associated with circulation around an aerofoil, the growth of circulation gets slowed down by the counteracting vortices. Hence from a change of AoA to change in aerodynamic

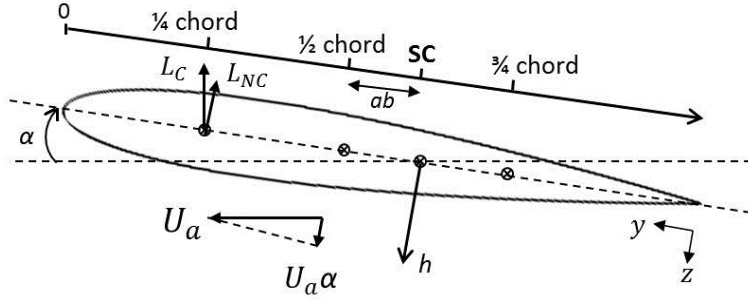


Figure 2.6: Aerofoil Model with Pitching and Plunging

loadings, an algorithm is needed to quantify this transition. Wagner's theory gave an explanation and quantification to this transition. Wagner considered an aerofoil undergoing step changes of AoA in a flow, and formulated the circulatory part of the unsteady lift [37]. Based on the theory of oscillating aerofoils, the circulation is determined by the downwash velocity at the 3/4 chord point from the leading edge, which is a similar concept to the instantaneous AoA discussed in Section 2.3, and consists of the following three components:

- $\frac{dh}{dt}$ Downwash due to vertical translation;
- $U_a \alpha$ Downwash component from the advancing speed at a pitching angle α ;
- $b(\frac{1}{2} - a) \frac{d\alpha}{dt}$ Downwash due to torsional motion.

These three components are exactly the same three contributors to the instantaneous AoA. Combining these three components, downwash velocity at the 3/4 chord point can be formulated in dimensionless time ($\tau = U_\infty t/b$) domain as

$$w_{3/4}(\tau) = \frac{U_\infty}{b} \dot{h} + U_a \alpha + (\frac{1}{2} - a) U_\infty \dot{\alpha}, \quad \text{where } \dot{h} = \frac{dh}{d\tau} \text{ and } \dot{\alpha} = \frac{d\alpha}{d\tau}. \quad (2.4)$$

To keep track of step changes in the AoA at every time step for its transition towards steady-state status, the downwash at every time step is integrated against the Wagner's function $\phi(\tau)$

$$\phi(\tau) = 1 - A_1 e^{-b_1 \tau} - A_2 e^{-b_2 \tau},$$

where $A_1 = 0.165$, $A_2 = 0.335$, $b_1 = 0.0455$ and $b_2 = 0.300$. Wagner's function $\phi(\tau)$, as illustrated in Figure 2.7, describes the growing pattern of aerodynamic lift and is determined by Bessel functions [84].

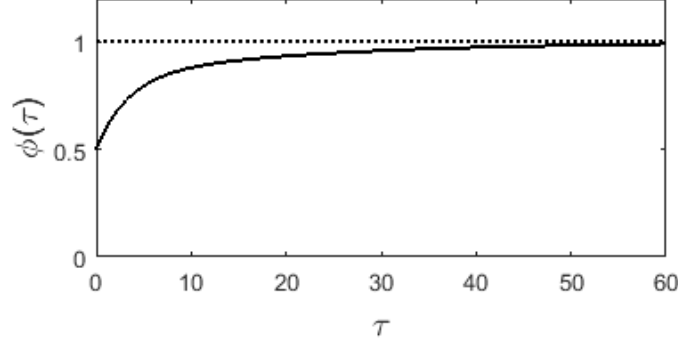


Figure 2.7: Wagner's function $\phi(\tau)$ against dimensionless time describing transition to steady state

In here, the Wagner's function is expressed using R.T. Jones' approximation [85, 86] as it is easy to manipulate, especially for its simplicity with the application of the recursive algorithm. Other forms of approximation can be found in [82, 84], but will not be considered here.

When there is a step change of the AoA, the induced lift would not instantaneously attain its steady-state value. Instead, when $\tau = 0$, it starts with half of the steady-state value. As τ increases, $\phi(\tau)$ is gradually going towards unity indicating that the lift is gradually growing towards a steady-state value. Hence the circulatory lift L_C can be obtained through a convolution integral of the downwash $w_{3/4}$ and the Wagner's function $\phi(\tau)$ as

$$L_C(\tau) = -C_L b \rho U_a \left(\phi(\tau) w_{3/4}(0) + \int_0^\tau \phi(\tau - \tau_0) \frac{dw_{3/4}}{d\tau_0} d\tau_0 \right), \quad (2.5)$$

where C_L is the gradient for lift coefficient against the AoA, here taken as 2π due to thin aerofoil theory, b is the half chord length, a is the dimensionless position measuring the location of shear centre from mid-chord, ρ is the air density, U_a is the flow approaching speed, and $\phi(\tau)$ is the Wagner's function.

Recalling the lift formulation in Equation 2.1, the convolution integral of downwash velocity and Wagner's function can also be regarded as the effective AoA at each time interval. With the

basic format of lift generation, similar to Equation (2.1), the circulatory lift can be presented as

$$L_C(\tau) = -C_L b \rho U_a^2 \alpha_{\text{AoA}}^{\text{eff}} \quad \text{where} \quad \alpha_{\text{AoA}}^{\text{eff}} = \frac{1}{U_a} \left(\phi(\tau) w_{3/4}(0) + \int_0^\tau \phi(\tau - \tau_0) \frac{dw_{3/4}}{d\tau_0} d\tau_0 \right), \quad (2.6)$$

The circulatory lift is always normal to the resultant advancing velocity, as illustrated in Figure 2.6. With a small angle of incidence, the corresponding moment M_C can be written as

$$M_C(\tau) = -b \left(\frac{1}{2} + a \right) L_C. \quad (2.7)$$

At the same time, the acceleration of fluid particles surrounding the aerofoil also contributes to the aerodynamic loading. This is commonly termed as apparent mass. The loads generated from this origin is not due to circulation created by the AoA, hence it is from a non-circulatory nature and determined by the apparent mass $\pi \rho b^2$, as follow [84]

- $\pi \rho b^2 \left(\frac{d^2 h}{dt^2} - ab \frac{d^2 \alpha}{dt^2} \right)$ Lift due to vertical acceleration at mid-chord;
- $\pi \rho b^2 U_a \frac{d\alpha}{dt}$ Lift due to centrifugal effect at 3/4 chord.

As for the non-circulatory moment, besides the ones corresponding to each lift components, one extra term associated with the nose-down couple (pure moment) is present, which can be written as $-\frac{\pi \rho b^4}{8} \frac{d^2 \alpha}{dt^2}$.

By summing up all the lift components and the nose-down couple, the non-circulatory lift and moment can be written as

$$\begin{aligned} L_{NC}(\tau) &= -\frac{1}{2} \rho C_L U_\infty^2 (\ddot{h} - ab\ddot{\alpha}) - \frac{1}{2} \rho C_L b U_a U_\infty \dot{\alpha} \\ M_{NC}(\tau) &= +\frac{1}{2} ab \rho C_L U_\infty^2 (\ddot{h} - ab\ddot{\alpha}) - \frac{1}{2} \left(\frac{1}{2} - a \right) \rho C_L b^2 U_a U_\infty \dot{\alpha} - \frac{1}{16} \rho C_L b^2 U_\infty^2 \ddot{\alpha}. \end{aligned} \quad (2.8)$$

Note that the expressions for \ddot{h} , \dot{h} , $\ddot{\alpha}$ and $\dot{\alpha}$ in Equation (2.8) are differentiations with respect to dimensionless time τ . These non-circulatory loads are not included in the quasi-steady aerodynamic theory. Under the supersonic flow regime, the reduced frequency k tends to be low, in which case the non-circulatory loads have a minor effect in bending-torsion flutter of cantilever wing as stated by Fung [84]. However, under subsonic flow, the reduced frequency is higher which leads

to non-circulatory loads having a much greater effect. Hence, unsteady aerodynamic theories, that take into account those effects, are better suited.

With the addition of a propeller, the flow approaching velocity U_a is not uniform along the span. Therefore, it is important to distinguish between aircraft advancing velocity U_∞ and U_a in the formulation process. With Wagner's model, velocity variation along the span U_a can be considered together with the instantaneous and historical motions of the lifting surface. However, the Wagner's model uses convolution integrals to take into account the aerofoils aerodynamic history. Consequently, a large set of data is needed at each iteration of the numerical process performed, decreasing the numerical efficiency of such a simplified approach. To overcome inefficiency brought by convolution integrals, a recursive algorithm is implemented to update the loading status based on one previous data point. Since the convolution integral is a common feature for time-domain aerodynamic theories, the application of the recursive algorithm will be discussed at the end of this section, when all unsteady aerodynamic theories are covered.

2.4.2 Frequency-domain unsteady response: Theodorsen's model

Theodorsen's approach is widely used for frequency-domain analyses of fixed-wing aircraft and helicopter rotor dynamics. It gives a solution for aerodynamic lift and moment of an aerofoil undergoing small harmonica oscillations in inviscid incompressible flow. Since Wagner's theory and Theodorsen's theory both were derived from linear potential flow theory, they share the same principles, such as determining the effective AoA through downwash velocity at the 3/4 chord and the formulation of non-circulatory loads. Theodorsen found that the circulatory lift can be formulated in the frequency domain as

$$L_C = -C_L b \rho U_a C(k) w_{3/4}, \quad (2.9)$$

where $C(k)$ is the lift deficiency function proposed by Theodorsen defined as a combination of Bessel functions

$$C(k) = \frac{H_1^{(2)}(k)}{H_1^{(2)}(k) + jH_0^{(2)}(k)}, \quad \text{where} \quad H_n^{(2)}(k) = J_n(k) - jY_n(k).$$

$H_n^{(2)}(k)$ is Hankel functions of the second kind, which can be expressed in Bessel functions of the first kind $J_n(k)$ and second kind $Y_n(k)$. As reduced frequency k is one of the parameters that defined steadiness of the system, plotting the real and imaginary parts of $C(k)$ helps understanding the lift deficiency pattern throughout its development from transient towards steady state.

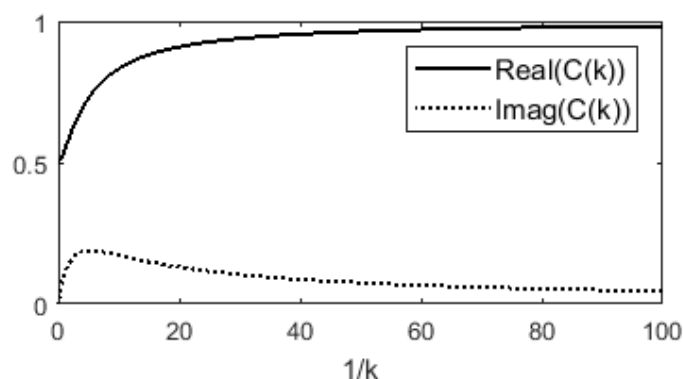


Figure 2.8: Theodorsen's function $C(k)$ against $1/k$ describing transition of lift and phase lag

It can be seen in Figure 2.8 that when k tends to infinity ($1/k \approx 0$), the Theodorsen's function gives $C(k) = 0.5$. This indicates that as the angle of attack changes, lift starts with half of its steady-state value, which aligns with the statement of Wagner's function $\phi(0) = 0.5$. As k gets smaller, going towards a steady state, the real part increases, showing an increase in lift amplitude. Meanwhile, a phase lag is introduced. Finally, when k approaches zero, $C(k)$ marches towards unity for a steady state.

Going back to the basic format of lift generation, in Theodorsen's theory, the effective AoA is expressed as $\alpha_{\text{AOA}}^{\text{eff}} = C(k)w_{3/4}/U_a$. If $C(k) = 1$, one can find that this expression is identical to the AoA in quasi-steady definition, as given by Equation (2.3). Again, the circulatory lift is

perpendicular to the resultant advancing velocity as illustrated in Figure 2.6. With a small incident angle, the corresponding moment M_C is formulated as

$$M_C = -b(1/2 + a)L_C. \quad (2.10)$$

Non-circulatory terms again share the identical formulations with the Wagner's model referring to the shear centre. Therefore, the aerodynamic lift and moment can be written, similarly to Equation (2.8), but in the frequency domain, as

$$\begin{aligned} L_{NC}(k) &= -\frac{1}{2}\rho C_L U_\infty^2 (\ddot{h} - ab\ddot{\alpha}) - \frac{1}{2}\rho C_L b U_a U_\infty \dot{\alpha}; \\ M_{NC}(k) &= +\frac{1}{2}ab\rho C_L U_\infty^2 (\ddot{h} - ab\ddot{\alpha}) - \frac{1}{2}\left(\frac{1}{2} - a\right)\rho C_L b^2 U_a U_\infty \dot{\alpha} - \frac{1}{16}\rho C_L b^2 U_\infty^2 \ddot{\alpha}. \end{aligned} \quad (2.11)$$

Theodorsen's theory is one of the most commonly featured tools for the investigation of aeroelastic instability, especially with proven validity for analyses in the subsonic flow regime [83]. However, when it comes to solving time-domain transient response, frequency-domain theory as Theodorsen's has very limited usage, the Wagner's theory is better suited instead.

2.4.3 Time-domain arbitrary gust field response: Küssner's model

With the configuration of a tip-mounted propeller, some part of the wing is immersed in the non-uniform propeller-wake flow. Clearly, the propeller-wake flow would affect the overall airloads on the wing. To distinguish effects from changes of AoA taken into account by Wagner's or Theodorsen's theory and effects induced from vertical velocity field, Küssner's theory is introduced for mathematical modelling of the propeller-wing aerodynamics.

For the case studies, in the vertical direction, several velocity components need to be taken into consideration. Firstly, to reproduce effects of the wing's built-in angle (ε_0), an equivalent step gust ($w_0 = U_a \tan \varepsilon_0$) going through a horizontally-placed wing can be used along the full length of the wing span. As discussed earlier, the aerodynamic loadings are all introduced based on the relative angle between the advancing flow and the chord. As long as the relative angle is kept, the aerodynamic effects caused by a structural pre-twist and a step gust along the span

are equivalent. It is also important to point out that the nature of pre-twist effect is not based on incoming wake flow, however, the representation of pre-twist effect through step-like gust is to simplify the structural mathematical equations. By aligning the aircraft horizontal axis and the advancing velocity, stiffness coupling due to the pre-twist angle can be simply treated as a coordinate rotation problem. The step-like gust distributions along the span and along time are presented in Figure 2.9.

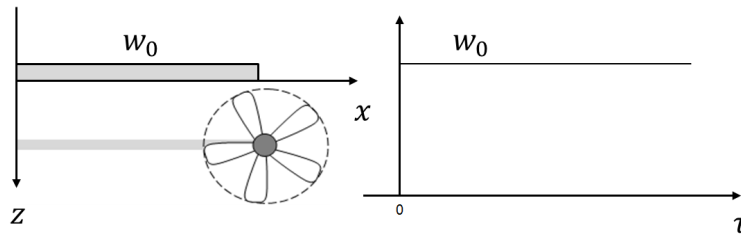


Figure 2.9: Uniform step-gust $w_0(\tau)$ along span

As for the propellers, in the propeller-covered area, a velocity profile w_p is present with sinusoidal variation w_i . As each blade passes, there is a vertical velocity profile induced onto the wing surface, symmetrical to the propeller axis. Due to the propeller location being tip-mounted, only the first symmetrical half is overlapping with the wing span, and it is considered as w_p . The velocity profile is illustrated in Figure 2.10.

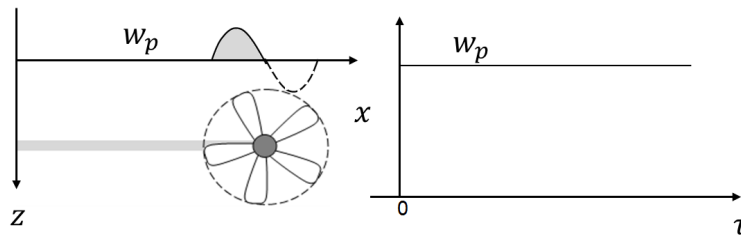


Figure 2.10: Step velocity profile $w_p(\tau)$ along span

The sinusoidal variation w_i captures the periodic nature of propeller slipstream. As illustrated in Figure 2.11, a sinusoidal gust with amplitude of w_i^a , frequency of ω_p and advancing speed of U_a is approaching an aerofoil. For previously determined reference point being the aerofoil shear

centre, the vertical gust can be expressed as below

$$w_i(x, t) = w_i^a(x) \sin \omega_p(t - b(1 + a)/U_a) \implies w_i(x, \tau) = w_i^a(x) \sin k_p(\tau - U_\infty(1 + a)/U_a),$$

where ω_p is the blade-passing frequency relative to the wing, $k_p = \omega_p b/U_\infty$ is the blade-passing frequency in the dimensionless time domain.

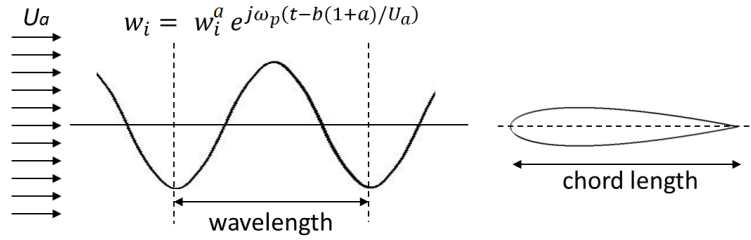


Figure 2.11: Sinusoidal Gust

Combining these three components, overall, the total vertical velocity component can be written as

$$w_G(x, \tau) = \begin{cases} w_0(x, \tau) & \text{without propeller} \\ w_0(x, \tau) + w_p(x, \tau) + w_i(x, \tau) & \text{with propeller.} \end{cases} \quad (2.12)$$

Similar with the unsteady aerodynamic loading presented in Section 2.4.1, lift and pitching moment exerted on the aerofoil can be expressed with Küssner's function, considering the convolution integral to find the time-domain transient lift response to an arbitrary vertical upwash field [14, 82].

Recalling the definition for dimensionless time τ , it is the amount of time needed for an aerofoil to travel half of its chord length. In Wagner's theory, the AoA changes instantaneously over the whole chord at $\tau = 0$. Whereas in Küssner's theory, the AoA changes progressively as an aerofoil penetrates into the gust field. At $\tau = 2$, which is the amount of time needed to travel the whole chord, the aerofoil is then fully immersed in the gust. Hence, Küssner proposed a function which describes the lift progression from $\tau = 0$ towards steady state, as illustrated in Figure 2.12.

Instead of having half of the steady-state lift from $\tau = 0$, Küssner considered the transient lift starting from zero. Like the Wagner's function $\phi(\tau)$, the exact formulation of the Küssner's function $\psi(\tau)$ consist of Bessel functions, however, for easy implementation, it is replaced by an

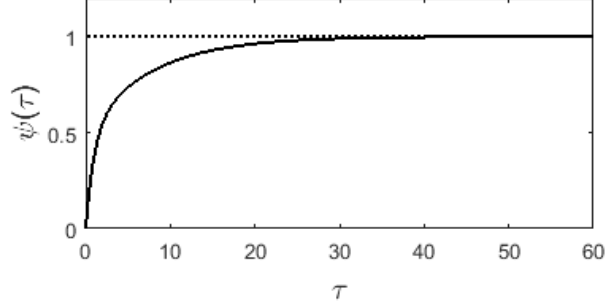


Figure 2.12: Küssner's function $\psi(\tau)$ against dimensionless time τ describing transition towards steady state

exponential approximation. Here, the Küssner's function $\psi(\tau)$ is defined as approximated by Sears and Sparks [42] as

$$\psi(\tau) = 1 - A_3 e^{-b_3 \tau} - A_4 e^{-b_4 \tau},$$

where $A_3 = 0.500$, $A_4 = 0.500$, $b_3 = 0.130$ and $b_4 = 1.000$ and other approximate forms of the Küssner's function can be found in [14, 82].

To integrate gust effects at every time step and their influence on the overall solution, the convolution integral of the defined velocity field with Küssner's function is implemented. Like Equation (2.5), the lift due to arbitrary velocity upwash field can be expressed as

$$L_g(\tau) = -C_L b \rho U_a \left(w_G(0) \psi(\tau) + \int_0^\tau \psi(\tau - \tau_0) \frac{\partial w_G(\tau_0)}{\partial \tau_0} d\tau_0 \right). \quad (2.13)$$

Since gust load is entirely circulatory, lift is exerted at the 1/4 chord from the leading edge. Accordingly, the corresponding moment can be written as

$$M_g(\tau) = -b \left(\frac{1}{2} + a \right) L_g. \quad (2.14)$$

To summarise, Küssner's theory is very versatile and can consider any air-load induced by a defined velocity field. At the same time, just like the Wagner's and the Theodorsen's theory, Küssner's model originates from linear potential flow theory, in which different aerodynamic effects can be superimposed individually.

2.4.4 Frequency-domain sinusoidal gust response: Sears' model

In this section, Sears' model, giving air-loads solutions for an aerofoil moving in vertical sinusoidal gust field, is introduced. Due to the operating condition of a propeller, the wing structure is experiencing sinusoidal velocity variation in the vertical direction. This coincides with the simple harmonic expression used for frequency-domain solutions. Hence, this model can be more efficient than Küssner's model when only the steady-state analyses are to be performed. Sears' model provides the steady-state air-loads generated when an aerofoil is travelling through sinusoidal gust field.

In this special case, the sinusoidal velocity field is excluded from Equation (2.12) in the Küssner's model related calculations. Hence the following equation is replacing Equation (2.12)

$$w_G(x, \tau) = \begin{cases} w_0(x, \tau) & \text{without propeller} \\ w_0(x, \tau) + w_p(x, \tau) & \text{with propeller.} \end{cases} \quad (2.15)$$

Sinusoidal velocity field $w_i(x, t)$ is then considered separately with Sears' theory. Developed by von Kármán and Sears [41], the original theory took the mid-chord as the point of reference and gave results for lift and moment based on the oncoming propeller velocity variation w_i . In this case, w_i is defined as below

$$w_i = w_i^a \sin(\omega_p t - \omega_p x_{\text{ref}}/U_a) = w_i^a \sin k_p \left(\tau - \frac{U_\infty}{U_a} \right), \quad (2.16)$$

in which x_{ref} defines the referencing point from the leading edge and $x_{\text{ref}} = b$ for the original work. Accordingly, Sears defined a function describing loading behaviours as reduced propeller frequency k_p changes. $k_p = \omega_p b/U_\infty$, defined in the previous section, is the dimensionless expression of the blade passing frequency. As each blade passes the wing, repetitive cycles of velocity variation result in a sinusoidal velocity field. Since the wavelength λ_p can be written as U_a/ω_p , the reduced frequency k_p can also be expressed as $\frac{b}{\lambda_p} \frac{U_a}{U_\infty}$. In most cases, aircraft advancing velocity U_∞ and the flow approaching velocity U_a are identical. Even with the addition from propeller inflow, the difference is not significant in the present case. Therefore, k_p is a ratio between aerofoil half chord and the wavelength, measuring how many cycles there is within one half-chord length.

Sears' function is dependent on k_p . The original form of Sears' function $S(k_p)$ is computed in terms of Bessel functions and given as below and its real and imaginary parts are plotted in Figure 2.13

$$S(k_p) = [J_0(k_p) - jJ_1(k_p)]C(k_p) + jJ_1(k_p),$$

in which $C(k_p)$ is the formulation for the Theodorsen's function for frequency domain analysis of unsteady aerodynamic loadings for 2D aerofoil, which is also the frequency domain equivalence of the Wagner's function.

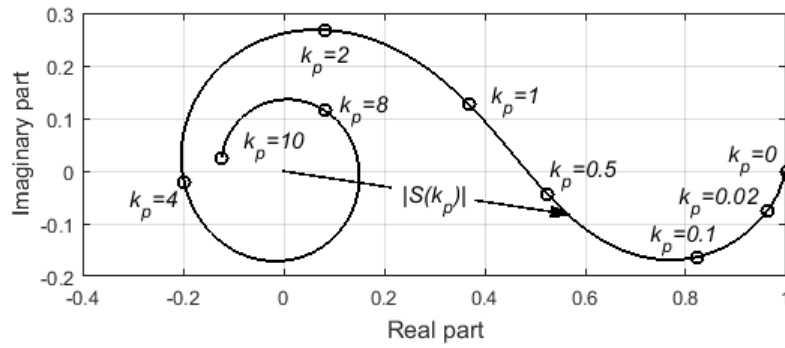


Figure 2.13: Real and imaginary part of the original Sears' function $S(k_p)$ describing lift and phase lag transitions

As illustrated in Figure 2.13, the real and imaginary parts of the Sears' function experience fluctuations between the positive and negative quadrants. However, a clear indication of the amplitude increment is shown by the magnitude of the Sears' function $|S(k_p)|$. As k_p becomes smaller, $|S(k_p)|$ shows a smooth growing tendency and settles at unity, as k_p approaches zero. In a physical sense, when the sinusoidal wavelength is smaller than or comparable to the aerofoil half chord, the air-load would be compromised compared to its steady aerodynamics. As the wavelength gets larger and going towards infinity, k_p approaches zero. The effect of upwash velocity field can be taken into account as in steady aerodynamics. Based on this theory, the lift and moment can be computed as follow

$$L_S(x, \tau) = -C_L \rho b U_a w_i^a S(k_p) e^{jk_p \tau} \quad ; \quad M_S(x, \tau) = -b \left(\frac{1}{2} + a \right) L_S. \quad (2.17)$$

In the case present, the point of reference is the shear centre, hence the original theory should be modified. Changing the point of reference would result in a different formulation of the sinusoidal velocity field, as well as the Sears' function. In [82], the aerofoil leading edge was taken as the point of reference and the modification of Sears' theory was discussed. In fact, alternation of the referencing point is equivalent to a phase shift, which reflects on expressions for the velocity field and the Sears' function. For the sinusoidal velocity field, the definition regarding the shear centre is written as

$$w_i = w_i^a \sin \omega_p(t - b(1 + a)/U_a) = w_i^a \sin k_p(\tau - (1 + a)\frac{U_\infty}{U_a}). \quad (2.18)$$

Comparing with the original expression in Equation (2.16), there is a frequency dependent phase change of $-k_p a \frac{U_\infty}{U_a}$. Accordingly, in the frequency domain, Sears' function is modified by an anticlockwise rotation of the same phase change. Hence, the modified Sears' function $S'(k_p)$ defined as

$$\begin{aligned} \Re S'(k_p) &= \Re S(k_p) \cos \phi_p + \Im S(k_p) \sin \phi_p \\ \Im S'(k_p) &= -\Re S(k_p) \sin \phi_p + \Im S(k_p) \cos \phi_p \end{aligned} \quad (2.19)$$

with a phase change $\phi_p = -k_p a \frac{U_\infty}{U_a}$.

2.5 Model integration and optimisation

The aerodynamic theories introduced above are all derived based on an aerofoil in two-dimensional space, hence, some simple applications of these aerodynamic theories can be studied on a sectional aerofoil model. As illustrated in Figure 2.14, an aerofoil with plunging and pitching degrees of freedoms is set up to verify the appropriate application of the aerodynamic model.

Having two degrees of freedom, being plunging (h) and pitching (α), the configuration is able to represent the case of a typical aerofoil section along a finite wing, with the discrete spring (k_h and k_α) reflecting the wing structural bending and torsional stiffness [52]. The equations of motion are derived by the Lagrange's equation through the system kinetic and potential energy (KE and

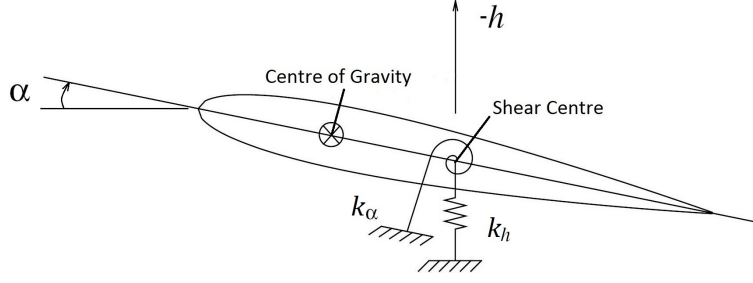


Figure 2.14: Aerofoil Model with Pitching and Plunging

PE) given as

$$KE = \frac{1}{2}m\left(\frac{dh}{dt} - \frac{S_\alpha}{m}\frac{d\alpha}{dt}\right)^2 + \frac{1}{2}I_{GC}\frac{d\alpha^2}{dt} \quad PE = \frac{1}{2}k_h h^2 + \frac{1}{2}k_\alpha \alpha^2, \quad (2.20)$$

where m is the aerofoil mass per unit span, I_{GC} is the mass moment of inertia per unit span measured at the centre of gravity, h and α are the plunging and pitching displacements respectively, S_α is the static unbalance about the elastic axis, caused by offset between the shear and gravitational centres, positive when the mass centre is in the front, k_h and k_α are the stiffness coefficients for plunging and pitching motions. The Lagrange's equation is applied to compute governing equations for the degrees of freedoms present

$$\frac{\partial}{\partial t} \left(\frac{\partial KE}{\partial \dot{q}_i} \right) - \frac{\partial KE}{\partial q_i} + \frac{\partial PE}{\partial q_i} = Q_i. \quad (2.21)$$

Note that q_i is the generalised displacement coordinate, hence h and α . Q_i is the generalised load associated with the displacement coordinate, in another words, total lift L_h and the total pitching moment M_α at the aerofoil shear centre.

The general form for the equations of motion for a typical aerofoil section with pitching and plunging degrees of freedom can be written as

$$\begin{aligned} m \frac{d^2 h}{dt^2} - S_\alpha \frac{d^2 \alpha}{dt^2} + k_h h &= L_h \\ I_\alpha \frac{d^2 \alpha}{dt^2} - S_\alpha \frac{d^2 h}{dt^2} + k_\alpha \alpha &= M_\alpha. \end{aligned} \quad (2.22)$$

Also, a similar form of equations of motion and its derivation can be found in [52] and [84]. L_h and M_α consist of unsteady air-loads predicted by unsteady aerodynamic theories addressed in

Section 2.4. In principle, those air-loads are also results of the simultaneous plunging and pitching motions. Therefore, a common practice is to confirm stability under a given flight condition. This is termed as aeroelastic instability analysis which will be discussed explicitly in Chapter 4. For this section, without having to consider aeroelastic instabilities, cases from previous studies can help to validate partially the aerodynamic model, as well as give an insight into the computational power required. As stability is not the main concern, time-domain theories, Wagner's and Küssner's models, leading to solutions for dynamic responses are studied and validated in this section. With a small flow incident angle, the lift and moments from advancing flow with any arbitrary gust field can be formulated as

$$L_h = L_C + L_{NC} + L_g ; \quad M_\alpha = M_C + M_{NC} + M_g. \quad (2.23)$$

Recalling the Wagner's theory, L_C and L_{NC} are the circulatory and non-circulatory lifts in Equation (2.5) and (2.7), while M_C and M_{NC} are moments exerted from L_C and L_{NC} respectively. L_g and M_g are lift and moment from the Küssner's theory in Equation (2.13) and (2.14). At the same time, the Wagner's and Küssner's theories are both featured in the dimensionless time domain $\tau = U_\infty t/b$. Hence, Equation (2.22) can be modified with dimensionless parameters as

$$\begin{aligned} \ddot{\xi} - \chi_\alpha \ddot{\alpha} + A\xi &= l_h \\ \ddot{\alpha} - \frac{\chi_\alpha}{r_\alpha^2} \ddot{\xi} + \left(\frac{1}{V}\right)^2 \alpha &= m_\alpha, \end{aligned} \quad (2.24)$$

In Equation (2.24), time differentials $\ddot{\xi}$, $\dot{\xi}$, $\ddot{\alpha}$ and $\dot{\alpha}$ are with respect to dimensionless time τ . $\xi = h/b$ is the dimensionless plunging displacement, $\chi_\alpha = S_\alpha/mb$ is the dimensionless static unbalance coefficient, $r_\alpha = (I_\alpha/mb^2)^{\frac{1}{2}}$ is the dimensionless radius of gyration, $A = \omega_h^2 b^2/U_\infty^2$ is the dimensionless stiffness parameter, $\omega_h = (k_h/m)^{\frac{1}{2}}$ is the plunging natural frequency, $V = U_\infty/b\omega_\alpha$ is the dimensionless speed, $\omega_\alpha = (k_\alpha/I_\alpha)^{\frac{1}{2}}$ is the pitching natural frequency, l_h is the total aerodynamic lift in dimensionless form, and m_α is the total pitching moment in dimensionless form. The expressions for l_h and m_α resemble Equation (2.23), however with modified dimensionless formulations of those loading components as listed in Equation (2.25). They are derived from Equation

(2.6), (2.7), (2.8), (2.13) and (2.14).

$$\begin{aligned}
l_C(\tau) &= -\frac{2}{\mu} \bar{u}_f^2 \alpha_{\text{AoA}}^{\text{eff}} ; \quad m_C(\tau) = -\frac{1}{r_\alpha^2} \left(\frac{1}{2} + a \right) l_C ; \\
l_{NC}(\tau) &= -\frac{1}{\mu} (\ddot{\xi} - a\ddot{\alpha}) - \frac{1}{\mu} \bar{u}_f \dot{\alpha} ; \quad m_{NC}(\tau) = +\frac{1}{r_\alpha^2 \mu} a (\ddot{\xi} - a\ddot{\alpha}) - \frac{1}{r_\alpha^2 \mu} \left(\frac{1}{2} - a \right) \bar{u}_f \dot{\alpha} - \frac{1}{8} \frac{1}{r_\alpha^2 \mu} \ddot{\alpha} \\
l_g(\tau) &= -\frac{2}{\mu} \int_0^\tau \bar{u}_f \frac{w_G(\tau)}{U_\infty} \frac{\partial \psi(\tau - \tau_0)}{\partial \tau} d\tau_0 ; \quad m_g(\tau) = -\frac{1}{r_\alpha^2} \left(\frac{1}{2} + a \right) l_g
\end{aligned} \tag{2.25}$$

In the above equations, $\mu = m/\pi\rho b^2$ is the dimensionless mass parameter and $\bar{u}_f = U_a/U_\infty$ is the ratio between aircraft advancing velocity and the airflow approaching velocity. Under a sectional model, it is assumed that flow condition is uniform across the wing span, hence the aircraft advancing velocity U_∞ is of the same magnitude with the airflow approaching velocity U_a and $\bar{u}_f = 1$ for all the aerofoil case studies in this section. In cases with presence of propellers, a beam model in three-dimensional space is needed as uniformity becomes invalid and \bar{u}_f turns into a function of the wing span, which will be further discussed in Chapter 5.

2.5.1 Plunging response under sharpe-edged gust

In 1941, Sears and Sparks studied the plunging dynamic response of an aircraft wing undergoing sharp-edged gust and solved the governing equations analytically through the Heaviside's operational methods [42]. In his study, an aerofoil section was used to represent a modern aircraft wing, whose parameters were featured by A.E. Lombard, Jr. in his thesis [87] and writes as

$$\begin{aligned}
c &= 7.5 \text{ ft.} \quad m = 0.7354 \text{ slugs per ft. span} \quad k_h = 622.5 \text{ lbs. per ft. per ft. span} \\
\rho &= 0.002378 \text{ slugs per ft.}^3
\end{aligned}$$

Under four flight conditions featuring four different advancing speeds ($U_a=562.5\text{ft./s}$, 375ft./s , 187.5ft./s and 93.75ft./s), a sharp-edged gust is present across the span, hence, U_∞ is identical to U_a for all flight conditions discussed. A sharp-edged gust is a step vertical velocity component. In Sears and Sparks' example, the sharp-edged gust has the same magnitude as airflow advancing velocity U_a and starts from $t=0$. With one degree of freedom, a governing equation for the aerofoil

model can be written and modified into dimensionless time domain as

$$m \frac{dh^2}{dt^2} + k_h h = L_h \implies \dot{\xi} + A\xi = l_h \text{ where } A = k_h b^2 / m U_\infty^2,$$

in which A is the dimensionless stiffness parameter. With four cases under different advancing velocities, A has four different values accordingly as 0.0375, 0.0845, 0.338 and 1.355. On the RHS, $l_h = l_C + l_{NC} + l_g$ is the aerodynamic loading prediction as a result of the Wagner's and Küssner's theories. By taking pitching as rigid, loading components can be derived based on Equation (2.25) and the corresponding aeroelastic response is obtained numerically. A numerical approach based on the Newmark-beta solution method [88] is applied and compared against the results obtained by Sears and Sparks in [42]. The plunging responses for four different operating conditions are plotted in Figure 2.15, showing good agreement between the obtained results and what was presented in [42].

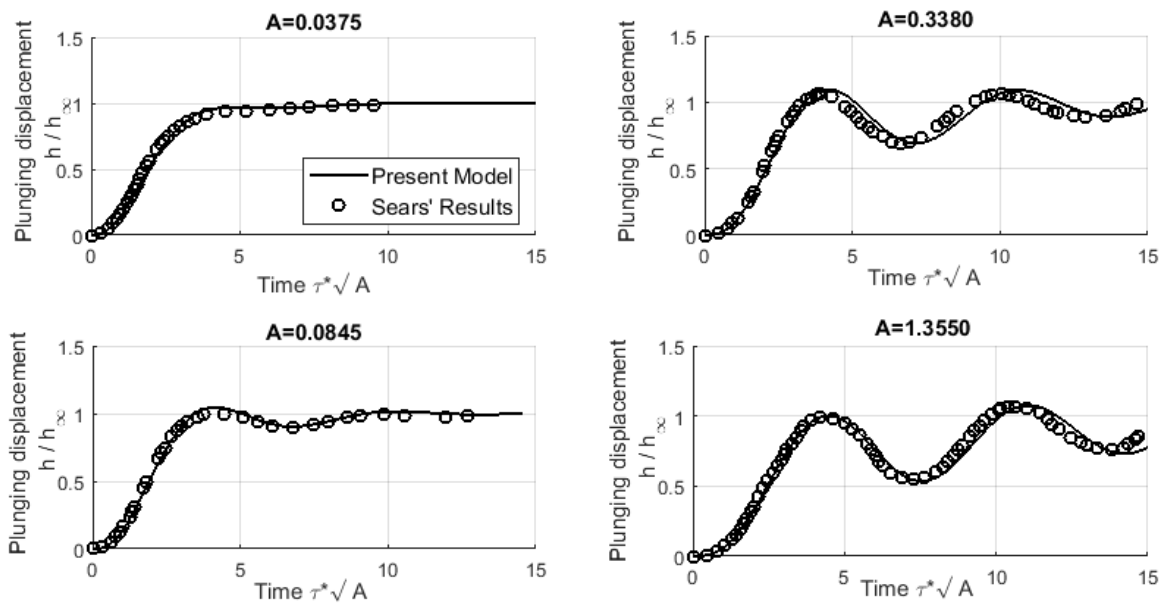


Figure 2.15: Newmark-beta solver results aligned with results presented [42]

The unsteady behaviour can sometimes be considered as quasi-steady, in which case the instantaneous change of the AoA results directly in the aerodynamic loadings without any transitional period. This can be applicable when the harmonic motion is slow or variation of non-harmonic

motion is slow [52]. There is not, however, a quantitative measure of how slow the motion is to be acceptable for quasi-steady aerodynamic theory. In here, under the same four flight conditions, the results obtained by Wagner's unsteady aerodynamic model and quasi-steady aerodynamic theory are compared and illustrated in Figure 2.16. It can be observed that a better agreement is achieved with less varying motion, and quasi-steady aerodynamics always gives a larger estimation for system damping. Theoretically, Wagner's model considers transitional lift deficiency effect and non-circulatory effects. In reality, the motion history affects the aerodynamic loadings through the wake. Quasi-steady aerodynamics ignores the transition, making aerodynamic loadings change simultaneously with the AoA. Non-circulatory lift, on the other hand, is from added mass due to the fluid particles around the moving aerofoil, termed as apparent mass. For quasi-steady aerodynamics, a smaller system mass would then result in a larger system damping. As shown in Figure 2.16, the quasi-steady results are more damped compared to the unsteady results. Ignoring lift deficiency effect would weaken the damping behaviour, while the non-circulatory mass strengthens it. In this case, the non-circulatory effect is more significant than the lift deficiency effect.

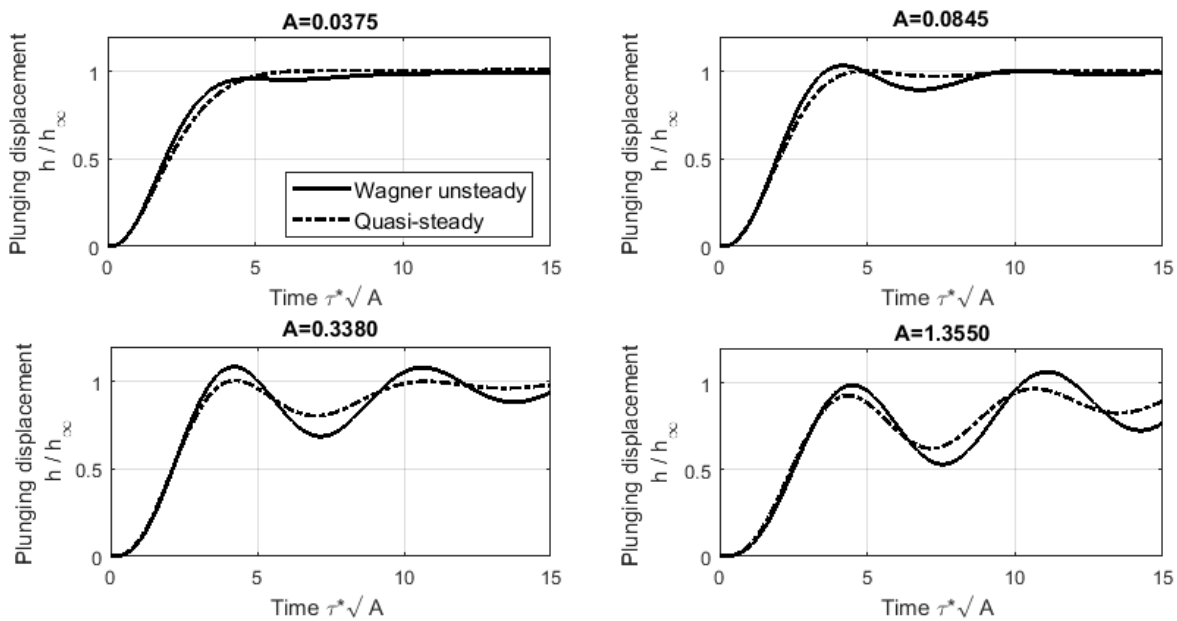


Figure 2.16: Results obtained by Wagner's unsteady and quasi-steady aerodynamics

It is also found that when doubling the simulation time span, the computational effort needed would increase 10 times or more. Tracing back to the analytical formulations for the aerodynamic theories, one can find that the convolution integral is commonly featured in the time-domain theories. Convolution integration takes into account all historical data and integrates against a pattern function $\phi(\tau)$ or $\psi(\tau)$, hence, doubling simulation time span would result in a significant increment of computational effort. A solution to this is discussed in the next section.

2.5.2 Recursive algorithm for the convolution integral

Time-domain prediction of the aerodynamic loads, due to wing-propeller interaction, relies on analytical sectional theories that commonly feature the convolution integral, in order to take into account all time history variations. Consequently, a relatively large amount of data is needed at each iterative step, decreasing the numerical efficiency of such a simplified approach. In this section, an alternative recurrence approach is introduced and implemented in the current model to overcome inefficiency brought by the convolution integral. This is a common practice for numerical analyses involving the convolution integral. One can refer to Leishman's book [82] for more details. Here, Wagner's model is taken as an example to demonstrate the simplification process. The same formulation applies to Küssner's model, by replacing $w_{3/4}(\tau)$ with defined gust field $w_g(\tau)$, and the Wagner's function $\phi(\tau - \tau_0)$ with the Küssner's function $\psi(\tau - \tau_0)$.

As discussed in Section 2.4.1, in the formulation of circulatory lift L_C , the effective downwash can be written as

$$\alpha_{\text{AoA}}^{\text{eff}}(\tau)U_a(\tau) = w_{3/4}(0)\phi(\tau) + \int_0^\tau \dot{w}_{3/4}(\tau_0)\phi(\tau - \tau_0)d\tau_0, \quad (2.26)$$

in which $\phi(\tau - \tau_0)$ is the Wagner's function and the approximation derived by R.T. Jones [85, 86] is used, which can be simplified mathematically as

$$\alpha_{\text{AoA}}^{\text{eff}}(\tau)U_a(\tau) = w_{3/4}(0)(-A_1e^{-b_1\tau} - A_2e^{-b_2\tau}) + w_{3/4}(\tau) - X(\tau) - Y(\tau), \quad (2.27)$$

where $X(\tau)$ and $Y(\tau)$ contain the convolution integral and are expressed as

$$X(\tau) = A_1 \int_0^\tau \dot{w}_{3/4} e^{-b_1(\tau-\tau_0)} d\tau_0 \quad Y(\tau) = A_2 \int_0^\tau \dot{w}_{3/4} e^{-b_2(\tau-\tau_0)} d\tau_0.$$

According to [82], the term $w_{3/4}(0)(-A_1 e^{-b_1\tau} - A_2 e^{-b_2\tau})$ is representing short-term transients and can be neglected. Therefore, the downwash can be written as

$$\alpha_{\text{AoA}}^{\text{eff}}(\tau) U_a(\tau) = w_{3/4}(\tau) - X(\tau) - Y(\tau). \quad (2.28)$$

When sampling with time step $\Delta\tau$, one will have X at $\tau + \Delta\tau$ written as

$$\begin{aligned} X(\tau + \Delta\tau) &= A_1 \int_0^{\tau+\Delta\tau} \dot{w}_{3/4} e^{-b_1(\tau+\Delta\tau-\tau_0)} d\tau_0 \\ &= A_1 e^{-b_1\Delta\tau} \int_0^\tau \dot{w}_{3/4} e^{-b_1(\tau-\tau_0)} d\tau_0 + A_1 \int_\tau^{\tau+\Delta\tau} \dot{w}_{3/4} e^{-b_1(\tau+\Delta\tau-\tau_0)} d\tau_0. \end{aligned}$$

At this stage, a backward-difference approximation can be applied so that

$$\dot{w}_{3/4}(\tau + \Delta\tau) = \frac{w_{3/4}(\tau + \Delta\tau) - w_{3/4}(\tau)}{\Delta\tau} = \frac{\Delta w_{3/4}(\tau + \Delta\tau)}{\Delta\tau}.$$

The remaining part within the integration can be evaluated exactly, the detail derivation is presented in Appendix A. Therefore, by following the same procedure for $Y(\tau)$, integrations along the time history can be avoided with $X(\tau)$ and $Y(\tau)$ being simplified recursively as

$$\begin{aligned} X(\tau) &= e^{-b_1\Delta\tau} X(\tau - \Delta\tau) + A_1 \frac{1 - e^{-b_1\Delta\tau}}{b_1} \frac{\Delta w_{3/4}(\tau - \Delta\tau)}{\Delta\tau} \\ Y(\tau) &= e^{-b_2\Delta\tau} Y(\tau - \Delta\tau) + A_2 \frac{1 - e^{-b_2\Delta\tau}}{b_2} \frac{\Delta w_{3/4}(\tau - \Delta\tau)}{\Delta\tau}. \end{aligned} \quad (2.29)$$

Hence, indicial lift at τ can be written as

$$L_C = -C_L b \rho U_a (w_{3/4}(\tau) - X(\tau) - Y(\tau)) \quad (2.30)$$

Similarly, for Küssner's model, the unsteady lift $L_g(\tau)$ can also be formulated in this fashion

$$L_g(\tau) = -C_L b \rho U_a (w_G(\tau) - X_g(\tau) - Y_g(\tau)), \quad (2.31)$$

$$\begin{aligned} \text{where } X_g(\tau) &= e^{-b_3\Delta\tau} X(\tau - \Delta\tau) + A_3 \frac{1 - e^{-b_3\Delta\tau}}{b_3} \frac{\Delta w_G(\tau - \Delta\tau)}{\Delta\tau} \\ Y_g(\tau) &= e^{-b_4\Delta\tau} Y(\tau - \Delta\tau) + A_4 \frac{1 - e^{-b_4\Delta\tau}}{b_4} \frac{\Delta w_G(\tau - \Delta\tau)}{\Delta\tau}. \end{aligned} \quad (2.32)$$

The recursive algorithm replaces the tedious process of convolution integration and overcomes inefficiency it brought. Taking the plunging aerofoil model in Section 2.5.1 as an example, on a standard desktop PC, the computational power required for the original convolution integral and its recursive alternative are compared in Table 2.1. One can clearly tell that the recursive formulation is much faster and a lot more efficient than its original convolution expression. When dealing with very simple cases with short time-span, the computational time required for the convolution formulation may be reasonable. As the model develops, however, more degrees of freedom will be taken into account and sectional loads will be integrated along the wing span, the level of solution complexity would naturally increase, hence, the application of the recursive algorithm is a prerequisite at this stage for further development of the aerodynamic model.

Table 2.1: Computational time comparison for convolution integral and its recursive formulation

| Case | Simulation time span (s) | Recursive formulation (s) | Convolution integral (s) |
|----------|--------------------------|---------------------------|--------------------------|
| A=0.0375 | 50 | 0.23 | 13.81 |
| A=0.0845 | 50 | 0.24 | 13.49 |
| A=0.3380 | 25 | 0.10 | 2.14 |
| A=1.3550 | 15 | 0.07 | 0.70 |

2.5.3 Plunging and pitching response under sharp-edged gust

Introducing one more degree of freedom into the aerofoil model, namely plunging and pitching motions, dynamic response under a sharp-edged gust can be characterised by Equation (2.24). Studied by Shams et al. in 2006, a similar aerofoil system featuring both plunging and pitching motions undergoing a sharp-edged gust was solved analytically in [49]. In their study, there are several constant dimensionless parameters as listed

$$\chi_\alpha = 0 \quad r_\alpha = 0.5 \quad V = 1 \quad \bar{u}_f = 1 \quad a = 0,$$

which means coincidence of the mid-chord, the shear centre and the gravitational centre. A constant ratio was kept between the moment of inertia, sectional mass and pitching stiffness. Under these parameters, four cases were studied. They are different in mass and advancing velocity. Specified by a stiffness parameter $A = \frac{k_h U_\infty^2}{mb^2}$ and a mass parameter $\mu = m/\pi\rho b^2$, these four conditions are listed here

$$\text{Case 1: } m = 0.0261 \text{ slugs/ft. } U_a = 159.68 \text{ ft./s } \mu = 14 \quad A = 0.0375$$

$$\text{Case 2: } m = 0.0261 \text{ slugs/ft. } U_a = 106.37 \text{ ft./s } \mu = 14 \quad A = 0.0845$$

$$\text{Case 3: } m = 0.0395 \text{ slugs/ft. } U_a = 43.426 \text{ ft./s } \mu = 21 \quad A = 0.3380$$

$$\text{Case 4: } m = 0.0392 \text{ slugs/ft. } U_a = 21.851 \text{ ft./s } \mu = 21 \quad A = 1.3350.$$

For these four cases, the aerofoil is stationary at the start and undergoes a unit step gust (sharp-edged gust) from $\tau = 0$ as written

$$w_G(\tau) = \begin{cases} 0 & \text{when } \tau < 0 \\ 1 \text{ ft. per sec.} & \text{when } \tau > 0. \end{cases}$$

With zero initial conditions, all the unsteady airloads are taken into account via Wagner's and Küssner's theories and dynamic responses of plunging and pitching motions are solved by a Newmark-beta solver. Comparing with the results obtained by Shams et al., Figure 2.17 is plotted. The present aerofoil model shows good agreement with the one developed in [49], therefore verifies the application of Wagner's and Küssner's formulations in the current plunge-pitch numerical model.

This 2D model can also be applied to the propeller-wing system. The 2D aerofoil model represents a certain section of the wing span and gives an insight of the dynamic behaviour under certain flight conditions. Taking the wing tip section of the wing-propeller system as an example, the sectional parameter values are calculated as below.

$$m = 22.0864 \text{ kg/m} \quad I_\alpha = 0.3595 \text{ kgm} \quad c = 0.6 \text{ m} \quad U_a = 128 \text{ m/s} \quad \bar{u}_f = 1 \quad \chi_\alpha = -0.163$$

$$a = -0.277 \quad \rho = 1.225 \text{ kg/m}^3 \quad k_h = 7.0032 \times 10^4 \text{ N/m} \quad k_\alpha = 1.9508 \times 10^5 \text{ Nm}$$

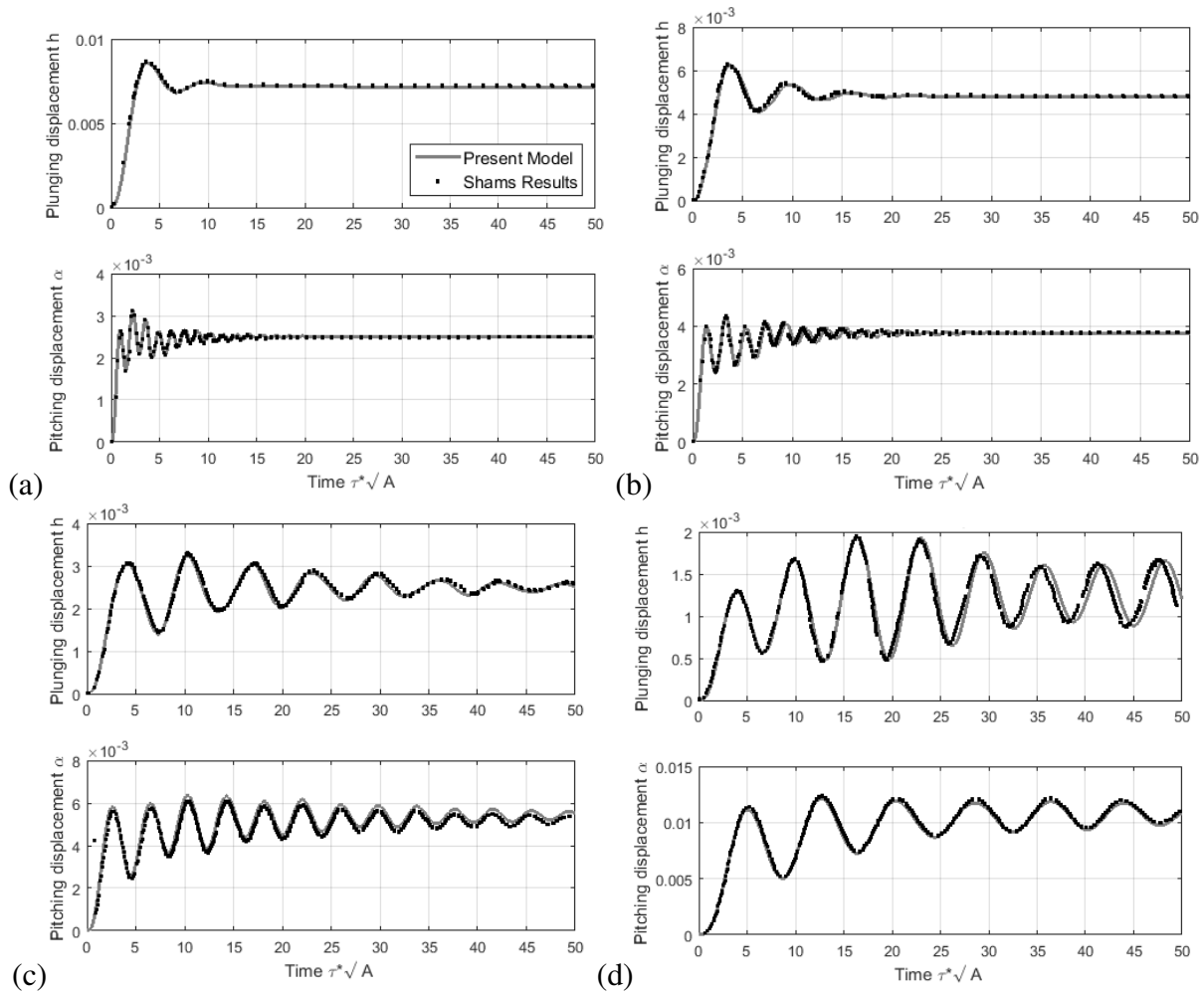


Figure 2.17: Verification results showing alignment in comparison with [49] (a) Case 1 (b) Case 2 (c) Case 3 (d) Case 4

Although the wing span could be uniform in cross-sectional geometry, mass and inertia, stiffness is varying with the span location. Here, the tip stiffness in plunging and pitching are calculated by the cross-sectional inertia and the span location based on a tip-loaded cantilever beam. The dynamic behaviour of the tip wing aerofoil under a unit sharp-edged gust is plotted in Figure 2.18. It shows under-damped transient behaviour of the system. In most cases with a cantilever wing, the tip is where its maximum deflection occurs, which makes the examination of tip behaviour an important one. If needed, the wing span can be split into finite pieces of aerofoil section, and each

one of them represented by a 2D aerofoil model.

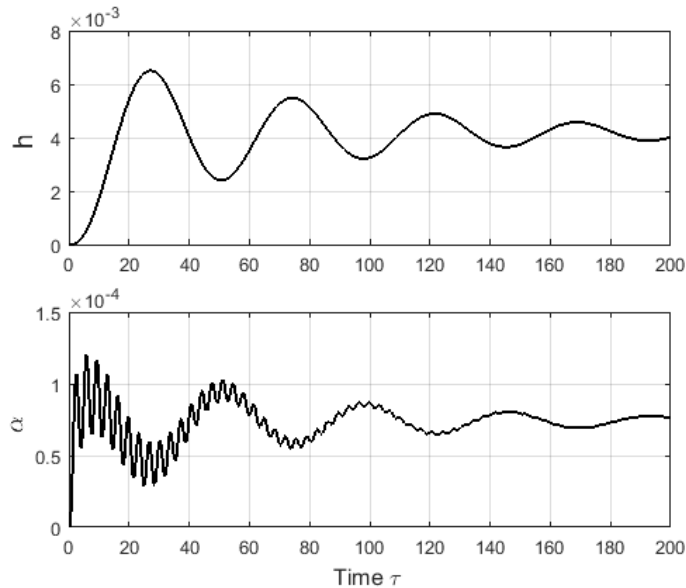


Figure 2.18: Wing tip plunging and pitching behaviour

As discussed earlier, a quasi-steady aerodynamic model can be applied to replace Wagner's model for investigating the transitional lift deficiency effect and non-circulatory effect. Figure 2.19, hence, is plotted based on results obtained by quasi-steady aerodynamic model and instability is shown. In fact, the prediction of the stability boundary can change with different aerodynamic theories used. The same phenomenon was observed in Haddapour and Firouz-Abadi's study where they stated that quasi-steady aerodynamics gives a very conservative estimation of the flutter boundary [83]. Hence, unsteady aerodynamic effects, such as non-circulatory loads, are playing a significant role in the system studied. In Chapter 4, flutter prediction based on quasi-steady aerodynamic and unsteady Theodorsen's aerodynamics will be discussed and compared.

2.6 Conclusion

In this chapter, an efficient numerical aerodynamic model has been built specifically for analysing responses of a 2D aerofoil. In the case of wing aerodynamics, strip theory, which integrates finite

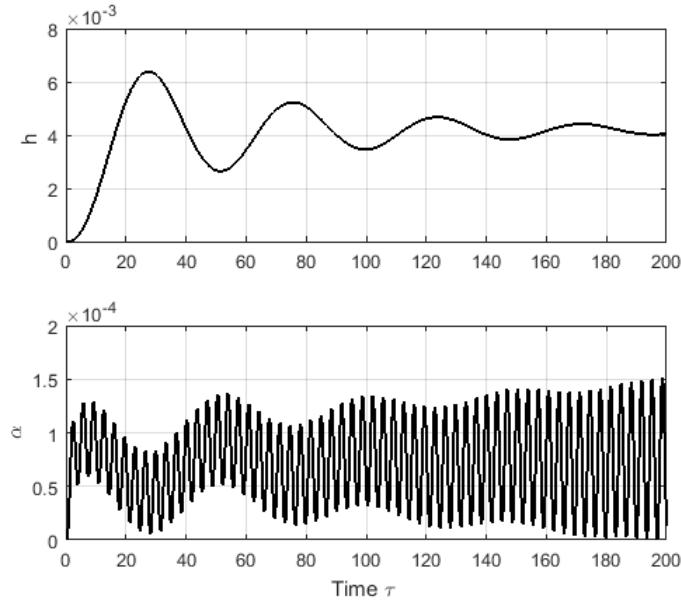


Figure 2.19: Wing tip plunging and pitching behaviour obtained by quasi-steady aerodynamics

sections of an aerofoil with infinitesimal length into a discrete wing, can be applied. For a wing in a propeller-wing system, it has several airflow components induced by advancing flow and propeller slipstream. Those simplified airflow velocity components can be taken into account through different aerodynamic theories or combinations of them. In Table 2.2, the combinations of theories are listed together with their functionalities. Starting with the simplest steady aerodynamic

Table 2.2: Combination of aerodynamic theories and their functionalities

| Aerodynamic theory/combination | Functionality |
|------------------------------------|---|
| Steady aerodynamic theory | Static steady-state response |
| Wagner's + Küssner's model | Transient + Dynamic steady-state response |
| Wagner's + Küssner's +Sears' model | Dynamic steady-state response |
| Theodorsen's aerodynamic theory | Instability (flutter) prediction |

theory, it is only applicable for analysing the static steady-state response. However, due to the harmonic nature of propeller slipstream, the steady-state response would be a dynamic one. Quasi-

steady aerodynamic theory mimics unsteady behaviour in a simplified way, however, it is proved to be insufficient in considering non-circulatory effects and limits the flight instability boundary, hence it is not included in Table 2.2. For a general dynamic response including transient and steady-state behaviour, Wagner's and Küssner's models are the most versatile combination in time-domain analyses. They consider lift deficiency transient as the AoA changes and non-circulatory effects. At the same time, excited by any defined gust field, the full dynamic response of the aeroelastic system can be obtained. The application of such aerodynamic model has been also verified against literature examples. Meanwhile, a wing tip section based on the wing-propeller configuration has been used for demonstration of the aerodynamic model. In cases when only the steady state is of concern, Sears' model can act as a short-cut to a solution. With sinusoidal gust field remaining in the steady state, the system's dynamic steady-state airloads can be formulated. Lastly, Theodorsen's unsteady aerodynamic theory is not ideal for time-domain analyses, however, it is extremely suitable for predicting instabilities boundaries. Its application will be discussed further in Chapter 4.

Chapter 3

Wing Structural Representation

In the aeroelastic system, the structural dynamics of the wing play one of the main roles in the fluid-structure interaction. Based on the wing parameters and their modal behaviours, how the wing structure interacts with the aerodynamics can be analysed. In this chapter, the wing is simplified as a cantilever beam. The structural equations are derived based on different beam theories, namely the Euler-Bernoulli beam theory for a slender wing and the Timoshenko beam theory for a short one.

Wings represented by the Euler-Bernoulli beam theory are very common for the analysis of classical fixed-wing aircraft and rotor blades, as they are all slender structures. The assumptions associated with Euler-Bernoulli beams are appropriate and sufficient for producing accurate results. For the case of a compound helicopter tip-loaded wing, however, having to provide lift, secure tractor propellers in place and still maintain the compatibility of existing helicopter facilities, the wing needs to be stiff and short. The effects of shear deformation and rotary inertia need to be evaluated. Hence, a linear model based on the Timoshenko beam theory is more suitable for characterising the wing's structural behaviour for this compound configuration. In this chapter, the equations of motion considering multiple modes of vibration, include beam-wise bending (flapping), chord-wise bending (lead-lag) and torsion, under a pretwist angle are derived through the Extended Hamilton's Principle. These motions are generally coupled, unless the wing is designed

with coincident shear and gravitational centres. At the same time, the coupling can bring noticeable differences in the dynamic behaviour comparing to a pure bending or torsion. Therefore, with the intention of investigating coupled aeroelastic behaviour, the modal properties of the coupled structure are obtained through a numerical modal analysis tool developed based on the transfer matrix method. In this chapter, this numerical approach is introduced and validated through analytical expressions and past publications. This numerical approach is able to provide natural frequencies and mode shapes with coupled motion, stiffness variation and any other cross-sectional property changes along the span. Therefore, it is considered as a versatile and applicable method for various of wing structures. At the same time, coupled mode shapes obtained by the transfer matrix method can improve the model efficiency when solving the aeroelastic responses in the later stage.

The outline of this chapter is as follows: dynamic equations of motion for the short wing will be derived based on the Euler-Bernoulli and the Timoshenko beam theories in Section 3.1 and 3.2. Before applying these theories to study the dynamic behaviour of the short wing, a numerical modal analysis approach based on the transfer matrix method will be introduced and validated against past publications in Section 3.3. Based on the developed approach, the short wing's modal behaviour will be studied and the most appropriate mathematical representation of the short wing will be evaluated in Section 3.4.

3.1 Euler-Bernoulli beam model

When considering a semi-wing under beam-wise bending (h), chord-wise bending (v) and torsion (α), it can be simplified as a clamped-free beam (cantilever) as shown in Figure 3.1.

Have x -axis coincident with the elastic axis, y -axis pointing towards the leading edge and z -axis going down, the equations of motion can be obtained through solving the Lagrangian function \mathcal{L} using the Extended Hamilton's Principle.

$$\delta \int_{t_1}^{t_2} \mathcal{L}(h, \frac{\partial h}{\partial t}, v, \frac{\partial v}{\partial t}, \alpha, \frac{\partial \alpha}{\partial t}, t) dt = \int_{t_1}^{t_2} (\delta KE - \delta PE + \delta W) dt = 0 \quad (3.1)$$

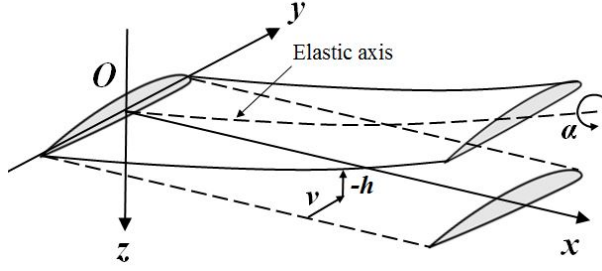


Figure 3.1: Beam Model - Cantilever wing with flapping, lead-lag and torsion modes

As described in Equation (3.1), the Lagrangian function \mathcal{L} is defined by KE which is the kinetic energy of the system, PE which is the potential energy and W the virtual work done to the system in the case studied. Zooming in on a section of the cantilever wing, a profile illustrated as Figure 3.2 is presented. With a built-in angle θ from the wing root, the total kinetic and potential energy for the cantilever wing, considering flapping h , lead-lag v and torsion α , can be characterised. Referring to the gravitational centre (GC) of the wing section, the kinetic energy can be written as

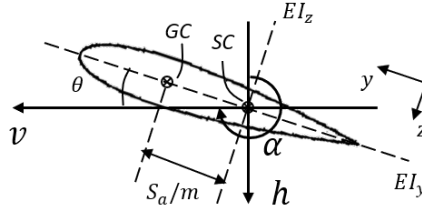


Figure 3.2: Cantilever beam section coordinates note

$$KE = \frac{1}{2} \int_0^l \left[m \left(\frac{\partial h}{\partial t} - \frac{S_a}{m} \cos \theta \frac{\partial \alpha}{\partial t} \right)^2 + m \left(\frac{\partial v}{\partial t} - \frac{S_a}{m} \sin \theta \frac{\partial \alpha}{\partial t} \right)^2 + I_{GC} \left(\frac{\partial \alpha}{\partial t} \right)^2 \right] dx, \quad (3.2)$$

where m is the sectional mass, S_α is the static unbalance and I_{GC} is the polar moment of inertia with respect to the gravitational centre. Similarly, by referring to the sectional properties defined in the xyz coordinate, the potential energy can be written as

$$PE = \frac{1}{2} \int_0^l \left[EI_y \left(\frac{\partial^2 h}{\partial x^2} \cos \theta + \frac{\partial^2 v}{\partial x^2} \sin \theta \right)^2 + EI_z \left(\frac{\partial^2 v}{\partial x^2} \cos \theta - \frac{\partial^2 h}{\partial x^2} \sin \theta \right)^2 + GJ \left(\frac{\partial \alpha}{\partial x} \right)^2 \right] dx, \quad (3.3)$$

where EI_y and EI_z are the bending stiffness defined in the y and z axis respectively, GJ is the torsional rigidity defined at the shear centre (SC). Note that $I_\alpha = I_{GC} + S_\alpha^2/m$ is the polar moment of inertia referring to the shear centre. Lastly, the virtual work term δW can be written as

$$\delta W = \int_0^l (L_h \delta h + L_v \delta v + M_\alpha \delta \alpha) dx. \quad (3.4)$$

After substituting Equation (3.2), (3.3) and (3.4) into Equation (3.1), the equations of motion in each coordinate h , v , and α can be obtained as

$$\begin{aligned} m \frac{\partial^2 h}{\partial t^2} - S_\alpha \cos \theta \frac{\partial^2 \alpha}{\partial t^2} + \frac{\partial^2}{\partial x^2} \left[(EI_y + (EI_z - EI_y) \sin^2 \theta) \frac{\partial^2 h}{\partial x^2} - \frac{EI_z - EI_y}{2} \sin 2\theta \frac{\partial^2 v}{\partial x^2} \right] &= L_h \\ m \frac{\partial^2 v}{\partial t^2} - S_\alpha \sin \theta \frac{\partial^2 \alpha}{\partial t^2} + \frac{\partial^2}{\partial x^2} \left[(EI_z - (EI_z - EI_y) \sin^2 \theta) \frac{\partial^2 v}{\partial x^2} - \frac{EI_z - EI_y}{2} \sin 2\theta \frac{\partial^2 h}{\partial x^2} \right] &= L_v \\ I_\alpha \frac{\partial^2 \alpha}{\partial t^2} - S_\alpha \cos \theta \frac{\partial^2 h}{\partial t^2} - S_\alpha \sin \theta \frac{\partial^2 v}{\partial t^2} - \frac{\partial}{\partial x} \left(GJ \frac{\partial \alpha}{\partial x} \right) &= M_\alpha. \end{aligned} \quad (3.5)$$

In the above expression, the modes of displacement h , v and rotation α are coupled through static unbalance S_α and built-in pretwist θ . Static unbalance would only disappear if the structural shear and gravitational centres coincide, but this is not usually a primary concern in aircraft designs comparing to lift generation performances. Looking at pretwist angle θ , this built-in angle at root is a common feature for rotor blades. Similar models involving three modes of vibration, therefore, are commonly used in characterising the dynamic behaviour for rotor blades [60, 61, 89]. For its application on fixed-wing configurations, any centrifugal terms presented in the formulation for helicopter blades are eliminated [78]. A similar beam model representing a fixed-wing, however with zero pretwist angle θ can be found in [90]. If this angle is taken as zero, lead-lag motion v can be uncoupled in the system. In fact, as mentioned earlier in Section 2.4.3, this pretwist effect can be taken into account aerodynamically as long as the relative angle between the resultant velocity and the chord is maintained. Considered alternatively as a step-gust by Küssner's aerodynamic model, the pretwist angle can be taken as zero in structural dynamics resulting in a much simpler formulation.

Another point to raise is that this thesis focuses on a much shorter and stiffer wing compared

to a fixed-wing aircraft or rotor blades. Although Euler-Bernoulli beam theory has its proven advantages in many structures, its prerequisites and assumptions should be re-examined. The Euler-Bernoulli beam model assumes negligible shear deformation and the cross-sections staying normal to the neutral axis as beam deforms. A slender beam would behave closely enough for those assumptions to be true. As a beam gets shorter, the assumptions on zero shear deformation and cross sections being perpendicular to the neutral axis would not be true. In the case of a short wing, the contribution of the shear deformation effect is not clear, therefore should be evaluated. For this purpose, other beam theories that consider those effects are to be introduced for comparison.

3.2 Timoshenko beam model

In the early 20th century, Timoshenko derived a beam theory that considers shear deformation and rotary inertia effects for thick/short beams [91, 92]. As illustrated in Figure 3.3, instead of assuming each cross-section to remain normal to the neutral axis, a Timoshenko beam allows shear deformation between beam cross-sections.

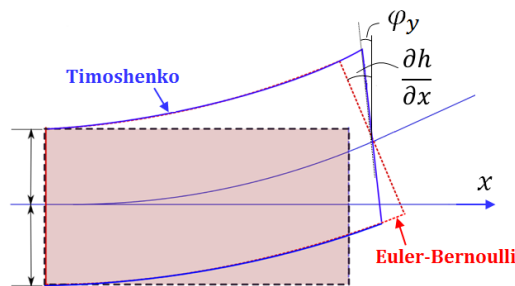


Figure 3.3: Timoshenko beam and shear deformation flexibility

Taking the flapping motion as an example, Euler-Bernoulli beam assumes that the cross-sectional rotation angle (φ_y) is equal to the bending slope ($\frac{\partial h}{\partial x}$). With shear deformation considered, Timoshenko beam allows a cross-section to rotate by an angle of $\varphi_y - \frac{\partial h}{\partial x}$. Therefore, the shear force S

and bending moment M at any point of a Timoshenko beam is written as

$$S = \kappa_y GA \left(\frac{\partial h}{\partial x} - \varphi_y \right) \quad \text{and} \quad M = \frac{\partial}{\partial x} \left(EI_y \frac{\partial \varphi_y}{\partial x} \right) \quad (3.6)$$

in which κ_y is the shear coefficient and the term $\kappa_y GA$ is known as the shear stiffness. The shear coefficient κ_y is dependent on the shape of beam cross-section. In many publications, shear coefficients for various of cross-sectional types were approximated if not specifically validated through experimental results. Although most beams have an arbitrary cross-section, simplification can be made in many cases. Shear coefficients for standard cross sections, such as rectangular, circular and hollow shapes etc., can be found in [93]. In the case of a wing, it usually contains a thin-walled shell, flanges and spars for support within. When considering a wing's structural properties, it can be simplified as a wing-box section, therefore a thin-walled box section is assigned. Recalling the Extended Hamilton's Principle introduced in the previous section, the equations of motion for a Timoshenko beam, under three vibration motions, can be obtained similarly by solving the Lagrangian function \mathcal{L} . With the same external loads, δW defined in Equation (3.4) remains the same. By considering the inertia caused by cross-sectional rotation φ_y and φ_z , the kinetic energy for a Timoshenko beam can be written as

$$KE = \frac{1}{2} \int_0^l \left[m \left(\frac{\partial h}{\partial t} - \frac{S_a}{m} \cos \theta \frac{\partial \alpha}{\partial t} \right)^2 + \rho_w I_y \left(\frac{\partial \varphi_y}{\partial t} \right)^2 + m \left(\frac{\partial v}{\partial t} - \frac{S_a}{m} \sin \theta \frac{\partial \alpha}{\partial t} \right)^2 + \rho_w I_z \left(\frac{\partial \varphi_z}{\partial t} \right)^2 + I_{GC} \left(\frac{\partial \alpha}{\partial t} \right)^2 \right] dx. \quad (3.7)$$

Note that ρ_w is the density of wing, while $\rho_w I_y$ and $\rho_w I_z$ are the rotary inertia referring to the bending motions in the y and z axis. While shear force and bending moments are defined as Equation (3.6), the potential energy of the system can be written as

$$PE = \frac{1}{2} \int_0^l \left[EI_y \left(\frac{\partial \varphi_y}{\partial x} \right)^2 + \kappa_y GA \left(\frac{\partial h}{\partial x} \cos \theta + \frac{\partial v}{\partial x} \sin \theta - \varphi_y \right)^2 + EI_z \left(\frac{\partial \varphi_z}{\partial x} \right)^2 + \kappa_z GA \left(\frac{\partial v}{\partial x} \cos \theta - \frac{\partial h}{\partial x} \sin \theta - \varphi_z \right)^2 + GJ \left(\frac{\partial \alpha}{\partial x} \right)^2 \right] dx. \quad (3.8)$$

The derivation from the Lagrangian function \mathcal{L} to the equations of motion is shown in Appendix B. By solving the Lagrangian function \mathcal{L} in each coordinate, the equations of motion for the Timoshenko beam under a pretwist angle θ is written as

$$\begin{aligned}
m \frac{\partial^2 h}{\partial t^2} - S_\alpha \cos \theta \frac{\partial^2 \alpha}{\partial t^2} - \frac{\partial}{\partial x} \left[(\kappa_y GA + (\kappa_z - \kappa_y) GA \sin^2 \theta) \frac{\partial h}{\partial x} - \frac{(\kappa_z - \kappa_y) GA}{2} \sin 2\theta \frac{\partial v}{\partial x} \right. \\
\left. - \kappa_y GA \cos \theta \varphi_y + \kappa_z GA \sin \theta \varphi_z \right] &= L_h \\
\rho_w I_y \frac{\partial^2 \varphi_y}{\partial t^2} - \frac{\partial}{\partial x} \left(EI_y \frac{\partial \varphi_y}{\partial x} \right) - \kappa_y GA \left(\cos \theta \frac{\partial h}{\partial x} + \sin \theta \frac{\partial v}{\partial x} - \varphi_y \right) &= 0 \\
m \frac{\partial^2 v}{\partial t^2} - S_\alpha \sin \theta \frac{\partial^2 \alpha}{\partial t^2} - \frac{\partial}{\partial x} \left[(\kappa_z GA - (\kappa_z - \kappa_y) GA \sin^2 \theta) \frac{\partial v}{\partial x} - \frac{(\kappa_z - \kappa_y) GA}{2} \sin 2\theta \frac{\partial h}{\partial x} \right. \\
\left. - \kappa_z GA \cos \theta \varphi_z - \kappa_y GA \sin \theta \varphi_y \right] &= L_v \\
\rho_w I_z \frac{\partial^2 \varphi_z}{\partial t^2} - \frac{\partial}{\partial x} \left(EI_z \frac{\partial \varphi_z}{\partial x} \right) - \kappa_z GA \left(\cos \theta \frac{\partial v}{\partial x} - \sin \theta \frac{\partial h}{\partial x} - \varphi_z \right) &= 0 \\
I_\alpha \frac{\partial^2 \alpha}{\partial t^2} - S_\alpha \cos \theta \frac{\partial^2 h}{\partial t^2} - S_\alpha \sin \theta \frac{\partial^2 v}{\partial t^2} - \frac{\partial}{\partial x} (GJ \frac{\partial \alpha}{\partial x}) &= M_\alpha.
\end{aligned} \tag{3.9}$$

The coupling between vertical bending h , lateral bending v and torsion α are caused by static unbalance S_α and pretwist angle θ . As discussed in Section 2.4.3 and 3.1, pretwist angle brings in structural coupling of all three vibration modes. Alternatively, the pretwist angle can be considered aerodynamically resulting in the structural uncoupling of the lead-lag motion v , hence, a much simpler formulation. Compared to the Euler-Bernoulli beam theory, the Timoshenko beam theory allows rotary inertia and shear deformation to be considered. For the short and stiff wing of this thesis, those effects can be evaluated through modal analysis. If rotary and shear effects would affect natural modal behaviour, it is an indication of significant importance in the coupled system. In the next section, analytical and numerical modal analysis approaches are to be introduced.

3.3 Modal Analysis

Modal analysis studies the natural frequencies and mode shapes of a system. It is useful itself for analysis of the structural behaviour, at the same time, mode shapes can be used to solve forced vibration responses. The modal properties can be analytically obtained for simple structures. The

derivation is a standard procedure which can be accomplished by knowing the equations of motion and the boundary conditions of a system [94]. The analytical approach starts with assuming simple harmonic vibration modes. Based on the order of differentiation associated with the equations of motion, the mode shape functions can be written in a general form with a number of constants. Substituting the general solutions back into the equations of motion with boundary conditions, the governing equations can be rearranged into a matrix form as $\mathbf{A}\mathbf{C} = \mathbf{0}$, in which \mathbf{C} is a column vector containing all non-zero constants. The necessary and sufficient condition for non-zero vector \mathbf{C} is that the determinant of matrix \mathbf{A} shall be zero [52]. Hence, the zero determinant $\det \mathbf{A} = 0$ gives the natural frequencies of the system. Accordingly, the vector \mathbf{C} can be defined and the mode shape function under this frequency can be obtained. For a system with multiple modes of vibration, the vibration motions can be studied separately or as coupled. At the same time, both analytical and numerical approaches are available for derivations. In this section, these approaches are introduced for the application of coupled and uncoupled vibration motions.

When studying the uncoupled vibration motions by the Euler-Bernoulli beam theory, the coordinates involved can be written as

$$h(x, t) = \Theta_h(x)e^{i\omega_h t} \quad v(x, t) = \Theta_v(x)e^{i\omega_v t} \quad \alpha = Z(x)e^{i\omega_\alpha t}, \quad (3.10)$$

where Θ_h , Θ_v and Z are mode shape functions for the flapping, lead-lag and torsional motions, and ω_h , ω_v and ω_α are the natural frequencies for flapping, lead-lag and torsion respectively. Since flapping and lead-lag are bending motions in the beam along different axes, their modal behaviour should be similar given the same boundary conditions. Since they are considered as uncoupled, each mode shape function can be derived separately.

For a uniform Euler-Bernoulli beam under bending only, analytical expressions for natural frequencies and mode shape functions can be found in standard reference textbooks, such as [52, 95]. A continuous system like a beam has infinite degrees of freedom, or modal vibration modes. Regarding one specific mode, its natural frequency and mode shape function can be analytically expressed with reference to its mode number j . So for the j^{th} mode, the natural frequencies $\omega_h(j)$

and $\omega_v(j)$, as well as the mode shape functions $\Theta_h(x, j)$ and $\Theta_v(x, j)$, are

$$\begin{aligned}\omega_h(j) &= \lambda_j^2 \sqrt{\frac{EI_y}{m}} & \omega_v(j) &= \lambda_j^2 \sqrt{\frac{EI_z}{m}} \\ \Theta_h(x, j) &= \Theta_v(x, j) = \cosh(\lambda_j x) - \cos(\lambda_j x) - \sigma_j [\sinh(\lambda_j x) - \sin(\lambda_j x)],\end{aligned}\quad (3.11)$$

where λ_j and σ_j are the mode shape function coefficients defined as in Table 3.1. While for beam

Table 3.1: Mode Shape Function Coefficients

| Mode | 1 | 2 | 3 | 4 | 5 |
|---------------|---------|---------|---------|---------|---------|
| $\lambda_j L$ | 1.875 | 4.6941 | 7.8548 | 10.9955 | 14.1372 |
| σ_j | 0.73410 | 1.01847 | 0.99922 | 1.00003 | 0.99999 |

torsion, modal properties can be derived similarly by the analytical approach, resulting in

$$\omega_\alpha(j) = (2j - 1) \frac{\pi}{2L} \sqrt{\frac{GJ}{I_\alpha}} \quad Z_j(x, j) = \sqrt{2} \sin\left(\frac{(2j - 1)\pi x}{2L}\right). \quad (3.12)$$

One important property of the mode shape functions ($\Theta_h(x, j)$, $\Theta_v(x, j)$, $Z(x, j)$) is that they are orthogonal, which can be written as

$$\int_0^L \Theta_h(x, m) \Theta_h(x, n) dx = \int_0^L \Theta_v(x, m) \Theta_v(x, n) dx = \int_0^L Z(x, m) Z(x, n) dx = \begin{cases} 0 & m \neq n \\ L & m = n. \end{cases}$$

The orthogonality conditions are very helpful when solving the forced response of a continuous system, such as a beam. Another property is that mode shape functions are arbitrary scaled and can be of any arbitrary magnitude as long as the pattern along the length of a beam is maintained. For the analytical expression above, the magnitude is defined relative to the orthogonality condition of these mode shape functions. Since these mode shapes are derived individually, when using them to solve forced response of a coupled system, the displacement in each coordinate needs to be solved separately. Therefore in the solution, if take $\theta_j(x) = \Theta_h(x, j)$, $\zeta_j(x) = \Theta_v(x, j)$ and $\eta_j(x) = Z(x, j)$, the system's forced response is written as

$$h(x, t) = \sum_{j=1}^{\infty} \theta_j(x) f_j(t) \quad v(x, t) = \sum_{j=1}^{\infty} \zeta_j(x) p_j(t) \quad \alpha(x, t) = \sum_{j=1}^{\infty} \eta_j(x) z_j(t), \quad (3.13)$$

where $f_j(t)$, $p_j(t)$ and $z_j(t)$ are the time-dependent functions that define the dynamic behaviour of each vibration mode.

For a more realistic representation of a coupled system, it is possible to consider coupled motions with coupled mode shapes through an analytical approach. Banerjee developed the analytical expression of coupled bending and torsional mode shapes for Euler-Bernoulli and Timoshenko beams [96, 97]. His solutions cover the coupling of flapping and torsion motions, as well as coupled flapping-lead-lag-torsion motions [90]. During modal analysis, the coordinates of interest are rewritten with the coupled mode shape functions sharing one simple harmonic frequency. The exact formulations can be found in [90, 96, 97]. Here, however, those analytical expressions are long and complex, they are not primary concern of the thesis. For the application of analytically derived mode shape functions, and obtaining the forced response of a coupled system, the solution can be written as

$$\begin{Bmatrix} h(x, t) \\ v(x, t) \\ \alpha(x, t) \end{Bmatrix} = \sum_{j=1}^{\infty} \begin{Bmatrix} \theta_j(x) \\ \zeta_j(x) \\ \eta_j(x) \end{Bmatrix} q_j(t). \quad (3.14)$$

Compare to Equation (3.13) which contains three time-dependent functions f_j , p_j and z_j to be solved, only one variable q_j is involved in the case of coupled mode shapes. As more vibration motions, such as shear deformation, are taken into consideration, coupled mode shapes can potentially improve efficiency for the approach developed.

For simple systems, the analytical modal analysis approach is efficient and accurate. The coupling motion brings complexity to the analytical derivation, hence a computational symbolic package is always needed. If possible, obtaining coupled mode shape functions without the complexity constraints on the structural system can definitely benefit the modal analysis process for the short wing structure in this thesis. In the next section, a numerical modal analysis approach based on the transfer matrix method is therefore introduced, which is easier to manage and applicable for a wider range of structures and variations in a system.

3.3.1 Numerical transfer matrix method

Unlike the analytical approach, the numerical transfer matrix approach allows property changes along the beam, including any variations of cross-sectional properties and hinge/spring connections between different segments on a beam. The procedure starts with the same assumption of harmonic motions. However, a general form of the solution would no longer be needed. Instead, the mode shape functions themselves can be rewritten into a state-space form as $\mathbf{z}' = \mathbf{A}\mathbf{z}$. Then, with the exponential of matrix \mathbf{A} , the state at any point of the beam or uniform segment can be written as $\mathbf{z}(x) = e^{\mathbf{A}x}\mathbf{z}(0)$. After this, the matrix equation can be rewritten in a homogeneous form by applying the boundary conditions. Finally, with a column vector representing the non-zero boundary conditions, the natural frequencies and mode shape functions can be obtained by solving the zero determinant of the homogeneous equation.

Here, a simple case with Euler-Bernoulli cantilever beam bending is taken as an example. First of all, the bending displacement h can be expressed in its exponential form as $h(x, t) = \Theta(x)e^{i\omega t}$ for free vibration with frequency ω . And the equation of motion can be rewritten as

$$m \frac{\partial^2 h}{\partial t^2} + EI_y \frac{\partial^4 h}{\partial x^4} = 0 \implies -m\omega^2 \Theta + EI_y \Theta'''' = 0. \quad (3.15)$$

Rearrange it into a state-space form, the equation is defined as

$$\mathbf{z}'(x) = \mathbf{A}\mathbf{z}(x), \quad (3.16)$$

in which

$$\mathbf{z} = \begin{Bmatrix} \Theta \\ \Theta' \\ \Theta'' \\ \Theta''' \end{Bmatrix} \quad \text{and} \quad \mathbf{A} = \begin{bmatrix} 0 & 1 & 0 & 0 \\ 0 & 0 & 1 & 0 \\ 0 & 0 & 0 & 1 \\ m\omega^2/EI_y & 0 & 0 & 0 \end{bmatrix}. \quad (3.17)$$

For cases with other beam theories or coupled degrees of freedom, the basic format in Equation (3.16) and its derivation in the following would still be applicable. The sizes and definitions of matrices \mathbf{z} and \mathbf{A} however would differ. Based on Equation (3.16), the state vector $\mathbf{z}(x)$ at any point of the beam can be obtained by the matrix exponential ($\mathbf{z}(x) = e^{\mathbf{A}x}\mathbf{z}(0)$).

Generally, the boundary conditions are defined in the form of displacement Θ , bending slope Θ' , bending moment M and shear force S . Therefore, the state vector $\mathbf{z}(x)$ needs to be modified into an expression as $\widehat{\mathbf{z}}(x)$, which contains the shear force S and bending moment M .

$$\widehat{\mathbf{z}}(x) = \mathbf{D}\mathbf{z}(x), \quad (3.18)$$

where

$$\widehat{\mathbf{z}}(x) = \begin{Bmatrix} \Theta(x) \\ \Theta'(x) \\ M(x) \\ S(x) \end{Bmatrix} \quad \text{and} \quad \mathbf{D} = \begin{bmatrix} 1 & 0 & 0 & 0 \\ 0 & 1 & 0 & 0 \\ 0 & 0 & -EI_y & 0 \\ 0 & 0 & 0 & -EI_y \end{bmatrix}.$$

For a Euler-Bernoulli cantilever beam, the clamped end is constrained so that there is zero displacement and zero bending slope. While for the free end, there is no bending moment or shear force. The boundary condition hence can be written as

$$\widehat{\mathbf{z}}(0) = \{0, 0, M(0), S(0)\}^T \quad \widehat{\mathbf{z}}(L) = \{\Theta(L), \Theta'(L), 0, 0\}^T. \quad (3.19)$$

Combining Equation (3.18), (3.19) and the matrix exponential equation ($\mathbf{z}(L) = e^{\mathbf{A}L}\mathbf{z}(0)$), the governing equations can be written as homogeneous as

$$\begin{Bmatrix} 0 \\ 0 \end{Bmatrix} = \mathbf{T}\mathbf{D}e^{\mathbf{A}L}\mathbf{D}^{-1}\mathbf{R} \begin{Bmatrix} M(0) \\ S(0) \end{Bmatrix} \quad \text{where} \quad \mathbf{T} = \begin{bmatrix} 0 & 0 & 1 & 0 \\ 0 & 0 & 0 & 1 \end{bmatrix}; \quad \mathbf{R} = \begin{bmatrix} 0 & 0 \\ 0 & 0 \\ 1 & 0 \\ 0 & 1 \end{bmatrix}. \quad (3.20)$$

Since $\{M(0), S(0)\}^T$ is a non-zero vector, yet the necessary and sufficient condition for a solution is that the determinant of transfer matrix $\mathbf{T}\mathbf{D}e^{\mathbf{A}L}\mathbf{D}^{-1}\mathbf{R}$ shall be zero. As the transfer matrix is a function of the harmonic frequency ω , the natural frequencies can be found. Accordingly, with each known natural frequency, $\Theta(x)$ at any point of the beam can be obtained. The mode shape function under this natural frequency is, therefore, formulated. However, this method would rely

on the direct and efficient computational procedures for matrix exponential. Fortunately, the matrix exponential is available as standard function routines in many commercial packages and open-source problem-solving environments, such as MATLAB [98], GNU Octave [99], Scilab [100] and many others.

When it comes to cantilever beam with non-uniform cross-sectional properties along its span, a numerical representation of multiple uniform segments connecting together can be used. With the transfer matrix approach, the boundary conditions are naturally compatible between each segment. As illustrated in Figure 3.4, a transfer matrix based on the function of matrix exponential is sufficient to characterise a non-uniform beam by connecting discrete uniform beam segments.

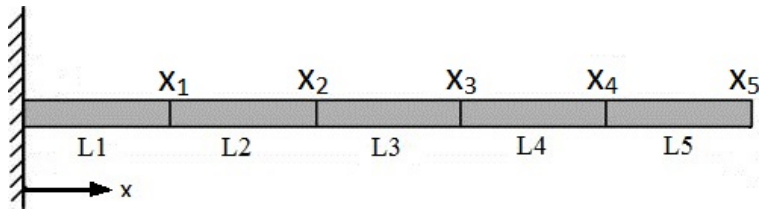


Figure 3.4: Segments to represent non-uniform beam cross-sections

$$z(x_5) = e^{\mathbf{A}_5 L_5} e^{\mathbf{A}_4 L_4} e^{\mathbf{A}_3 L_3} e^{\mathbf{A}_2 L_2} e^{\mathbf{A}_1 L_1} z(0). \quad (3.21)$$

By satisfying the boundary conditions, the system can be solved as a homogeneous equation and modal properties can be obtained. With the added complexity of the structural system, the numerical approach demonstrated is still relatively easy to manipulate. Hence, it is not limited to cases with Euler-Bernoulli beam theory or a cantilever beam. Based on the equations of motion, the method can be used to consider any beam bending or torsional theories, such as the Timoshenko beam theory, the Rayleigh beam theory and the Vlasov beam theory, to analyse effects brought by shear deformation, rotary inertia and warping. In the following section, the numerical approach is verified against established analytical expressions and the results reported in past publications.

3.3.2 Validation

In order to validate the modal analysis approach formulated in Section 3.3.1, analytical theories and past results focusing on analytically derived coupled modes are investigated in this section. The validation covers pure bending based on Euler-Bernoulli beam, the coupled flapping-torsion motion based on Euler-Bernoulli beam and Timoshenko beam and the coupled flapping-lead-lag-torsion motion based on Euler-Bernoulli beam. This is to test the approach's capability for considering multiple coupled vibration modes, rotary inertia, shear deformation and warping effects.

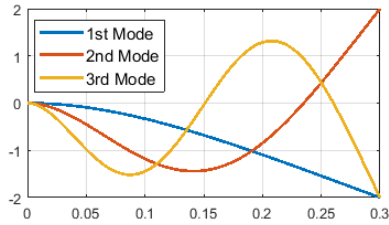
Cantilever beam bending

In most cases, uncoupled beam bending vibration can be characterised analytically. As previously discussed, mode shape functions and their corresponding frequencies can be analytically formulated for Euler-Bernoulli beam under pure bending as Equation (3.11). For validation, a uniform Euler-Bernoulli beam with clamp-free end conditions, with Young's modulus of 200 GPa, length of 0.3 m, a width of 0.02 m, a height of 0.01 m and mass density of 7960 kg/m², is analysed. With the governing Equation (3.15), the analytically derived natural frequencies and mode shapes are compared with the ones obtained from the transfer matrix method. In Table 3.2 and Figure 3.5, natural frequencies and mode shapes are shown. The natural frequencies derived are in very

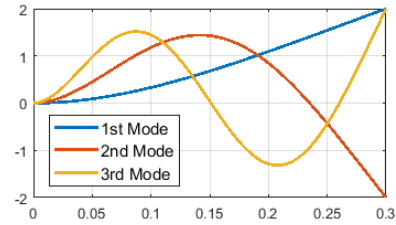
Table 3.2: Comparison of theoretical and transfer matrix derived natural frequencies

| Mode No. | Analytical theory (Hz) | Present approach (Hz) | Percentage difference |
|----------|------------------------|-----------------------|-----------------------|
| 1 | 90.53 | 90.54 | 0.011% |
| 2 | 567.41 | 567.41 | 0.000 % |
| 3 | 1588.77 | 1588.75 | 0.001 % |

close proximity of 0.01%. For mode shapes, two methods give the same pattern of magnitude distribution. This is because eigenvectors are not vectors filled with absolute values, instead it is arbitrarily scaled and only demonstrates the relative magnitude between each element. As long as



(a) Analytical mode shapes



(b) Transfer matrix derived mode shapes

Figure 3.5: Mode shape validation between analytical and numerical approaches

the ratio between each point and vibration modes are the same, it is considered as an agreement. The modal assurance criterion between Figure 3.5 (a) and (b) is at 99.9%. A good agreement, hence, is observed between the analytical and the numerical approaches, proving the validity and confirming the correct formulation for pure bending Euler-Bernoulli beam in the modal analysis tool developed.

Coupled flexural-torsional vibration

When there is coupling between bending and torsional motions, coupled flapping-torsional modes can be considered. From the point of view for understanding coupling effects, coupled flapping-torsion modes can give a better insight into the system's modal behaviour. If solely looking at determining forced-vibration responses, the results given by coupled and uncoupled modes are not going to be very different. This is because the forced response consists of two parts, namely the mode shape function and the time-dependent variable. The differences between uncoupled and coupled mode shapes will be corrected by their time-dependent variables. It does not mean that the coupled modes are meaningless in solving forced-vibration responses. The coupled modes bundle up multiple mode shape functions to one time-dependent variable, which optimises numerical efficiency when solving forced-vibration responses. Coupled modes were studied in the past, however, the application for obtaining aeroelastic response is still limited. Mostly, the coupled motion is studied for analytical derivation and its use on the investigation

of warping effects. In this section, the transfer matrix method is used to solve coupled modes numerically and they are compared with the analytical derivations accordingly.

Banerjee first derived the analytical formulation for coupled bending-torsion modal frequencies and shape functions in 1999 [96]. The analytical expression is lengthy and complex, whereas if derived from the transfer matrix method, minimal mathematical derivation is needed. The example parameters used is demonstrated as

$$EI_y=9.75 \times 10^6 \text{ Nm}^2 \quad GJ=9.88 \times 10^5 \text{ Nm}^2$$

$$m=37.75 \text{ kg/m} \quad I_\alpha=8.65 \text{ kgm}^2/\text{m} \quad S_\alpha=6.795 \text{ kgm/m} \quad l=6 \text{ m.}$$

The governing equations can be obtained from Equation (3.5) with zero pretwist angle θ and by removing the lead-lag coordinate. The governing equations then can be processed through the transfer matrix method, resulting in modal frequencies and shapes as illustrated in Figure 3.6. While the present transfer matrix method gives two natural frequencies at 48.31 rad/s and 97.35 rad/s, natural frequencies given by Banerjee [96] are 49.6 rad/s and 97.0 rad/s, resulting in differences as percentage within 3% overall. This confirms validity of the developed tool for solution of coupled flapping-torsion motion with the Euler-Bernoulli beam theory. Since the capability of the present transfer matrix method is not limited to any beam theory, combinations of other theories considering more structural effects are demonstrated in the following.

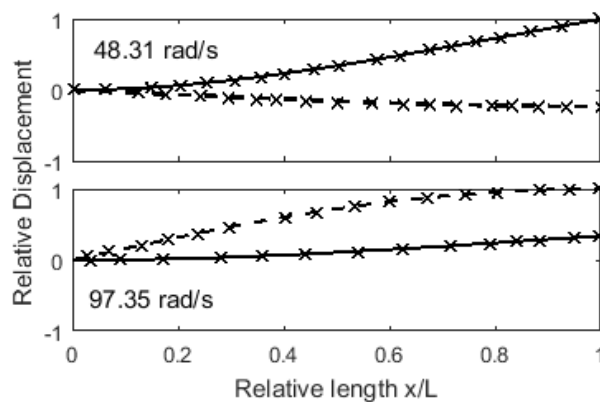


Figure 3.6: Coupled mode shape functions (Bending —; Torsion - - -; Results by [96] ×)

In Bercin and Tanaka's work [101], coupled flexural-torsional vibration with a thin-walled beam is considered through an analytical approach. In this case, rotary inertia and shear deformation effects are considered using the Timoshenko beam theory. Warping effect was also introduced as the cross-section studied is an open section. The beam parameters are given as

$$m=0.835 \text{ kg/m} \quad EI_y=6380 \text{ Nm}^2 \quad I_\alpha=5.01 \times 10^{-4} \text{ kgm}^2/\text{m} \quad l=0.82 \text{ m} \quad S_\alpha=0.012943 \text{ kgm/m}$$

$$\kappa_y GA=4.081 \times 10^6 \text{ N} \quad GJ=43.46 \text{ Nm}^2 \quad \rho_w I_y=2.51 \times 10^{-4} \text{ kgm}^2/\text{m} \quad EI_w=0.10473 \text{ Nm}^4.$$

Coupled bending-torsion is studied through the numerical modal analysis based on the transfer matrix method. The governing equation can be obtained by a zero pretwist angle θ , removing the lead-lag v coordinate from Equation (3.5) and adding the warping term EI_w as

$$m \frac{\partial^2 h}{\partial t^2} - S_\alpha \frac{\partial^2 \alpha}{\partial t^2} - \kappa_y GA \left(\frac{\partial^2 h}{\partial x^2} - \frac{\partial \varphi_y}{\partial x} \right) = 0,$$

$$\rho_w I_y \frac{\partial^2 \varphi_y}{\partial t^2} - EI_y \frac{\partial^2 \varphi_y}{\partial x^2} - \kappa_y GA \left(\frac{\partial h}{\partial x} - \varphi_y \right) = 0,$$

$$I_\alpha \frac{\partial^2 \alpha}{\partial t^2} - S_\alpha \frac{\partial^2 h}{\partial t^2} - GJ \frac{\partial^2 \alpha}{\partial x^2} + \underline{EI_w \frac{\partial^4 \alpha}{\partial x^4}} = 0.$$

The underlined term characterises the warping effect, and can be removed to exclude consideration of warping. Accordingly, matrices \mathbf{z} , \mathbf{A} and \mathbf{D} as discussed in Section 3.3.1 can be obtained. The results computed are shown in Table 3.3. The transfer matrix method gave results for natural frequencies in good agreement. As for mode shapes, the case with the application of the Timoshenko beam with warping consideration are illustrated in Figure 3.7 and 3.8. Note that the bending slope and torsional mode shapes are multiplied by the offset distance between the gravitational centre and the shear centre (S_α/m) in order to compare directly with the flapping displacements. A good representation is also shown for relation of different motion and their coupling in each mode.

To summarise, the transfer matrix method developed is capable of producing reliable results for coupled flexural-torsional motion, given the validation against analytical and literature results. Coupled modes can be used to investigate structural effects, such as coupled motion or warping. For the case of flapping, lead-lag and torsion, potentially these three modes of vibration can be coupled together. In the next section, coupled flapping-lead-lag-torsion modes are studied.

Table 3.3: Comparison with [101] by derived natural frequencies of transfer matrix

| Mode no. | Timoshenko beam (Hz) | | | Timoshenko beam + warping (Hz) | | |
|----------|----------------------|---------------|---------|--------------------------------|---------------|---------|
| | From [101] | Present model | Diff. % | From [101] | Present model | Diff. % |
| 1 | 63.39 | 62.34 | 1.85 | 63.51 | 63.51 | - |
| 2 | 129.34 | 129.89 | -0.42 | 137.39 | 137.39 | - |
| 3 | 259.22 | 259.22 | - | 275.82 | 275.82 | - |
| 4 | 415.72 | 418.89 | -0.93 | 481.10 | 481.10 | - |
| 5 | 607.29 | 605.21 | 0.34 | 639.76 | 639.75 | - |

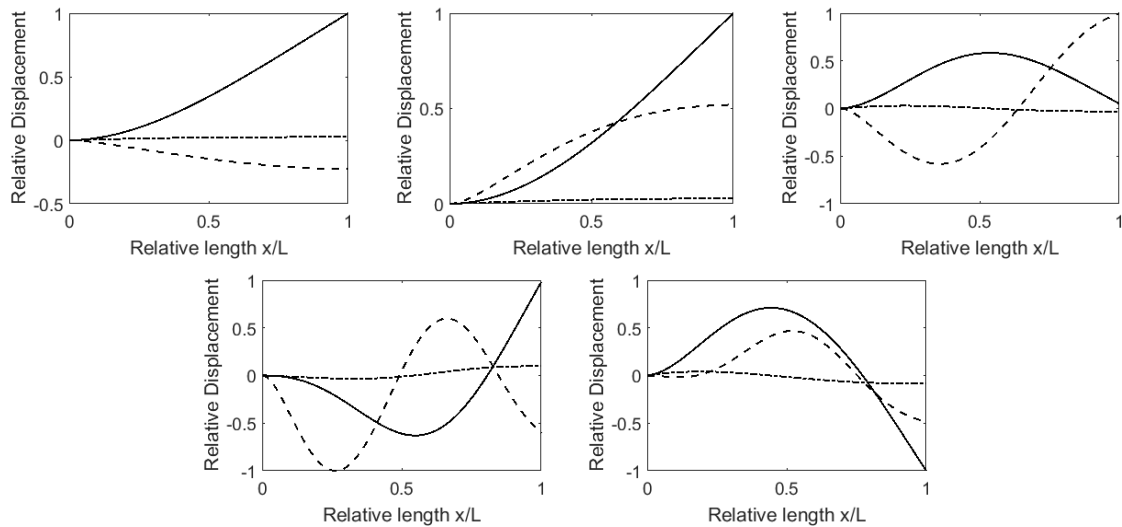


Figure 3.7: First five mode shapes derived for configuration in [101] via the transfer matrix method (Flap — ; Bending slope - - - ; Torsion ·····)

Lateral-vertical bending with coupled torsion

As for the case of coupled flapping-lead-lag-torsion motion, the same numerical approach as described in Section 3.3.1 can be applied. In this section, analytical expressions for coupled motion derived by Banerjee and Su [90] are compared with results obtained from the numerical transfer matrix method to validate the procedure developed.

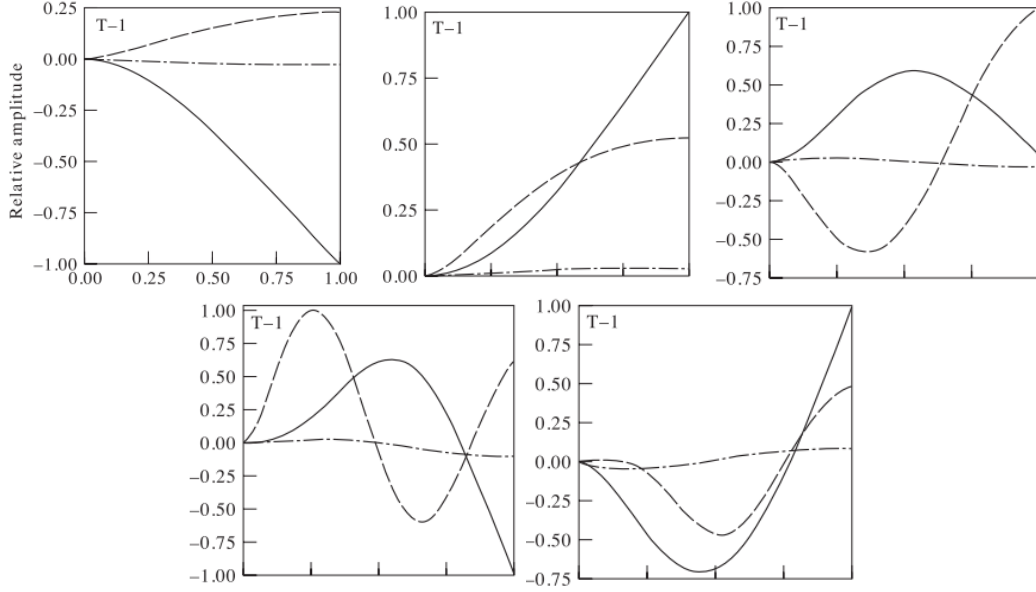


Figure 3.8: Mode shapes snapshot for the first five modes from case study demonstrated in [101]

Banerjee and Su developed the analytical expressions for modal analysis of three coupled motions, namely flapping, lead-lag and torsion [90]. Both flapping and lead-lag motions were characterised by the Euler-Bernoulli beam theory. In the structural model discussed in Section 3.1 and 3.2, a symmetric aerofoil is assumed. This assumption makes the shear centre and the gravitational centre aligned with the aerofoil chord, and there is a zero vertical offset between them. Under zero pretwist angle, the only static unbalance is caused by the lateral offset between the shear and gravitational centres. In Banerjee and Su's work, an asymmetric cross-section is assigned. The gravitational centre hence has a vertical offset to the shear centre, creating another static unbalance between the lead-lag and torsion. In this section, both lateral and vertical offsets are considered, giving for the equations of motion as

$$\begin{aligned}
 m \frac{\partial^2 h}{\partial t^2} - S_\alpha^y \frac{\partial^2 \alpha}{\partial t^2} + EI_y \frac{\partial^4 h}{\partial x^4} &= 0 \\
 m \frac{\partial^2 v}{\partial t^2} - S_\alpha^z \frac{\partial^2 \alpha}{\partial t^2} + EI_z \frac{\partial^4 v}{\partial x^4} &= 0 \\
 I_\alpha \frac{\partial^2 \alpha}{\partial t^2} - S_\alpha^y \frac{\partial^2 h}{\partial t^2} - S_\alpha^z \frac{\partial^2 v}{\partial t^2} - GJ \frac{\partial^2 \alpha}{\partial x^2} &= 0.
 \end{aligned}$$

The vertical and lateral static unbalances are denoted as S_α^y and S_α^z respectively here. With param-

eters given below, the developed method’s capability dealing with these three coupled motions can be investigated [90].

$$m = 0.261 \text{ kg/m} \quad I_\alpha = 1.242\text{e-}4 \text{ kgm} \quad GJ = 1.352 \text{ Nm}^2 \quad l = 1 \text{ m}$$

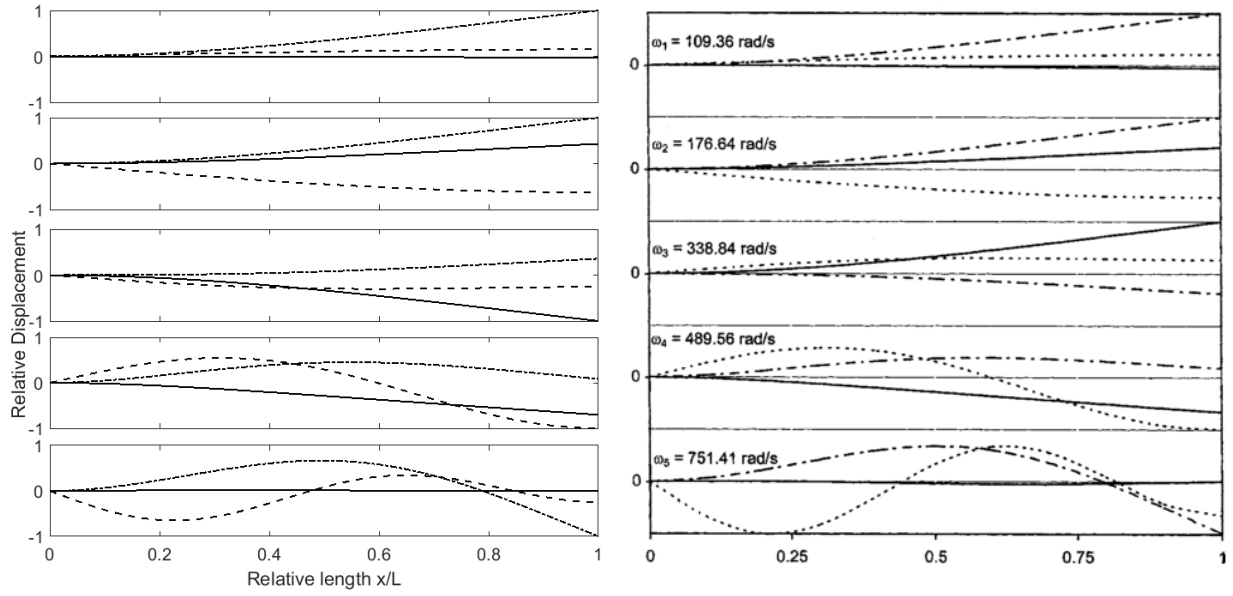
$$S_\alpha^y = 2.722\text{e-}3 \text{ kgm/m} \quad S_\alpha^z = 2.372\text{e-}3 \text{ kgm/m} \quad EI_y = 1637.09 \text{ Nm}^2 \quad EI_z = 286.53 \text{ Nm}^2.$$

Processed by the transfer matrix method, the modal frequencies and shape functions are obtained and illustrated in Table 3.4 and Figure 3.7. As shown in Table 3.4, the natural frequencies are exactly reproduced, giving percentage difference all within 0.1%. As for mode shapes, a comparison is illustrated in Figure 3.9 showing agreements in shape patterns as well as relative magnitude between each mode of vibration. The torsional mode shapes are multiplied by the distance between the gravitational centre and the shear centre in order to compare directly with bending displacements.

Table 3.4: Comparison of [90] and transfer matrix derived natural frequencies

| Mode No. | Results from [90] (rad/s) | Present approach (rad/s) | Diff. % |
|----------|---------------------------|--------------------------|---------|
| 1 | 109.36 | 109.43 | 0.06 |
| 2 | 176.64 | 176.67 | 0.02 |
| 3 | 338.84 | 338.91 | 0.02 |
| 4 | 489.56 | 489.59 | 0.01 |
| 5 | 751.41 | 751.62 | 0.03 |

As more vibration modes are included, the structural system gets more complex. For the transfer matrix developed, the size of matrices \mathbf{z} , \mathbf{A} and \mathbf{D} would grow, the actual procedures, however, stay the same. Comparing to any analytical approach, additional mode of vibration means additional terms for the general solution. Through symbolic derivations, added terms would naturally increase the complexity of analytical formulation itself. One of the main advantages of the transfer matrix method, therefore, is its numerical efficiency. The benefit is more obvious when structural system gets more complex. With validity proved for the transfer matrix modal analysis, the modal



(a) Results obtained by present model

(b) Results from [90]

Figure 3.9: Mode shapes based on transfer matrix method and analytical method for configuration in [90](Flap; Lead-lag - - - ; Torsion —)

behaviour of the short wing within propeller-wing configuration is to be studied and analysed in the following section.

3.4 Modal study of compound helicopter wings

At this stage, the modal analysis is validated and ready to be applied onto the short wing structure for this thesis. The modal analysis, however, is not just to investigate the modal behaviour of the wing. More importantly, it is also to understand effects brought by motion coupling, shear deformation and rotary inertia. The aim is to find the most suitable beam theory or combination of theories to represent the short wing structure in the propeller-wing configuration. In this section, modal analyses results derived from different beam theories and degrees of coupling are demonstrated and compared. It is important to note that the mode shape function does not affect significantly the forced dynamic response solution. This is because mode shapes are all relatively standard pat-

terns. With a set of weighting factors for each mode, they constitute the forced-vibration response. A different mode shape function, either coupled or uncoupled, will only result in a different set of weighting factors rather than a drastic change in the forced-vibration response itself.

Table 3.5: Estimated wing structural parameters

| | | | | | |
|--|--|------------------|--|---------------------------------------|------------|
| $E=69 \times 10^9$ Pa | $G=27 \times 10^9$ Pa | $m=22.0864$ kg/m | $J=1.8063 \times 10^{-5}$ m ⁴ | | |
| $I_y=5.2862 \times 10^{-6}$ m ⁴ | $I_z=1.0745 \times 10^{-4}$ m ⁴ | $b=0.3$ m | $\theta=0$ deg | $\chi_\alpha=-0.163$ | $a=-0.277$ |
| $\rho_w=2720$ kg/m ³ | $A=0.00812$ m ² | $\kappa_y=0.80$ | $\kappa_z=0.05$ | $I_\alpha=0.3594$ kgm ² /m | |

In this thesis, an estimated wing configuration was used. The cross-sectional and structural parameters are estimated based on publications and verification studies shown in Appendix C. The finite semi-wing is 2.5 m in length ($l = 2.5$ m) and has a uniform sectional profile along the span. The aerofoil section can be simplified as a thin-walled box section, the structural properties involved in this analysis are listed in Table 3.5. These parameter values are calculated in Patran beam library with an estimated aerofoil profile, which can be found in Appendix C. Meanwhile, a modal analysis strategy is developed as illustrated in Figure 3.10. With the aid of Equations (3.5) and (3.9), the investigation starts with analyses on uncoupled flapping and torsion motions as they are the two key coordinates of interests in wing aeroelasticity. Under the pure flapping motion, two beam theories are compared and the effects of shear deformation and rotary inertia will be evaluated. Followed by a modal study of coupled flapping-torsion motion, the coupling effect can be quantified and analysed. The coupling between flapping and torsion is introduced by static unbalance from the gravitational centre offset, therefore, cannot be eliminated. The flapping and torsional motions, hence, should definitely be taken into consideration as a whole. Moving onto the lead-lag motion (lateral bending), its pure uncoupled motion is firstly considered under two different beam theories similar to the analyses carried out on the flapping motion. As lead-lag motion is uncoupled from the system via zero pretwist angle $\theta = 0$. Whether or not to consider this motion with other coordinates is discussed then and the most suitable representation for the

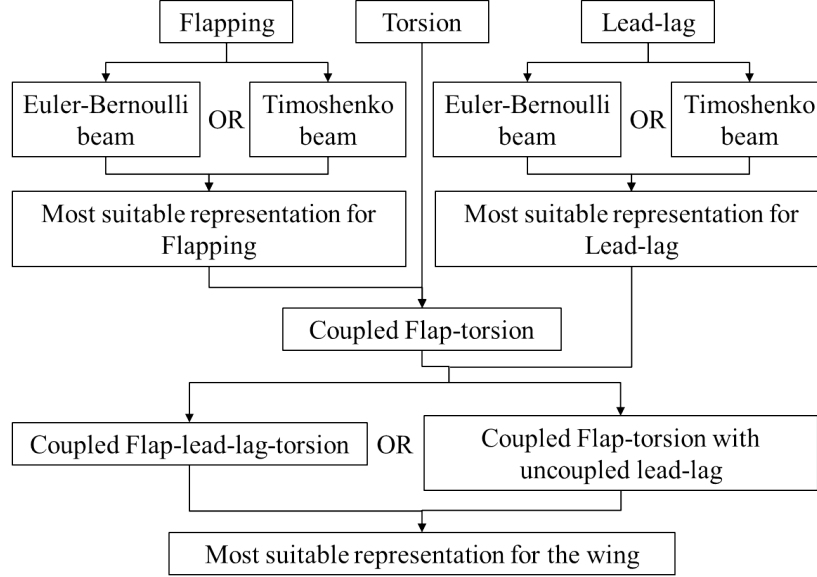


Figure 3.10: Modal analysis strategy

short wing can be obtained.




3.4.1 Flapping-torsion modal study

Firstly, the pure flapping motion is studied. Static unbalance S_α is ignored in the formulation, and the Euler-Bernoulli expression and the Timoshenko expression can be written as

$$\begin{aligned} \text{Euler-Bernoulli beam:} \quad & m \frac{d^2 h}{dt^2} + EI_y \frac{d^4 h}{dx^4} = 0, \\ \text{Timoshenko beam:} \quad & \begin{cases} m \frac{d^2 h}{dt^2} - \kappa_y GA \left(\frac{d^2 h}{dx^2} - \frac{d\varphi_y}{dx} \right) = 0, \\ \rho_w I_y \frac{d^2 \varphi_y}{dt^2} - EI_y \frac{d^2 \varphi_y}{dx^2} - \kappa_y GA \left(\frac{dh}{dx} - \varphi_y \right) = 0. \end{cases} \end{aligned}$$

The natural frequencies and mode shapes can be obtained both analytically and numerically. Since the numerical approach is based on the transfer matrix method have been validated, a numerical approach is used here. Following the procedures demonstrated in Section 3.3.1, the detail derivation can be found in Appendix D. The modal analyses results are obtained and listed in Table 3.6. For cantilever beam bending, the mode shape functions are of standard shapes regardless of beam

Table 3.6: Flapping modal frequencies based on two beam theories

| Euler-Bernoulli beam | Timoshenko beam | Mode shape illustration | Diff. % |
|----------------------|-----------------|--|---------|
| 11.51 | 11.49 |  | 0.17 |
| 72.11 | 71.60 |  | 0.71 |
| 201.90 | 198.59 |  | 1.67 |

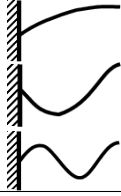
theory used, hence they are only illustrated as basic patterns. Between the Euler-Bernoulli and the Timoshenko beam theories, the differences given on natural frequencies are small. Even though the difference increases with higher frequencies, these values are still similar, which indicates a minimal shear deformation and rotary inertia effects in the flapping direction. The lack of shear deformation and rotary inertia contribution is reasonable in the flapping motion. In fact, beam theories are 1D structural models. When viewing the short wing from the aircraft front, the slenderness can be defined by the ratio between the beam length and the aerofoil height. The beam is a slender one from this point of view, hence does fulfil assumptions under the Euler-Bernoulli beam theory. The Euler-Bernoulli beam theory is much simpler and efficient to deal with numerically, therefore, it is better suited for characterising bending behaviour in the flapping direction.

Unlike bending motions, the torsional motion does not have many variations in mathematical models. Aerofoil simplified as a thin-walled box has a closed cross-section, therefore, warping effects are eliminated. When ignoring the coupling effect from flapping motion, the governing equation is written as

$$I_{\alpha} \frac{d^2 \alpha}{dt^2} - GJ \frac{d^2 \alpha}{dx^2} = 0.$$

Following the same modal analysis procedures, either analytically or numerically, natural frequencies and mode shape functions can be obtained. Through the numerical approach introduced in Section 3.3.1, the modal properties are shown in Table 3.7. Combined with the flapping modal behaviour in Table 3.6, the structure would resonate at 11.51 Hz and 71.60 Hz for bending, 116.48 Hz for torsion, followed by 201.90 Hz for bending again, if the system is perfectly designed with

Table 3.7: Torsion modal frequencies and shapes

| Modal frequency (Hz) | Mode shape illustration |
|----------------------|--|
| 116.48 |  |
| 349.45 | |
| 582.41 | |

uncoupled flapping and torsional motion. In reality, however, flapping and torsion are coupled through static unbalance S_α . With the transfer matrix approach, the coupled modal behaviour can be analysed and the significance of coupling in the present system can be revealed. Recalling the coupled equations of motion, Equations (3.5) and (3.9), the coupled flapping-torsion system is characterised by setting θ to be zero and removing v and the equations of motion for coupled flapping-torsion system can be written as

$$\text{Euler-Bernoulli beam: } \begin{cases} m \frac{d^2 h}{dt^2} - S_\alpha \frac{d^2 \alpha}{dt^2} + EI_y \frac{d^4 h}{dx^4} = 0, \\ I_\alpha \frac{d^2 \alpha}{dt^2} - S_\alpha \frac{d^2 h}{dt^2} - GJ \frac{d^2 \alpha}{dx^2} = 0, \end{cases}$$

$$\text{Timoshenko beam: } \begin{cases} m \frac{d^2 h}{dt^2} - S_\alpha \frac{d^2 \alpha}{dt^2} - \kappa_y GA \left(\frac{d^2 h}{dx^2} - \frac{d\varphi_y}{dx} \right) = 0, \\ \rho_w I_y \frac{d^2 \varphi_y}{dt^2} - EI_y \frac{d^2 \varphi_y}{dx^2} - \kappa_y GA \left(\frac{dh}{dx} - \varphi_y \right) = 0, \\ I_\alpha \frac{d^2 \alpha}{dt^2} - S_\alpha \frac{d^2 h}{dt^2} - GJ \frac{d^2 \alpha}{dx^2} = 0. \end{cases}$$

The above expression can be employed in the numerical transfer matrix modal analysis discussed in Section 3.3.1. The size of \mathbf{z} , \mathbf{A} and \mathbf{D} may vary from case to case, yet the general procedures related to handling of those matrices stay the same. The natural frequencies and mode shapes, therefore, are obtained as listed in Table 3.8 and Figure 3.11 respectively. Note that, in order to compare directly the flapping and torsional displacements, flapping displacements are nondimensionlised by half chord length as $\xi = h/b$. When comparing between the Euler-Bernoulli and the Timoshenko beam theories, similar level of difference is observed as before, which further confirmed the choice

Table 3.8: Coupled flapping torsion modal frequencies based on two beam theories

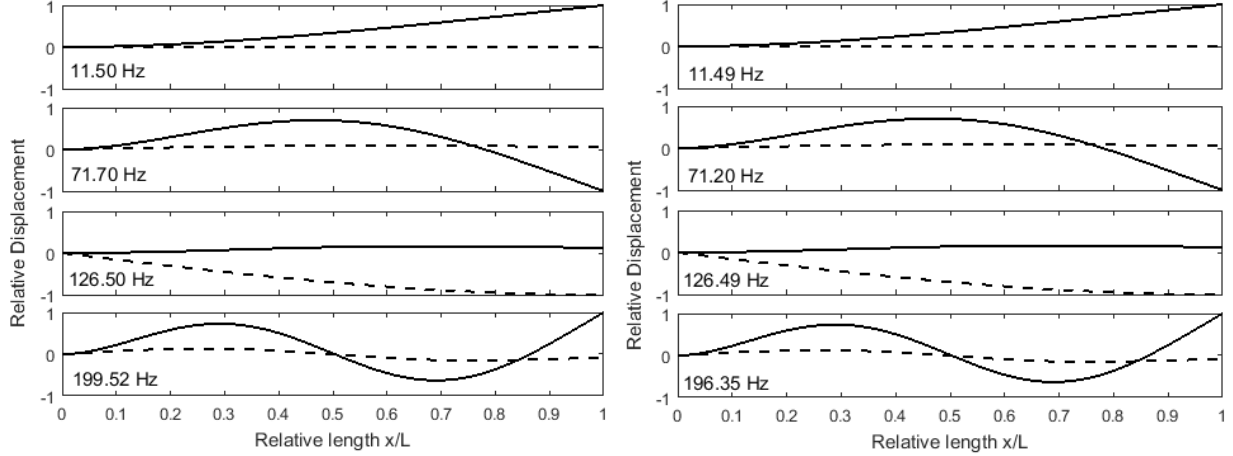
| Euler-Bernoulli beam | Timoshenko beam | Diff. % |
|----------------------|-----------------|---------|
| 11.50 | 11.48 | 0.17 |
| 71.70 | 71.20 | 0.72 |
| <u>126.50</u> | <u>126.49</u> | 0.01 |
| 199.52 | 196.35 | 1.61 |
| <u>377.68</u> | <u>372.64</u> | 1.35 |

of the Euler-Bernoulli beam theory for flapping. On the other hand, the underlined terms are the torsion-governed modes at 126.50 Hz (or 126.49 Hz) and 377.68 Hz (or 372.64 Hz) while the rest are flapping-governed modes. If compared with pure flapping and torsion, one can see that the flapping motion maintains most of its modal behaviour for flapping-governed modes. The torsion-governed modes, however, are shifted from 116.48 Hz to 126.50 Hz (or 126.49 Hz), also from 349.45 Hz to 377.68 Hz (or 372.64 Hz). Giving a percentage difference around 8%, making the coupling effect a significant one to the overall structural dynamics regardless which beam bending theory is used.

As discussed previously, modal analysis not only gives an insight into the modal behaviour of the system, it is also of importance to investigate the most suitable representation of the structural system. With very little differences between the Euler-Bernoulli and the Timoshenko beam derived results, for this particular specification of the wing studied, the most suitable representation so far is a coupled flapping-torsion system with Euler-Bernoulli defined vertical bending.

3.4.2 Lead-lag motion modal study

Compared to flapping and torsion, lead-lag motion is a relatively less coupled mode of vibration occurring in the wing structure, therefore, it can be preliminarily studied in an uncoupled fashion. Lead-lag, also known as lateral bending, is very similar to flapping in many ways. In principle,



(a) Derived by Euler-Bernoulli beam theory

(b) Derived by Timoshenko beam theory

Figure 3.11: Coupled flap-torsion mode shapes comparison between Euler-Bernoulli and Timoshenko beam theory (ξ — ; α - - -)

they are both bending behaviour, hence, they both can be characterised using the Euler-Bernoulli or the Timoshenko beam theory. The only difference is the direction or coordinate defined and the cross-sectional properties with respect to the coordinate. The governing equations can be written as

$$\text{Euler-Bernoulli beam: } m \frac{d^2 v}{dt^2} + EI_z \frac{d^4 v}{dx^4} = 0,$$

$$\text{Timoshenko beam: } \begin{cases} m \frac{d^2 v}{dt^2} - \kappa_z GA \left(\frac{d^2 v}{dx^2} - \frac{d\varphi_z}{dx} \right) = 0, \\ \rho_w I_z \frac{d^2 \varphi_z}{dt^2} - EI_z \frac{d^2 \varphi_z}{dx^2} - \kappa_z GA \left(\frac{dv}{dx} - \varphi_z \right) = 0. \end{cases}$$

This expression is identical to the pure flapping equations if one replaces v with h and z with y , showing that these are in theory the same motion in different directions. Based on cross-sectional properties in the lead-lag coordinate, the modal frequencies and mode shapes can be obtained by undertaking the numerical transfer matrix approach. The Euler-Bernoulli beam based transfer matrix formulation can be found in the previous example demonstrated in Section 3.3, and the Timoshenko beam based transfer matrix formulation is described in Appendix D. In Table 3.9, natural frequencies derived from the Euler-Bernoulli and the Timoshenko beam theories are listed. For lead-lag motion, the Timoshenko beam theory gives a smaller value for natural frequencies com-

Table 3.9: Lead-lag motion modal frequency based on two beam theories

| Euler-Bernoulli beam (Hz) | Timoshenko beam (Hz) | Diff. % |
|---------------------------|----------------------|---------|
| 51.87 | 42.05 | 23.35 |
| 325.09 | 155.62 | 108.90 |

paring to the case of a Euler-Bernoulli beam, but a much greater difference is observed relative to the discrepancy in flapping. This indicates a dominating effect brought by shear deformation and rotary inertia in the lead-lag motion. Mode shapes at these two frequencies for Euler-Bernoulli and Timoshenko beam are plotted in Figure 3.12. Note that the lead-lag displacements are shown in its dimensionless form $\nu = v/b$ in order to make a direct comparison with the bending slope dv/dx and the section angle of rotation φ_z . The lead-lag mode shapes are fairly similar in both cases, however, the angles of rotation dv/dx for the Euler-Bernoulli beam and φ_z for the Timoshenko beam are very much different. As discussed in Section 3.2, the Timoshenko beam allows

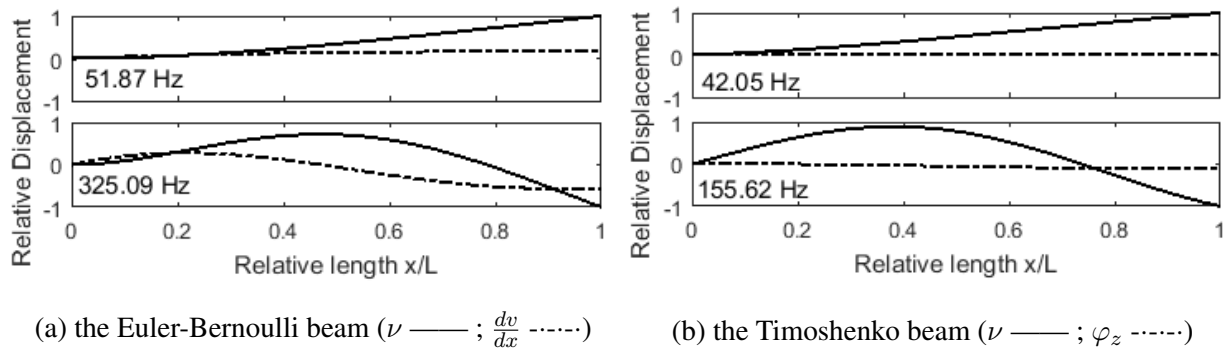


Figure 3.12: Lead-lag 1st and 2nd mode shapes derived by Euler-Bernoulli beam and Timoshenko beam theories

the rotation of cross-section relative to the neutral axis while the Euler-Bernoulli beam assumes perpendicularity. To characterise this, the angle of rotation φ_z is defined relative to the vertical axis as illustrated in Figure 3.3. This is also to say that if the beam behaves like a Euler-Bernoulli beam, φ_z and dv/dx should be the same, or at least similar. Whereas in Figure 3.12, φ_z is not similar

to dv/dx at all and has a much smaller relative displacement value across the span. Physically speaking, it means that cross-sections across the span are significantly deformed due to shear and it confirms a strong presence of the shear deformation and rotary inertia effects. If looking at the short wing from above, the aspect ratio for the beam is defined by the wing semi-span length and the aerofoil chord, in which case the wing is not slender and resembles towards a plate. The shear deformation and rotary inertia effects, therefore, are within expectation much stronger than in a slender beam. To conclude on the short wing of such specification, the lead-lag motion is better suited to be characterised by the Timoshenko beam theory due to the strong presence of shear and rotary inertia effects.

3.4.3 Coupled flapping-lead-lag-torsion modal study

With zero pretwist angle ($\theta=0$), Equation (3.5) can be simplified, for the lead-lag motion to be independent of the coupled flapping-torsion motion. The same also applies to Equation (3.9). Based on the previous modal studies, it is established that flapping and torsional motion can be analysed by the Euler-Bernoulli beam theory in a coupled fashion, while for lead-lag motion, the Timoshenko beam theory needs to be applied. The governing equations can then be written as

$$\begin{aligned}
 m \frac{d^2 h}{dt^2} - S_\alpha \frac{d^2 \alpha}{dt^2} + EI_y \frac{d^4 h}{dx^4} &= 0, \\
 m \frac{d^2 v}{dt^2} - \kappa_z GA \left(\frac{d^2 v}{dx^2} - \frac{d\varphi_z}{dx} \right) &= 0, \\
 \rho_w I_z \frac{d^2 \varphi_z}{dt^2} - EI_z \frac{d^2 \varphi_z}{dx^2} - \kappa_z GA \left(\frac{dv}{dx} - \varphi_z \right) &= 0, \\
 I_\alpha \frac{d^2 \alpha}{dt^2} - S_\alpha \frac{d^2 h}{dt^2} - GJ \frac{d^2 \alpha}{dx^2} &= 0.
 \end{aligned} \tag{3.22}$$

As already discussed, the developed transfer matrix approach tool allows combination of three modes of vibration to be considered as one system. If all coordinates can be considered under one modal frequency, the overall numerical efficiency for solving forced-vibration responses can be improved. The practicality for including lead-lag motion into the coupled flapping-torsion motion is discussed in this section. Overall, there are four general coordinates involved, bending (h) in

the vertical direction is coupled with torsion (α) while lateral bending (v) and shear deformation (ϕ_z) forms another coupled pair. Two coupled systems can be studied combined or separately by the numerical approach introduced in Section 3.3.1. The natural frequencies from the two approaches are listed in Table 3.10. The underlined terms are the lead-lag governed modes. The

Table 3.10: Uncoupled and coupled lead-lag modal frequencies comparisons

| Uncoupled Lead-lag motion (Hz) | Coupled lead-lag motion(Hz) |
|--------------------------------|-----------------------------|
| 11.50 | 11.50 |
| <u>42.05</u> | <u>42.05</u> |
| 71.70 | 71.70 |
| 126.50 | 126.50 |
| <u>155.62</u> | <u>155.63</u> |
| 199.52 | 199.52 |

identical results obtained shows that the lead-lag motion does not affect any modal behaviour of the flapping-torsion system. Instead of studying two coupled systems separately, it is very convenient that all natural frequencies can be captured within one combined system.

As for mode shapes, they are illustrated in Figure 3.11(a) and Figure 3.12(b) if studied separately. When considered combined, Figure 3.13 illustrated mode shapes obtained from the combined approach. Both flapping and lead-lag motions are shown in their dimensionless forms as ξ and ν respectively in order to make a direct comparison with the torsional displacement α . At lead-lag governed modes (42.05 Hz and 155.62 Hz), however, the lead-lag mode shapes showed zero magnitude in displacement along the span. Instead, flapping motion appears to be much more significant. This certainly does not represent the actual modal behaviour under these frequencies in reality. The combined approach hence should be reconsidered. In theory, natural frequencies and mode shape functions are eigenvalues and eigenvectors of a homogeneous equation and the derivation of eigenvector starts with assuming unity for one of the vector elements. In the nu-

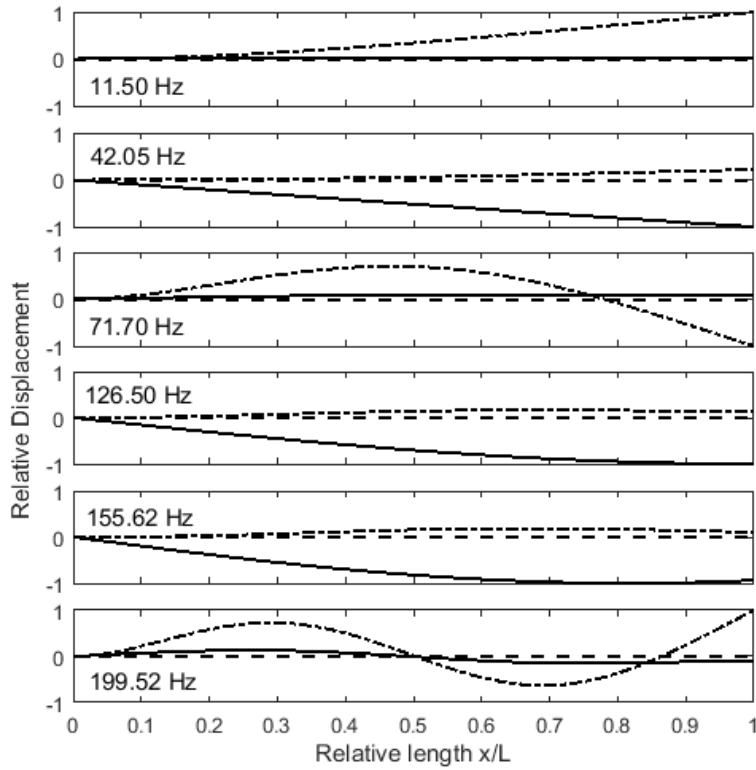


Figure 3.13: Coupled flap-torsion-lead-lag motion mode shape derived by developed tool based on transfer matrix method (Flap - · - · - ·; Lead-lag - - - ; Torsion —)

merical process of the transfer matrix method, the flapping displacement is assumed unity in the eigenvector derivation. Since lead-lag motion is structurally uncoupled with flapping, under lead-lag governed modes, any assumption in the flapping would not reflect onto the lead-lag motion. The mode shape function for lead-lag motion cannot be solved in this case. This points out one of the prerequisites for obtaining valid coupled mode shape function. The vibration coordinates need to be structurally coupled. Under the current parameters for the short wing in the propeller-wing configuration, the lead-lag motion is not structurally coupled with flapping and torsion. The modal analysis, therefore, should separate these two coupled systems, one with coupled-flap-torsional motion and the other with Timoshenko lead-lag motion.

3.5 Conclusion

In this section, basic beam theories for characterising the short wing in a propeller-wing configuration have been firstly introduced, namely the Euler-Bernoulli and the Timoshenko beam theories. Based on three modes of vibration (flapping, lead-lag and torsion) considered, the equations of motion with those vibration modes and coupling between them have been obtained through the Extended Hamilton's Principle. To determine which theory or combination of these theories are the most suitable representation of a short wing structure in this thesis, modal analyses have been carried out. Instead of using analytical formulations, a numerical approach based on the transfer matrix method has been developed and validated against past literature. The transfer matrix method showed advantages in terms of versatility and simplicity when dealing with structural coupling at various levels. Utilising the developed modal analysis, contributions of shear deformation, rotary inertia and structural coupling effects have been characterised under the short wing in the present study. Neglecting coupling effect, a percentage difference of 8% was found in torsional natural frequencies, which makes the coupling between flapping and torsion motion a significant contribution to the overall structural dynamics. Regarding the lead-lag motion, it is structurally uncoupled for the specification considered here. However, due to the ratio between the chord and a short span length, shear deformation and rotary inertia dominate the classical beam behaviour, resulting in at least 23% difference between natural frequencies. A coupled Euler-Bernoulli beam-based flapping-torsional motion with a separate Timoshenko beam-based lead-lag has been therefore found to be the most suited for the short wing under this specification. To integrate with the aerodynamic model discussed in Chapter 2, the dynamic responses can be obtained now. The integration of aerodynamics and structural dynamics will be discussed in the next chapter and the derived mode shapes from the transfer matrix method as illustrated in Figure 3.11 (a) and Figure 3.12 (b) will be used as a standard basis in obtaining solutions for forced-vibration responses.

Chapter 4

Aeroelastic Instability and Numerical Application

In Chapters 2 and 3, aerodynamics and structural dynamics were studied separately. In structural dynamics, the interaction between elastic and inertia forces are studied and the system's behaviour in motion displacements, velocities and accelerations under excitation can be characterised by a set of governing equations. Aerodynamic loads, at the same time, are directly dependent on motion displacements, velocities and accelerations. For structures subjected to aerodynamic loads, external loads can change their motion behaviour, in turn, motions can further define external loadings. This interaction between fluid and structure is termed aeroelasticity. It also means that, in a fluid-structure coupled system, the participation of aerodynamics will change the mass, damping and stiffness behaviour comparing to a pure structure system and it can lead to instabilities resulting in catastrophic consequences. The integration of the aerodynamic model and the structural model, hence, needs to be considered in the early stages of aircraft design specifying the range of feasibility and stability boundaries. Before solving the dynamic response of an aeroelastic system, those instabilities under certain flight conditions need to be discussed. In this chapter, the sectional 2D aerodynamic model and beam-like wing model are combined and developed into the complete aeroelastic model. The static and dynamic instabilities in aeroelasticity are firstly introduced on

a 2D aerofoil model used in Chapter 2 and then extended onto the beam-like model developed in Chapter 3. The reliability of such instability analyses is verified through benchmark case studies from the literature. Another important application of the aeroelastic model is to predict dynamic responses for the aeroelastic system. Numerical algorithms for the aeroelastic solution are also discussed and applied. Finally, the different capabilities of the model are verified against the literature results.

In this chapter, the aeroelastic instability will be discussed on a 2D aerofoil example, the wing tip sectional model of the short wing, the Goland wing and the short wing itself. Starting with the static instability phenomenon, a 2D aerofoil model will be used to demonstrate the scientific principle and the analytical derivation for divergence in Section 4.1.1, and the wing tip section model on the short wing will be investigated analytically for its divergence boundary. In Section 4.1.2, a dynamic aeroelastic phenomenon, flutter, will be introduced and a numerical approach based on the p-k method will be built and validated against benchmark examples, followed by an investigation of the dynamic stability boundary for the wing tip section of the short wing. Extending the stability studies onto the beam-like model, divergence and flutter behaviour on finite wings will be discussed in Section 4.2. Within Section 4.2, the Goland wing example [29] will be used to validate the numerical approach and the application of coupled mode shapes will also be introduced. Lastly, investigation of the aeroelastic stability boundary will be carried out on the short wing structure from the propeller-wing configuration.

4.1 Instabilities on aerofoil model

4.1.1 Static aeroelasticity - Divergence analysis

Recalling steady aerodynamic theory and the sectional aerofoil model discussed in Section 2.2 and 2.5, a simple aeroelastic model in steady flow can be built. As illustrated in Figure 4.1, an aerofoil attached to translational and rotational springs, representing stiffness in the plunging and pitching

motion, is presented. In steady aerodynamics, the steady lift and moment are dependent on the

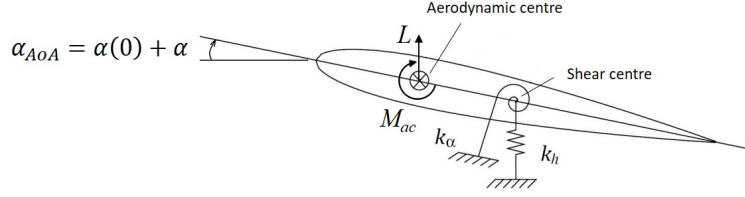


Figure 4.1: Aerofoil under aerodynamic forces

angle of attack α_{AoA} , which is a function of the pitching displacement α and its initial condition $\alpha(0)$ [52]. An equilibrium equation, hence, can be written in the pitching motion as

$$M_{ac} + \rho U_a^2 b^2 C_L \alpha_{AoA} (0.5 + a) = k_\alpha \alpha, \quad \text{where} \quad \alpha_{AoA} = \alpha(0) + \alpha. \quad (4.1)$$

M_{ac} is the steady aerodynamic moment, ρ is the air density, U_a is the flow approaching velocity, b is the half chord length, C_L is the lift coefficient, a is the dimensionless measure for the offset distance between the shear centre and the gravitational centre and k_α is the discrete spring stiffness for torsion. The pitching angle α then can be rearranged into

$$\alpha = \frac{M_{ac} + \rho U_a^2 b^2 C_L \alpha(0) (0.5 + a)}{k_\alpha - \rho U_a^2 b^2 C_L (0.5 + a)}. \quad (4.2)$$

Regarding the denominator in Equation (4.2), the difference between k_α and $\rho U_a^2 b^2 C_L (0.5 + a)$ can be treated as the effective torsional stiffness of the aeroelastic system. Pitching stiffness k_α comes from a torsional spring, hence, has a non-zero and relatively fixed value. $\rho U_a^2 b^2 C_L (0.5 + a)$ is the gradient between pitching angle and pitching moment, which can also be considered as the stiffness introduced aerodynamically. When there is a change in pitching angle α , the restoring moment from the spring k_α always needs to be equal to or larger than the aerodynamic pitching moment to maintain a stable system, hence, stability can be expressed mathematically as $k_\alpha \geq \rho U_a^2 b^2 C_L (0.5 + a)$. A critical situation, when the denominator (effective stiffness of the system) becomes negative, is a static instability phenomenon in aeroelasticity called divergence. For a given aerofoil geometry, flight conditions need to be defined carefully, especially the advancing

velocity the given geometry can stably allow. This critical condition can be written as

$$k_\alpha = \rho U_D^2 b^2 C_L (0.5 + a), \quad (4.3)$$

where the divergence velocity U_D can be expressed as

$$U_D = \sqrt{\frac{k_\alpha}{\rho b^2 C_L (0.5 + a)}}. \quad (4.4)$$

At this critical speed, any perturbation to the system will develop into an increment of pitching displacement until structural failure. For the given wing geometry, the structure can only operate below this critical velocity. On the other hand, the aerodynamic stiffness is also highly dependent on the aerofoil geometry. When $a \leq -0.5$, which indicates that the shear centre is positioned forwards of the aerodynamic centre, Equation (4.4) becomes invalid. The effective stiffness, however, would always be larger or equal to k_α and therefore stability is ensured. Thanks to linearity between pitching angle and pitching moment, as well as U_a^2 and aerodynamic stiffness, the divergence boundary can be predicted when only limited information about the system is available, also without any destructive experiment. For more details about divergence, one can refer to books by Hodges and Pierce [52], Fung [84] and Wright and Cooper [102].

Recalling the sectional aerofoil model for wing tip on the short wing discussed in Section 2.5.3, the estimated aerofoil parameters related to a divergence study are listed as

$$k_\alpha = 1.9508 \times 10^5 \text{ Nm} \quad \rho = 1.225 \text{ kg/m}^3 \quad c = 2b = 0.6 \text{ m} \quad a = -0.277 \quad C_L = 2\pi.$$

The critical divergence velocity can be computed for Equation (4.4) and it is found that the static instability would happen at $U_D = 1123.76 \text{ m/s}$. This is a velocity beyond the subsonic assumption. However, the result showed that, in the subsonic regime, the aircraft will not encounter any divergence. The critical condition will be further confirmed with the numerical stability analysis in later sections. As for the wing tip, it has the least elastic torsional stiffness. The comparison with aerodynamic stiffness, hence, becomes crucial and static stability can be insured when operating within subsonic regime.

4.1.2 Unsteady aeroelasticity - Flutter analysis

Instability phenomena also exist in unsteady aeroelastic behaviour. When applying quasi-steady or unsteady aerodynamic theories to the aerofoil model, the structural dynamics and unsteady aerodynamic loads are coupled. The governing equations can be written in matrix form as

$$\mathbf{M} \frac{d^2 \mathbf{u}}{dt^2} + \mathbf{C} \frac{d\mathbf{u}}{dt} + \mathbf{K} \mathbf{u} = \mathbf{F}_{aero}, \quad (4.5)$$

in which

$$\mathbf{M} = \begin{bmatrix} m & -S_\alpha \\ -S_\alpha & I_\alpha \end{bmatrix} \quad \mathbf{C} = \begin{bmatrix} c_h & 0 \\ 0 & c_\alpha \end{bmatrix} \quad \mathbf{K} = \begin{bmatrix} k_h & 0 \\ 0 & k_\alpha \end{bmatrix} \quad \mathbf{u} = \begin{Bmatrix} h \\ \alpha \end{Bmatrix} \quad \mathbf{F}_{aero} = \begin{Bmatrix} L_h \\ M_\alpha \end{Bmatrix}.$$

The LHS of Equation (4.5) describes the structural dynamics of the system, while the RHS of Equation (4.5) quantifies the aerodynamic loadings. The damping matrix \mathbf{C} is introduced here and the damping parameters are taken as zero ($c_h = c_\alpha = 0$), as the structure considered has no damping present. The vector for the \mathbf{F}_{aero} forcing varies with the aerodynamic theory used. Recalling aerodynamic theories discussed in Chapter 2, a general format, however, is shared amongst all unsteady and quasi-steady theories, which consist of aerodynamic mass, damping and stiffness matrices as

$$\mathbf{F}_{aero} = \mathbf{M}_a \frac{d^2 \mathbf{u}}{dt^2} + \mathbf{C}_a \frac{d\mathbf{u}}{dt} + \mathbf{K}_a \mathbf{u}. \quad (4.6)$$

When quasi-steady aerodynamics is considered, the aerodynamic matrices are defined as

$$\mathbf{M}_a = \begin{bmatrix} 0 & 0 \\ 0 & 0 \end{bmatrix} \quad \mathbf{C}_a = 2\pi\rho b U_a \begin{bmatrix} -1 & -b(\frac{1}{2} - a) \\ b(\frac{1}{2} + a) & b^2(\frac{1}{4} - a^2) \end{bmatrix} \quad \mathbf{K}_a = 2\pi\rho U_a^2 b \begin{bmatrix} 0 & -1 \\ 0 & b(\frac{1}{2} + a) \end{bmatrix}.$$

Whereas for Theodorsen's unsteady theory, the matrices are defined as

$$\mathbf{M}_a = \pi\rho b^2 \begin{bmatrix} -1 & ab \\ ab & -a^2 b^2 - b^2/8 \end{bmatrix} \quad \mathbf{K}_a = 2\pi\rho U_a^2 b C(k) \begin{bmatrix} 0 & -1 \\ 0 & b(\frac{1}{2} + a) \end{bmatrix}$$

$$\mathbf{C}_a = \pi\rho b U_a \begin{bmatrix} -2C(k) & -2bC(k)(\frac{1}{2} - a) - b \\ 2bC(k)(\frac{1}{2} + a) & 2b^2C(k)(\frac{1}{4} - a^2) - b^2(\frac{1}{2} - a) \end{bmatrix}.$$

No matter which aerodynamic theory is applied, the general solution for all the degrees of freedom can be assumed. One can write \mathbf{u} in time domain as

$$\mathbf{u} = \bar{\mathbf{u}}e^{st} = \begin{Bmatrix} \bar{h} \\ \bar{\alpha} \end{Bmatrix} e^{st}, \text{ where } st = (\lambda\omega + i\omega)t, \quad (4.7)$$

λ is the damping/decaying parameter and ω is the harmonic frequency. Recalling all the unsteady aerodynamic theories studied in Section 2.4, the characterisation of aerodynamic loadings commonly features the dimensionless time τ and reduced frequency k . For compatibility and a better understanding of the aeroelastic model, the general solution above can be modified as

$$\mathbf{u} = \bar{\mathbf{u}}e^{p\tau}, \text{ where } p\tau = (\lambda k + ik)\tau \text{ and } k = \omega b/U_\infty. \quad (4.8)$$

After substituting the above expression into Equation (4.5), one will have a homogeneous set of equations expressed as

$$\left[p^2(\mathbf{M} - \mathbf{M}_a)\frac{U_\infty^2}{b^2} + p(\mathbf{C} - \mathbf{C}_a)\frac{U_\infty}{b} + (\mathbf{K} - \mathbf{K}_a) \right] \bar{\mathbf{u}} = 0. \quad (4.9)$$

For a non-trivial solution of $\bar{\mathbf{u}}$ to exist, the determinant of the square matrix in the front must be set to zero. Within that expression, structural and aerodynamic matrices are filled with known parameters for a given geometry and flight condition. Hence, the characteristic roots can be solved and are typically two pairs of complex conjugates as

$$p_1 = \lambda_1 k_1 \pm ik_1 \quad \text{and} \quad p_2 = \lambda_2 k_2 \pm ik_2. \quad (4.10)$$

The sign of damping factor λ and reduced frequency k would give an insight into the dynamic behaviour pattern, showing which instability can be discovered. For the damping factor λ , it is possible to have a value that is larger than zero, equal to zero or less than zero. And the reduced frequency k can be larger than zero or equal to zero. As shown in Figure 4.2, the damping parameter λ gives a converging pattern when it is negative, a standard sinusoidal wave when it equals to zero and a diverging pattern when it is positive. Accordingly it means that when $\lambda < 0$, stability is ensured, the stability boundary is for $\lambda = 0$ and instability is present when $\lambda > 0$. Meanwhile,

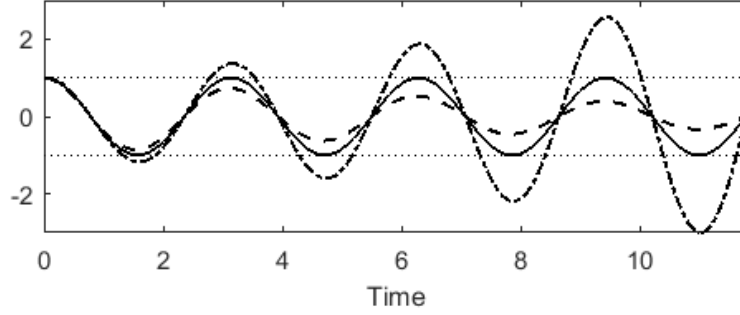


Figure 4.2: Solution pattern when $\lambda < 0$ (- - -), $\lambda = 0$ (—) and $\lambda > 0$ (-·-·-)

the reduced frequency k is a much more straightforward concept. When $k > 0$, this indicates an unsteady behaviour. When $k = 0$, static behaviour is present. From [52], the type of motion and stability based on values of λ and k is illustrated as in Table 4.1.

Table 4.1: Types of motion based on λ and k values [52]

| λ | k | Type of motion | Stability characteristics |
|-----------|-------|---------------------------------|---------------------------|
| < 0 | $= 0$ | Continuous converging | Stable |
| $= 0$ | $= 0$ | Time independent | Stability boundary |
| > 0 | $= 0$ | Divergence | Unstable |
| < 0 | > 0 | Converging oscillation | Stable |
| $= 0$ | > 0 | Simple harmonic | Stability boundary |
| > 0 | > 0 | Diverging oscillation (Flutter) | Unstable |

In the case when $\lambda > 0$ and $k > 0$, the system is an unsteady aeroelastic instability called flutter and the stability boundary at $\lambda = 0$ and $k > 0$ is the flutter boundary. Physically speaking, during flutter, the restoring resistance from the structure is less than aerodynamic energy feeding into the system, hence a negative damping is present. The energy input results in the aerostructure to vibrate with increasing amplitude until structure failure happens.

As discussed in Section 4.1.1, for a given aerofoil geometry, flight conditions need to be defined carefully to avoid divergence happening. This is mainly controlled by the advancing velocity and

the critical value, which is also the maximum velocity a given geometry allows, can be obtained. This is similar in the unsteady instability regime. For a given aerofoil geometry, finding the critical velocity representing the flutter boundary is the key in any flutter analysis.

There are many methods for analysing flutter: p-method, classic flutter analyses method, k-method and p-k method. They are different in the way dynamic motions are assumed. The derivation discussed previously in this section falls into the p-method. It assumes complex exponential motion as in Equation (4.8). With this assumption, both the damping and the frequency can be monitored for the different flight conditions studied. The damping and frequency behaviour gives insights into the stability margin as well as the physical mechanism that causes instability. With this information, one can attempt to eliminate the instability. On the other hand, unsteady aerodynamic theories like the Theodorsen's theory are derived based on simple harmonic motion in incompressible flow. The technique has also been proven adequate under subsonic conditions. Having to consider amplitude variation of the oscillatory motion for the unsteady aerodynamic theories becomes inefficient. The classic flutter analysis and k-method, therefore, assume the general motions to be simple harmonic. The classic flutter analysis process is similar to the p-method described above, but assumes simple harmonic motion as $\mathbf{u} = \bar{\mathbf{u}}e^{i\omega t}$. It is not difficult to point out that classic flutter analysis method is then not capable of analysing the system's damping behaviour. k-method is developed by introducing damping participation, and this is done by manually adding in dissipative structural damping terms in the classic flutter analysis. Discussion, however, about the inappropriate assumption of simple harmonic motions would need consideration. Detailed explanations and comparisons of those methods can be found in [52, 102]. For flutter analysis in this chapter, the p-k method is used. It is an efficient and accurate flutter analysis approach widely used by aeroelasticians in aircraft designs. It assumes generic motions as exponential functions for the inertia and elastic forces and combines with simple harmonic motion assumption in the unsteady aerodynamic model.

Unlike other flutter analysis approaches, different assumptions are made for structural dynamics and aerodynamic loads in p-k method. For the LHS of Equation (4.5) where structural be-

haviour is described, it is assumed that

$$\mathbf{u} = \bar{\mathbf{u}}e^{p\tau} \quad \text{where} \quad p\tau = (\lambda k + ik)\tau \quad \text{and} \quad k = \omega b/U_\infty. \quad (4.11)$$

The structural part then becomes

$$[p^2\mathbf{M}_s + p\mathbf{C}_s + \mathbf{K}_s]\bar{\mathbf{u}} = \mathbf{F}_{aero}, \quad \text{where} \quad \mathbf{M}_s = \frac{U_\infty^2}{b^2}\mathbf{M}, \quad \mathbf{C}_s = \frac{U_\infty}{b}\mathbf{C} \quad \text{and} \quad \mathbf{K}_s = \mathbf{K}. \quad (4.12)$$

Whereas for the aerodynamic loadings \mathbf{F}_{aero} , a simple harmonic motion is assumed as $\mathbf{u} = \bar{\mathbf{u}}e^{ik\tau}$.

The aerodynamic loading terms, therefore, can be integrated as a function of reduced frequency k .

$$\mathbf{F}_{aero} = \mathbf{A}(ik)\bar{\mathbf{u}}e^{ik\tau} \quad \text{where} \quad \mathbf{A}(ik) = -k^2\frac{U_\infty^2}{b^2}\mathbf{M}_a + ik\frac{U_\infty}{b}\mathbf{C}_a + \mathbf{K}_a \quad (4.13)$$

Combining Equation (4.12) and (4.13), governing equations for the flutter analysis are obtained as

$$[p^2\mathbf{M}_s + p\mathbf{C}_s + [\mathbf{K}_s - \mathbf{A}(ik)]]\bar{\mathbf{u}} = 0, \quad (4.14)$$

which can be formulated and solved numerically as an eigenvalue problem as

$$p \begin{Bmatrix} p\bar{\mathbf{u}} \\ \bar{\mathbf{u}} \end{Bmatrix} = \begin{bmatrix} \mathbf{0} & \mathbf{I} \\ \mathbf{M}_s^{-1}\mathbf{C}_s & \mathbf{M}_s^{-1}[\mathbf{K}_s - \mathbf{A}(ik)] \end{bmatrix} \begin{Bmatrix} p\bar{\mathbf{u}} \\ \bar{\mathbf{u}} \end{Bmatrix}.$$

At a given advancing velocity U_∞ , the analysis starts with assuming an initial k , which defines the initial aerodynamic loadings $\mathbf{A}(ik)$. The eigenvalues p can be solved and come as complex conjugate pairs. Convergence would lead to the solution of eigenvalues p , in which one of the imaginary parts should be equal to the input k . It normally takes a few iterations to find the true value of k . Therefore, the imaginary part of p is an input as the new k into $\mathbf{A}(ik)$ and is used again to solve the eigenvalues. This process is repeated until the input and output k agree with each other, and the corresponding real part of the eigenvalues indicate the damping property at the given U_∞ . By mapping out the damping and reduced frequency k at each velocity, instabilities can be found when damping reaches zero, which physically means aerodynamics keep feeding energy into the structure without any available damping, causing the system to resonant. In a special case when both damping and frequency are at zero, this leads to a static instability termed as divergence. In

other cases when the damping reaches zero but the frequency is not at zero, it is the phenomenon known as flutter. At this point, the frequency is called flutter frequency and the corresponding velocity is called critical flutter velocity. With the same approach, the divergence boundary can also be obtained by setting k to zero. This would bring p to zero and $C(k)$ to unity. Recalling Equation (4.14), the same eigenvalue problem is formed. Inputting different advancing velocity, the critical divergence velocity can be obtained when determinant of $[\mathbf{K}_s - \mathbf{A}(ik)]$ reaches zero.

2D flutter model validation

An example case study carried out by Hodges and Pierce [52] and Shams et al. [49], with parameters listed below, is presented in the following to demonstrate the validity of the 2D flutter analysis model:

$$m = 1 \text{ slug} \quad I_\alpha = 1.606 \text{ slug.ft}^2 \quad a = -0.2 \quad x_\alpha = 0.1 \quad c = 5.18 \text{ ft}$$

$$k_h = 100 \text{ lbs per ft} \quad k_\alpha = 1003.75 \text{ ft.lb/rad} \quad \rho = 0.002378 \text{ slug/ft}^3$$

The imperial units were used in [49], hence, the same unit system is applied here. The results are reproduced and compared against [52] in Figure 4.3. Damping factor λ/ω_α and dimensionless frequency ω/ω_α are plotted against dimensionless velocity $U_\infty/\omega_\alpha b$. As shown, the present model gives a good agreement with the results obtained in [52]. Note that the eigenvalues obtained from the p-k method are symmetrical to the horizontal velocity axis (complex conjugate), therefore only the stable or the negative part is compared in the figure shown. The critical flutter velocity and frequency are defined at the speed where the damping factor reaches zero. According to Figure 4.3, it is when dimensionless velocity $U_\infty/\omega_\alpha b$ is at 2.2. The root under this condition gives a dimensionless frequency ω_F/ω_α of 0.65. Translating the dimensionless parameters back into physical space, flutter will occur at a velocity of 141 ft./s and the oscillation is at 2.6 Hz.

The same analysis procedures can be applied to the sectional wing-tip model discussed earlier in Section 2.5.3. The damping factor and dimensionless frequencies can be computed along with a range of advancing velocities, and Figure 4.4 can be plotted. It is clear that the damping factor reaches zero as the dimensionless velocity goes towards 3.8. In the physical space, the critical

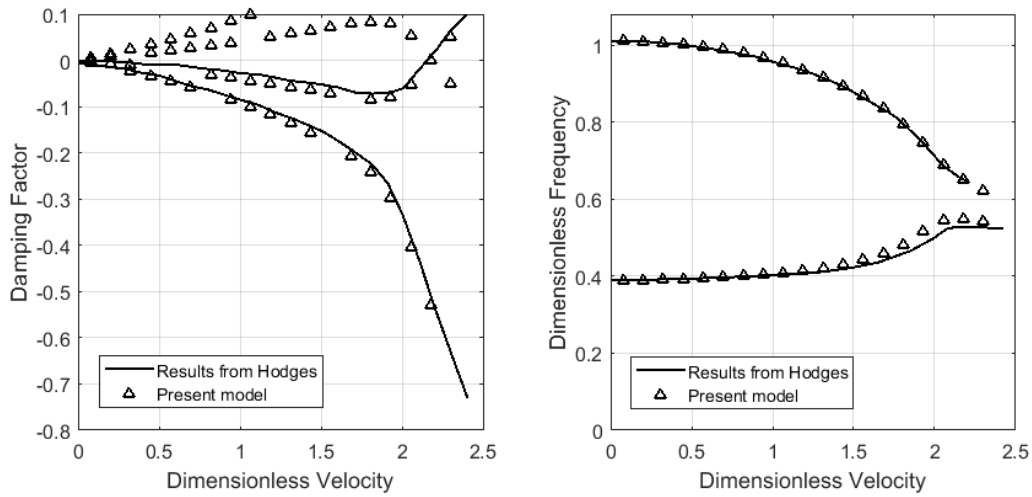


Figure 4.3: Damping and reduced frequency against dimensionless velocity based on case studied in [52]

flutter velocity is at 849.3 m/s. Under this flutter condition, the frequency is reported as 0.42 dimensionlessly which physically means the system will oscillate at a frequency of 49.6 Hz. This further confirmed the feasibility of flight condition studied, which is at an advancing velocity of 128m/s. Inputting k as zero, the divergence boundary can be investigated for the wing-tip model.

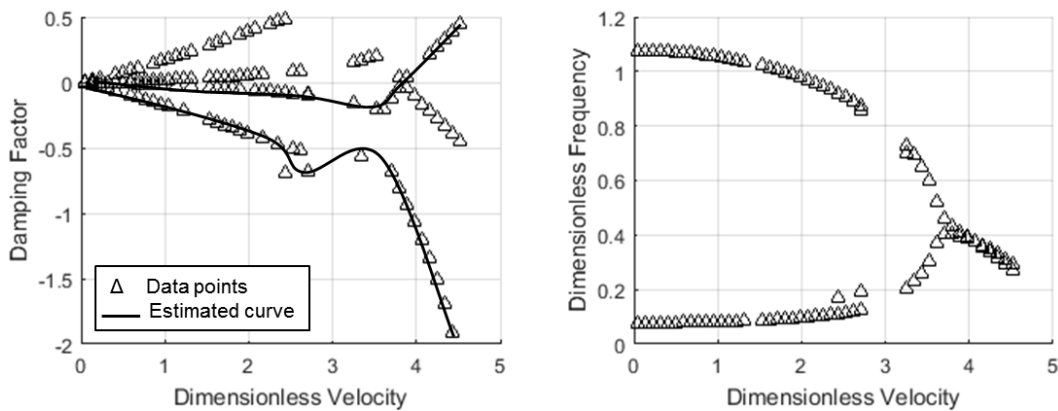


Figure 4.4: Flutter analysis on wing-tip sectional model for the short wing configuration given in Table3.5

Under a range of advancing velocities, the static aeroelastic system is analysed and the determinant

of matrix $[\mathbf{K}_s - A(ik)]$ is mapped accordingly. As illustrated in Figure 4.5, the critical velocity is found at 1123.76 m/s, identical to the critical velocity defined analytically in Section 4.1.1.

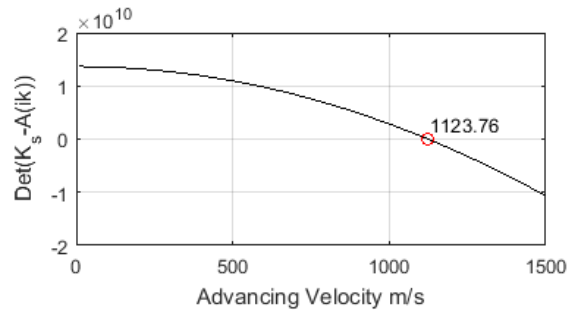


Figure 4.5: Divergence velocity on wing-tip sectional model for the short wing configuration given in Table 3.5

4.2 Instabilities on wings

In the case of propeller/wing configuration, an aerofoil section model cannot take into account variation in airflow velocity and pressure distribution along the wing span. At the same time, a sectional aerofoil model does not show continuity within the structure. A beam-like model described in Chapter 3, on the other hand, is able to numerically represent wing structures under various beam theory assumptions. It can be numerically discretised into several aerofoil segments of infinitesimal length. Sectional aerodynamic theories, hence, can be applied to characterise lift and moment locally. The integration of these two models is the core for simulating aeroelastic behaviour of propeller-wing configurations. In this section, the integration of the beam model is briefly discussed first and the attention is mainly focused on static and unsteady aeroelastic instability based on the beam model. Similar to the sectional model, instabilities in the flapping and torsional direction will be discussed. Lead-lag motion, on the other hand, is uncoupled from the other motions structurally and aerodynamically. Furthermore, the lead-lag motion has a much higher bending stiffness. It is, therefore, not a crucial element in the energy feeding loop here. The stability study, hence, only considers coupled flapping and torsional motion. As demonstrated

previously, the divergence boundary can be obtained through unsteady instability (flutter) analysis if manually setting k to zero. A stability analysis approach, hence, is developed numerically, taking consideration of both divergence and flutter. On the other hand, the analytical derivation for wing divergence is eliminated.

Recalling the modal analysis discussed in Section 3.3, the flapping and torsional motion displacements can be treated as combinations of different modal shape functions as

$$h = \sum_{j=1}^{\infty} \theta_j(x) f_j(t) \quad \alpha = \sum_{j=1}^{\infty} \eta_j(x) z_j(t). \quad (4.15)$$

With θ_j and η_j obtained through modal analysis developed in Section 3.3.2, the unknowns left to be investigated are the time-dependent functions f_j and z_j . Recalling the coupled flapping-torsional motion equations

$$\begin{aligned} m \frac{d^2 h}{dt^2} - S_{\alpha} \frac{d^2 \alpha}{dt^2} + EI_y \frac{d^4 h}{dx^4} &= L_h, \\ I_{\alpha} \frac{d^2 \alpha}{dt^2} - S_{\alpha} \frac{d^2 h}{dt^2} - GJ \frac{d^2 \alpha}{dx^2} &= M_{\alpha}. \end{aligned}$$

Equation (4.15) can be substituted to the above expression, the coupled flapping-torsion motion, neglecting pretwist angle, can be characterised according to Equation (3.5) as

$$\begin{aligned} \sum_{j=1}^{\infty} \left[m \theta_j \frac{d^2 f_j}{dt^2} - S_{\alpha} \eta_j \frac{d^2 z_j}{dt^2} + EI_y \theta_j'''' f_j \right] &= L_h, \\ \sum_{j=1}^{\infty} \left[I_{\alpha} \eta_j \frac{d^2 z_j}{dt^2} - S_{\alpha} \theta_j \frac{d^2 f_j}{dt^2} - GJ \eta_j'' z_j \right] &= M_{\alpha}. \end{aligned}$$

In order to discretise the continuous system into its modal space, Galerkin's method is applied by integrating modal shape functions along the wing span, and the governing equation can be computed in the form of a matrix system as

$$\mathbf{M} \frac{d^2 \mathbf{u}}{dt^2} + \mathbf{C} \frac{d\mathbf{u}}{dt} + \mathbf{K} \mathbf{u} = \mathbf{F}_{aero}, \quad (4.16)$$

in which the mass, damping and stiffness matrices are defined as

$$\mathbf{M} = \left[\begin{array}{c|c} [\int m\theta_i\theta_j dx]_{N_f \times N_f} & [-\int S_\alpha\theta_i\eta_j dx]_{N_f \times N_z} \\ \hline [-\int S_\alpha\eta_i\theta_j dx]_{N_z \times N_f} & [\int I_\alpha\eta_i\eta_j dx]_{N_z \times N_z} \end{array} \right] \quad \mathbf{u} = \left\{ \begin{array}{l} [f_j(t)]_{N_f \times 1} \\ [z_j(t)]_{N_z \times 1} \end{array} \right\}$$

$$\mathbf{C} = \left[\begin{array}{c|c} [\int c_h\theta_i\theta_j dx]_{N_f \times N_f} & \mathbf{0} \\ \hline \mathbf{0} & [\int c_\alpha\eta_i\eta_j dx]_{N_z \times N_z} \end{array} \right] \quad \mathbf{F}_{aero} = \left\{ \begin{array}{l} [\int \theta_i L_h dx]_{N_f \times 1} \\ [\int \eta_i M_\alpha dx]_{N_z \times 1} \end{array} \right\}$$

$$\mathbf{K} = \left[\begin{array}{c|c} [\int EI_y\theta_i\theta_j''' dx]_{N_f \times N_f} & \mathbf{0} \\ \hline \mathbf{0} & [-\int GJ\eta_i\eta_j'' dx]_{N_z \times N_z} \end{array} \right].$$

In comparison to the 2D sectional flutter model, the system is presented featuring mode shape functions derived from modal analysis, and the matrices sizes are dependent on the number of modes considered. Subscripts i and j are integers which run through the number of modes and indicate element positions in the sub-matrices. If taking N_f modes of flapping and N_z modes of torsion into consideration, the mass, damping and stiffness matrices would have $(N_f + N_z)$ rows and $(N_f + N_z)$ columns, whereas vectors \mathbf{u} and \mathbf{F}_{aero} would have a single column with $(N_f + N_z)$ rows. Based on the formulation from Theodorsen's theory, the aerodynamic lift and moment can also be processed in a similar fashion as

$$\mathbf{F}_{aero} = \mathbf{M}_a \frac{d^2 \mathbf{u}}{dt^2} + \mathbf{C}_a \frac{d\mathbf{u}}{dt} + \mathbf{K}_a \mathbf{u}, \quad (4.17)$$

$$\text{where } \mathbf{M}_a = \pi \rho b^2 \left[\begin{array}{c|c} [-\int \theta_i\theta_j dx]_{N_f \times N_f} & [\int ab\theta_i\eta_j dx]_{N_f \times N_z} \\ \hline [\int ab\eta_i\theta_j dx]_{N_z \times N_f} & [\int (-a^2b^2 - b^2/8)\eta_i\eta_j dx]_{N_z \times N_z} \end{array} \right],$$

$$\mathbf{C}_a = \pi \rho b U_\infty \left[\begin{array}{c|c} [-\int 2C(k)\theta_i\theta_j dx]_{N_f \times N_f} & [-\int (2bC(k)(\frac{1}{2} - a) + b)\theta_i\eta_j dx]_{N_f \times N_z} \\ \hline [\int 2bC(k)(\frac{1}{2} + a)\eta_i\theta_j dx]_{N_z \times N_f} & [\int [2b^2C(k)(\frac{1}{4} - a^2) - b^2(\frac{1}{2} - a)]\eta_i\eta_j dx]_{N_z \times N_z} \end{array} \right],$$

$$\mathbf{K}_a = 2\pi \rho U_\infty^2 bC(k) \left[\begin{array}{c|c} \mathbf{0} & [-\int \theta_i\eta_j dx]_{N_f \times N_z} \\ \hline \mathbf{0} & [\int b(\frac{1}{2} + a)\eta_i\eta_j dx]_{N_z \times N_z} \end{array} \right].$$

Accordingly, the aerodynamically defined mass, damping and stiffness matrices are of the same size as the structural matrices \mathbf{M} , \mathbf{C} and \mathbf{K} . Applying the p-k method assumptions onto the aeroelastic system, general exponential ($\mathbf{u} = \bar{\mathbf{u}}e^{p\tau}$) and simple harmonic motion ($\mathbf{u} = \bar{\mathbf{u}}e^{ik\tau}$) are

assigned to the structural and aerodynamic terms respectively. Following the derivation procedures described by Equations (4.12), (4.13) and (4.14), the eigenvalue problem can be formed. Flutter analysis proceeds as discussed Section 4.1.2, the damping and reduced frequency can be mapped out at each given advancing velocity.

For wing flutter, the Goland wing is a classic example to validate against and has been used in a number of publications [29, 59, 68, 103–106]. An example is shown here to validate the present wing flutter model with the Goland wing parameters and the parameter values are listed as

$$m = 35.72 \text{ kg/m} \quad I_\alpha = 8.6469 \text{ kgm} \quad EI_y = 99772200 \text{ N/m}^2 \quad GJ = 987600 \text{ N/m}^2$$

$$a = -0.34 \quad x_\alpha = -0.2 \quad c = 1.829 \text{ m} \quad L = 6.096 \text{ m} \quad \rho = 1.225 \text{ kg/m}^3$$

Starting by obtaining the modal frequencies and shape functions, uncoupled analytical mode shapes as described in Equation (3.11) and (3.12) are implemented initially here. The damping factor and frequencies can be obtained and are plotted for a range of advancing velocities in Figure 4.6. As il-

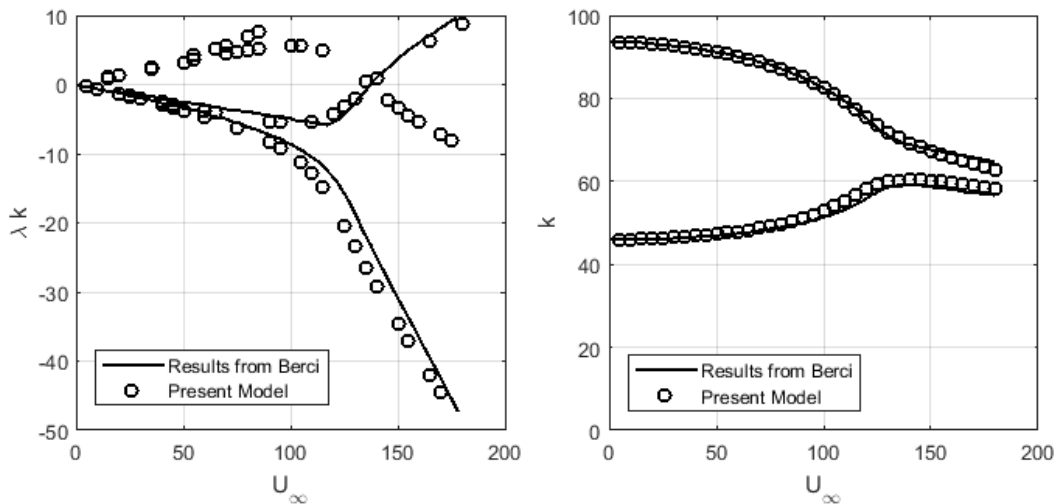


Figure 4.6: Wing flutter analysis based on uncoupled bending and torsional modes for the Goland wing

lustrated, when considering one bending and one torsional modes, the damping factor reaches zero when the aircraft is advancing at 136.81 m/s, and this velocity defines the critical flutter boundary.

Accordingly, at the critical flutter velocity, the flutter frequency is found to be 11.1 Hz (70 rad/s), which matches with the results reported in [29, 59, 68, 103–106]. As Goland reported in [29, 68], the exact flutter velocity was found at 137.25m/s. Results from the present uncoupled model give an error of only -0.32%. This error can be contributed by the number of discrete data point, as well as the number of beam element considered in the structural model. In the next section, the coupled modal functions are used and the error involved reduces significantly. As for mapping the damping and frequency at each advancing velocity, a good agreement can also be observed between results given by the present wing flutter model and [59]. In Reference [29, 59, 68, 103, 104, 106], bending and torsion motion mode shapes were studied separately and implemented in the flutter analysis. Therefore, Figure 4.6 is also obtained by using uncoupled bending and torsion mode shapes in Equation (4.12) and (4.13).

4.2.1 Coupled modes in aeroelastic stability analysis

Bending and torsion are, however, structurally coupled due to offset between shear and gravitational centres ($x_\alpha = -0.2$). As discussed in Section 3.3.1, the numerical transfer matrix method can consider coupled modes which contain different vibration motions at one harmonic frequency and give a more realistic representation of the system's modal behaviour. With parameters of a Goland wing, the coupled modal frequencies are found at 7.7 Hz, 15.2 Hz, 38.8 Hz and 55.3 Hz by numerical modal analysis tool developed. The same coupled frequencies were also obtained by Berci and Cavallaro in [59] using NASTRAN's FEM, however, not implemented in his flutter model. This, however, further confirms the feasibility and accuracy the transfer matrix method can afford. On the other hand, Banerjee developed CALFUN which is a flutter analysis software, programmed in FORTRAN, using normal mode method and generalised coordinates to compute the flutter speed of an aircraft wing based on its structural and aerodynamic data [105]. The normal mode method is similar to the transfer matrix method described earlier in Section 3.3.1 and it considers coupling effects between modes of vibrations. Flutter analysis on Goland wing was car-

ried out by CALFUN in [105]. Flutter velocity and frequencies obtained, however, are not much different in comparison to results obtained by uncoupled modes. Theoretically, this is the expectation, because the solution process essentially resembles standard patterns which are the modal shape functions. As long as those shape functions satisfy with the boundary conditions given, their choice will not affect the stability boundary. More importantly, however, coupled modes bundle multiple vibration modes with one time-dependent function, reducing the number of unknowns in the already complex analysis. Hence the initiative of implementing coupled modes is to improve numerical efficiency and the application of coupled modes into stability analysis is discussed in this section.

Implementing coupled modes does not change the procedures of flutter analysis described by Equation (4.12), (4.13) and (4.14). The only term that would be different is the vector \mathbf{u} as

$$\text{for uncoupled modes: } h = \sum_{j=1}^{N_f} \theta_j(x) f_j(t) \text{ and } \alpha = \sum_{j=1}^{N_z} \eta_j(x) z_j(t), \text{ hence } \mathbf{u} = \begin{Bmatrix} [f_j(t)]_{N_f \times 1} \\ [z_j(t)]_{N_z \times 1} \end{Bmatrix},$$

$$\text{for coupled modes: } \begin{Bmatrix} h \\ \alpha \end{Bmatrix} = \sum_{j=1}^{N_q} \begin{Bmatrix} \theta_j(x) \\ \eta_j(x) \end{Bmatrix} q_j(t), \text{ hence } \mathbf{u} = \begin{Bmatrix} [q_j(t)]_{N_q \times 1} \\ [q_j(t)]_{N_q \times 1} \end{Bmatrix}.$$

During the solution process, q_j of the same mode can easily be rearranged and summed up together. This may reduce the number of unknowns and improves numerical efficiency for the computational process. For the case of Golland wing, when implementing two coupled modes (7.7 Hz and 15.2 Hz) derived from transfer matrix method, the damping and frequency plots are shown in Figure 4.7. The system damping reaches zero at 137.29 m/s. Under this condition, the wing would oscillate at 11.1 Hz. Giving similar flutter velocity and identical frequency comparing to the uncoupled case, a good agreement between Figure 4.6 and 4.7 is clearly presented. Comparing to the flutter velocity of 137.25m/s reported by Golland [29], an error of 0.03% was involved, making the coupled model much more accurate than the uncoupled one.

With the instability analysis approach developed, the flutter and divergence boundary can be found for the short wing in the propeller-wing configuration. Recalling the estimated wing's properties in Table 3.5, it is shown as

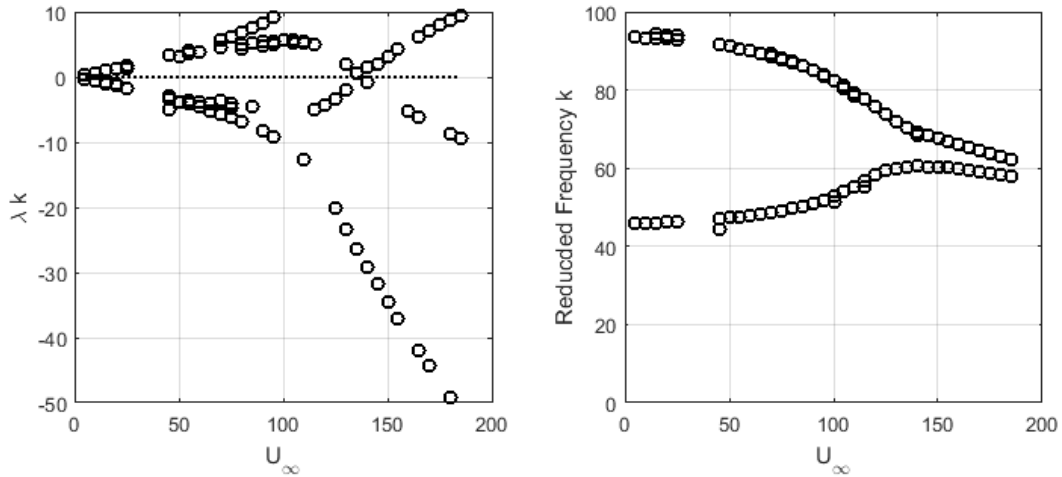


Figure 4.7: Wing flutter analysis based on coupled bending-torsion modes for Goland wing

Table 3.5: Estimated wing structural parameters

| | | | | | |
|---|---|--------------------------|---------------------------------------|---------------------------------|------------|
| $E=69 \times 10^9 \text{ Pa}$ | $G=27 \times 10^9 \text{ Pa}$ | $m=22.0864 \text{ kg/m}$ | $J=1.8063 \times 10^{-5} \text{ m}^4$ | | |
| $I_y=5.2862 \times 10^{-6} \text{ m}^4$ | $I_z=1.0745 \times 10^{-4} \text{ m}^4$ | $b=0.3 \text{ m}$ | $\theta=0 \text{ deg}$ | $\chi_\alpha=-0.163$ | $a=-0.277$ |
| $\rho_w=2720 \text{ kg/m}^3$ | $A=0.00812 \text{ m}^2$ | $\kappa_y=0.80$ | $\kappa_z=0.05$ | $I_\alpha=0.3594 \text{ kgm/m}$ | |

Three coupled modes, covering two bending-governed and one torsion-governed modes, are included. The damping factor and reduced frequency can be plotted at each advancing velocity as in Figure 4.8. As velocity goes towards 800m/s, damping is approaching zero. If zooming in between 750 m/s and 850 m/s, one can find the flutter velocity at 784.7 m/s. Under this condition, the wing structure would vibrate at a frequency of 71.6 Hz. Flutter occurs at a smaller velocity comparing to results obtained by the 2D sectional model, however, the difference between these two results lies within 10%. Consideration of beam integrity certainly affects the results, and the wing tip sectional model is not representative for the whole wing's dynamic behaviour. The difference could be introduced by how the structural coupling and the degrees of freedom are considered in a 2D aerofoil model and a beam-like model.

The aerofoil model can represent a typical section on a finite wing and is appealing for its

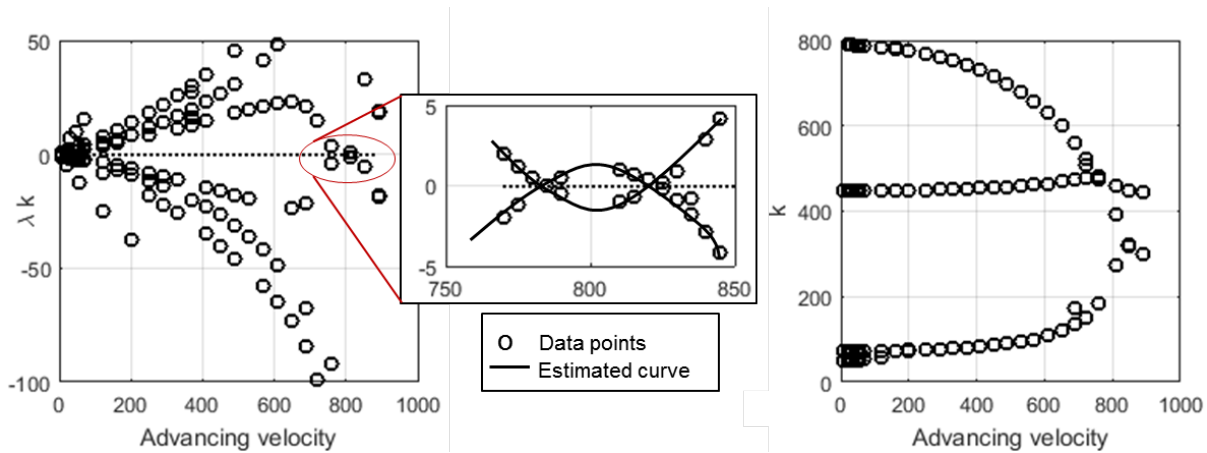


Figure 4.8: Wing flutter analysis based on coupled bending-torsion modes for the short wing

physical simplicity. The rigid assumption across wingspan, however, may lead to unreliable flutter results. From the aerofoil to the beam model, the scope is to develop a more realistic mathematical representation for the structure itself which leads to more realistic flutter calculations. According to [52], the present-day industry practice for aeroelastic instability uses both full FEM models as well as beam models with FEM-derived modes. As discussed earlier, the transfer matrix method derived modes have a similar level of realism compared to FEM derived modes. It is demonstrated, in this section, that beam model flutter analysis featuring coupled modes can be performed in a relatively simple way while still maintaining a good level of realism and the approach produces reliable flutter results.

If inputting k to be zero, the divergence boundary can be found. Since divergence is based on torsional motion, three coupled modes were considered in order to include the first torsion-governed mode. Shown in Figure 4.9, the critical divergence velocity is found at 1123.97 m/s as determinant of matrix $[\mathbf{K}_s - \mathbf{A}(ik)]$ reaches zero. Comparing to stability results obtained by sectional model, the critical divergence velocities are found to be identical. This is due to the simple physical mechanism behind this phenomenon. The wing tip is naturally the least structurally stiff section along the whole span, as divergence itself is about balancing between the structural and aerodynamic stiffness, the wing tip sectional model is crucial and representative for the whole

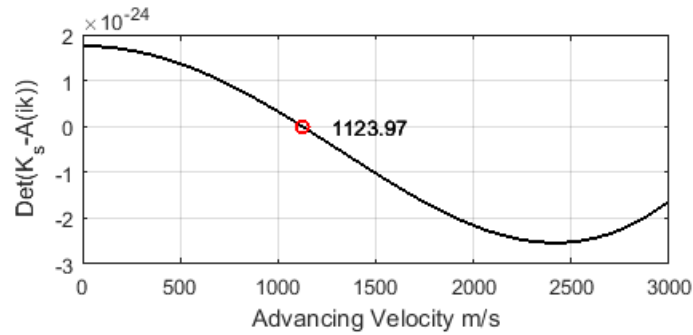


Figure 4.9: Divergence boundary for the short wing

wing span.

4.3 Conclusion

A numerical procedure for aeroelastic stability has been developed in this chapter. By implementing the static and unsteady aerodynamic theory, Theodorsen's model, a sectional aerofoil model has been first built. With the 2D model, static and dynamic instability phenomena are introduced and analysed. Validation has been carried out based on a similar aerofoil case reported in Hodges and Pierce [52] and Shams et al. [57], followed by a demonstration of the model on a short wing tip aerofoil. Extending by considering the overall motion coupling for the cantilever wing, the beam-like model developed in Chapter 3 has been integrated together with frequency domain strip theory. The extended model has been validated against published results for Goland wing. Application of uncoupled and coupled modes in flutter analyses has been compared based on Goland wing. Both applications gave good agreement, -0.3% for uncoupled modes and 0.03% for the coupled modes. The advantage of the considering coupling effects has been proven as it gives a much closer result compare to the exact solution. With the confidence of a validated method incorporating coupled modes, instability phenomena, namely divergence and flutter, have been studied for the short wing structure.

Chapter 5

Dynamic Response Solution

With the completion of the aerodynamic model in Chapter 2, the structural model and modal analyses in Chapter 3 and the instability studies in Chapter 4, all the building elements towards a solution of the dynamic response are discussed. In this chapter, all these elements are integrated together and a solution process, featuring results and procedures covered in previous chapters, is introduced. Starting with integrating loading results from the aerodynamic model into the beam-like representation for the short wing, an explicit time-marching scheme is proposed for obtaining the dynamic response for the aeroelastic problem. Coupled modes derived by the transfer matrix method are also incorporated into the solution process. Just as with all finite element methods, a convergence study strategy is also discussed, considering the number of modes, size of the iterative time step and the choice of algorithm parameters. With the solution process defined, the complete aeroelastic solver is able to give a reliable solution for the dynamic response for the short wing under propeller influences.

For the outline of this chapter, in Section 5.1, an aeroelastic model is developed combining the aerodynamic and the structural models developed in Chapter 2 and 3 and a solution strategy towards obtaining the dynamic response is proposed. In order to obtain reliable and accurate results, a convergence study scheme is introduced in Section 5.2. The complete aeroelastic solver is then validated under different flight conditions with literature examples in Section 5.3. With

the confidence of the complete aeroelastic solver, the dynamic response for the short wing under propeller inflow is obtained in the time domain in Section 5.4.

5.1 Aeroelastic model integration and solution strategy

Introduced in Chapter 3, the displacements considered here are functions of span length and time. As dimensionless time τ and displacements (ξ, ν, α) are used, modifications of the time derivatives are needed. As for a wing, a cantilever beam is a continuous structural system and has infinite degrees of freedom. With the aid of modal analysis approach discussed in Section 3.3, the continuous behaviour of the system can be discretised into finite number of modes, each representing a mode shape that satisfies the boundary conditions. As discussed in Section 3.4, coupled flapping-torsion with separate lead-lag motion is considered for the aeroelastic system presented and the governing equations are written as

$$\text{Coupled flap-torsion motion: } \begin{cases} m \frac{\partial^2 h}{\partial t^2} - S_\alpha \frac{\partial^2 \alpha}{\partial t^2} + EI_y \frac{\partial^4 h}{\partial x^4} = L_h, \\ I_\alpha \frac{\partial^2 \alpha}{\partial t^2} - S_\alpha \frac{\partial^2 h}{\partial t^2} - GJ \frac{\partial^2 \alpha}{\partial x^2} = M_\alpha, \end{cases}$$

$$\text{The lead-lag motion: } \begin{cases} m \frac{\partial^2 \nu}{\partial t^2} - \kappa_z GA \left(\frac{\partial^2 \nu}{\partial x^2} - \frac{\partial \varphi_z}{\partial x} \right) = L_\nu, \\ \rho_w I_z \frac{\partial^2 \varphi_z}{\partial t^2} - EI_z \frac{\partial^2 \varphi_z}{\partial x^2} - \kappa_z GA \left(\frac{\partial \nu}{\partial x} - \varphi_z \right) = 0. \end{cases}$$

In the dimensionless domain, time $\tau = U_\infty t/b$, flapping displacement $\xi = h/b$ and lead-lag displacement $\nu = v/b$ are used, and the equations of motion can be rearranged and written as

$$\begin{aligned} m \frac{U_\infty^2}{b} \ddot{\xi} - S_\alpha \frac{U_\infty^2}{b^2} \ddot{\alpha} + EI_y b \xi'''' &= L_h, \\ m \frac{U_\infty^2}{b} \ddot{\nu} - \kappa_z GA (b\nu'' - \varphi_z') &= L_\nu, \\ \rho_w I_z \frac{U_\infty^2}{b^2} \ddot{\varphi}_z - EI_z \varphi_z'' - \kappa_z GA (b\nu' - \varphi_z) &= 0, \\ I_\alpha \frac{U_\infty^2}{b^2} \ddot{\alpha} - S_\alpha \frac{U_\infty^2}{b} \ddot{\xi} - GJ \alpha'' &= M_\alpha. \end{aligned} \tag{5.1}$$

The coupled flapping-torsion motion and the lead-lag motion are assumed in the form of

$$\begin{Bmatrix} \xi \\ \alpha \end{Bmatrix} = \sum_{j=1}^{\infty} \begin{Bmatrix} \theta_j(x) \\ \eta_j(x) \end{Bmatrix} q_j(\tau) \quad \begin{Bmatrix} \nu \\ \varphi_z \end{Bmatrix} = \sum_{j=1}^{\infty} \begin{Bmatrix} \zeta_j(x) \\ \phi_j^z(x) \end{Bmatrix} p_j(\tau) \quad (5.2)$$

The mode shapes are functions of span/beam length. Through modal analysis, certain standard shapes which satisfy the boundary conditions are derived and associated with different natural frequencies. In the solution of forced responses, these standard shapes are the basic functions which are used to define the actual response. Hence, the only unknowns are the time-dependent function $q_j(\tau)$ and $p_j(\tau)$. Substituting the above assumption into the governing equations, one can obtain

$$\begin{aligned} \sum_{j=1}^{\infty} \left[m \frac{U_{\infty}^2}{b} \theta_j \ddot{q}_j - S_{\alpha} \frac{U_{\infty}^2}{b^2} \eta_j \ddot{q}_j + EI_y b \theta_j'''' q_j \right] &= L_h, \\ \sum_{j=1}^{\infty} \left[m \frac{U_{\infty}^2}{b} \zeta_j \ddot{p}_j - \kappa_z GA (b \zeta_j'' - \phi_j^{z'}) p_j \right] &= L_v, \\ \sum_{j=1}^{\infty} \left[\rho_w I_z \frac{U_{\infty}^2}{b^2} \phi_j^z \ddot{p}_j - EI_z \phi_j^{z''} p_j - \kappa_z GA (b \zeta_j' - \phi_j^z) p_j \right] &= 0, \\ \sum_{j=1}^{\infty} \left[I_{\alpha} \frac{U_{\infty}^2}{b^2} \eta_j \ddot{q}_j - S_{\alpha} \frac{U_{\infty}^2}{b} \theta_j \ddot{q}_j - GJ \eta_j'' q_j \right] &= M_{\alpha}. \end{aligned}$$

When combining with the aerodynamic loadings along with estimated mode shapes, a general matrix form of the governing equations can be obtained

$$\mathbf{M}\ddot{\mathbf{u}} + \mathbf{K}\mathbf{u} = \mathbf{F}, \quad (5.3)$$

where \mathbf{M} and \mathbf{K} are the mass and stiffness matrices respectively, \mathbf{u} and \mathbf{F} are time-dependent displacement and loading vectors. The sizes of those matrices are dependent on the number of modes considered. When considering N_q modes for coupled flapping-torsional motion and N_p for lead-lag motion, the sizes for \mathbf{M} and \mathbf{K} are $(2N_q + 2N_p) \times (2N_q + 2N_p)$. The column vectors, \mathbf{u} and \mathbf{F} , are of $(2N_q + 2N_p) \times 1$. The exact expressions for these matrices are displayed in Appendix E.

Vector \mathbf{F} contains the external loadings in each coordinate L_h , L_v and M_{α} in their generalised form, while loading L_h , L_v and M_{α} consist of aerodynamic lift, drag, propeller weight and any

moment introduced on the elastic axis. Taking a lift-drag ratio of $\frac{1}{10}$, drag is calculated based on circulatory lift L_C and L_g . If considering all general loadings within \mathbf{F} , it can be written that

$$\begin{aligned} L_h &= L_C + L_{NC} + L_g + F_{tip}, \\ L_v &= \frac{1}{10}(L_C + L_g) + F_{thrust}, \\ M_\alpha &= M_C + M_{NC} + M_g + M_{tip}. \end{aligned}$$

Recalling the aerodynamic model developed in Chapter 2, L_C , L_{NC} , L_g , M_C and M_{NC} are the aerodynamic loadings derived from analytical theories.

An explicit approach is used here for defining aerodynamic loads and structural responses. Within aerodynamic loads, however, non-circulatory effects are taken into account implicitly. Non-circulatory loads are induced by attached virtual mass (apparent mass) due to acceleration of surrounding fluid particles, which has an instantaneous effect. Explicit approximation for non-circulatory loading terms may result in numerical instability and affect the number of modes that can be taken into account for aeroelastic solutions. The non-circulatory terms, hence, are isolated from the general loading \mathbf{F} . Equation (5.3) can be rearranged as

$$\mathbf{M}\ddot{\mathbf{u}} + \mathbf{K}\mathbf{u} = \mathbf{M}_{NC}\ddot{\mathbf{u}} + \mathbf{K}_{NC}\mathbf{u} + \mathbf{F}. \quad (5.4)$$

Detail expressions of these matrices can be found in Appendix E.

Recalling time-domain aerodynamic loadings formulated by Wagner's and Küssner's models in Section 2.4.1 and 2.4.3 with the recursive algorithm applied for optimisation, one can point out that L_h and M_α are functions of structural displacements and their rates of change against time. The time integration of the structural and aerodynamic model follows a strategy as shown in Figure 5.1. To start with, aerodynamic loads are first formulated based on initial structural conditions $\{\xi, v, \alpha\}_{\tau=0} = \{\xi_0, v_0, \alpha_0\}$. According to Equations (2.5), (2.8) and (2.13), the initial aerodynamic lift can be formulated as

$$L_C(0) = -2\pi b\rho U_a\phi(\tau)[U_a\alpha_0 + U_\infty\dot{\xi}_0 + U_\infty(\frac{1}{2} - a)\dot{\alpha}_0] \quad \text{and} \quad L_g(0) = 0.$$

and the aerodynamic moments can be written consequently as

$$M_C(0) = -b\left(\frac{1}{2} + a\right)L_C(0) \quad \text{and} \quad M_g(0) = 0.$$

Projecting onto the corresponding modes, the initial loads $\{L_C^0, L_g^0, M_C^0, M_g^0\}$ can be formulated. Proceeding to the first iteration, the initial loads will give a new structural status $\{\xi_1, v_1, \alpha_1\}$ to the system by solving the governing equations. Having the new structural data, aerodynamic lifts $\{L_C^1, L_g^1\}$ moments $\{M_C^1, M_g^1\}$ can be recursively updated through analytical expressions of the Wagner's and the Küssner's functions. At this point, entering the next iteration, the updated loads F_1 can again be applied to update the structural status $\{\xi_2, v_2, \alpha_2\}$. At each iteration step, aerodynamic loads are determined by the previous status of the system, including aerodynamic and structural states. Then the loads are used to predict the structural displacements, velocities and accelerations for the next iteration step using the Newmark-beta algorithm [88]. As $\Delta\tau$ marching along the timeline, dynamic behaviour of the system can be captured.

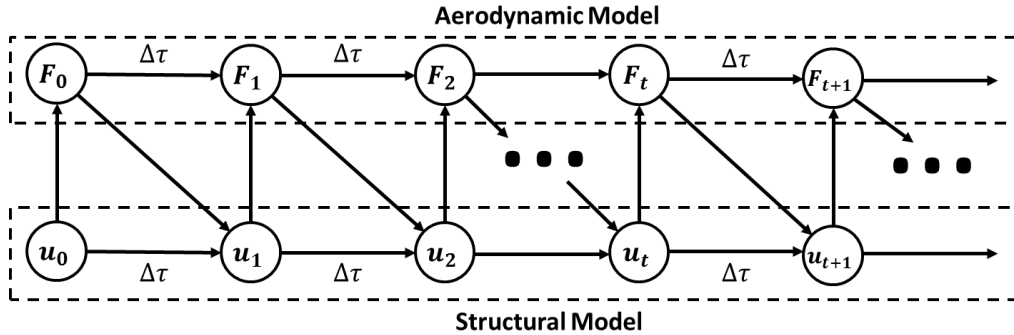


Figure 5.1: Solution strategy for aerodynamic and structural model iterations

Having a numerical formulation of the aerodynamic and structural models, a solution needs to be obtained in the time domain. For the topic of fluid-structure interaction, there are many studies in different fields looking into the efficient approach to obtain accurate solutions. In this case, an explicit Newmark-beta approach [88] is used to solve the aeroelastic response. The Newmark-beta approach is very commonly used for structural dynamic applications and requires relatively low computational efforts, which is suited for a simplified model like ours. The aeroelastic system in

Equation (5.3) is solved using the Newmark-beta algorithm to obtain the displacement vector \mathbf{u} . The key computational settings in this method are the β and γ parameters. β defines the velocity and acceleration assumptions during the integration and γ defines whether there is numerical damping introduced to the system. These two parameters are investigated here and the most efficient is selected to perform the analyses. Another important parameter in the time integration is the time step. Convergence analyses relating to iteration time step are also performed and discussed in the next sections.

5.2 Convergence study strategy

Just as with all finite element methods, the number of nodes/elements included in the study directly lead to the discussion of reliability and accuracy. In this case, the number of modes to be included N_q and N_p can strongly affect the model output reliability and accuracy. At the same time, the selection of parameters and time step for numerical methods determine the error involved and the computational effort needed. For the study presented, following the strategy illustrated in Figure 5.2, a steady-state condition is taken into account for a convergence analysis against the number of modes and the iterative time step. The latter is always compared with the smallest period present in the analyses, as evaluated from the modal natural frequencies and the propeller frequency. Moreover, the β parameter used in the Newmark-beta algorithm is compared, considering two basic types, corresponding to constant acceleration and linear acceleration methods [88]. Constant acceleration method takes β to be $1/4$, which means when predicting velocity and displacement for the next point, acceleration is constant over the time step. On the other hand, linear acceleration which takes β to be $1/6$ considered a linear variation within the iterative time step [88]. In the study present, the steady-state amplitude for each motion is compared to evaluate convergence condition. Also, a margin of 5% for differences in results between two successive iterations is set to be satisfactory for a preliminary design tool. Convergence analysis will be demonstrated in detail later for obtaining dynamic responses for a short wing under propeller inflow. The following steps will be

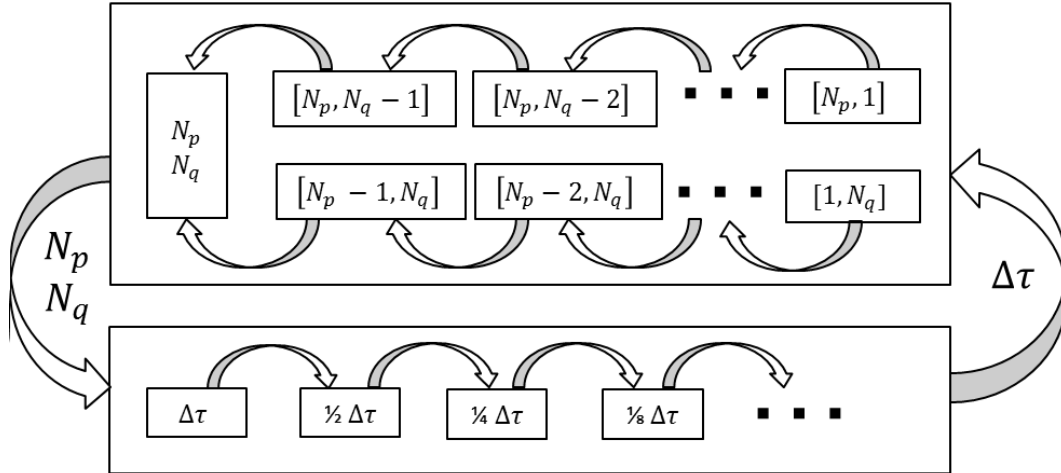


Figure 5.2: Convergence study strategy

followed:

1. Firstly, fixing time-step size to be 1/10 of the smallest period involved in the analysis. This is determined within all the natural frequencies involved and the propeller blade passing frequency. Cases with different values of N_p and N_q are compared. When increasing the number of modes, the steady-state amplitude is approaching its true value. The values of N_p and N_q are studied separately by taking into account a fixed number of modes in the other coordinates.
2. As for the number of modes used in the numerical process, another convergence study is carried out to study the impact of different time steps on the numerical results. This analysis is performed using $[N_p, N_q]$ values obtained in the first step.
3. Step 1 and Step 2 repeat in alternation until convergence is reached

5.3 Aeroelastic response solution verification

As discussed in Section 1.1.2, aeroelastic simulations featuring beam-like structure and 2D aerodynamic theories were used to predict dynamic responses of fixed wings under different flight

conditions before. Therefore, some of the results can be reproduced for verification of the present model. The nonlinear aeroelastic response of a continuous beam system was studied by Shams et al. in 2008 using a similar numerical approach [57]. Two examples were investigated, one with geometrically uncoupled bending and torsional motion and the other with geometrically coupled bending-torsion motion. Both cases were initially excited by a 0.2 m bending disturbance at the beam tip. As for the uncoupled case, a cantilever wing of length $l = 16$ m is featured. The cross-sectional aerofoil has a chord length of $c = 1$ m. The mass and polar inertia per span are $m = 0.75$ kg/m and $I_\alpha = 0.1$ kgm²/m respectively. At the same time, the shear centre coincides with the gravitational centre ($S_\alpha = 0$ kgm) and the mid-chord point ($a = 0$). In the bending direction, a stiffness of $EI = 2 \times 10^4$ Nm² is present. As for torsion, the torsional stiffness is at $GJ = 1 \times 10^4$ Nm². The air density for the flight condition is at $\rho = 0.0889$ kg/m³. The aircraft advances at $U_\infty = 30$ m/s and relatively the flow is approaching uniformly across the whole span $\bar{u}_f = 1$. The parameter values are summarised as below

$$\begin{array}{cccccc}
 l = 16 \text{ m} & c = 1 \text{ m} & m = 0.75 \text{ kg/m} & I_\alpha = 0.1 \text{ kgm}^2/\text{m} & a = 0 & S_\alpha = 0 \text{ kgm} \\
 EI = 2 \times 10^4 \text{ Nm}^2 & GJ = 1 \times 10^4 \text{ Nm}^2 & \rho = 0.0889 \text{ kg/m}^3 & U_\infty = 30 \text{ m/s} & \bar{u}_f = 1.
 \end{array}$$

A linear Euler-Bernoulli beam model with the Wagner's aerodynamic theory is solved to reproduce the pre-flutter behaviour of the nonlinear model by Shams et al. and results are obtained by the present model and demonstrated in Figure 5.3. Any external loadings can be taken into the generalised coordinates. However, in the case of examples by Shams et al., an initial bending disturbance of 0.2 m is present. Due to the discretisation of several natural modes, it is difficult to specify how the initial displacement is distributed between these natural modes without knowing the contribution of each natural mode to the total displacement. However, it is known that the first natural mode would be the most significant compared to the rest. The initial disturbance, hence, can be imposed only onto the first bending mode. It might not be a realistic representation of the physical reality, however, can be easily tuned to match the reality condition. Alternatively, an equivalent step load can be applied to settle the system at a 0.2m bending displacement and then

removing the step load to represent the actual physical initial conditions of the case studied. These two means of considering initial conditions are discussed in the coupled example as there is a very obvious difference. Here in this example, the former approach is applied.

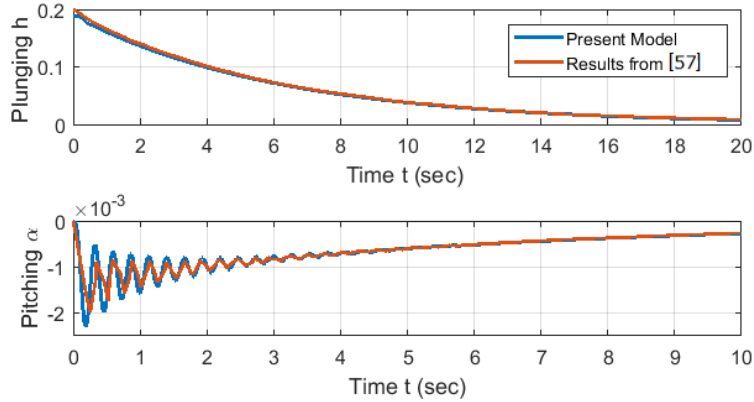


Figure 5.3: Agreement in aeroelastic responses derived from present model and results from [57]

One point to bear in mind is that Shams et al. studied nonlinearity of the aeroelastic system while the present model is based on linear systems. Therefore, the results are not expected to be identical, but should be similar. As illustrated in Figure 5.3, the overall pattern is similar for both torsion and bending displacements. However for the torsional motion, an initial difference of 37.5% is observed. Eventually the difference settled at 1.2%. The differences are contributed by two main factors. One is that Shams studied nonlinearity of the system, while this study ignored nonlinear effects. Secondly, the Shams' results were digitalised from published figures, and the digitalisation accuracy is highly sensitive to the quality of the figure.

Another example with coupled bending and torsion motion is also presented in [57] with parameter values listed as

$$l = 1 \text{ m} \quad c = 1.83 \text{ m} \quad m = 19.6 \text{ kg/m} \quad I_\alpha = 2.75 \text{ kgm}^2/\text{m} \quad a = -0.2 \quad S_\alpha = 7.17 \text{ kgm}$$

$$\bar{u}_f = 1 \quad EI = 159 \text{ Nm}^2 \quad GJ = 1039 \text{ Nm}^2 \quad \rho = 1.225 \text{ kg/m}^3 \quad U_\infty = 30 \text{ m/s.}$$

This is to verify the capability of considering the coupled motion for the present model. In the solution in [57], all mode shapes were based on uncoupled analytical expressions and solved in an

uncoupled fashion. The mode shapes are found at natural frequencies as listed in Table 5.1. On the other hand, the coupled modes can be computed via the transfer matrix method discussed in Chapter 3, natural frequencies and mode shapes can be found as displayed in Table 5.2 and Figure 5.4. It is clear that a strong coupling between bending and torional motions is present. Both

Table 5.1: Uncoupled natural frequencies from [57]

| | | | |
|---------|---------|----------|----------|
| Bending | 1.59 Hz | 9.99 Hz | 27.97 Hz |
| Torsion | 4.86 Hz | 14.58 Hz | 24.30 Hz |

Table 5.2: Coupled natural frequencies derived from the example parameters in [57]

| | | | | | |
|----------------|---------|---------|----------|----------|----------|
| Coupled motion | 1.52 Hz | 7.65 Hz | 17.36 Hz | 25.20 Hz | 29.99 Hz |
|----------------|---------|---------|----------|----------|----------|

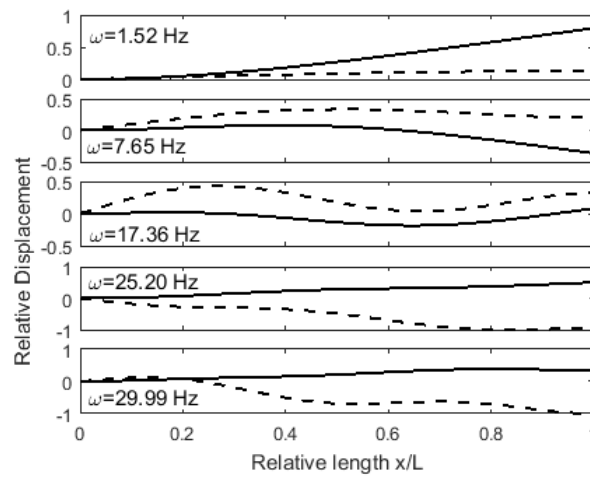


Figure 5.4: Coupled mode shapes based on parameters from [57] (Bending —; Torsion - - -)

uncoupled and coupled solver are applied and compared here. This is to investigate the coupling effect as well as to demonstrate capability of the present model. As illustrated in Figure 5.5, uncoupled solution shows good agreement with aeroelastic response result by Shams et al. [57].

Solutions derived from coupled bending-torsion modes are shown in Figure 5.6. The plots exhibit differences from ones solved by uncoupled mode shapes. In the steady state, results from

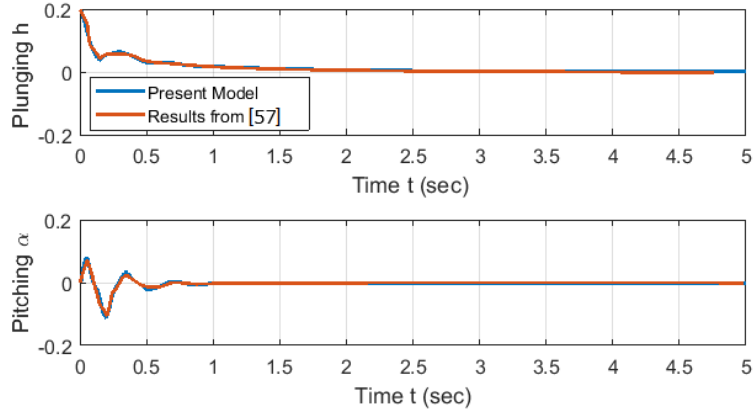


Figure 5.5: Agreement in aeroelastic response results between uncoupled model and [57]

both solvers settled at zero. Theoretically, mode shapes are specifically derived for describing transient behaviour under excitations, the loadings and stiffness terms relating to the steady state of the system would stay unchanged. To emphasise the difference, transient responses up to 4 seconds of flapping and 2 seconds of torsion are displayed here. Comparing with results obtained from uncoupled modes, the coupled flapping appears to settle slower, hence, showing more damping. While for coupled torsional response, it experiences more oscillation in the transient period with larger overshoot, hence, showing less damping. This is most likely caused by a different mechanism of energy distribution when taking coupling effects into account. As in theory, if the overall dynamics is considered uncoupled, there is no torsional motion under a pure bending mode and vice versa. Coupled modes, however, considering both motions to be present at a given frequency, allowing energy to transmit between each motion. Since initial disturbance was introduced on bending originally, more potential energy is transferred onto torsion with coupled modes and introduces larger transient torsional displacements at higher oscillation rates.

However, this difference in energy distribution can also be contributed based on how the initial condition is assigned. In the uncoupled solver, bending and torsion are relatively separated. When imposing a tuned initial displacement onto the first bending mode, the torsional motion would not be so much affected. In the case of coupled solver, the initial displacement distribution becomes more complicated because not only the initial bending displacement needs to be satisfied, also

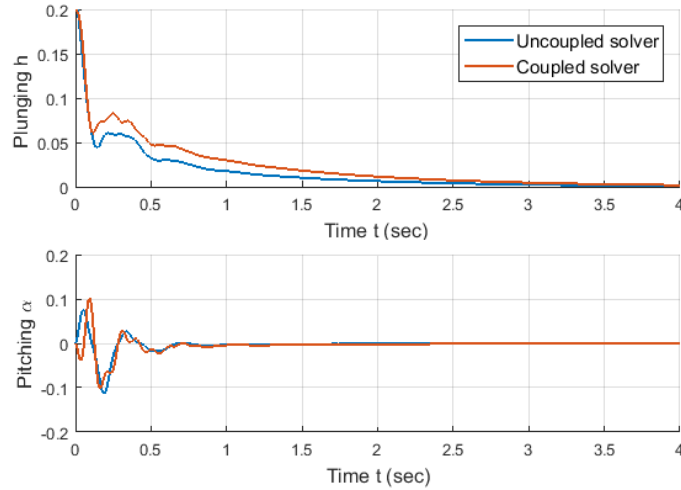


Figure 5.6: Aeroelastic response comparison with initial condition assumption on 1st coupled mode

the zero-displacement condition for torsion. For the results obtained by coupled solver shown in Figure 5.6, the initial condition is imposed on two coupled modes, maintaining a 0.2 m bending displacement and zero torsional angle. To investigate the cause of this discrepancy in energy distribution, dynamic responses with initial conditions applied as equivalent step-like tip load is obtained as illustrated in Figure 5.7.

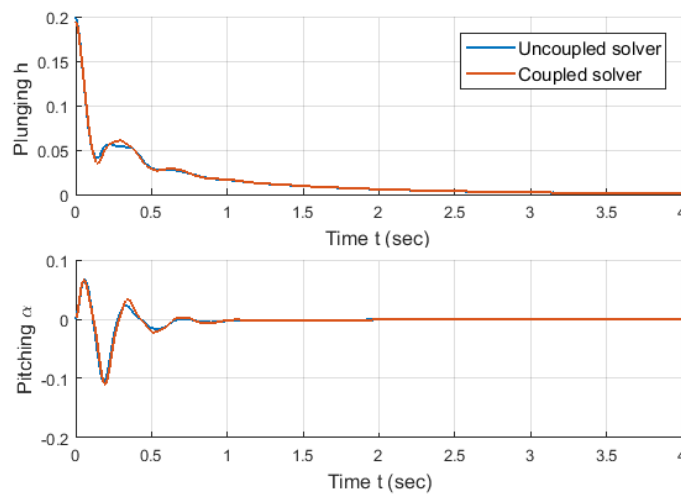


Figure 5.7: Aeroelastic response comparison with initial condition assumed as step loads

Compared with Figure 5.6, a better agreement between coupled and uncoupled solver is observed here when the initial condition is applied as an equivalent step-like tip load, which indicates that the discrepancy of energy distribution is caused by implementation of the initial condition. Again, mode shapes are base functions when it comes to solving forced dynamic responses. The time-dependent functions in the solution would accommodate differences in mode shapes while the actual response itself would not be affected drastically. The example demonstrated here puts emphasis on the implementation of initial conditions when using coupled modes. Equivalent step-like loads to represent initial displacement conditions are preferred, especially when using coupled modes.

5.4 Aeroelastic response for short-wing under propeller inflow

The developed and verified aeroelastic model is utilised to study dynamic responses of the short-wing under propeller inflow in the bending, lead-lag and torsional directions. As discussed in Chapter 2, the propeller slipstream effects are taken into consideration via additional velocity components in the vertical and axial directions, as illustrated and defined in Figure 2.2 and 5.8. Due

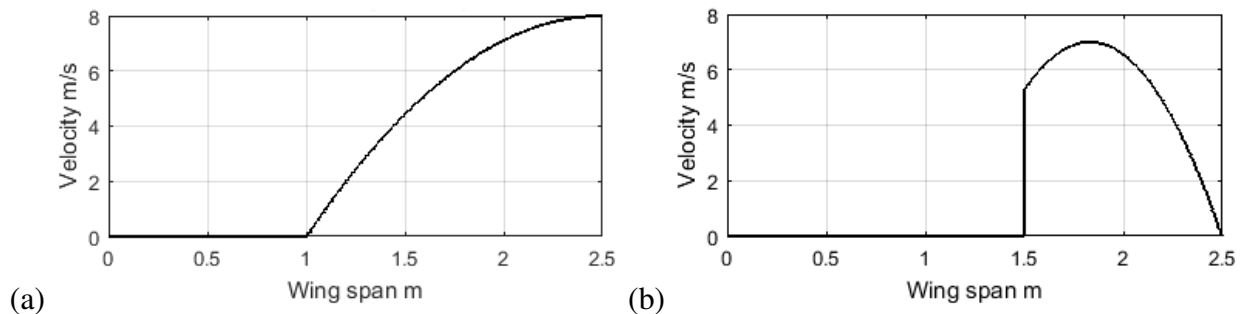


Figure 5.8: Propeller parabolic addition velocity profile in (a) axial and (b) vertical directions

to the sinusoidal nature of propeller inflow, in the vertical direction, 10% fluctuation of additional vertical velocity is assigned at a blade passing frequency of 136.5 Hz in the propeller covered area. The flight simulated is under aircraft cruising condition at 120 m/s, well below the flutter and divergence instability boundaries investigated in Section 4.2. Hence, the \bar{u}_f distribution is defined as

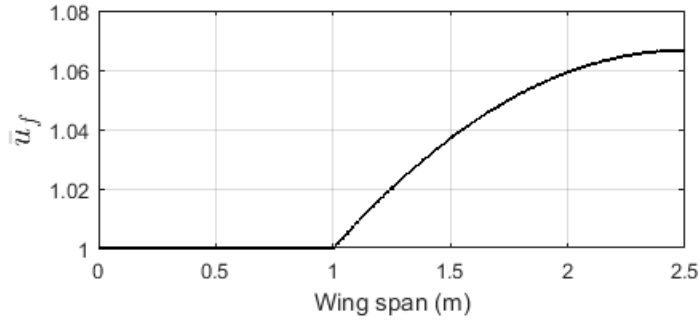


Figure 5.9: \bar{u}_f distribution

illustrated in Figure 5.9. At the same time, a propeller of mass 50kg is mounted at the wing tip, providing 5000 N of thrust along the advancing direction. A pretwist angle of 2° is present as step-like gust at each aerofoil segment and strip theory is used to integrate the sectional aerodynamic model along the wing span. The wing structural parameters are defined in Table 3.5 of Chapter 3. With an appropriate modal analysis method, Euler-Bernoulli beam flapping, Timoshenko beam lead-lag and torsion are represented by a set of equations as defined in Equation (3.22). The application of the uncoupled and coupled solvers will be compared in this section, in both solvers mode shapes and natural frequencies are derived by the transfer matrix method. To reach a solution, the integrated aeroelastic model can be discretised by Galerkin's method and solved by Newmark-beta algorithm.

5.4.1 Convergence study

As discussed in Section 5.2, the selection of parameters, the number of modes included in the simulation, as well as the iterative time steps, determine the error involved and the computational effort needed. Though the model developed is able to solve dynamic responses of the system, those factors need to be studied in order to ensure reliability of the obtained results. Following strategies developed in Section 5.2, convergence analysis is demonstrated step-by-step in this section. Since lead-lag motion is relatively independent of the coupled bending and torsion, the number of pure lead-lag modes is studied firstly. Taking into account six modes of coupled bending-torsion

($N_q = 6$), results obtained by varying N_p are compared and plotted in Figure 5.10. The dashed red

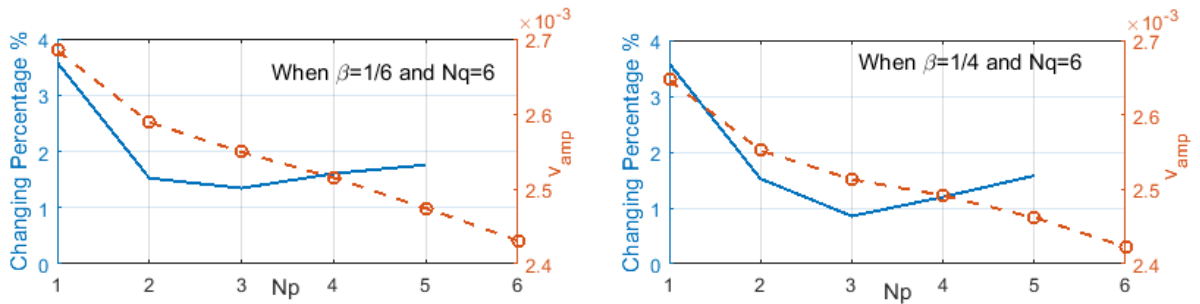


Figure 5.10: Steady-state amplitude comparison with fixed N_q (Dashed red line: lead-lag vibration amplitude; Solid blue line: percentage of changes)

curves show the numerical values of the steady-state amplitude (refer to right-hand side y-axis), plotted against the number of modes taken into account. The solid blue curves show the percentage change comparing the solution at the point considered with the next data point obtained increasing number of modes included (refer to left-hand side y-axis). In the lead-lag direction, the steady-state amplitude does not fluctuate significantly as more modes are included. When including only the first mode, a difference within 5% can be found and hence N_p can be set to be 1. Meanwhile, with the same number of modes included, the linear acceleration method featuring $\beta = 1/6$ gives smaller fluctuations as N_p increases.

Keeping $N_p = 1$, the number of coupled bending-torsion modes is investigated comparing steady-state amplitude results obtained with varying N_q . The comparison is illustrated in Figure 5.11. Referring to left-hand side y-axis, the steady-state amplitude for coupled bending-torsion experiences a jump in its value at $N_q = 3$. This is due to inclusion of the first torsion-governed mode within the coupled system. As more modes are included, up to $N_q = 5$ a satisfactory convergence (within 5%) is achieved. Besides, as stated before, also the effect of the β parameter is studied and linear acceleration approximation, in which $\beta = 1/6$, is found to give smaller percentage difference between iterations compared to the case of $\beta = 1/4$, hence makes it more efficient in this study.

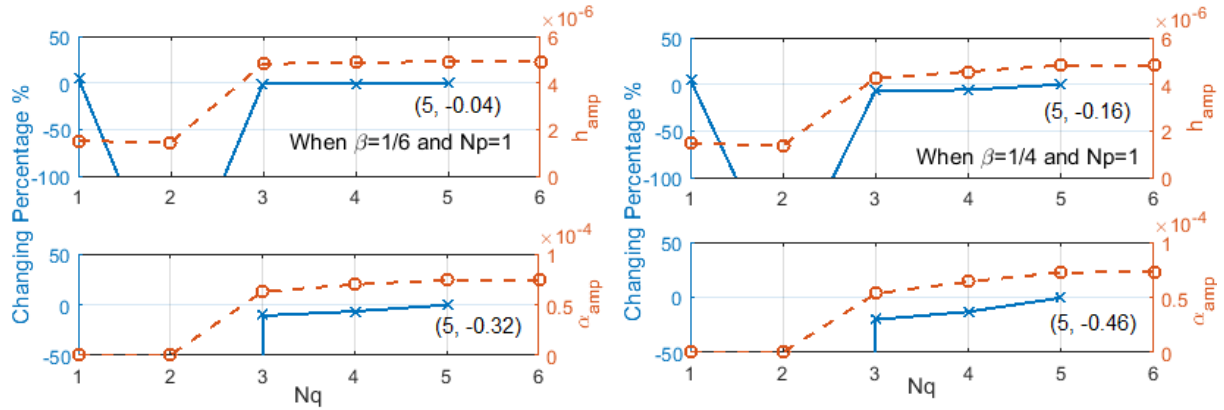


Figure 5.11: Steady-state amplitude comparison with fixed N_p (Dashed red line: lead-lag vibration amplitude; Solid blue line: percentage of changes)

Since analyses for N_p was done under the condition of $N_q = 6$, convergence for lead-lag motion needs to be further confirmed under $N_q = 5$. As shown in Figure 5.12, similar patterns are observed

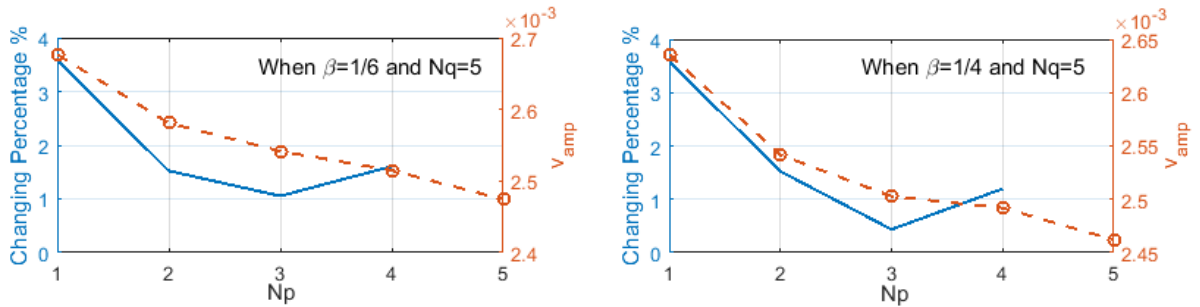


Figure 5.12: Confirmation on convergence with $N_q = 5$ (Dashed red line: lead-lag vibration amplitude; Solid blue line: percentage of changes)

comparing to Figure 5.10 and a satisfactory convergence can be achieved at $N_p = 1$. Meanwhile, the linear acceleration approximation again gives less fluctuation in percentage differences between iterations. Hence, a combination of $[N_q, N_p] = [5, 1]$ can be confirmed and $\beta = 1/6$ is preferred at this stage.

As for the number of modes used in the numerical process, a convergence study is carried out to study the impact of different time steps on the numerical results. This analysis is performed

using five coupled flapping-torsion and one lateral bending (lead-lag) for the beam. Within these five coupled modes, three are flapping-governed and two are torsion-governed. Also, in this case, two different values for β parameter are explored and the dashed and solid curves have the same meaning as in Figure 5.10 to 5.12.

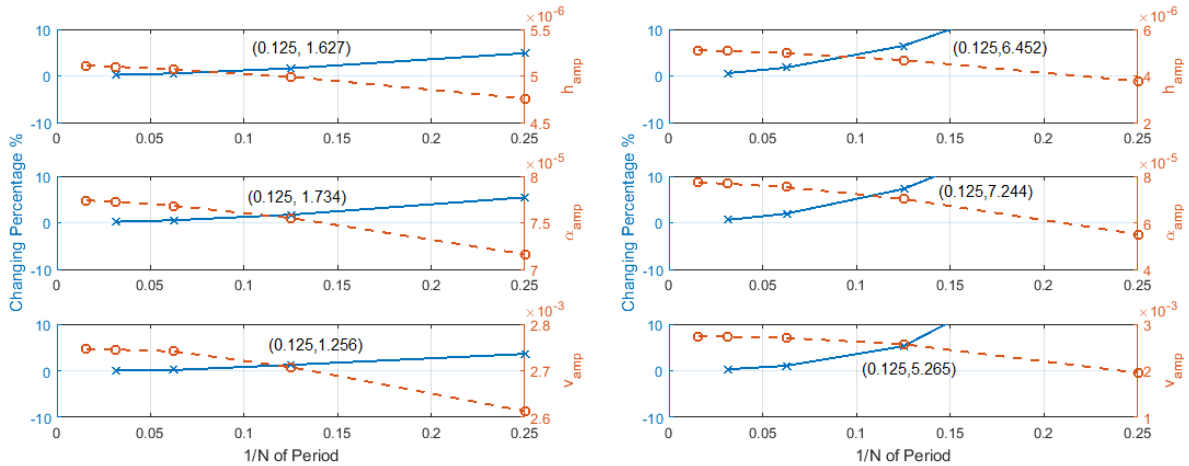


Figure 5.13: Convergence study on iterative time step (Dashed red line: lead-lag vibration amplitude; Solid blue line: percentage of changes)

In Figure 5.13, numerical values of the steady-state amplitude show a smooth curve starting from the solution obtained with 1/4 of the smallest period involved. In terms of percentage difference, towards the extremely small time step, the change in steady state value approaches zero. A 5% satisfactory convergence can be attained when using 1/8 of the smallest period involved ($\delta\tau = 0.1284$). Comparing the two β values, the linear acceleration approximation is again proven to be more efficient, giving a smaller value variation for the same time step. Therefore, the linear acceleration method with 1/8 of the smallest period is chosen in the study presented in the following section for representing overall a more efficient numerical method for the behaviour studied.

By repeating procedures for study of $[N_q, N_p]$ under this time step, the same $[N_q, N_p]$ values are found as illustrated Figure 5.14. Therefore, the convergence study can be concluded. To obtain reliable and converging results for dynamic responses of the short wing under propeller inflow,

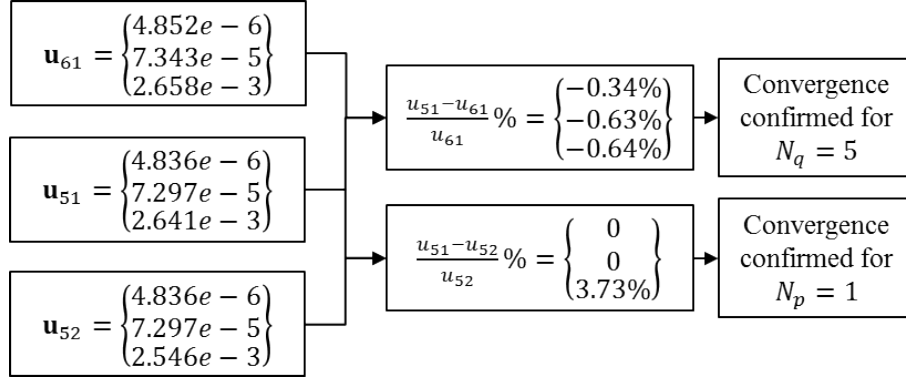


Figure 5.14: Final Confirmation for convergence parameters $N_q, N_p, \delta\tau, \beta$

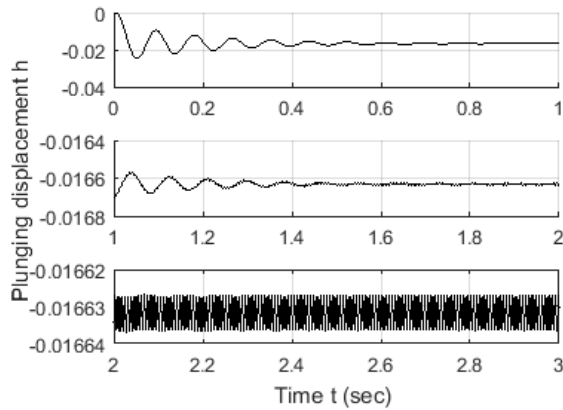
five coupled flap-torsion modes ($N_q = 5$) with one Timoshenko beam lead-lag mode ($N_p = 1$) are included under time step size being 1/8 of the smallest period involved.

5.4.2 Dynamic response using coupled modes

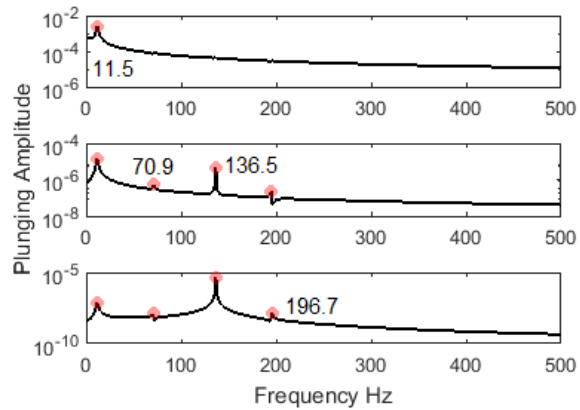
Here, results related to the wing response in the presence of propeller-wing interaction are obtained. The wing is assumed to be at the unloaded initial condition and to be excited by the propeller stream, already in regime condition. This situation is not realistic during the aircraft flight but it is considered here to show the capability of the method developed in modelling transient responses of the system with changing the propeller regime.

In Figures 5.15, 5.16 and 5.17, the transient wing response is shown from time $t=0$ s to $t=3$ s, split into three different plots.

The transient responses in the time domain are shown, while the corresponding frequency-domain responses are illustrated as well. The dynamic response for all three vibration modes are measured at the 75% of the span length away from the fuselage. The propeller-wing system experiences a transient period and reaches its steady state around $t=3$ s. During the transient period, the lowest modes of each motion are governing the main wing behaviour before the rising of the sinusoidal oscillations due to the interaction with the propeller stream. For plunging (flapping) behaviour, during 1-3 s, as the first mode weakens, the second and third coupled modes starts

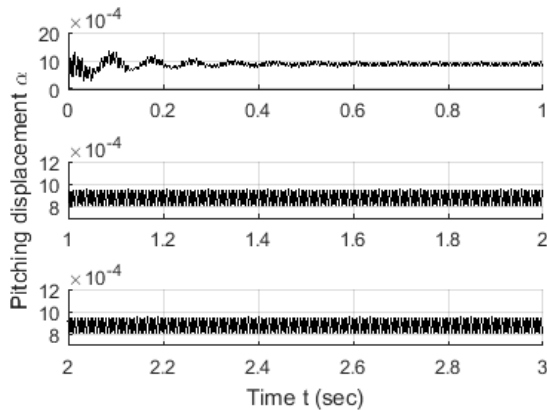


(a) in time domain

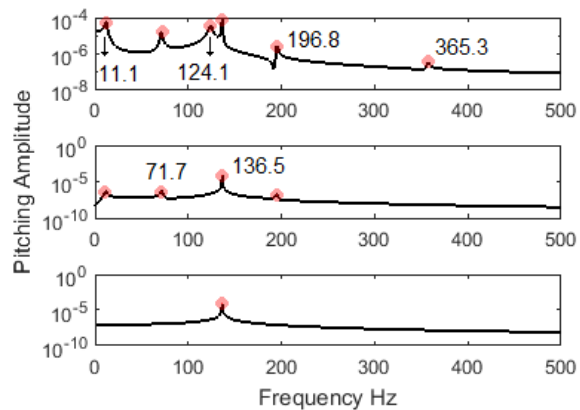


(b) in frequency domain

Figure 5.15: Flapping transient response of a short wing configuration under propeller inflow (Solved by coupled modes)



(a) in time domain



(b) in frequency domain

Figure 5.16: Torsional transient response of a short wing configuration under propeller inflow (Solved by coupled modes)

to show, while the propeller frequency starts to grow in relative contribution. The torsional and lead-lag behaviour showed a similar pattern, as demonstrated. Finally, the propeller takes over into the steady-state wing response, after the transient behaviour is completely damped. However, as lead-lag motion is not strongly coupled with the other two coordinates, its first structural vibration

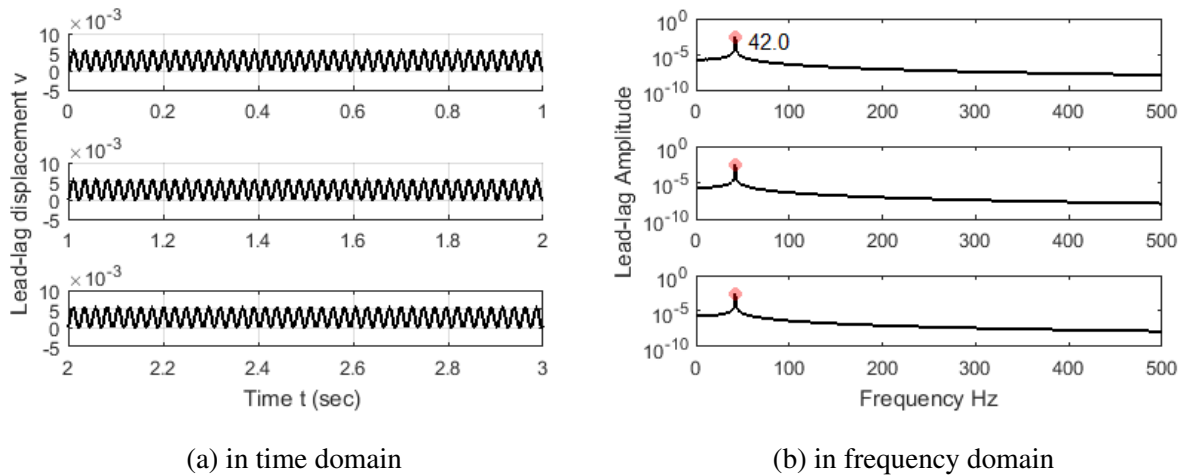


Figure 5.17: Lead-lag transient response of a short wing configuration under propeller inflow (Solved by coupled modes)

mode remains its governing position in the steady state.

The steady-state response, both in time and frequency domain, of the aeroelastic system is shown in Figure 5.18. Following the transient phase, the propeller effect governs now the steady-state oscillations for the flapping and torsional modes. While for the lead-lag direction, the governing frequency is its first structural frequency. This is due to the lack of coupling for the lead-lag motion. Concerning flapping and torsion motions, they directly govern lift and moment, which again determine the flapping and torsional displacements. On the other hand, lead-lag motion is relatively independent. Therefore, a different pattern is observed.

5.4.3 Uncoupled solver results and comparisons

With the same equations of motion, a solution can also be obtained using pure flapping, torsion and lead-lag modes. Here, dynamic responses obtained by uncoupled modes in time and frequency domains are also presented. With the convergence study procedures introduced in Section 5.2, three modes of flapping, one mode of lead-lag and two modes of torsion motion need to be taken into consideration under a time step sizing 1/8 of the smallest period involved ($\delta\tau = 0.1431$).

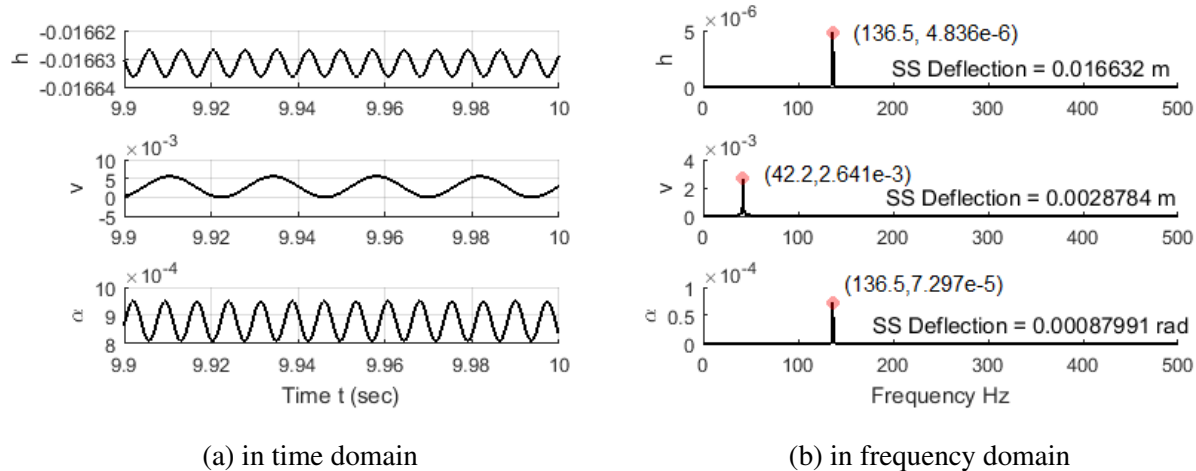
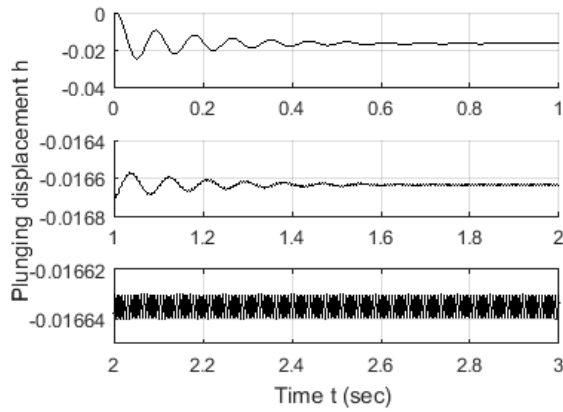


Figure 5.18: Steady-state response of a short wing configuration under propeller inflow for all three motions (Solved by coupled modes)

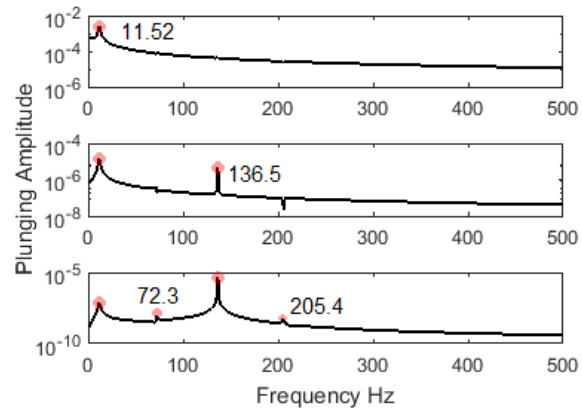
For the coupled solver used, five coupled flapping-torsion modes were used, within which three flapping-governed modes and two torsion-governed modes. This matches with the number of modes needed to be considered for the uncoupled solver. Besides, the same time step size and β parameter are also set. This setup for the uncoupled solver means that the number of time-dependent unknowns stays the same and both numerical simulations, in coupled and uncoupled fashion, would require a similar level of computational effort.

The transient responses in time and frequency domains at the same point (75% span length away from the fuselage) are considered. The flapping transient responses are shown in Figure 5.19 for 0-3 s. It can be observed that the behaviour is extremely similar to the one obtained from the coupled solver. Starting with the first structural frequency of flapping, its natural modal behaviour is decaying. The second and third flapping modes are also becoming visible as the first mode weakens, however, they will be damped out eventually. In the meantime, the propeller frequency starts to dominate the motion. In terms of torsion, the transient response is plotted in Figure 5.20.

It shows a combination of effects, including flapping motion, torsional modal behaviour and the propeller inflow. From 0 to 1 s, the frequencies of three flapping modes, two torsional modes

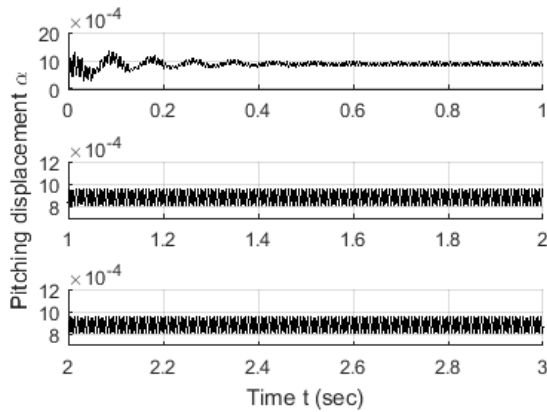


(a) in time domain

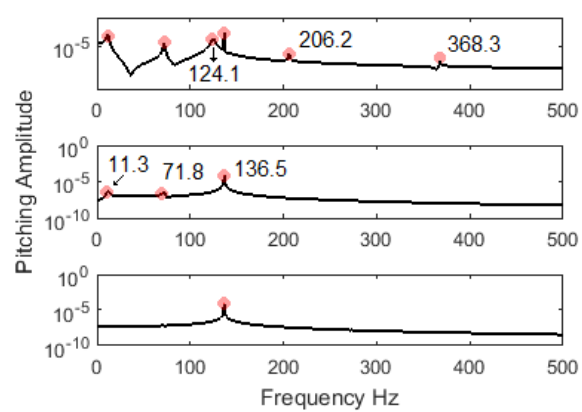


(b) in frequency domain

Figure 5.19: Flapping transient response of a short wing configuration under propeller inflow (Solved by uncoupled modes)



(a) in time domain



(b) in frequency domain

Figure 5.20: Torsional transient response of a short wing configuration under propeller inflow (Solved by uncoupled modes)

and propeller inflow can be observed at 124.2 Hz and 368.3 Hz. Pure torsion modal frequencies are derived at 116.5 Hz and 349.5 Hz. As shown in Figure 5.20, the observed frequencies relating to the torsional motion, however, resembles closely the coupled modal frequencies at 126.5 Hz and 377.7 Hz. This confirms that the coupled modes give a much more realistic representation of

structural behaviour. Approaching towards the steady state, the structural modal effect weakens and the propeller inflow dominates.

Pure lead-lag modes are considered in both solvers due to the relative independent nature of lead-lag motion and the minimal difference is expected for lead-lag responses. In Figure 5.21, lead-lag transient response is shown, which gives a similar pattern compared to the one of the coupled solver.

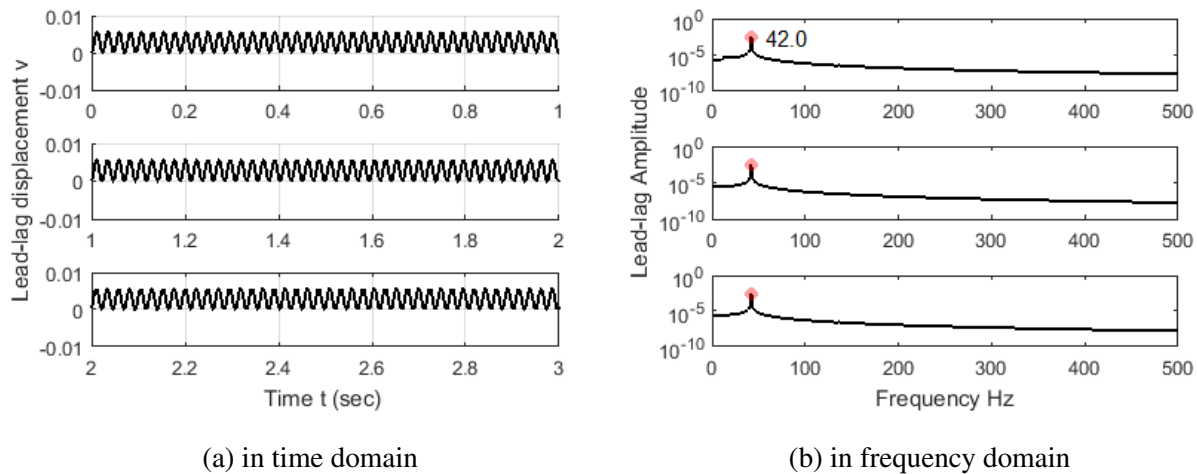


Figure 5.21: Lead-lag transient response of a short wing configuration under propeller inflow (Solved by uncoupled modes)

Eventually, structural modal behaviour in flapping and torsion is damped out completely while the propeller frequency dominates in the steady state. With the exception of lead-lag motion, the steady-state response maintains its structural modal behaviour at its first natural frequency. Steady-state responses in both time- and frequency domains are illustrated in Figure 5.22. Comparing results obtained from coupled and uncoupled solvers, differences in these steady-state parameters can be quantified as listed in Table 5.3. A good agreement can be observed, which confirms that the modal shape functions are basic units for solution projections and their differences introduced by coupled or uncoupled motions are compensated by the time-dependent variables.

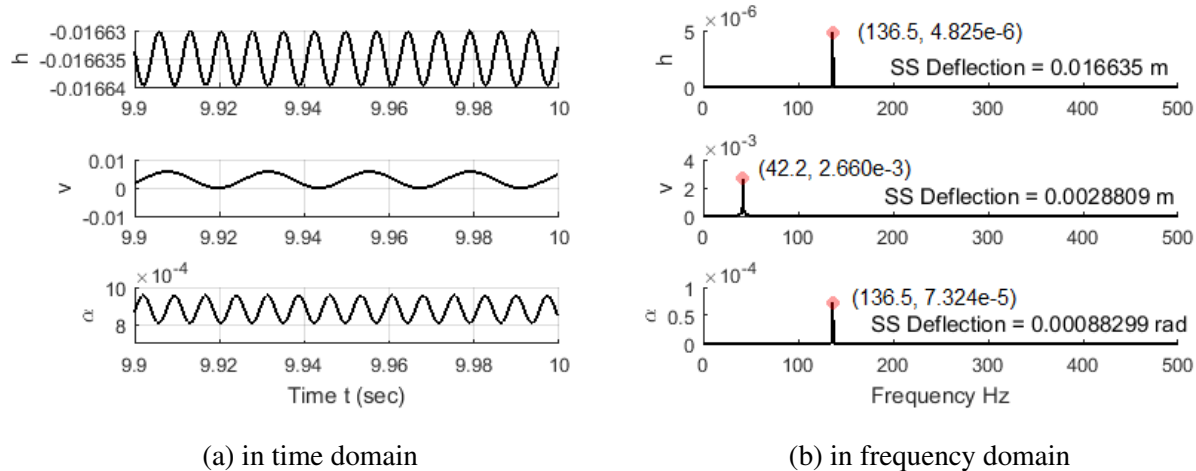


Figure 5.22: Steady-state response of a short wing configuration under propeller inflow for all three motions (Solved by uncoupled modes)

5.5 Conclusion

In this chapter, a numerical solver for time-domain dynamic responses has been developed. Solution strategy, time-marching solution method and convergence analyses scheme for forced vibration response have been introduced. Verification of the developed procedure was carried out against two examples reported by Shams et al. [57], one with uncoupled motion and the other with coupled motion. During the validation process, attention has been drawn to the application of non-zero initial displacement conditions. Within the modal space, the distribution of non-zero initial condition is unclear. The initial condition can be imposed onto the first few modes, or it can be reproduced by introducing an equivalent step pre-load. For solving coupled motion, an equivalent step-like load is preferred as it gives a much more accurate result than imposing the displacement onto the first few modes.

Regarding the actual solution process, the number of modes to include and the iterative step for the time-marching solution method directly affect the accuracy and reliability of the solver output. A convergence analysis scheme has been introduced and demonstrated on the short-wing propeller case. With the capability to reach time-domain dynamic response, the short wing under propeller

Table 5.3: Steady-state response comparison for coupled and uncoupled solver

| Steady-state parameters | Coupled solver | Uncoupled solver | Diff. % |
|-------------------------|----------------------------|----------------------------|---------|
| Flapping amplitude | 4.836×10^{-6} m | 4.825×10^{-6} m | 0.23 |
| Flapping deflection | 1.663×10^{-2} m | 1.664×10^{-2} m | -1.90 |
| Lead-lag amplitude | 2.641×10^{-3} m | 2.660×10^{-3} m | -0.72 |
| Lead-lag deflection | 2.878×10^{-3} m | 2.881×10^{-3} m | -0.10 |
| Torsional amplitude | 7.297×10^{-5} rad | 7.324×10^{-5} rad | -0.37 |
| Torsional deflection | 8.800×10^{-4} rad | 8.830×10^{-4} rad | -0.34 |

inflow was studied in the time and frequency domain. The application of coupled and uncoupled modes has been compared. There was not a significant difference in terms of computational effort and the response solution as expected. The transient behaviour still showed that the coupled modes give a much more realistic representation for structural modal behaviour.

Chapter 6

Aeroelastic Model Exploitation and Further Analyses

Since there is a gap identified for simple and numerically efficient analytical tools for aeroelastic behaviour of short-wing/propeller configurations, the aeroelastic model developed is ideal as a preliminary method to give an insight into the complex phenomenon in early design stages. Following the completion of the aeroelastic model and the case study, further exploitation of the model are carried out by varying dimensional parameters and flight conditions. Hence, parameter analyses for combination of design variables and structural responses, as well as alternating different flight conditions, can be conducted. This chapter is to demonstrate how the tool can be used when limited information about the detailed design is available and how the propeller parameters can be considered in the preliminary design stage using the low-fidelity tool developed in this project.

Recalling the aeroelastic tool developed in previous chapters, it is formed by the modules as shown in Figure 6.1. This framework forms the core of any further exploitation of the developed tool. With a set of parameters describing wing-propeller configuration and flight condition, these information are input into the structural and aerodynamic solver to build a representative and suitable mathematical model.

With regard to wing configuration modifications, Chapter 3 described the development of struc-

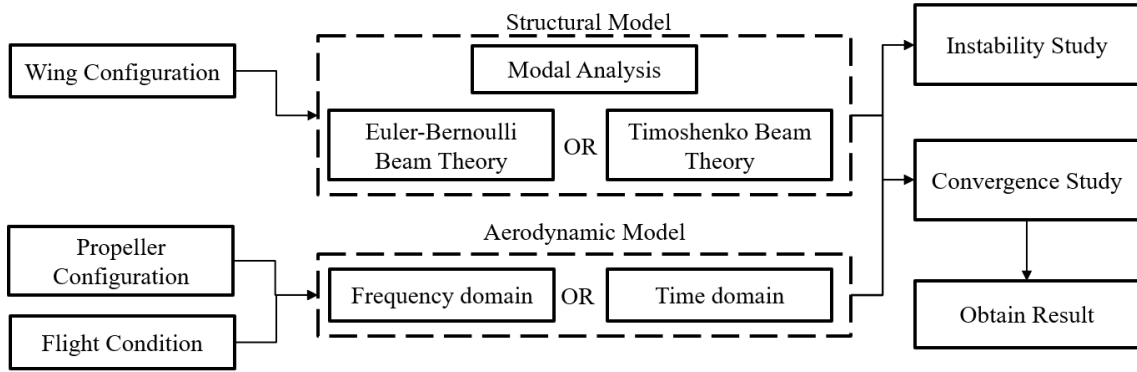


Figure 6.1: Aeroelastic Model Framework

tural model in detail. In brief, the development of structural model starts with analysing the validity of Euler-Bernoulli beam assumptions. By performing modal analysis and comparing modal frequencies derived based on Euler-Bernoulli and Timoshenko beam theories, the effect of shear deformation and rotary inertia can be analysed for each vibration mode. The consideration of structural coupling between vibration motions is also included. The modal analysis study would lead to the most representative mathematical formulation for the short wing studied. However, with a complex mathematical expression, the analytical modal analysis approach is no longer suitable. Hence, a transfer matrix approach is proposed and applied. The demonstration of analysis processes are described in Section 3.4 for the short-wing structure.

In respect of changes in propeller configuration and flight condition, Chapter 2 detailed the development of aerodynamic model. To summarise, unsteady aerodynamic theories in frequency and time domain were studied and combined for different flow conditions and forms of solution. While Theodorsen's and Wagner's models focus on the fluid-structure interacted transition of disturbance to a steady state, Sears' and Küssner's models address the effect of any arbitrary gust field. In regard to obtaining results, frequency-domain theories, such as Theodorsen's and Sears' models, are ideal for obtaining steady-state behaviour as well as characterising instability. Time-domain theories, such as Wagner's and Küssner's model, are suitable for solving transient responses. A case study demonstrating the development of aerodynamic model is shown in Section 2.5.

As for instability and convergence studies, in Chapter 4 and 5, models have been developed for aeroelastic instability and solution convergence for the aeroelastic tool. Detailed formulation for instability study and solution strategy were presented in Section 4.2 and 5.2.

This chapter would study the following phenomena involved with wing dimension, propeller configuration and flight condition in more detail. The relationship between each module developed is illustrated in Figure 6.1. For example, update or any changes in wing configuration would require re-establishing of the structural model. To obtain time-domain dynamic response, the updated structural model would be integrated with the existing aerodynamic model. Convergence study would need repeating and time-domain response can be obtained at last. Similarly, change of propeller configuration or flight condition, would require re-examination of the aerodynamic model and other relevant processes.

Besides parameter variation, different incoming gust field pattern, namely 1-cosine gust and continuous turbulence, are also explored. 1-cosine gust is used as a representation of any discrete gust in the design stage. Since it can be expressed analytically with respect to time. Airloads generated by it can be formulated through the Küssner's model. Therefore, dynamic responses can be obtained and visualised under different gust lengths. Lastly, structural behaviour under continuous turbulence are investigated. Continuous turbulence is gust excitations of irregular pattern. Utilising the frequency domain model, the root mean square deflections are calculated.

6.1 Parameter set definition

The input parameters chosen for this study are the wingspan length, airspeed, flight altitude, propeller radius and propeller operating speed. They range from flight conditions, structural dimension and propeller performance, and they are all crucial design variables that need to be taken into account, and of high benefit for the preliminary design stage.

When considering the wing structure dimension, wingspan is a key design parameter. Changing wingspan would require reconsideration of the structure modal behaviour, modal analysis and

Table 6.1: Parameters and their range of studies

| | |
|------------------|----------------------|
| Wingspan | 2.0m to 2.5m |
| Airspeed | 110m/s to 130m/s |
| Altitude | 0m to 4000m |
| Propeller radius | 0.8m to 1.6m |
| Propeller speed | 20 rev/s to 40 rev/s |

convergence studies are also performed. A brief example of the mathematical procedures is demonstrated with the wingspan length study. Since they are repetitive procedures described and demonstrated in Section 2.5, 3.3, 4.2 and 5.2, the detailed processes for other parameters are not shown in this chapter.

Regarding the flight condition, airspeed is the relative advancing velocity of the aircraft to surrounding air. For a similar configuration of rotorcraft, Eurocopter X3 has a cruising speed around 113 m/s and maximum speed of 131 m/s [107, 108]. Hence, in the parameter study, the range of 110 m/s to 130 m/s is considered. For the same rotorcraft, it was reported that its service ceiling is up to 3810 m [109]. Therefore, altitudes from sea level to 4000 m are investigated in this study.

Lastly, the propeller performance is taken into account. Since the model has the novelty of considering propeller performance, parameter variations and their impact on the wing dynamic behaviour are examined here. Propeller radius, as well as propeller operational speed, are investigated for their impacts on the short wing by utilising an analytical thrust model and slipstream assumptions.

Despite all changes in different parameters, the dynamic behaviour of the wing is always measured at its 75% length.

6.1.1 Wingspan effect

Wingspan is a key parameter for designing a wing structure and certainly also in the case of propeller-wing system. A greater length of wingspan would provide larger lifting area, hence increase lift. However, it would also decrease the stiffness of the wing, making the wing more flexible and giving larger deflection. At the same time, wingspan affects the modal behaviour. Especially under the influences of propeller, vibration resonance should be studied for prevention. In this section, the wingspan is analysed for its impact on wing deflection. Modal analyses are also carried out before solving the time-domain response, as well as convergence studies for natural mode inclusion and time step.

According to the aeroelastic model framework, the modification of structural parameter leads to redefinition of the structural model. Therefore, the governing equation of short wing (Equation 3.22) is re-introduced as

$$\text{Coupled flap-torsion motion: } \begin{cases} m \frac{\partial^2 h}{\partial t^2} - S_\alpha \frac{\partial^2 \alpha}{\partial t^2} + EI_y \frac{\partial^4 h}{\partial x^4} = L_h, \\ I_\alpha \frac{\partial^2 \alpha}{\partial t^2} - S_\alpha \frac{\partial^2 h}{\partial t^2} - GJ \frac{\partial^2 \alpha}{\partial x^2} = M_\alpha, \end{cases} \quad (3.22)$$

$$\text{The lead-lag motion: } \begin{cases} m \frac{\partial^2 v}{\partial t^2} - \kappa_z GA \left(\frac{\partial^2 v}{\partial x^2} - \frac{\partial \varphi_z}{\partial x} \right) = L_v, \\ \rho_w I_z \frac{\partial^2 \varphi_z}{\partial t^2} - EI_z \frac{\partial^2 \varphi_z}{\partial x^2} - \kappa_z GA \left(\frac{\partial v}{\partial x} - \varphi_z \right) = 0. \end{cases}$$

The above equations characterise flapping motion based on the Euler-Bernoulli beam theory, also consider coupling with torsion. Meanwhile the lead-lag motion is modelled based on the Timoshenko beam theory, considering the shear and inertia effects. In Equation 3.22, h, α, v are flapping, torsional and lead-lag displacements respectively, m is the mass per unit length, S_α is the static unbalance, E, G are the Young's modulus and Shear modulus, I_y and I_z are the second moment of area in the y- and z- directions, I_α is the mass moment of inertia, L_h, M_α, L_v are forces and moments exerted in flapping, torsional and lead-lag direction respectively, J is the torsional constant, κ_z is the shear coefficient in z-direction, A is the cross-sectional area, φ_z is the cross-

sectional rotation in z-direction, ρ_w is the wing material density. The position on wingspan is described by the x-coordinate as is one of the independent variables. The other independent variable is time. However, as dimensionless domain is used for the study, equations above can be re-written as

$$\begin{aligned}
m \frac{U_\infty^2}{b} \ddot{\xi} - S_\alpha \frac{U_\infty^2}{b^2} \ddot{\alpha} + EI_y b \xi'''' &= L_h, \\
I_\alpha \frac{U_\infty^2}{b^2} \ddot{\alpha} - S_\alpha \frac{U_\infty^2}{b} \ddot{\xi} - GJ \alpha'' &= M_\alpha, \\
m \frac{U_\infty^2}{b} \ddot{\nu} - \kappa_z GA (b\nu'' - \varphi_z') &= L_v, \\
\rho_w I_z \frac{U_\infty^2}{b^2} \ddot{\varphi}_z - EI_z \varphi_z'' - \kappa_z GA (b\nu' - \varphi_z) &= 0.
\end{aligned} \tag{5.1}$$

In Equation 5.1, U_∞ is the aircraft advancing speed, b is the half chord length, ξ and ν are the dimensionless flapping and lead-lag displacement ($\xi = h/b$ and $\nu = v/b$).

The solution of displacements can be written as collective product of the time-dependent functions and the mode shapes as

$$\begin{Bmatrix} \xi \\ \alpha \end{Bmatrix} = \sum_{j=1}^{\infty} \begin{Bmatrix} \theta_j(x) \\ \eta_j(x) \end{Bmatrix} q_j(\tau) \quad \begin{Bmatrix} \nu \\ \varphi_z \end{Bmatrix} = \sum_{j=1}^{\infty} \begin{Bmatrix} \zeta_j(x) \\ \phi_j^z(x) \end{Bmatrix} p_j(\tau). \tag{5.2}$$

With discretization, the governing equation can be rearranged into a matrix form as

$$\mathbf{M}\ddot{\mathbf{u}} + \mathbf{K}\mathbf{u} = \mathbf{F}, \tag{5.3}$$

The detailed description of mass matrix \mathbf{M} and stiffness matrix \mathbf{K} , as well as time-dependent displacement vector \mathbf{u} and loading vectors \mathbf{F} can be found in Appendix E. The sizes of those matrices are dependent on the number of modes considered.

Within this study, the input variable is the length of wingspan, which directly determinates the mode shape functions. Solving the above equation, time-dependent functions are now obtained. Hence the output dynamic behaviour, which is the product of mode shape and time-dependent function, is computed. The relationship between wingspan and its effect on dynamic behaviour can be analysed.

The mode shape function can be acquired based on known wingspan as an eigenvalue problem. This procedure is described in detail in Section 3.3 via the transfer matrix method. In summary,

the process assumes a simple exponential expression for the time-dependent function with zero external loading. The homogenous equation can be solved for its eigenvalue and eigenvector. The eigenvalue results for each wingspan are listed in Table 6.2.

Table 6.2: Coupled bending-torsional natural frequencies for wingspans from 2.0 m to 2.5 m

| Wingspan (m) | Natural frequencies (Hz) | | | |
|--------------|--------------------------|--------|--------|--------|
| 2.0 | 17.96 | 111.48 | 158.73 | 308.78 |
| 2.1 | 16.29 | 101.26 | 150.99 | 280.83 |
| 2.2 | 14.85 | 92.37 | 144.00 | 256.45 |
| 2.3 | 13.58 | 84.59 | 137.64 | 235.06 |
| 2.4 | 12.48 | 77.75 | 131.83 | 216.21 |
| 2.5 | 11.49 | 71.70 | 126.50 | 199.52 |

Regarding the external loadings F , the flight condition remains unchanged for this study. Hence, the original aerodynamic model can be integrated.

With complete integration of the aeroelastic model, convergence study is carried out, based on strategies discussed in Section 5.2, determining time step size and number of modes. Lastly, the dynamic behaviour of short-wing/propeller system can be obtained. For each wingspan length studied, the entire process from structural model modification to convergence study is repeated. Therefore, the dynamic behaviour of the wing can be explored against variations in wingspan length from 2.0 m to 2.5 m. The results are discussed in the following.

The flapping and torsion steady-state motion are governed by propeller blade-passing frequency. However, the lead-lag motion vibrates at its first natural frequency, hence, changes as wingspan alters. In Table 6.3, the steady-state mean deflections are captured for these three vibration motions. Their variation against wingspan length is also plotted and illustrated in Figure 6.2. As expected, the steady-state mean deflections for all three vibration motions increase as the wingspan increases. A longer wingspan with the same cross-section profile results in a more

Table 6.3: Steady-state mean displacement comparison

| Wingspan (m) | h (m) | v (m) | α (rad) |
|--------------|-------------------------|-------------------------|-------------------------|
| 2.0 | 6.8353×10^{-3} | 1.8792×10^{-3} | 6.0557×10^{-4} |
| 2.1 | 8.2936×10^{-3} | 2.0964×10^{-3} | 6.5597×10^{-4} |
| 2.2 | 1.0046×10^{-2} | 2.3468×10^{-3} | 7.1030×10^{-4} |
| 2.3 | 1.1948×10^{-2} | 2.6013×10^{-3} | 7.6390×10^{-4} |
| 2.4 | 1.4208×10^{-2} | 2.8905×10^{-3} | 8.2184×10^{-4} |
| 2.5 | 1.6632×10^{-2} | 3.1855×10^{-3} | 8.7991×10^{-4} |

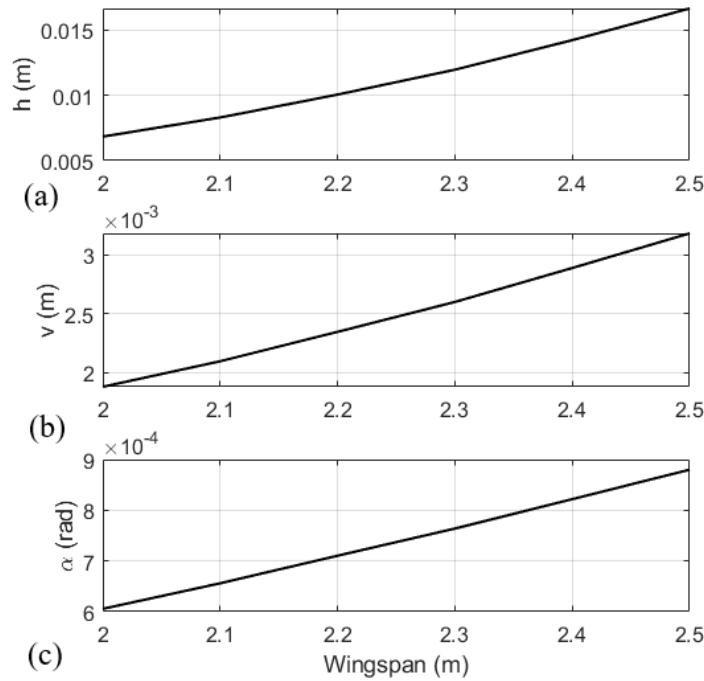


Figure 6.2: Steady-state mean displacement against wingspan: (a) flapping motion; (b) lead-lag motion; (c) torsional motion

flexible wing, hence larger deflections.

As for the steady-state amplitude, Table 6.4 lists the steady-state amplitudes for each vibration

Table 6.4: Steady-state amplitude comparison

| Wingspan (m) | h (m) | v (m) | α (rad) |
|--------------|------------------------|------------------------|------------------------|
| 2.0 | 8.776×10^{-7} | 1.799×10^{-3} | 5.065×10^{-5} |
| 2.1 | 2.555×10^{-6} | 2.030×10^{-3} | 7.918×10^{-5} |
| 2.2 | 7.743×10^{-6} | 2.270×10^{-3} | 1.75×10^{-4} |
| 2.3 | 2.787×10^{-5} | 2.522×10^{-3} | 5.141×10^{-4} |
| 2.4 | 8.045×10^{-6} | 2.722×10^{-3} | 1.306×10^{-4} |
| 2.5 | 4.836×10^{-6} | 2.924×10^{-3} | 7.297×10^{-5} |

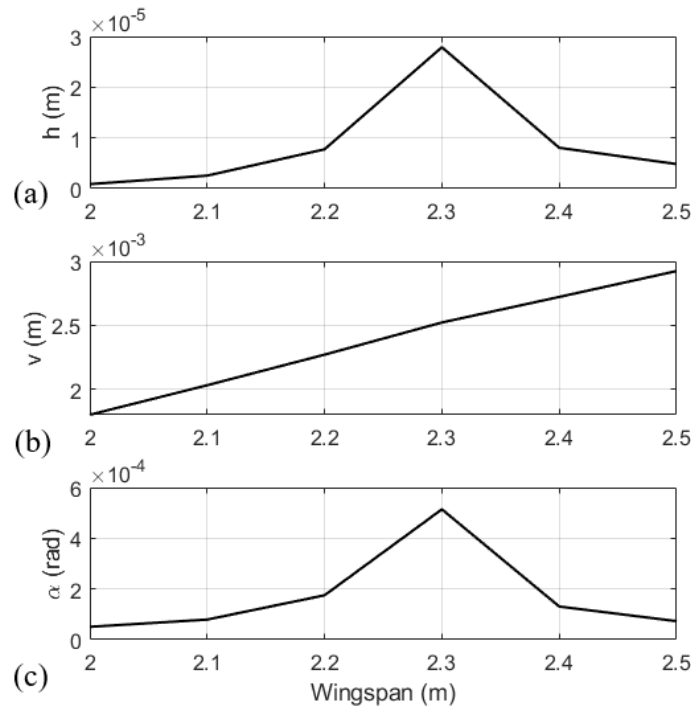


Figure 6.3: Amplitude comparison against wingspan: (a) flapping motion; (b) lead-lag motion; (c) torsional motion

motion under wingspan variation. The results are plotted in Figure 6.3. A rise in amplitude is observed for flapping and torsional motions when wingspan is at 2.3 m. According to Table 6.2

one can find that, at 2.3 m wingspan, the wing would natural vibrates at 137.64 Hz as its 3rd coupled natural frequency. Recalling the propeller blade-passing frequency, it is at 136.5 Hz, which is sufficiently close for these two frequencies to interact with each other. Therefore, due to harmonic resonance between the blade passing frequency and the 3rd coupled natural frequency, a rise in steady-state amplitude at 2.3m wingspan length is observed.

6.1.2 Aircraft advancing velocity effect

During a full flight, aircraft does not only fly at one fixed velocity. Even for its cruising condition, there is a range of advancing velocity the aircraft can operate at. In general, more lift would be generated at a higher flight velocity. However, the aeroelastic behaviour would be affected. In this section, the dynamic behaviour of the propeller-wing system is studied under different airspeeds.

The aircraft advancing velocity is controlled by both the main rotor and the propellers. However, the thrust distribution and control algorithm between these two main propulsive systems are not defined yet in such early stage of design. Therefore, the correlation between advancing velocity and propeller thrust are not considered here. While alternating advancing velocity, the propeller thrust is assumed to remain unchanged. It may not reflect the true reality, but the effect of advancing airspeed is still captured.

The advancing velocities ranging from 110 m/s to 130 m/s are studied in this section. Since the flight condition is altered, the aerodynamic model would need modification. Recalling Section 2.4, the aerodynamic model were formulated based on established unsteady aerodynamic theories. In this section, the only changing parameter is the magnitude of advancing velocity. The types of aerodynamic disturbance and their patterns stay the same. Meanwhile the result of interest remains as the dynamic response of the short wing. Therefore, according to Table 2.2, the composition of aerodynamic model remains the same. Recalling aerodynamic formulation derived in Section 2.5, the aerodynamic loadings at each advancing velocity can be analytically obtained by Equation 2.25. Based on instability study concluded in Section 4.2.1, the critical flutter velocity for the

short-wing/propeller system is at 784.7 m/s. The range of study is well below the flutter threshold, hence no additional instability study is needed.

Referring to the aeroelastic model framework in Figure 6.1, a convergence study is carried out for each advancing velocity determining the appropriate time step and mode numbers. Finally, the dynamic responses under these flight conditions are obtained. The first initial transient responses, in which the first peaks of displacements are captured, are illustrated in Figure 6.4. As aircraft

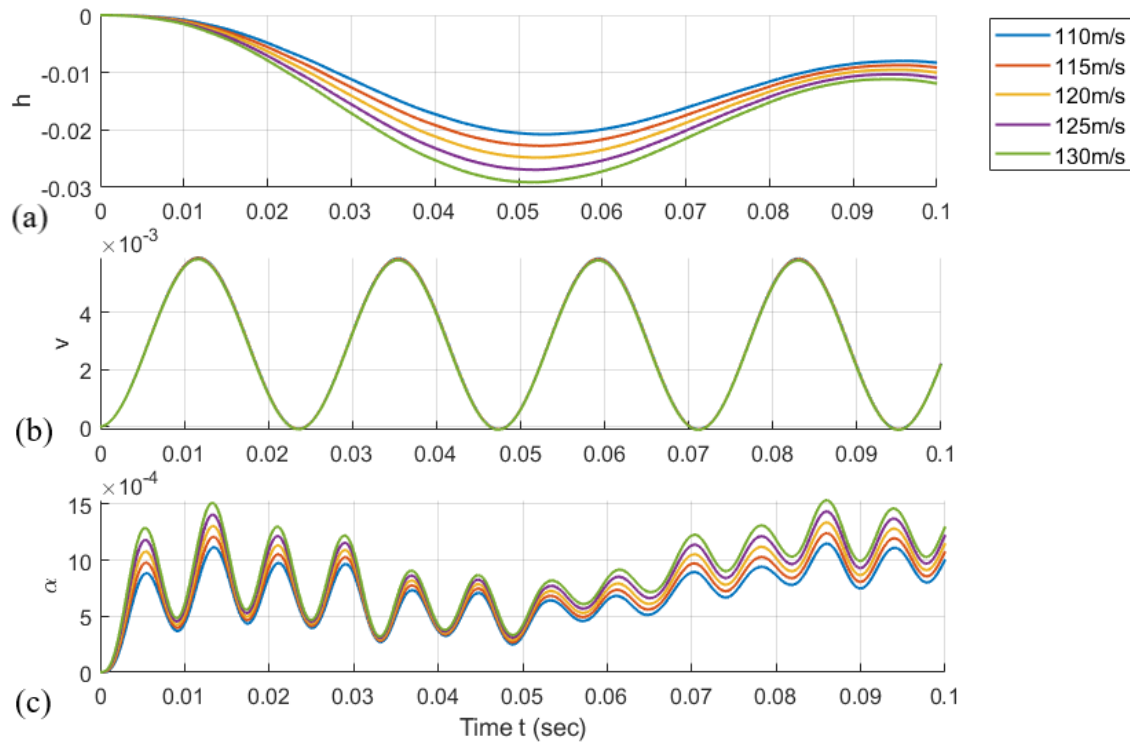


Figure 6.4: Initial transient displacement comparison against airspeed

advancing velocity increases, the aero-structure would experience a larger flapping and torsional deflections. Lead-lag deflection does not appear to have any significant change. Utilising the FFT tool developed for steady-state analysis, the differences in displacement relating to advancing velocity variation are further discussed and quantified in Table 6.5.

When plotting the steady-state mean displacements against airspeeds, a linear relationship is found as shown in Figure 6.5. As expected, flapping and torsional steady-state deflections increase

Table 6.5: Steady-state mean displacement comparison

| Airspeed (m/s) | h (m) | v (m) | α (rad) |
|----------------|---------|-------------------------|-------------------------|
| 110 | 0.0141 | 3.1666×10^{-3} | 7.7005×10^{-4} |
| 115 | 0.0153 | 3.1759×10^{-3} | 8.2409×10^{-4} |
| 120 | 0.0166 | 3.1855×10^{-3} | 8.7991×10^{-4} |
| 125 | 0.0180 | 3.1953×10^{-3} | 9.3752×10^{-4} |
| 130 | 0.0193 | 3.2054×10^{-3} | 9.9696×10^{-4} |

linearly as airspeed increases. Meanwhile, lead-lag deflection also increases linearly. The displacement change percentages for flapping and torsion motions are much higher than those of lead-lag motion.

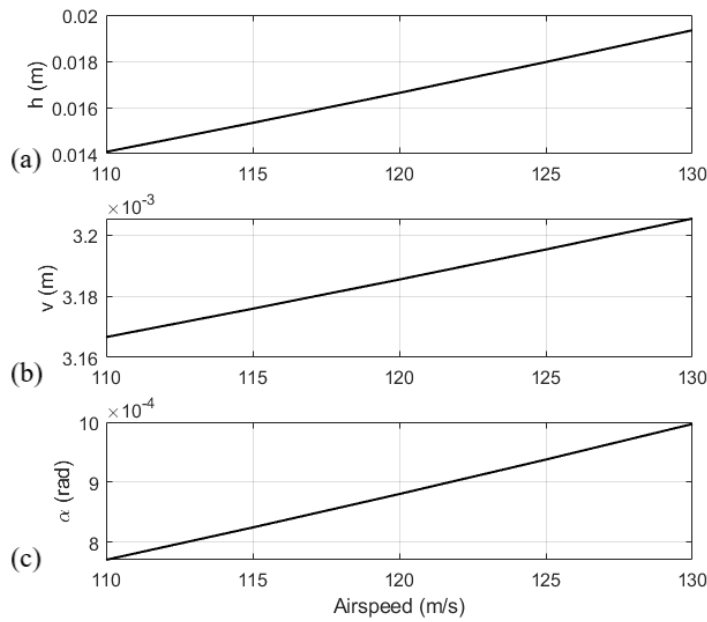


Figure 6.5: Mean displacement comparison against airspeed: (a) flapping motion; (b) lead-lag motion; (c) torsional motion

Statically, aircraft advancing velocity directly affects the effective stiffness of the aero-structure. Since aerodynamic lift and moment are dependent on the displacements, and their rates of changes, the elastic stiffness of the system no longer represents the actual stiffness behaviour. Hence in divergence analysis, instability occurs as airspeed increases, when the effective stiffness reaches zero. The flapping and torsional behaviour here were affected by the change of airspeed through effective stiffness of the system. Meanwhile, the lead-lag motion changes very slightly as airspeed increases, the range of variation across 110m/s to 130 m/s is within 1.5%. Lead-lag deflection is initiated by aerodynamic drag and propeller thrust. The aerodynamic drag is directly proportional to circulatory lift, which is also a function of flapping and torsional displacements. Hence, as flapping and torsional displacements get larger, circulatory lift and aerodynamic drag increase. However, given that the lead-lag motion is structurally uncoupled from the flapping-torsion motion, the deflections are mainly due to the propeller thrust at the wing-tip. Since aerodynamic drag does not have a dominating effect, variation across different airspeeds has a much smaller effect on the lead-lag motion.

Meanwhile, linearity was observed for all of the vibration motions studied. Mathematically, airspeed has a quadratic progression with the effective stiffness. Therefore, quadratic growth was observed for all of the vibration motions studied within the airspeed range selected.

Table 6.6: Steady-state amplitude comparison

| Airspeed (m/s) | h (m) | v (m) | α (rad) |
|----------------|------------------------|------------------------|------------------------|
| 110 | 4.217×10^{-6} | 2.914×10^{-3} | 6.358×10^{-5} |
| 115 | 4.508×10^{-6} | 2.919×10^{-3} | 6.799×10^{-5} |
| 120 | 4.836×10^{-6} | 2.924×10^{-3} | 7.297×10^{-5} |
| 125 | 5.207×10^{-6} | 2.929×10^{-3} | 7.861×10^{-5} |
| 130 | 5.546×10^{-6} | 2.935×10^{-3} | 8.376×10^{-5} |

The same analysis is carried out on the steady-state amplitude for the three vibration motions

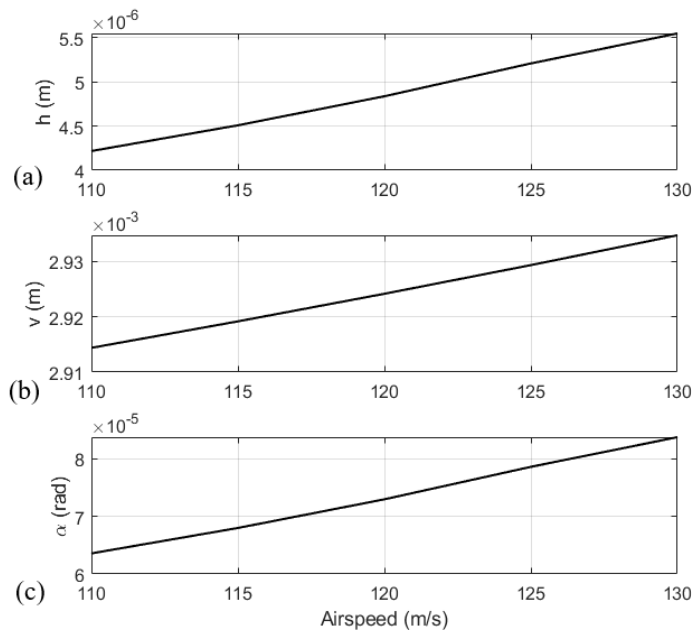


Figure 6.6: Amplitude comparison against airspeed: (a) flapping motion; (b) lead-lag motion; (c) torsional motion

and similar behaviour is observed. In the flapping and torsional motion, the steady-state amplitudes increase linearly as airspeed increases. The change of airspeed affects the effective stiffness then impacts on the steady-state amplitude. While in lead-lag motion, the variation is similar yet at a much smaller scale within 0.8%. Hence the variation of aerodynamic drag caused by changing airspeed is not significant compare to the effect of propeller thrust in the lead-lag motion.

6.1.3 Altitude effect

All aircraft are designed to fly at their own range of altitudes. At a different altitude, a different air density is present. Even within its designed range, changing of air density directly affects aerodynamic loadings, hence will have an impact on the structural behaviour. Therefore, the effect of altitude is studied here in this section. As with the advancing velocity, altitude is another parameter that requires both the main rotor and propeller systems to control, and the correlation between

altitude and thrust is not clear enough in such initial design stage. Hence, all other parameters are kept unchanged when altering the flight altitude. With The air pressure, temperature, density and viscosity at different altitude given by the U.S. Standard Atmosphere [103], dynamic responses under flight altitude ranging from sea level to 4000 m are investigated and analysed in this section.

According to the U.S. standard atmosphere 1976, the air density at each altitude is given as shown in Table 6.7 and it varies linearly across altitude 0 to 4000 m as illustrated in Figure 6.7.

Table 6.7: Altitude vs. air density

| Altitude (m) | Sea level | 1000 | 2000 | 3000 | 4000 |
|----------------------------------|-----------|-------|-------|--------|--------|
| Air density (kg/m ³) | 1.225 | 1.112 | 1.007 | 0.9093 | 0.8194 |

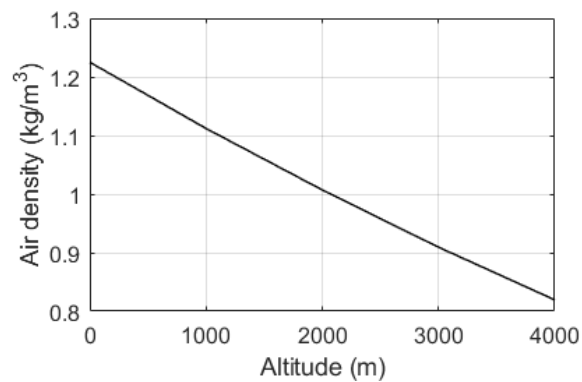


Figure 6.7: Air density changes with variation of altitude from 0 to 4000m

Inputting each air density, the airloads at corresponding altitude can be simulated. The dynamic time-domain responses are obtained and the initial transient responses are illustrated in Figure 6.8. In all three vibration motions, there are clear decreases in the initial displacements as altitude gets higher. To further quantify this observation, steady-state displacements and amplitudes under different altitudes are analysed.

The steady state mean displacements of the three vibration motions under five different altitude levels are given in Table 6.8 and plotted in Figure 6.9.

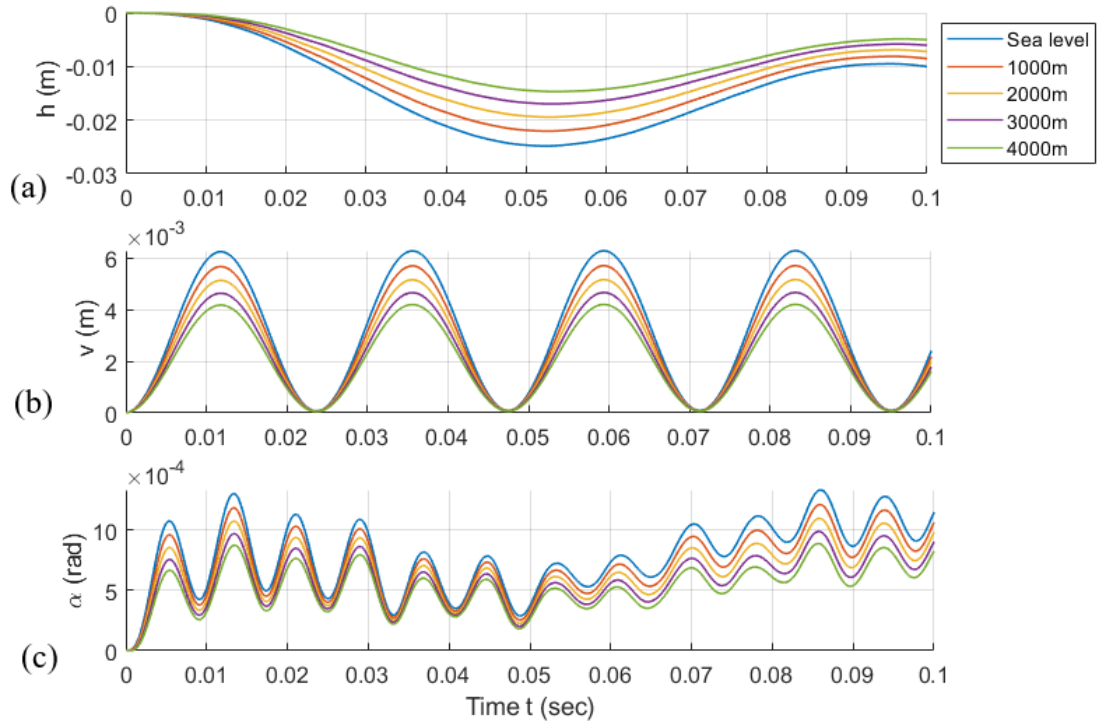


Figure 6.8: Initial transient displacement at different altitudes: (a) flapping motion; (b) lead-lag motion; (c) torsional motion

Table 6.8: Steady-state mean displacement comparison at different altitude

| Altitude (m) | h (m) | v (m) | α (rad) |
|--------------|---------|-------------------------|-------------------------|
| 0 | 0.0166 | 3.1855×10^{-3} | 8.7991×10^{-4} |
| 1000 | 0.0147 | 2.8916×10^{-3} | 7.9756×10^{-4} |
| 2000 | 0.0128 | 2.6186×10^{-3} | 7.2121×10^{-4} |
| 3000 | 0.0112 | 2.3645×10^{-3} | 6.5032×10^{-4} |
| 4000 | 0.0096 | 2.1308×10^{-3} | 5.8522×10^{-4} |

With increasing altitude, mean displacements for the flapping and torsional motions decrease linearly, while lead-lag mean displacement also decreases at a much smaller scale. In reality, at a

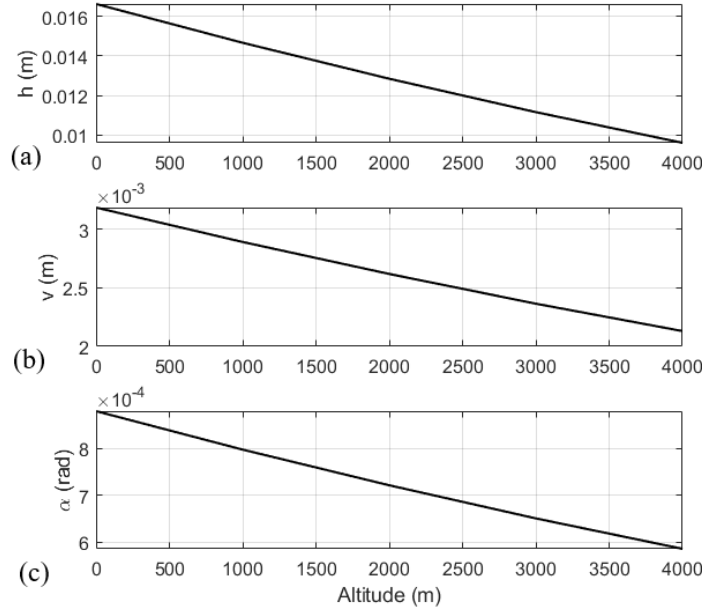


Figure 6.9: Linear variation of mean displacements against altitude: (a) flapping motion; (b) lead-lag motion; (c) torsional motion

higher altitude, air density decreases. Hence with the same airspeed and aerofoil configuration, the airloads would decrease linearly. For flapping-torsion motion, its structural behaviour is governed by aerodynamic loads, hence mean displacement decreases. Lead-lag motion is mainly exerted by the propeller thrust, which is proportional to air density as

$$F_{thrust} = k_T \rho n_p^2 D_p^2, \quad (6.1)$$

where k_T is the thrust coefficient, n_p is the propeller speed and D_p is the propeller diameter. These parameters were assumed unchanged, hence making propeller thrust change proportionally with air density. Furthermore, lead-lag motion shows linear variation across different altitude. Quantitative investigation on the steady-state amplitudes are also carried out, with results displayed in Table 6.9 and Figure 6.10.

The steady-state amplitudes for all three vibration motions showed similar patterns as of the mean displacements. This is within expectation due to the linear relationship between air density

Table 6.9: Steady-state amplitude comparison at different altitude

| Altitude (m) | h (m) | v (m) | α (rad) |
|--------------|------------------------|------------------------|------------------------|
| 0 | 4.836×10^{-6} | 2.924×10^{-3} | 7.287×10^{-5} |
| 1000 | 4.449×10^{-6} | 2.654×10^{-3} | 6.723×10^{-5} |
| 2000 | 4.080×10^{-6} | 2.404×10^{-3} | 6.173×10^{-5} |
| 3000 | 3.728×10^{-6} | 2.171×10^{-3} | 5.648×10^{-5} |
| 4000 | 3.397×10^{-6} | 1.956×10^{-3} | 5.151×10^{-5} |

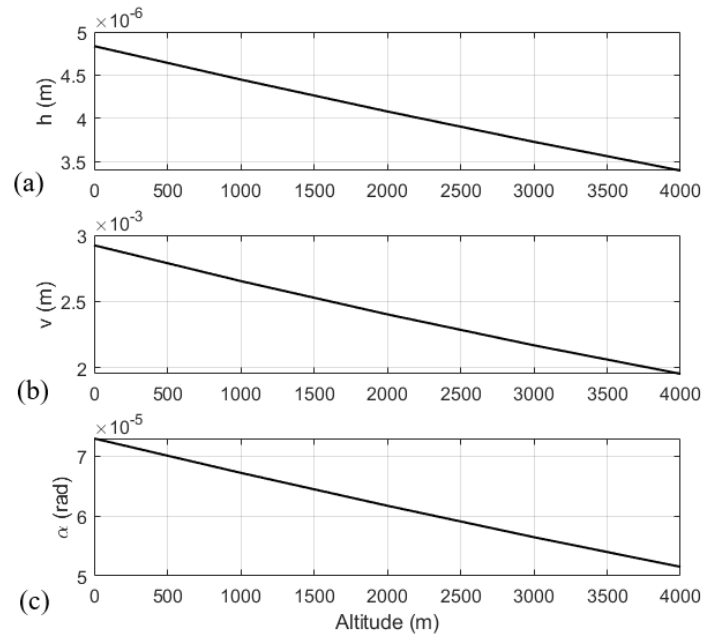


Figure 6.10: Variation of amplitudes against altitude: (a) flapping motion; (b) lead-lag motion; (c) torsional motion

and aerodynamic loads, lift, drag and induced thrust.

6.1.4 Propeller size effect

Likewise, propeller performance can be simulated in the developed tool, in a similar way to flight conditions or wing structural parameters discussed in previous sections. Propellers generate thrust to drive the aircraft forward, at the same time, affect the wing structure via their slipstreams. Changing propeller operational parameters would result in changes in thrust performance and slipstream characteristics. Thrust would then impact on the lead-lag motion, as well as the propeller-axial velocity distribution. As for in the vertical direction, slipstream would project a velocity distribution profile on the wing as discussed in Chapter 2. In the following sections, propeller size and operational speed are studied. Both parameters directly affect the thrust performance and slipstream definition. Relevant changes in thrust and slipstream are considered in the simulation. However, the other parameters, such as advancing velocity, altitude, are assumed to remain unchanged as described in Section 5.4.

In this section, a study on the influence of propeller size, which is defined as the propeller radius, is carried out. Its impact on axial velocities, slipstream radius and vertical velocity distribution are explained. Firstly, the link between propeller radius and thrust needs to be understood. As discussed in Section 6.1.3, propeller size has a direct effect on propeller thrust described as

$$F_{thrust} = k_T \rho n_p^2 D_p^2. \quad (6.1)$$

Increasing in propeller radius would bring a larger thrust due to the increase of lifting area. When thrust increases, the velocity difference between aircraft advancing and slipstream axial addition also changes. Between air-entry velocity, air-exit velocity and resultant thrust, momentum theory can be used. Propeller thrust is the result of pressure unbalance between the entry and exit, hence it can be written as

$$F_{thrust} = \Delta p A_p = (p_0 - p_e) A_p, \quad (6.2)$$

in which Δp is the pressure difference across the propeller interface, A_p is the propeller disk

area. The pressures ahead and behind the propeller disk are

$$p_0 = p_{static} + \frac{1}{2}\rho v_0^2; \quad p_e = p_{static} + \frac{1}{2}\rho v_e^2,$$

where they consist of the static pressure p_{static} , and the dynamic pressure as a function of the local velocity. Substitute the above expressions to Equation (6.2), the resultant thrust can be obtained with respect to the velocity difference as

$$F_{thrust} = 1/2\rho A_p(v_e^2 - v_0^2), \quad (6.3)$$

Knowing the velocity change, the slipstream can be defined. The slipstream axial addition term $v_e - v_0$ from Equation (6.3) is considered as the average axial velocity addition. With a larger propeller radius, a larger area would be affected on the wing. Hence, by incorporating v_e and D_p into a more realistic parabolic velocity distribution, the analytical expression for axial velocity addition can be redefined. Besides changes in the axial direction, the vertical velocity distribution profile is also affected by the change of propeller radius. The maximum vertical velocity addition is assumed to be constant. However, a larger area would experience the additional vertical velocity as well as the sinusoidal variation. Hence the distribution is reshaped.

With respect to propeller radius, resultant steady-state responses are presented. Table 6.10 lists the steady-state mean deflections, while Figure 6.11 visualises the change as propeller gets larger.

Table 6.10: Steady-state mean displacement comparison

| Propeller radius (m) | h (m) | v (m) | α (rad) |
|----------------------|------------------------|-------------------------|------------------------|
| 0.8 | 1.733×10^{-2} | 1.400×10^{-3} | 0.886×10^{-3} |
| 1.0 | 2.648×10^{-2} | 3.242×10^{-3} | 1.183×10^{-3} |
| 1.2 | 3.794×10^{-2} | 6.588×10^{-3} | 1.731×10^{-3} |
| 1.4 | 6.060×10^{-2} | 12.101×10^{-3} | 2.689×10^{-3} |
| 1.6 | 9.767×10^{-2} | 20.562×10^{-3} | 4.286×10^{-3} |

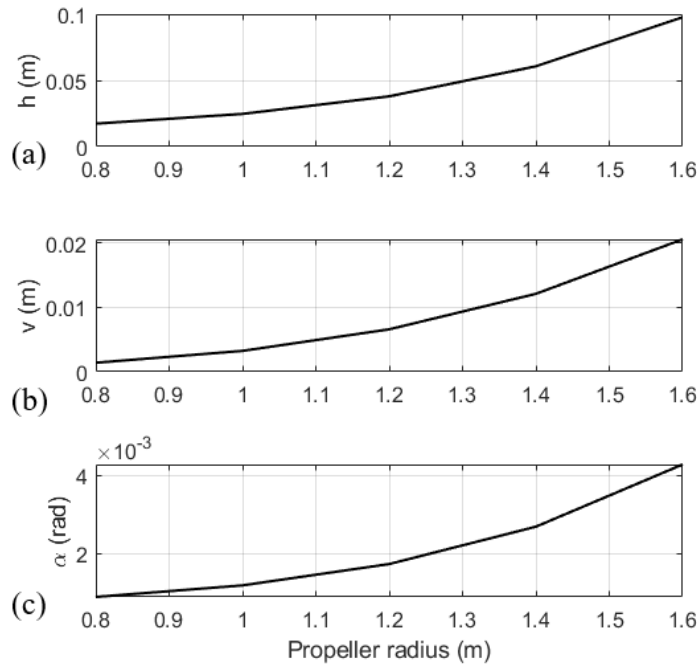


Figure 6.11: Mean displacement comparison against propeller size: (a) flapping motion; (b) lead-lag motion; (c) torsional motion

Figure 6.11 shows that the steady-state deflections grow as the propeller gets larger. For all three vibration motions, they exhibit similar patterns too. For flapping and torsional motion, this is due to the analytical quadratic relationship between velocities and propeller radius. Among all the vibration motions, the lead-lag motion experiences the largest variation across the study regime. This is due to the quartic relationship between propeller radius and thrust.

As for the steady-state amplitude, all three motions get larger vibration amplitudes with increasing propeller radius. Again, all three motions have very similar growing patterns as the propeller becomes bigger. Especially for lead-lag motion, the percentage in growth is much larger compare to flapping and torsion. Again, it is an result of the quartic relationship between thrust and propeller radius. In summary, when designing the short-wing/propeller system, the propeller size needs to be considered carefully between its effect of thrust and advancing velocity addition and

Table 6.11: Steady-state amplitude comparison

| Propeller radius (m) | h (m) | v (m) | α (rad) |
|----------------------|-------------------------|-------------------------|------------------------|
| 0.8 | 4.339×10^{-6} | 1.222×10^{-3} | 0.634×10^{-4} |
| 1.0 | 5.846×10^{-6} | 2.945×10^{-3} | 0.881×10^{-4} |
| 1.2 | 7.932×10^{-6} | 6.057×10^{-3} | 1.199×10^{-4} |
| 1.4 | 10.573×10^{-6} | 11.182×10^{-3} | 1.566×10^{-4} |
| 1.6 | 13.334×10^{-6} | 19.045×10^{-3} | 1.899×10^{-4} |

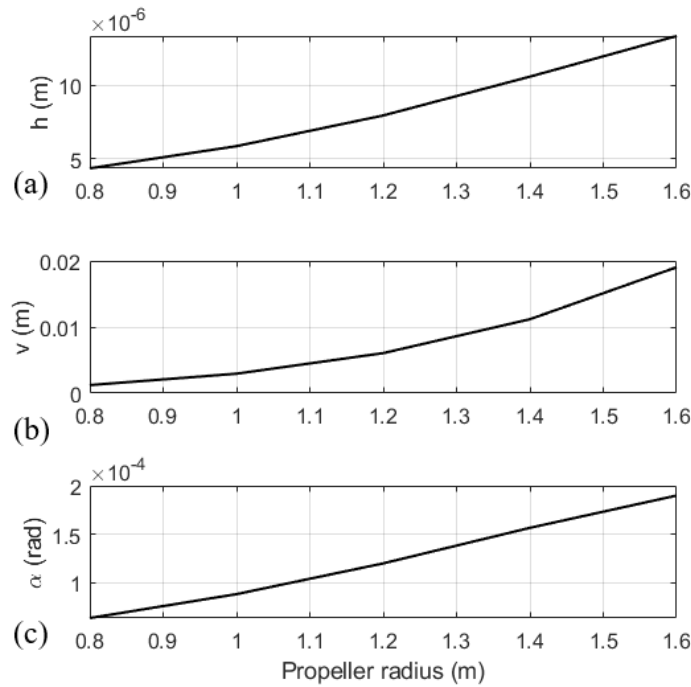


Figure 6.12: Amplitude comparison against propeller size: (a) flapping motion; (b) lead-lag motion; (c) torsional motion

large resultant deflections of the wing structure.

6.1.5 Propeller speed effect

As with propeller sizing, the rotational speed also directly impacts the propulsive thrust given to the aircraft. Increasing propeller speed, hence, would increase the velocity difference between flow upon entry and exit according to Equation (6.2). Knowing the average flow exiting velocity, the parabolic profile for the propeller axial addition can be written. As for the vertical direction, the velocity remains the same while the sinusoidal variation frequency changes with the propeller operating speed.

Steady-state responses are presented in Table 6.12 and 6.13 while visualisations of the data are illustrated in Figure 6.13 and 6.14.

Table 6.12: Steady-state mean displacement comparison

| Blade passing frequency (Hz) | h (m) | v (m) | α (rad) |
|------------------------------|------------------------|------------------------|------------------------|
| 100 | 2.025×10^{-2} | 1.807×10^{-3} | 1.016×10^{-3} |
| 125 | 2.314×10^{-2} | 2.741×10^{-3} | 1.125×10^{-3} |
| 150 | 2.666×10^{-2} | 3.883×10^{-3} | 1.257×10^{-3} |
| 175 | 3.081×10^{-2} | 5.232×10^{-3} | 1.412×10^{-3} |
| 200 | 3.560×10^{-2} | 6.790×10^{-3} | 1.591×10^{-3} |

For all three vibration motions, steady-state deflections increase as propeller operates faster. Again, since increasing propeller speed would result in quadratic thrust increment, lead-lag motion has the most significant changes compared to flapping and torsion across the range of speed studied.

As for the steady-state amplitudes, they are not dominated by the increase of thrust or velocity magnitude. At 25 rev/s, a peak is observed in the coupled flapping and torsional motion. Given that there are five blades, blade passes the wing level at 125 Hz when propeller operates at 25 rev/s. Recalling modal analysis performed in Chapter 3, the coupled flapping and torsion motion has its 2nd natural frequency at 126.5 Hz. This brings resonance between the blade pass frequency and

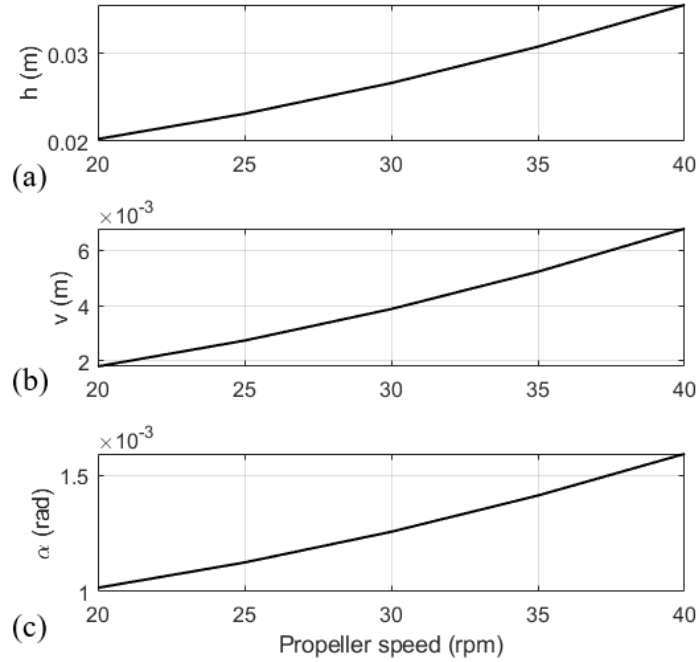


Figure 6.13: Mean displacement comparison against propeller speed: (a) flapping motion; (b) lead-lag motion; (c) torsional motion

Table 6.13: Steady-state amplitude comparison

| Blade passing frequency (Hz) | h (m) | v (m) | α (rad) |
|------------------------------|-------------------------|------------------------|-------------------------|
| 100 | 0.744×10^{-6} | 1.591×10^{-3} | 6.188×10^{-5} |
| 125 | 32.321×10^{-6} | 2.477×10^{-3} | 60.707×10^{-5} |
| 150 | 2.814×10^{-6} | 3.543×10^{-3} | 3.907×10^{-5} |
| 175 | 0.649×10^{-6} | 4.803×10^{-3} | 1.782×10^{-5} |
| 200 | 8.513×10^{-6} | 6.358×10^{-3} | 0.328×10^{-5} |

the structural natural frequency, resulting in flapping and torsional amplitude peaks at 25 rev/s.

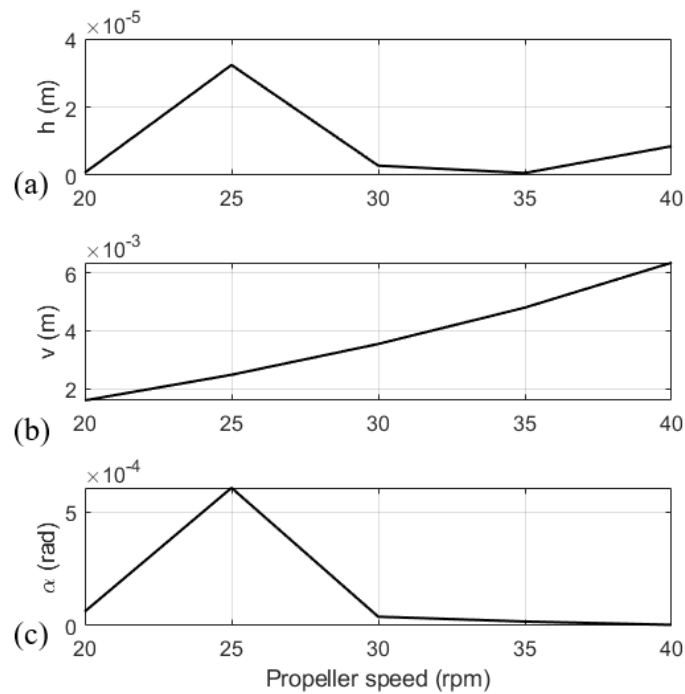


Figure 6.14: Amplitude comparison against propeller speed: (a) flapping motion; (b) lead-lag motion; (c) torsional motion

6.2 Dynamic response under different disturbance

The case study performed in Chapter 5 and parameter studies above are all excited by series of sharp-edge gusts, representing propeller slipstream conditions. However, during flight operation, the aircraft is also likely to experience different excitations. They can be discrete gusts, which are known and forms a velocity field with identified patterns. This type of gust is often simulated as 1-cosine gust. Besides, not all the conditions are predictable during a flight operation. Hence in this section, continuous turbulence is also introduced. That is when excitations of irregular and unpredictable patterns are exhibited.

All excitations can be treated as a discrete gust or continuous turbulence. In order to obtain response under discrete gust, the same mathematical process described in Chapter 5 can be applied incorporating 1-cosine gust loadings via Küssner's model. While continuous turbulence consist

of gusts with different velocities of random patterns and usually are analysed statistically in the frequency domain. In this section, responses under both excitations are examined for the short wing-propeller configuration.

6.2.1 1-cosine gust

Recalling the sharp-edged gust condition discussed in previous chapters, it can be categorised as a discrete gust with deterministic pattern. However, sudden step change of velocities is an ideal condition. In reality, changes between velocities are in forms of 1-cosine gust, which gives a gradual change over a velocity peak. Hence, 1-cosine gust is used to represent any discrete gust in the design stage. The mathematical procedures to obtain dynamic response have been discussed in Chapter 5 and the exact procedures are applied. In this section, time-domain dynamic responses under 1-cosine gusts of various lengths are investigated.

Starting with defining the 1-cosine gust, as illustrated in Figure 6.15, gust velocity varies in the vertical direction, normal to the aircraft advancing velocity U_∞ . It is a gradual change from one velocity to another. With velocity peak at w_{cos}^{max} over gust length of L_{cos} , the velocity profile can

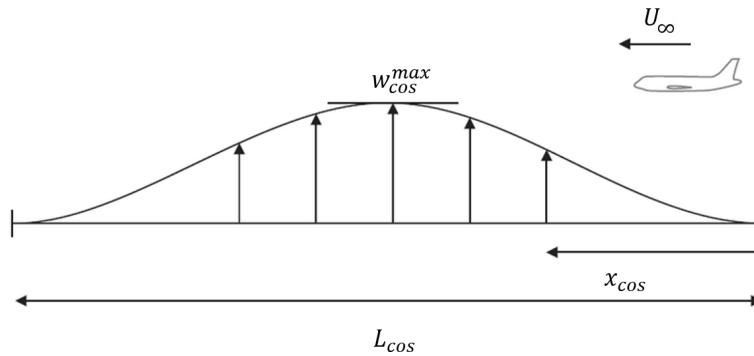


Figure 6.15: 1-cosine gust schematic

be written with respect to the aircraft location x_{cos} in the gust field, which is directly proportional to time.

$$w_{cos} = \frac{w_{cos}^{max}}{2} \left(1 - \cos \frac{2\pi x_{cos}}{L_{cos}} \right) = \frac{w_{cos}^{max}}{2} \left(1 - \cos \frac{2\pi U_\infty t}{L_{cos}} \right) \quad (6.4)$$

In the dimensionless time domain, the same expression can be written as

$$w_{cos} = \frac{w_{cos}^{max}}{2} \left(1 - \cos \frac{2\pi b}{L_{cos}} \tau\right). \quad (6.5)$$

Recalling the aerodynamic model described in Chapter 2, the aeroelastic loadings from any arbitrary gust field can be analytically determined in the time domain, hence leads to solution of the aeroelastic response. The 1-cosine gust, as analytical expressed above, can be input into the aeroelastic model and the aeroelastic response can be obtained accordingly. Within this section, an 1-cosine gust field is presented showing the capability of the aeroelastic model as well as analysing the relationship between gust length and structural response.

The flight condition considered here is the short-wing propeller system advancing at 120 m/s encountering an 1-cosine gust of peak velocity at 5.5m/s. Ranging from gradual to steep gusts, the gust field varies in length, from 10 to 50 times of the chord length. The effect of gust length on the structural response is captured and investigated by inputting gust information together with advancing flow and propeller slipstream.

Illustrated in Figure 6.16 and 6.17, transient responses are plotted against both time and gust length. Only the coupled flapping-torsion motion is studied here as it is directly affected by the lift and moment induced by gust velocities. Meanwhile the lead-lag motion is dominated by the propeller thrust which would remain the same in this study. Figure 6.16 shows that the flapping displacement experiences sinusoidal fluctuation while being damped along time. Similar patterns are exhibited at all gust length studied. However, from 10 to 50 times of the chord length, the maximum displacement peaks at 25 chord lengths.

At 25 chord lengths, the maximum displacement peaked at 0.04 mm. Meanwhile, through 10 to 50 chord lengths, the maximum displacement location moves further along the time axis, meaning the maximum displacement happens later for longer gust length. Similarly, the peak for minimum displacement also sits at 25 chord lengths. This is due to the large amplitude in the initial response.

When varying gust length from 10 to 50 times of chord length, the frequency term within the 1-cosine expression changes. It goes from 40 Hz to 8 Hz, as gust length increases. This range

of frequencies is also where the first modal frequency sits. Therefore, it is reasonable to expect a peak in maximum displacement within this range. However, there are many factors at play in the first initial period, such as the modal frequency, propeller blade passing frequency, as well as the 1-cosine excitation. It is difficult to analytically predict where the peak will appear. In this particular use case, the peak for maximum displacements sits at 25 chord lengths. At 25 chord lengths, the frequency term is at the value of 16 Hz. In other use cases, this is going to be different. The developed tool can capture the peak without any analytical derivation, which is likely to be labour intensive.

If the 1-cosine gust carries on its periodic behaviour, the maximum displacement would occur at where there is a coincidence between the gust and modal frequencies due to resonance. However, the gust field in this case is only active for a limited time in the very beginning of the simulation. This means the frequency resonance effect would not be apparent. The dynamic behaviour obtained by the developed aeroelastic tool reveals the complex relationship between discrete gust length and maximum transient displacement.

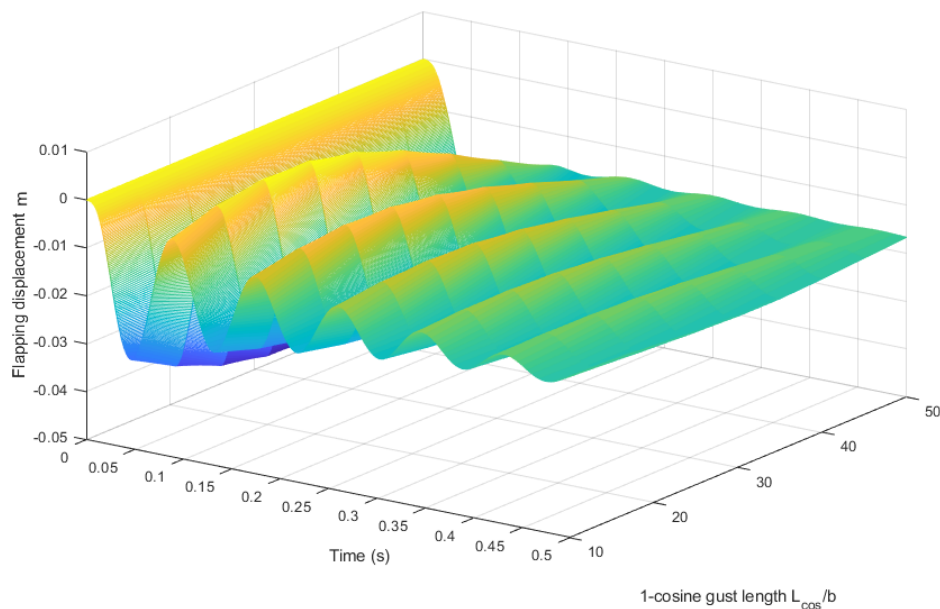


Figure 6.16: Flapping transient response against 1-cosine gust length

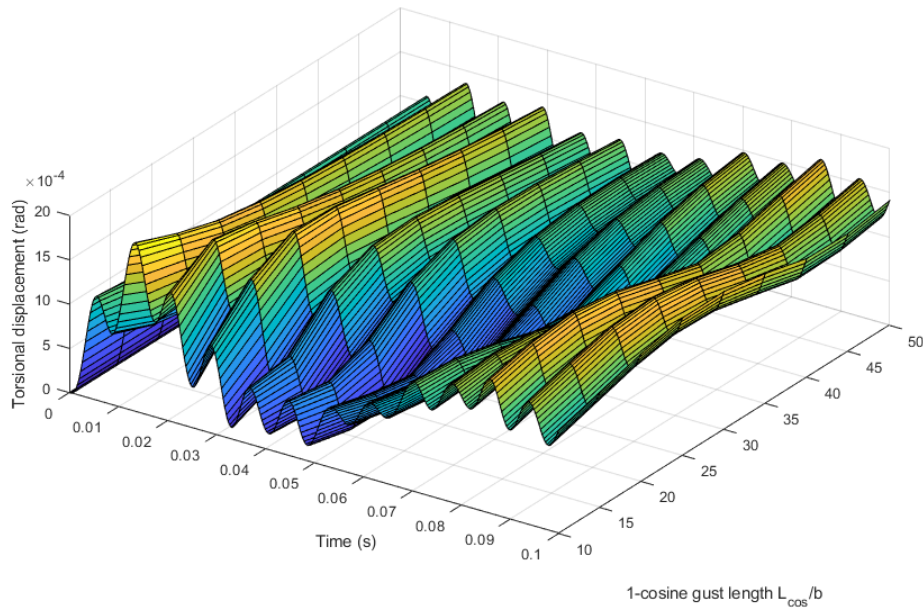


Figure 6.17: Torsion transient response against 1-cosine gust length

6.2.2 Continuous turbulence

Having considered the responses under discrete gusts, continuous turbulence response is looked at in this section. When the gust field has unknown and irregular pattern, analytical expression for the specific gust field becomes impossible to acquire. Therefore, time-domain response becomes unachievable. The system response under continuous turbulence is an issue in the frequency domain rather than in the time domain. Continuous turbulence consists of random gusts without pattern and there are unlimited possible combinations of random gusts at different frequencies and velocities. Hence, the condition can only be described as a statistical problem rather than any particular reality. To obtain responses under continuous turbulence, the results are in the form of power spectral density (PSD), which summarise the mean-squared displacements at each frequency. This can be obtained by knowing the PSD for the random gust field and frequency response function (FRF) of the aeroelastic system. Similarly, PSD for random gust field summarises the mean-square gust amplitude at different frequencies, while the FRF reflects on the response of the system under any given frequency with a uniformly distributed gust of unit magnitude. The PSD of system response

can be then obtained by

$$\Phi_r(\omega) = |FRF(\omega)|^2 \Phi_g(\omega), \quad (6.6)$$

where, ω is the frequency in rad/s, Φ_r is the PSD for aeroelastic response. $FRF(\omega)$, the frequency response function, can be derived from the frequency domain aeroelastic model developed in Chapter 4. Meanwhile, $\Phi_g(\omega)$ is the PSD for gust amplitude, which has established turbulence models that was summarised from experiences. One of the most commonly used mathematical model for random gust is the von Kármán model. It summarised translational and angular irregular gust field in all six degrees of freedom. However, an example applying only vertical turbulence is used in this section. Since the flight condition assumed is not an ad-hoc representation, and the previous case studied and parameter analysis are presented for the demonstration purpose of the tool's capability. This section is also demonstrating the compatibility between the developed tool and established turbulence model. The linear and angular turbulence not included in this example can be applied in the same fashion and forms a more complex turbulence environment. However, it does not lie within the scope of this project, hence not included.

According to von Kármán [110, 111], the PSD at any given frequency in the flapping direction can be written as

$$\Phi_g = \sigma_g^2 \frac{L_t}{\pi} \frac{1 + (8/3)(1.339\Omega L_t)^2}{[1 + (1.339\Omega L_t)^2]^{11/6}}, \quad (6.7)$$

where $\Omega = \omega/U_\infty$ is the scaled frequency (rad/m), hence the function is independent of the aircraft velocity, σ_g is the root-mean-square gust velocity intensity (typically taken as 1m/s) and L_t is the characteristic wavelength of the turbulence (typically taken as 2500 ft, which in SI unit is 762 m) [102]. Since ω is the frequency of the unit gust, as well as the input variable, the von Kármán function can be visualised against ω and the logarithmic scale plot is illustrated as in Figure 6.18. The gust of lower frequencies has a PSD larger than one and will enhance the displacement behaviour. While at higher frequencies, the PSD is smaller than one and will damp the displacement behaviour.

Knowing the atmospheric gust behaviour, the deformation caused by the continuous turbulence

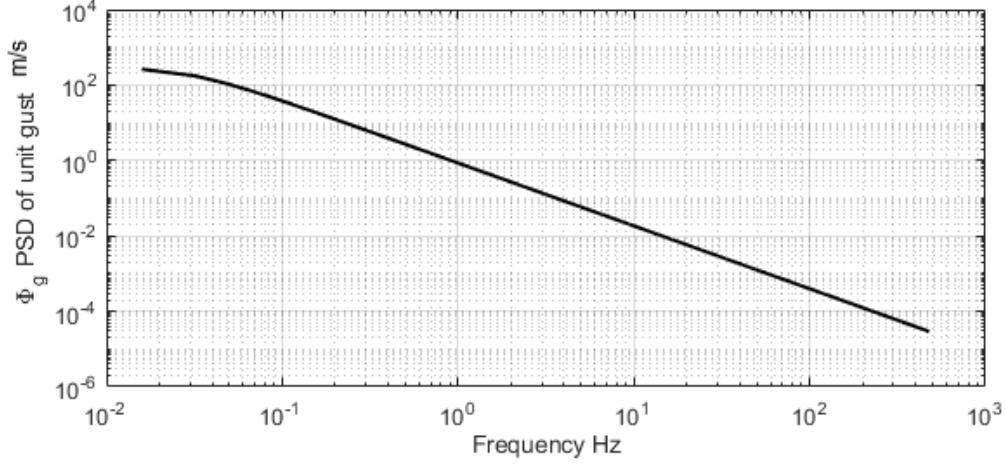


Figure 6.18: von Kármán turbulence model defining PSD at each frequency

only depends on the aeroelastic properties of the short-wing/propeller system. In the frequency domain, it is the frequency response function (FRF), which quantifies the deformation output resulted by any unit gust input. The FRF can be derived based on the frequency domain aeroelastic model discussed in Section 4.2. The general EoMs can be expressed in the time domain as

$$\mathbf{M} \frac{d^2 \mathbf{u}}{dt^2} + \mathbf{C} \frac{d\mathbf{u}}{dt} + \mathbf{K} \mathbf{u} = \mathbf{F}_{aero}. \quad (6.8)$$

Featuring coupled modes, the mass, damping and stiffness matrices are defined as

$$\mathbf{M} = \begin{bmatrix} [\int m \theta_i \theta_j dx]_{N_q \times N_q} & [-\int S_\alpha \theta_i \eta_j dx]_{N_q \times N_q} \\ [-\int S_\alpha \eta_i \theta_j dx]_{N_q \times N_q} & [\int I_\alpha \eta_i \eta_j dx]_{N_q \times N_q} \end{bmatrix} \quad \mathbf{u} = \begin{Bmatrix} [q_j(t)]_{N_q \times 1} \\ [q_j(t)]_{N_q \times 1} \end{Bmatrix}$$

$$\mathbf{C} = \begin{bmatrix} [\int c_h \theta_i \theta_j dx]_{N_q \times N_q} & \mathbf{0} \\ \mathbf{0} & [\int c_\alpha \eta_i \eta_j dx]_{N_q \times N_q} \end{bmatrix} \quad \mathbf{F}_{aero} = \begin{Bmatrix} [\int \theta_i L_h dx]_{N_q \times 1} \\ [\int \eta_i M_\alpha dx]_{N_q \times 1} \end{Bmatrix}$$

$$\mathbf{K} = \begin{bmatrix} [\int EI_y \theta_i \theta_j'''' dx]_{N_q \times N_q} & \mathbf{0} \\ \mathbf{0} & [-\int GJ \eta_i \eta_j'' dx]_{N_q \times N_q} \end{bmatrix}.$$

In previous studies, the number of coupled modes included N_q is 5. In computing the frequency response function (FRF), aerodynamic loading term \mathbf{F}_{aero} needs to include unsteady aerodynamic effects as well as the unit periodic gust input. Propeller contribution, given at a fixed frequency,

towards the steady-state amplitude can be superimposed later on top of the FRF. Here, the flexible wing structure without the propellers is investigated first.

$$\mathbf{F}_{aero} = \mathbf{F}_a + \mathbf{F}_{in}, \quad (6.9)$$

in which unsteady aerodynamic effects (\mathbf{F}_a) is characterised by Theodorsen's model. As investigated in Chapter 2 and 4, analytical expression can be formulated as

$$\mathbf{F}_a = \mathbf{M}_a \frac{d^2 \mathbf{u}}{dt^2} + \mathbf{C}_a \frac{d\mathbf{u}}{dt} + \mathbf{K}_a \mathbf{u}, \quad (6.10)$$

$$\text{where } \mathbf{M}_a = \pi \rho b^2 \left[\begin{array}{c|c} [-\int \theta_i \theta_j dx]_{N_q \times N_q} & [\int ab \theta_i \eta_j dx]_{N_q \times N_q} \\ \hline [\int ab \eta_i \theta_j dx]_{N_q \times N_q} & [\int (-a^2 b^2 - b^2/8) \eta_i \eta_j dx]_{N_q \times N_q} \end{array} \right],$$

$$\mathbf{C}_a = \pi \rho b \left[\begin{array}{c|c} [-\int 2C(k) U_a \theta_i \theta_j dx]_{N_q \times N_q} & [-\int (2bC(k)(\frac{1}{2} - a) + b) U_a \theta_i \eta_j dx]_{N_q \times N_q} \\ \hline [\int 2bC(k)(\frac{1}{2} + a) U_a \eta_i \theta_j dx]_{N_q \times N_q} & [\int [2b^2 C(k)(\frac{1}{4} - a^2) - b^2(\frac{1}{2} - a)] U_a \eta_i \eta_j dx]_{N_q \times N_q} \end{array} \right],$$

$$\mathbf{K}_a = 2\pi \rho b C(k) \left[\begin{array}{c|c} \mathbf{0} & [-\int U_a^2 \theta_i \eta_j dx]_{N_q \times N_q} \\ \hline \mathbf{0} & [\int b(\frac{1}{2} + a) U_a^2 \eta_i \eta_j dx]_{N_q \times N_q} \end{array} \right].$$

A unit gust input ($|w_{in}| = 1m/s$) of frequency ω can be considered via Sears' model, with Sears' function $S(k)$ featuring the reduced frequency $k = \frac{\omega b}{U_a}$. It can expressed as

$$\mathbf{F}_{in} = \bar{\mathbf{F}}_{in} e^{i\omega t}, \quad (6.11)$$

$$\text{where } \bar{\mathbf{F}}_{in} = \left\{ \begin{array}{c} [\int \theta_i \bar{L}_{in} dx]_{N_q \times 1} \\ [\int \eta_i \bar{M}_{in} dx]_{N_q \times 1} \end{array} \right\} \text{ and } \left\{ \begin{array}{c} \bar{L}_{in} \\ \bar{M}_{in} \end{array} \right\} = \left\{ \begin{array}{c} -2\pi \rho b U_a |w_{in}| S(k) \\ -b(1/2 + a) \bar{L}_{in} \end{array} \right\}.$$

In this case, the response of steady-state amplitude under different frequencies of unit gust velocity is studied. Starting by assuming steady-state condition $\mathbf{u} = \bar{\mathbf{u}} e^{i\omega t}$, the general EoM can be written in frequency domain as

$$[-\omega^2(\mathbf{M} - \mathbf{M}_a) + i\omega(\mathbf{C} - \mathbf{C}_a) + (\mathbf{K} - \mathbf{K}_a)] \bar{\mathbf{u}} = \bar{\mathbf{F}}_{in}, \quad (6.12)$$

With respect to a unit gust input, the response output can be obtained as

$$\frac{\bar{\mathbf{u}}}{|w_{in}|} = \frac{[-\omega^2(\mathbf{M} - \mathbf{M}_a) + i\omega(\mathbf{C} - \mathbf{C}_a) + (\mathbf{K} - \mathbf{K}_a)]}{\bar{\mathbf{F}}_{in}}. \quad (6.13)$$

Recalling the discretisation for the beam model, the flapping and torsional displacements are formulated by mode shape function and time-dependent function and the expression is written as

$$\begin{Bmatrix} h \\ \alpha \end{Bmatrix} = \begin{Bmatrix} \bar{h} \\ \bar{\alpha} \end{Bmatrix} e^{i\omega t} = \sum_{j=1}^{\infty} \begin{Bmatrix} \theta_j(x) \\ \eta_j(x) \end{Bmatrix} \bar{q}_j e^{i\omega t}. \quad (6.14)$$

The FRF of the aeroelastic system can be obtained by correcting $\bar{\mathbf{u}}$ into $\{\bar{h}, \bar{\alpha}\}^T$. Hence by inputting unit gust at different frequencies, the flapping and torsional amplitudes at 75% length of the wing are plotted against frequency as illustrated in Figure 6.19. Peaks are shown at the flexible model natural frequencies. The peak amplitude is the largest when input gust is at the first natural frequency, and peak amplitude decreases when meeting higher natural frequencies. When inputting propeller influence at a fixed frequency and a given velocity magnitude, the frequency and amplitude responses due to propeller presence are characterised and superimposed onto the FRF of a fixed wing. In Figure 6.19, the FRFs with and without propeller inflow are presented.

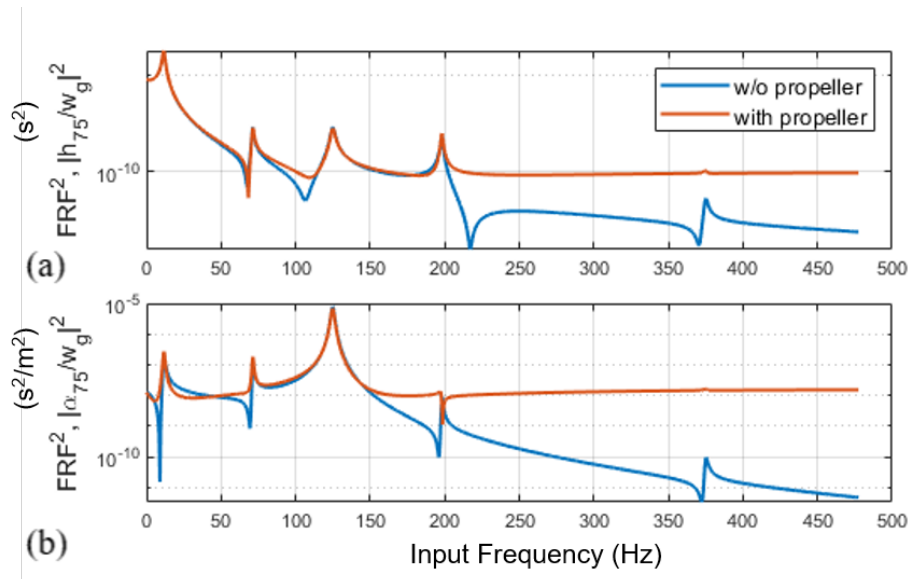


Figure 6.19: Frequency response function for coupled flapping-torsion motion: (a) flapping motion; (b) torsional motion

The peaks remain at the flexible natural frequencies, while propeller additional amplitude being superimposed linearly onto the overall behaviour at each frequency. For the first four peaks, the

amplitude values are at similar level of magnitude, which means the propeller inflow is less significant comparing to the fixed-wing behaviour. While at the fifth peak, propeller flow has a more dominating effect.

Multiplying by the continuous gust excitation via von Kármán's model, the system's response PSD at 75% length under continuous gust can be obtained and it is illustrated along a range of frequencies as Figure 6.20. As shown, the peaks at natural frequencies still remains under the

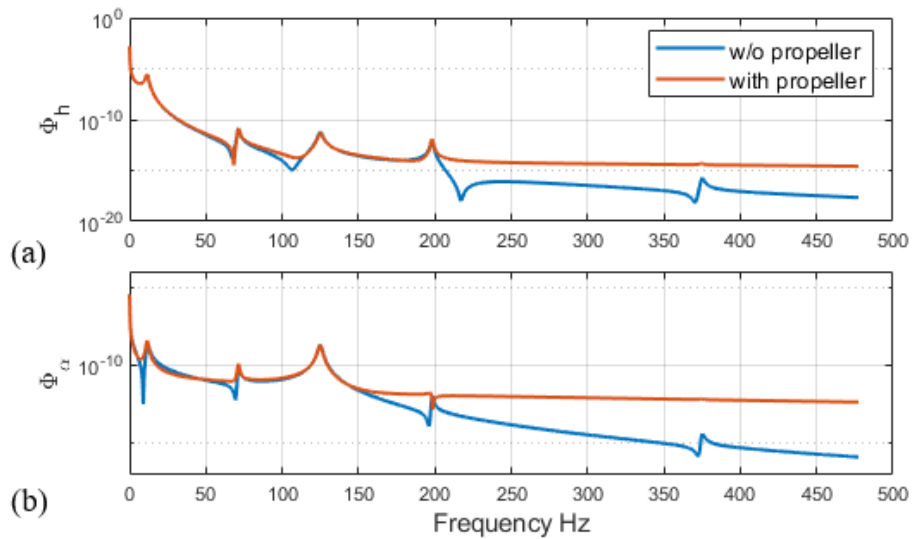


Figure 6.20: the PSD of displacements response in continuous gust: (a) flapping motion; (b) torsional motion

influence of continuous turbulence. As expected, at the extreme low frequency range, the displacement was enhanced by the continuous turbulence, comparing with the original system FRF. As the frequencies get higher, an damping effect from the turbulence is observed.

Since PSD is the mean-square values at each frequency, the root-mean-square displacements at any given point on the beam can be obtained by integrating along the frequency range considered as

$$\sigma_r^2 = \int_0^{\omega_{max}} \Phi_r(\omega) d\omega. \quad (6.15)$$

For the short-wing structure, the root-mean-square displacement along the wing can be obtained

and it is illustrated as in Figure 6.21. The wing structure would deflect the most at its tip. Under propeller inflow and continuous turbulence, the root-mean-square displacements are at 0.037m for flapping and 0.012 rad for torsion.

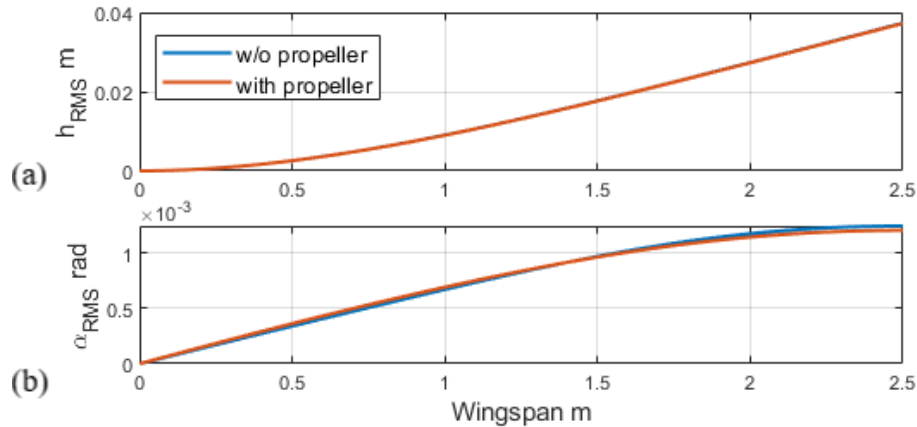


Figure 6.21: RMS displacement along wingspan: (a) flapping motion; (b) torsional motion

At 75% length, the root-mean-square displacement is around 0.03 mm. When comparing with the maximum displacement 0.04 mm from 1-cosine gust, they are at a similar level of magnitude. Maximum displacement happens in the transient response and root-mean-square describes the steady-state response. They cover the overall system behaviour under cruising condition. For the short wing/propeller system, one can expect the overall deformation to be at this scale. The overall system behaviour can then be utilised further in the design optimisation and control synthesis processes.

6.3 Conclusion

In this chapter, further exploitation of the developed aeroelastic model was carried out to demonstrate how the tool can be used when limited information about the detailed design is available and how the propeller parameters can be considered in the preliminary design stage using the low-fidelity tool developed in this project. The further exploitation and analyses were conducted

in the form of parameter studies, as well as response studies under 1-cosine gust and continuous turbulence. The parameter study is an extension of the case study presented in Section 5.4. By using models and procedures developed in the thesis, relationships between flight conditions, design parameters and structural performance are investigated. Combining results obtained and theoretical background, the variation of aircraft advancing velocity, altitude, wingspan, propeller size and propeller speed and their effects on wing deformation are discussed. As a result, aircraft advancing velocity is one of the determinative parameters for wing stiffness. Higher advancing velocity results in less stiff aero-structures, hence larger deformation. Altitude, on the other hand, changes air density and directly affects aerodynamic loadings. Higher altitude gives less aerodynamic loading, therefore smaller deformation. As for wingspan, extending the wingspan results in more flexibility, thus, larger deformation. However, wingspan is also critical for the modal behaviour. Resonance needs to be avoided in the presence of propeller periodic slipstream. In terms of propeller performances, increasing propeller size or speed directly raises propeller thrust, and changes the slipstream profile. Therefore, wing deformations in all three coordinates increase with larger propeller size and speed.

The parametric study gave some insight into the design consideration needed for any short-wing/propeller system. There are several key parameter changes that would lead to steady-state displacement increase. These key parameter changes include larger wingspan length, airspeed increase, altitude decrease, larger propeller radius and increasing propeller speed. Apart from the aeroelastic instabilities discussed in Chapter 6, extra attention is needed when designing wingspan length and propeller operational speed. Propeller operation speed is directly linked with blade passing frequency. When modal frequency is close to the blade-passing frequency, the wing structure will experience larger amplitude, which may lead to material fatigue and might significantly reduce the lifespan of the aerostructure. Therefore, the modal frequency and the blade passing frequency need to be designed to be separate from each other. This is to avoid the large deformation of the aerostructure, as well as any possibility of resonance.

On the other hand, wing deformation responses under different flight conditions were further

examined. Dynamic responses under 1-cosine gust and continuous turbulence were studied. They are common velocity inputs for aeroelastic studies for discrete gust and any irregular velocity field. For 1-cosine gust, after obtaining the dynamic responses, the variation in gust length was analysed. The transient response peaked when the gust is at 25 times of the chord length. As for continuous turbulence, a frequency domain model, previously derived in Section 4.2, is applied in conjunction with the von Kármán turbulence model. Frequency responses under continuous turbulence was obtained, as well as the root-mean-square deflection under the random turbulence field.

Chapter 7

Conclusions and Future Work

7.1 Review of initial aims and objectives

In this section, the aims and objectives described in Section 1.2 are reviewed. The main aim of this project is to model and investigate the aeroelastic behaviour associated with the short-wing propeller configuration, similar to the compound helicopter and tilt-rotor configurations. As an outcome of this project, a numerically efficient computational model has been developed for understanding modal behaviour, aeroelastic stability and dynamic responses for the short-wing/propeller configuration. In each chapter, different phases of the project have been developed and its aims and objectives, and outcomes of each chapter are reviewed as follow.

Chapter 1: Introduction and Literature Review

In Chapter 1, the research background and motivation have been introduced and potential solution frameworks have been discussed. A literature review has been carried out in the scope of basic simulation approaches used in the subject of aeroelasticity. Two- and three- dimensional aerodynamic and structural theories have been discussed for the application on the short-wing/propeller configuration, and research aims and objectives have been set.

Chapter 2: Representation of Aerodynamic Loadings

With tip-mounted propeller introducing slipstream, simplification of the inflow has been carried out. Velocity components in the aircraft advancing direction, propeller vertical and axial directions have been implemented to simulate the cruising flight condition of a compound helicopter or tilt-rotor aircraft. Accordingly, an aerodynamic model based on thin aerofoil theory has been built based on its compatibility with both 2D and 3D structures. From static to quasi-steady and unsteady aerodynamics, analytical theories have been studied and reviewed for suitability regarding the short-wing/propeller configuration. Different combinations of analytical theories in time- and frequency- domains, namely the Wagner's, the Küssner's, the Theodorsen's and the Sears' theories, have been investigated for predicting aerodynamic loadings for different purposes. The combination of Wagner's and Küssner's model has been found to be the most applicable for obtaining time-domain dynamic responses for this project. Hence, application on a simple aerofoil model has been carried out for validating its functionality and formulation in the present work.

Chapter 3: Wing Structural Representation

A short wing with flapping, torsion and lead-lag motion has been represented by a combination of the Euler-Bernoulli and the Timoshenko beam theories. The structural model is capable of considering the coupling between flapping and torsional motion, rotary inertia and shear deformation in the lead-lag motion, which have been found to contribute significantly to the structure's modal dynamics. A numerical approach based on the transfer matrix also has been developed for modal analyses. This tool requires minimal analytical derivation and is able to consider any cross-sectional variation numerically. The effect of structural coupling between flapping and torsional motion results in the introduction of coupled modes. The coupled modes, in which multiple vibration modes under one natural frequency, have been obtained through the transfer matrix method and its validity have been confirmed against FEM and analytical results from past literature.

Chapter 4: Aeroelastic Instability and Numerical Application

Aeroelastic instabilities have been investigated firstly on an aerofoil model then on a beam-like wing model. Featuring the Theodorsen's theory, on the aerofoil model, static and dynamic aeroelastic behaviour have been studied, and the 2D aeroelastic model has been validated against the Goland wing. Extending the aeroelastic model, the beam-like structural model developed in Chapter 3 has been integrated with the Theodorsen's unsteady aerodynamic model via strip theory. Incorporating coupled modes, effect of structural coupling on the aeroelastic instability have been demonstrated on the Goland wing and also briefly discussed for the short wing configuration. The static and dynamic stability boundaries for the short wing configuration have been investigated and a stable flight condition has been confirmed for performing time-domain dynamic response solutions.

Chapter 5: Dynamic Response Solution

Integrating the propeller slipstream conditions, Wagner's and Küssner's models and the beam-like wing model, a complete aeroelastic model has been developed. A numerical algorithm for the time-marching solution method and optimisation have been introduced and implemented. Solution strategies towards reliable and convergent results also have been developed. Due to the lack of published data, the functionality of the developed tool was validated against similar results in the literature. A case study featuring a short wing was performed and time domain dynamic responses under propeller inflow were obtained. Finally, the contribution of structural coupling towards dynamic responses has been analysed and discussed.

Chapter 6: Aeroelastic Model Exploitation and Further Analyses

By connecting all structural, aerodynamic and solver models developed in this thesis, an overview of the tool framework is illustrated guiding any further exploitation of the aeroelastic model. Utilising the framework, as well as the developed modular solvers, a parameter study was performed

investigating effects of wing and propeller configuration and flight conditions on the dynamic behaviour of the short-wing/propeller system. Finally, two different types of flight conditions, representing discrete gust and continuous turbulence, were studied. Fully exploiting the time-domain and frequency-domain solvers, the dynamic responses were obtained and discussed.

7.2 Conclusions

In this thesis, a computational approach has been developed for characterising aeroelastic behaviour of a short-wing/propeller configuration on small rotorcrafts. The computational approach consists of different structural and aerodynamic components and their integration. Firstly, a two-dimensional aerodynamic model has been developed based on thin aerofoil theories, including Wagner's, Küssner's, Theodorsen's and Sears' unsteady models. The combinations of those theories have been investigated for different output. The combination of Wagner's and Küssner's theories have been proven to be the most suitable for obtaining time-domain dynamic responses, which was one of the main objectives from this thesis. Theodorsen's model, formulated in the frequency domain, is better suited for instability analyses, and the Sears' model is suitable for dynamic steady-state response solutions. At the same time, propeller inflow has been simplified in the form of several velocity components in its axial and vertical directions, based on the general characteristic of propeller slipstream. Hence, the propeller effects on the wing structure have been taken into account by the two-dimensional aerodynamic model.

As for the mathematical representation of a short wing structure, beam theories have been reviewed. Considering flapping, torsion and lead-lag motion, the governing equations based on different beam theories have been derived. In order to evaluate different structural effects and form a simple, yet realistic, representation, modal analyses based on different theories have been compared. To perform efficient modal analysis, a numerical approach based on the transfer matrix method has been introduced and validated. Structural coupling between flapping and torsion has been examined with coupled modes introduced. With the aid of modal analyses results, structural

coupling, rotary inertia and shear deformation have been found to contribute significantly towards the structural modal behaviour. Hence, coupled flapping-torsion motion characterised by the Euler-Bernoulli beam theory and a separate lead-lag motion defined as a Timoshenko beam have been found to be the most appropriate.

The integration of aerodynamic and structural models allows further investigation of the aeroelastic stability boundary and the time-domain dynamic responses under forced conditions. A numerical approach has been developed featuring coupled modes, which has been proven to be more accurate compared to experimental results. Instabilities, both statically and dynamically, have been then studied and flight condition defined. To obtain solutions of aeroelastic response under a defined flight condition, solution strategy and procedures for convergence analyses have been specified. A case study on the short wing under propeller inflow has been presented and the time-domain dynamic responses have been obtained.

Integrating different models developed in previous chapters, further exploitation of the model were carried out by varying dimensional parameters and flight conditions. A core framework is developed connecting a structure model, an aerodynamic model and numerical solver into a computational strategy diagram. Through the core framework, parameter variations in structural configuration, propeller design and flight conditions were studied for their effects on the overall dynamic behaviour. Furthermore, two different types of flight condition, namely 1-cosine gust and continuous turbulence, were investigated. Utilising the same framework and the modular models developed, the responses were obtained and analysed.

7.3 Contributions

This section summarises the contributions in this thesis to knowledge in aeroelastic modelling and analyses for the short-wing/propeller configuration in small rotorcrafts. The main contributions are:

- *Propeller inflow effect simulated with two-dimensional thin aerofoil theories for aeroelas-*

ticity: The propeller inflow associated with rotorcrafts is often modelled through a three-dimensional aerodynamic model, ranging from the vortex lattice method, the panel method to the Navier-Stokes equations. In this thesis, they have been simplified into several velocity components in the axial and vertical directions, so those inflow effects on the wing can be characterised through 2D thin aerofoil theories. In the axial direction, a velocity profile has been assigned in the propeller covered area. In the vertical direction, a parabolic distribution with sinusoidal amplitude variation has been employed. These velocity component contributions have been assumed purely based on the general characteristics of the propeller slipstream. Though they are only assumed, ad-hoc distribution of the velocity profile can be input if available.

- *Combination of beam representations for short-wing structure in coupled flapping-torsion and lead-lag motion*: In this thesis, the equations of motion for a short-wing considering flapping, torsion and lead-lag motion, together with structural coupling, rotary inertia and shear deformation effects, have been derived. Each effect in motion directions has been evaluated for a realistic and efficient representation for a short wing.
- *Numerical modal analyses tool based on the transfer matrix method*: In order to evaluate the different effects, structural coupling, rotary inertia and shear deformation, a numerical modal analysis approach has been developed. Since the derivation of natural frequencies and mode shapes mainly relies on the analytical derivation in the literature, an efficient approach based on the transfer matrix method has been introduced in this thesis for computing accurate modal properties based on any beam equations of motions given. The modal analysis approach has the capability to consider any structural linear effects and cross-sectional property variations with given boundary conditions. The approach has been validated against analytical natural frequency and mode shape functions for a cantilever beam.
- *Numerical derivation and the application of coupled modes*: With the aid of the transfer matrix method, motion coupling has been numerically derived and considered in the modal

space. For motions that are coupled structurally, they are under one modal frequency with different modal shape functions. The classically considered bending or torsion mode has been treated as bending-governed or torsion-governed mode if the coupling is weak. In the case of strong coupling, the modal frequencies would be shifted, with comparable magnitude of modal shape contribution in one coupled mode. The developed numerical approach has been validated against literature results where analytical expressions and FE derived data are available.

- *Application of coupled modes in aeroelastic studies:* The coupled modes have been incorporated in the aeroelastic stability analyses and the solution for dynamic responses. The coupling effects have been further investigated in the subject of aeroelastic instability. The application of coupled modes for the flutter prediction has been proven to be more accurate based on the experimental data of the Goland wing. In dynamic responses, the application of coupled modes simplifies the solution process when compared to the one with uncoupled modes.
- *Simplified modelling and simulation for aeroelastic responses of the short-wing/propeller configuration:* With the aid of all the developed modules, namely the aerodynamic model, the beam-like structural model, the numerical modal analyses model and the aeroelastic stability model, the aeroelastic response of a short-wing under propeller inflow have been studied, capturing the very essential effects while maintaining a good numerical efficiency. A basic understanding of the scientific background of the complex aeroelastic behaviour has been formed. The developed tool is informative and beneficial especially in the early design stages for small rotorcrafts such compound helicopters and tilt-rotor aircraft.
- *Consideration of propeller configuration together with wing dynamic behaviour to aid early design decisions:* The developed model is able to study the effects of propeller dimensional as well as operational configuration on the overall wing behaviour. With numerical efficiency and reasonable computational cost, the propeller effect information is helpful in any design

decision making and optimisation process in the early stages of design.

7.4 Future work suggestions

In the research of this thesis, a simplified modelling with sufficient scope for a very complex aeroelastic problem has been given. For the application to a wider range of configurations, there are a number of possible additions and extensions of the present work, which are discussed in this section.

- *Propeller slipstream modelling*: The consideration of propeller effects is a simplified one purely based on the general characteristic of a slipstream. A separate, more accurate, aerodynamic model can be built for the detailed studies in propeller-wing interaction. In performing aeroelastic analyses, distributed aerodynamic loads can be evaluated by span-wise integration of loads given by sectional models. Three-dimensional, unsteady effects deriving from the wake vorticity hence can be taken into account through a proper wake inflow correction. Evaluation of wake inflow can be carried out through a more accurate aerodynamic tool, which will receive from the structural deformations the boundary conditions for analysis of the wing-propeller interaction.
- *Whirl Flutter*: Aeroelastic instability analyses for the short-wing/propeller system have been studied as a fixed wing and the connection between propeller and wing have been considered as rigid in this thesis. The addition of propeller would possibly create another dynamic instability phenomenon called whirl flutter, especially with the case of tilt-rotor aircraft. An investigation into the propeller connection and instability would form a fuller picture of the overall aeroelastic behaviour for short-wing/propeller configuration.
- *Beam open-section and warping*: Due to the manufacturing process and maintenance requirements, the short wing structure is not an ideal aerofoil shape in reality. In some cases, power transmission from the main rotor to the tip mounted rotors are embedded within the

wing. Sections of the wing then have been designed for giving access to the internal transmission parts. Open sections along the wing with warping effects can be taken into account in the beam-like structural model.

Bibliography

- [1] R. A. Ormiston. Revitalising advanced rotorcraft research - And the compound helicopter. *The Aeronautical Journal*, 120(1223):83–129, 2016.
- [2] I. E. Garrick. Aeroelasticity - Frontiers and beyond. *Journal of Aircraft*, 13(9):641–657, 2013.
- [3] R. H. Ricketts. Experimental Aeroelasticity - History, Status and Future in Brief. Technical report, 1990.
- [4] H. Ashley. Aeroelasticity. *Applied Mechanics Reviews*, 23:119–129, 1970.
- [5] E. Livne. Future of Airplane Aeroelasticity. *Journal of Aircraft*, 40(6):1066–1092, 2003.
- [6] P. P. Friedmann. Renaissance of Aeroelasticity and Its Future. *Journal of Aircraft*, 36(1):105–121, 1999.
- [7] I. E. Garrick and W. H. III. Reed. Historical Development of Aircraft Flutter. *Journal of Aircraft*, 18(11):897–912, 1981.
- [8] D. S. Woolston, H .L. Runyan, and R. E. Andrews. An Investigation of Effects of Certain Types of Structural NonHnearities on Wing and Control Surface Flutter. *Journal of the Aeronautical Sciences*, 24(1):57–63, 2012.
- [9] F. Afonso, J. Vale, É. Oliveira, F. Lau, and A. Suleman. A review on non-linear aeroelasticity of high aspect-ratio wings. *Progress in Aerospace Sciences*, 89(August 2016):40–57, 2017.

- [10] G. A. Flandro, H. M. McMahon, and R. L. Roach. *Basic Aerodynamics: Incompressible Flow*. Cambridge University Press, New York, 2011.
- [11] J. D. Anderson Jr. *Fundamentals of Aerodynamics*. McGraw-Hill, New York, 1991.
- [12] E. L. Houghton and P. W. Carpenter. *Aerodynamics for engineering students*. Butterworth Heinemann, Oxford, 5th edition, 1996.
- [13] A. M. Kuethe and C. Chow. *Foundations of aerodynamics: bases of aerodynamic design*. John Wiley & Sons, Inc., 5th edition, 1998.
- [14] R. L. Bisplinghoff, H. Ashley, and R. L. Halfman. *Aeroelasticity*. Addison-Wesley Publishing Company, Inc., Mineola, New York, 1983.
- [15] J. Loth and F. Loth. Induced drag reduction with wing tip mounted propellers. In *AIAA 2nd Applied Aerodynamics Conference*, page 7 pages, Seattle, Washington, 1984.
- [16] L. R. Miranda and J. E. Brennan. Aerodynamic effects of wingtip-mounted propellers and turbines. In *4th Applied Aerodynamics Conference*, pages 221–228, San Diego, California, USA, 1986.
- [17] J. Cho and J. Cho. Quasi-steady aerodynamic analysis of propeller-wing interaction. *International Journal for Numerical Methods in Fluids*, 30(8):1027–1042, 1999.
- [18] J. Cho and M. H. Williams. Propeller-wing interaction using a frequency domain panel method. *Journal of Aircraft*, 27(3):196–203, 1990.
- [19] M. H. Williams and C. C. Hwang. Three dimensional unsteady aerodynamics and aeroelastic response of advanced turboprops. *Journal of Aircraft*, 86(0846):116–124, 2013.
- [20] G. R. Benini, E. M. Belo, and F. D. Marques. Numerical model for the simulation of fixed wings aeroelastic response. *Journal of the Brazilian Society of Mechanical Sciences and Engineering*, 26(2):129–136, 2004.

- [21] S. Preidikman and D. Mook. Time-domain simulations of linear and nonlinear aeroelastic behavior. *Journal of Vibration and Control*, 6(8):1135–1175, 2000.
- [22] T. W. Strganac. *A numerical model of unsteady, subsonic aeroelastic behavior*. PhD thesis, Virginia Polytechnic Institute and State University, USA, 1987.
- [23] S. Preidikman. *Numerical simulations of interactions among aerodynamics, structural dynamics, and control systems: Bibliography*. PhD thesis, Virginia Polytechnic Institute and State University, USA, 1998.
- [24] L.L.M. Veldhuis. *Propeller wing aerodynamic interference*. PhD thesis, Delft University of Technology, 2005.
- [25] M. Dimchev. *Experimental and numerical study on wingtip mounted propellers for low aspect ratio UAV design*. Master thesis, Delft University of Technology, 2012.
- [26] D. P. Witkowski, A. K. H. Lee, and J. P. Sullivan. Aerodynamic interaction between propellers and wings. *Journal of Aircraft*, 26(9):829–836, 2008.
- [27] A. K. H. Lee. *A computational investigation of propeller-wing interaction*. PhD thesis, Purdue University, 1988.
- [28] D. Tang and E. H. Dowell. Experimental and theoretical study of gust response for high-aspect-ratio wing. *AIAA Journal*, 40(3):419–429, 2002.
- [29] M Goland. The Flutter of a Uniform Cantilever Wing. *Journal of Applied Mechanics*, 12(4):A197–A208, 1945.
- [30] W. P. Rodden and R.L. Harder. Aeroelastic Addition to NASTRAN. Technical report, 1979.
- [31] W. P. Rodden and E. H. Johnson. MSC/NASTRAN aeroelastic analysis user’s guide. Technical report, 2004.

- [32] E. C. Yates. AGARD standard aeroelastic configurations for dynamic response. Candidate configuration I.-wing 445.6. Technical report, 1987.
- [33] R. M. Bennett, C. V. Eckstrom, J. A. Rivera Jr., B. E. Dansberry, M. G. Farmer, and M. H. Durham. The benchmark aeroelastic models program: Description and highlights of initial results. Technical report, 1991.
- [34] J. Edwards, D. Schuster, C. Spain, D. Keller, and R. Moses. MAVRIC flutter model transonic limit cycle oscillation test. Technical Report May 2001, 2013.
- [35] T. M. Kier. Comparison of Unsteady Aerodynamic Modelling Methodologies with Respect to Flight Loads Analysis. In *Proceedings of the AIAA Atmospheric Flight Mechanics Conference*, page 14 pages, San Francisco, California, USA, 2005.
- [36] D. A. Peters. Two-dimensional incompressible unsteady airfoil theory-An overview. *Journal of Fluids and Structures*, 24(3):295–312, 2008.
- [37] H. Wagner. Über die Entstehung des dynamischen Auftriebes von Tragflügeln. (About the Development of Dynamic Lift of Wings). *Zeitschrift für Angewandte Mathematik und Mechanik*, 5(1):17–35, 1925.
- [38] H. G. Küssner. Beanspruchung von Flugzeugflügeln durch Boen. *Zeitschrift für Flugtechnik und Motorluftschiffahrt*, 22(19):579–586, 1931.
- [39] H. G. Küssner. Zusammenfassender Bericht über den instationären Auftrieb von Flügeln. (Summary Report about the Unsteady Lift of Wings). *Luftfahrt-Forschung*, 13(12):410–424, 1936.
- [40] T. Theodorsen. General theory of aerodynamic instability and the mechanism of flutter. Technical report, 1935.
- [41] T. von Karman. Airfoil Theory for Non-Uniform Motion. *Journal of the Aeronautical Sciences*, 5(10):379–390, 1938.

- [42] W. R. Sears and B. Sparks. On the reaction of an elastic wing to vertical gusts. *Journal of the Aeronautical Sciences*, 9(2):64–67, 1941.
- [43] M. H. Kargarnovin and A. Mamandi. Aeroelastic response for pure plunging motion of a typical section due to sharp edged gust, using Jones approximation aerodynamics. *World Academy of Science, Engineering and Technology*, 36:154–161, 2007.
- [44] S. Fichera, S. Jiffri, X. Wei, A. Da Ronch, N. Tantaroudas, and J. E. Mottershead. Experimental and numerical study of nonlinear dynamic behaviour of an aerofoil. In *Proceedings of the International Conference on Noise and Vibration Engineering ISMA 2014*, pages 3609–3618, Leuven, Belgium, 2014.
- [45] T. W. Strganac and D. T. Mook. Numerical model of unsteady subsonic aeroelastic behavior. *AIAA Journal*, 28(5):903–909, 1990.
- [46] T. O’Neil, H. Gilliatt, and T. W. Strganac. Investigations of aeroelastic response for a system with continuous structural nonlinearities. In *37th Structure, Structural Dynamics and Materials Conference*, page 9 pages, Salt Lake City, UT, U.S.A, 1996.
- [47] P. Marzocca, L. Librescu, D. Kim, and I. Lee. Linear/Nonlinear Unsteady Aerodynamic Modeling of 2-D Lifting Surfaces via a Combined CFD/Analytical Approach. In *44th AIAA/ASME/ASCE/AHS Structures, Structural Dynamics, and Materials Conference*, page 11 pages, Norfolk, Virginia, 2012.
- [48] P. Marzocca, L. Librescu, and G. Chiocchia. Aeroelastic response of 2-D lifting surfaces to gust and arbitrary explosive loading signatures. *International Journal of Impact Engineering*, 25(1):41–65, 2001.
- [49] S. Shams, H. Haddadpour, M. H. Sadr Lahidjani, and M. Kheiri. An Analytical Method in Computational Aeroelasticity Based on Wagner Function. In *25th International Congress of the Aeronautical Science*, page 9 pages, Hamburg, Germany, 2006.

- [50] M. Berci, P. H. Gaskell, R. W. Hewson, and V. V. Toropov. A semi-analytical model for the combined aeroelastic behaviour and gust response of a flexible aerofoil. *Journal of Fluids and Structures*, 38:3–21, 2013.
- [51] R. Kurniawan. Numerical study of flutter of a two-dimensional aeroelastic system. *ISRN Mechanical Engineering*, 2013(1):4 pages, 2013.
- [52] D. H. Hodges and G. A. Pierce. *Introduction to Structural Dynamics and Aeroelasticity*. Cambridge University Press, New York, 2nd edition, 2011.
- [53] C. Howcroft, R. Cook, D. Calderon, L. Lambert, M. Castellani, J. E. Cooper, M. H. Lowenberg, S. A. Neild, and E. Coetzee. Aeroelastic Modelling of Highly Flexible Wings. In *15th Dynamics Specialists Conference*, number January, page 26 pages, San Diego, California, USA, 2016.
- [54] C. Howcroft, S. A. Neild, M. H. Lowenberg, and J. E. Cooper. Efficient aeroelastic beam modelling and the selection of a structural shape basis. *International Journal of Non-Linear Mechanics*, 112:73–84, 2019.
- [55] O. Stodieck, J. E. Cooper, S. A. Neild, M. H. Lowenberg, and L. Iorga. Slender-wing beam reduction method for gradient-based aeroelastic design optimization. *AIAA Journal*, 56(11):4529–4545, 2018.
- [56] G. Frulla, E. Cestino, and P. Marzocca. Critical behaviour of slender wing configurations. *Proceedings of the Institution of Mechanical Engineers, Part G: Journal of Aerospace Engineering*, 224(5):587–600, 2010.
- [57] S. Shams, M. H. Sadr Lahidjani, and H. Haddadpour. Nonlinear aeroelastic response of slender wings based on Wagner function. *Thin-Walled Structures*, 46(11):1192–1203, 2008.

- [58] B. Ghadiri and M. Razi. Limit cycle oscillations of rectangular cantilever wings containing cubic nonlinearity in an incompressible flow. *Journal of Fluids and Structures*, 23(4):665–680, 2007.
- [59] M. Berci and R. Cavallaro. A Hybrid Reduced-Order Model for the Aeroelastic Analysis of Flexible Subsonic Wings—A Parametric Assessment. *Aerospace*, 5(3):23 pages, 2018.
- [60] D. H. Hodges and R. A. Ormiston. Stability of elastic bending and torsion of uniform cantilever rotor blades in hover with variable structural coupling. Technical report, NASA, 1976.
- [61] D. H. Hodges and E. H. Dowell. Nonlinear equations of motion for the elastic bending and torsion of twisted nonuniform rotor blades. Technical report, NASA, 1974.
- [62] P. P. Friedmann. Formulation and Solution of Rotary-Wing Aeroelastic Stability and Response Problems. In *8th European Rotorcraft Forum*, page 58 pages, Aix-En-Provence, France, 1982.
- [63] Z. Qin, P. Marzocca, and L. Librescu. Aeroelastic instability and response of advanced aircraft wings at subsonic flight speeds. *Aerospace Science and Technology*, 6(3):195–208, 2002.
- [64] Z. Qin and L. Librescu. Dynamic Aeroelastic Response of Aircraft Wings Modeled as Anisotropic Thin-Walled Beams. *Journal of Aircraft*, 40(3):532–543, 2003.
- [65] M. J. Patil. Nonlinear Gust Response of Highly Flexible Aircraft. In *48th AIAA/ASME/ASCE/AHS/ASC Structures, Structural Dynamics, and Materials Conference*, pages 456–468, Honolulu, Hawaii, 2007.
- [66] A. Arena, W. Lacarbonara, and P. Marzocca. Nonlinear Aeroelastic Formulation and Post-flutter Analysis of Flexible High-Aspect-Ratio Wings. *Journal of Aircraft*, 50(6):1748–1764, 2013.

- [67] M. Nejati, S. Shokrollahi, and S. Shams. Nonlinear aeroelastic analysis of high-aspect-ratio wings using indicial aerodynamics. *Journal of the Brazilian Society of Mechanical Sciences and Engineering*, 40(6):298, 2018.
- [68] M. Goland and Y. L. Luke. The Flutter of a Uniform Wing with Tip Weights. *Journal of Applied Mechanics*, 15(3):13–20, 1948.
- [69] W. T. Feldt and G. Herrmann. Bending-torsional flutter of a cantilevered wing containing a tip mass and subjected to a transverse follower force. *Journal of the Franklin Institute*, 297(6):467–478, 1974.
- [70] F. H. Gern and L. Librescu. Effects of externally mounted stores on aeroelasticity of advanced swept cantilevered aircraft wings. *Aerospace Science and Technology*, 2(5):321–333, 1998.
- [71] S. A. Fazelzadeh, A. Mazidi, and H. Kalantari. Bending-torsional flutter of wings with an attached mass subjected to a follower force. *Journal of Sound and Vibration*, 323:148–162, 2009.
- [72] A. Mazidi, H. Kalantari, and S. A. Fazelzadeh. Aeroelastic response of an aircraft wing with mounted engine subjected to time-dependent thrust. *Journal of Fluids and Structures*, 39:292–305, 2013.
- [73] Y. Xu, D. Cao, H. Lin, and C. Shao. An alternative simulation approach for the ONERA aerodynamic model and its application in the nonlinear aeroelastic analysis of slender wings with pylon-store system. *International Journal of Non-Linear Mechanics*, 105(July):55–76, 2018.
- [74] Y. Xu, D. Cao, C. Shao, and H. Lin. Effects of Externally Mounted Store on the Non-linear Response of Slender Wings. *Journal of Computational and Nonlinear Dynamics*, 13(4):041003, 2018.

- [75] Y. Xu, D. Cao, C. Shao, and H. Lin. Nonlinear Responses of a Slender Wing With a Store. *Journal of Vibration and Acoustics*, 141(3):031006, 2019.
- [76] L. A. Parnell. Flutter analysis of low aspect ratio wings. In *COSMIC 14th NASTRAN (R) Users' Colloquium*, pages 247–263, 1986.
- [77] S. Shokrollahi. Aeroelastic analyses of low aspect ratio wings based on non-classic plate theory including transverse shear deformation and rotary inertia. In *Proceedings of ISMA2006: International Conference on Noise and Vibration Engineering*, pages 3805–3816, Heverlee, Belgium, 2006.
- [78] M. Gennaretti, M. M. Colella, and G. Bernardini. Prediction of Tiltrotor Vibratory Loads with Inclusion of Wing-Proprotor Aerodynamic Interaction. *Journal of Aircraft*, 47(1):71–79, 2010.
- [79] K. Ferguson. *Towards a better understanding of the flight mechanics of compound helicopter configurations*. PhD thesis, University of Glasgow, 2015.
- [80] K. Ferguson and D. Thomson. Flight Dynamics Investigation of Compound Helicopter Configurations. *Journal of Aircraft*, 52(1):156–167, 2015.
- [81] Y Tanabe and H Sugawara. Aerodynamic validation of rFlow3D code with UH-60A data including high advance ratios. In *41st European Rotorcraft Forum*, page 9 pages, Munich Germany, 2015.
- [82] J. G. Leishman. *Principles of Helicopter Aerodynamics*. Cambridge University Press, New York, 2nd edition, 2006.
- [83] H. Haddadpour and R. D. Firouz-Abadi. Evaluation of quasi-steady aerodynamic modeling for flutter prediction of aircraft wings in incompressible flow. *Thin-Walled Structures*, 44(9):931–936, 2006.

- [84] Y. C. Fung. *An Introduction to the Theory of Aeroelasticity*. Dover Publications, Inc., New York, 1955.
- [85] R. T. Jones. Operational treatment of the nonuniform-lift theory in airplane dynamics. Technical report, NACA, 1938.
- [86] R. T. Jones. The unsteady lift of a wing of finite aspect ratio. Technical report, NACA, 1940.
- [87] A. E. Jr. Lombard. *An investigation of the conditions for the occurrence of flutter in aircraft, and, the development of criteria for the prediction and elimination of such flutter*. PhD thesis, California Institute of Technology, 1938.
- [88] N. M. Newmark. A Method of Computation for Structural Dynamics. *Journal of the Engineering Mechanics Division: Proceedings of the ASCE*, 85(3):67–94, 1959.
- [89] J. C. Houbolt and G. W. Brooks. Differential equations of motion for combined flapwise bending, chordwise bending, and torsion of twisted nonuniform rotor blades. Technical report, 1958.
- [90] J. R. Banerjee and H. Su. Free Transverse and Lateral Vibration of Beams with Torsional Coupling. *Journal of Aerospace Engineering*, 19(1):13–20, 2006.
- [91] S. P. Timoshenko. On the correction for shear of the differential equation for transverse vibrations of prismatic bars. *Philosophical Magazine*, 41(245):744–746, 1921.
- [92] S.P. Timoshenko. On the transverse vibrations of bars of uniform cross-section. *The London, Edinburgh, and Dublin Philosophical Magazine and Journal of Science*, 43(253):125–131, 1922.
- [93] W. C. Young and R. Plunkett. *Roark's Formulas for Stress and Strain*. McGraw-Hill, New York, 7th edition, 2002.

- [94] F. S. Tse, I. E. Morse, and R. T. Hinkle. *Mechanical Vibrations: Theory and Application*. Allyn & Bacon, 2nd edition, 1978.
- [95] S. S. Rao. *Vibration of Continuous Systems*. John Wiley & Sons, Inc., Hoboken, New Jersey, 2007.
- [96] J. R. Banerjee. Explicit frequency equation and mode shapes of a cantilever beam coupled in bending and torsion. *Journal of Sound and Vibration*, 224(2):267–281, 1999.
- [97] J. R. Banerjee. Explicit Modal Analysis of an Axially Loaded Timoshenko Beam With Bending-Torsion Coupling. *Journal of Applied Mechanics*, 67(2):307–313, 2000.
- [98] The MathWorks Inc. MATLAB. <http://www.mathworks.co.uk>, 2019. [Online; accessed 17-Jun-2019].
- [99] GNU Octave. <http://www.octave.org>, 2019. [Online; accessed 17-Jun-2019].
- [100] Scilab. <http://www.scilab.org>, 2019. [Online; accessed 17-Jun-2019].
- [101] A. N. Bercin and M. Tanaka. Coupled flexural-torsional vibrations of Timoshenko beams. *Journal of Sound and Vibration*, 207(1):47–59, 1997.
- [102] J. R. Wright and J. E. Cooper. *Introduction to Aircraft Aeroelasticity and Loads*. John Wiley & Sons, Ltd., 2nd edition, 2015.
- [103] NASA. U.S. Standard Atmosphere. Technical report, NASA, Washington, DC, USA, 1976.
- [104] I. Wang. *Component Modal Analysis of a Folding Wing*. PhD thesis, Duke University, 2011.
- [105] J. R. Banerjee. Flutter sensitivity studies of high aspect ratio aircraft wings. *WIT Transactions on The Built Environment*, 2:374–387, 1970.
- [106] Z. Sotoudeh, D. H. Hodges, and C. Chang. Validation Studies for Aeroelastic Trim and Stability of Highly Flexible Aircraft. *Journal of Aircraft*, 47(4):1240–1247, 2010.

- [107] Cécile Vion-Lanctuit. Flight testing of Eurocopter's X3 high-speed hybrid helicopter demonstrator marks a new milestone in the company's innovation roadmap, 2010.
- [108] Jason Paul. X3 Helicopter Sets Speed Record At Nearly 300 MPH, 2013.
- [109] John Croft. HELI-EXPO 2009: Rolls-Royce confirms role in Eurocopter X3 programme, 2009.
- [110] T. von Karman and L. Howarth. On the Statistical Theory of Isotropic Turbulence. *Proceedings of the Royal Society of London. Series A, Mathematical and Physical Sciences*, 164(917):192–215, 1938.
- [111] T. von Karman. Progress in the Statistical Theory of Turbulence. *Proceedings of the National Academy of Sciences*, 34(11):530–539, 1948.

Appendix A

Recursive Algorithm Derivation

In this chapter, the derivation of parameter X for the recursive algorithm is presented below.

$$\begin{aligned} X(\tau + \Delta\tau) &= A_1 \int_0^{\tau + \Delta\tau} \dot{\alpha}_{AoA} e^{-b_1(\tau + \Delta\tau - \tau_0)} d\tau \\ &= A_1 e^{-b_1 \Delta\tau} \int_0^{\tau} \dot{\alpha}_{AoA} e^{-b_1(\tau - \tau_0)} d\tau + A_1 \int_{\tau}^{\tau + \Delta\tau} \dot{\alpha}_{AoA} e^{-b_1(\tau + \Delta\tau - \tau_0)} d\tau \\ &= e^{-b_1 \Delta\tau} X(\tau) + A_1 e^{-b_1(\tau + \Delta\tau)} \int_{\tau}^{\tau + \Delta\tau} \dot{\alpha}_{AoA} e^{b_1 \tau_0} d\tau_0 \\ &= e^{-b_1 \Delta\tau} X(\tau) + A_1 e^{-b_1(\tau + \Delta\tau)} \dot{\alpha}_{AoA}(\tau) \frac{e^{b_1(\tau + \Delta\tau)} - e^{b_1(\tau)}}{b_1} \\ &= e^{-b_1 \Delta\tau} X(\tau) + A_1 \frac{1 - e^{-b_1 \Delta\tau}}{b_1} \dot{\alpha}_{AoA}(\tau) \end{aligned}$$

Appendix B

EoMs Derivation Based on Timoshenko

Beam

$$\begin{aligned} KE &= \frac{1}{2} \int_0^l \left[m \left(\frac{\partial h}{\partial t} - \frac{S_a}{m} \cos \theta \frac{\partial \alpha}{\partial t} \right)^2 + \rho_w I_y \left(\frac{\partial \varphi_y}{\partial t} \right)^2 \right. \\ &\quad \left. + m \left(\frac{\partial v}{\partial t} - \frac{S_a}{m} \sin \theta \frac{\partial \alpha}{\partial t} \right)^2 + \rho_w I_z \left(\frac{\partial \varphi_z}{\partial t} \right)^2 + I_{GC} \left(\frac{\partial \alpha}{\partial t} \right)^2 \right] dx \\ PE &= \frac{1}{2} \int_0^l \left[EI_y \left(\frac{\partial \varphi_y}{\partial x} \right)^2 + \kappa_y GA \left(\frac{\partial h}{\partial x} \cos \theta + \frac{\partial v}{\partial x} \sin \theta - \varphi_y \right)^2 \right. \\ &\quad \left. + EI_z \left(\frac{\partial \varphi_z}{\partial x} \right)^2 + \kappa_z GA \left(\frac{\partial v}{\partial x} \cos \theta - \frac{\partial h}{\partial x} \sin \theta - \varphi_z \right)^2 + GJ \left(\frac{\partial \alpha}{\partial x} \right)^2 \right] dx \\ \int_{t_1}^{t_2} \delta W dt &= \int_{t_1}^{t_2} \int_0^L (L_h \delta h + L_v \delta v + M_\alpha \delta \alpha) dx dt. \end{aligned} \tag{B.1}$$

$$\begin{aligned}
\int_{t_1}^{t_2} \delta K E dt &= \int_{t_1}^{t_2} \int_0^l \left[m \left(\frac{\partial h}{\partial t} - \frac{S_a}{m} \cos \theta \frac{\partial \alpha}{\partial t} \right) \delta \frac{\partial h}{\partial t} + \rho_w I_y \frac{\partial \varphi_y}{\partial t} \delta \frac{\partial \varphi_y}{\partial t} \right. \\
&\quad + m \left(\frac{\partial v}{\partial t} - \frac{S_a}{m} \sin \theta \frac{\partial \alpha}{\partial t} \right) \delta \frac{\partial v}{\partial t} + \rho_w I_z \frac{\partial \varphi_z}{\partial t} \delta \frac{\partial \varphi_z}{\partial t} \\
&\quad + m \left(\frac{\partial h}{\partial t} - \frac{S_a}{m} \cos \theta \frac{\partial \alpha}{\partial t} \right) \left(-\frac{S_\alpha}{m} \cos \theta \right) \delta \frac{\partial \alpha}{\partial t} \\
&\quad \left. + m \left(\frac{\partial v}{\partial t} - \frac{S_a}{m} \sin \theta \frac{\partial \alpha}{\partial t} \right) \left(-\frac{S_\alpha}{m} \sin \theta \right) \delta \frac{\partial v}{\partial t} + I_{GC} \left(\frac{\partial \alpha}{\partial t} \right) \delta \frac{\partial \alpha}{\partial t} \right] dx dt \\
&= \int_0^l \int_{t_1}^{t_2} \left[m \left(\frac{\partial h}{\partial t} - \frac{S_a}{m} \cos \theta \frac{\partial \alpha}{\partial t} \right) \frac{\partial}{\partial t} (\delta h) + \rho_w I_y \frac{\partial \varphi_y}{\partial t} \frac{\partial}{\partial t} (\delta \varphi_y) \right. \\
&\quad + m \left(\frac{\partial v}{\partial t} - \frac{S_a}{m} \sin \theta \frac{\partial \alpha}{\partial t} \right) \frac{\partial}{\partial t} (\delta v) + \rho_w I_z \frac{\partial \varphi_z}{\partial t} \frac{\partial}{\partial t} (\delta \varphi_z) \\
&\quad \left. + \left(-S_\alpha \cos \theta \frac{\partial h}{\partial t} - S_\alpha \sin \theta \frac{\partial v}{\partial t} + \frac{S_\alpha^2}{m} \frac{\partial \alpha}{\partial t} + I_{GC} \frac{\partial \alpha}{\partial t} \right) \frac{\partial}{\partial t} (\delta \alpha) \right] dx dt.
\end{aligned} \tag{B.2}$$

Integration by part,

$$\begin{aligned}
\int_{t_1}^{t_2} \delta K E dt &= \int_0^l \left[m \left(\frac{\partial h}{\partial t} - \frac{S_a}{m} \cos \theta \frac{\partial \alpha}{\partial t} \right) \delta h \right]_{t_1}^{t_2} + \left[\rho_w I_y \frac{\partial \varphi_y}{\partial t} \delta \varphi_y \right]_{t_1}^{t_2} \\
&\quad + \left[m \left(\frac{\partial v}{\partial t} - \frac{S_a}{m} \sin \theta \frac{\partial \alpha}{\partial t} \right) \delta v \right]_{t_1}^{t_2} + \left[\rho_w I_z \frac{\partial \varphi_z}{\partial t} \delta \varphi_z \right]_{t_1}^{t_2} \\
&\quad + \left[\left(-S_\alpha \cos \theta \frac{\partial h}{\partial t} - S_\alpha \sin \theta \frac{\partial v}{\partial t} + I_\alpha \frac{\partial \alpha}{\partial t} \right) \delta \alpha \right]_{t_1}^{t_2} dx \\
&\quad - \int_0^l \int_{t_1}^{t_2} \left[m \left(\frac{\partial^2 h}{\partial t^2} - \frac{S_a}{m} \cos \theta \frac{\partial^2 \alpha}{\partial t^2} \right) \delta h + \rho_w I_y \frac{\partial^2 \varphi_y}{\partial t^2} \delta \varphi_y \right. \\
&\quad + m \left(\frac{\partial^2 v}{\partial t^2} - \frac{S_a}{m} \sin \theta \frac{\partial^2 \alpha}{\partial t^2} \right) \delta v + \rho_w I_z \frac{\partial^2 \varphi_z}{\partial t^2} \delta \varphi_z \\
&\quad \left. + \left(-S_\alpha \cos \theta \frac{\partial^2 h}{\partial t^2} - S_\alpha \sin \theta \frac{\partial^2 v}{\partial t^2} + I_\alpha \frac{\partial^2 \alpha}{\partial t^2} \right) \delta \alpha \right] dx dt.
\end{aligned} \tag{B.3}$$

Underlined terms goes to zero,

$$\begin{aligned}
\int_{t_1}^{t_2} \delta PE dt = \int_{t_1}^{t_2} \int_0^l & \left[\kappa_y GA \left(\frac{\partial h}{\partial x} \cos \theta + \frac{\partial v}{\partial x} \sin \theta - \varphi_y \right) \cos \theta \delta \frac{\partial h}{\partial x} \right. \\
& - \kappa_z GA \left(\frac{\partial v}{\partial x} \cos \theta - \frac{\partial h}{\partial x} \sin \theta - \varphi_z \right) \sin \theta \delta \frac{\partial h}{\partial x} + EI_y \frac{\partial \varphi_y}{\partial x} \delta \frac{\partial \varphi_y}{\partial x} \\
& - \kappa_y GA \left(\frac{\partial h}{\partial x} \cos \theta + \frac{\partial v}{\partial x} \sin \theta - \varphi_y \right) \delta \varphi_y \\
& + \kappa_y GA \left(\frac{\partial h}{\partial x} \cos \theta + \frac{\partial v}{\partial x} \sin \theta - \varphi_y \right) \sin \theta \delta \frac{\partial v}{\partial x} \\
& + \kappa_z GA \left(\frac{\partial v}{\partial x} \cos \theta - \frac{\partial h}{\partial x} \sin \theta - \varphi_z \right) \cos \theta \delta \frac{\partial v}{\partial x} + EI_z \frac{\partial \varphi_z}{\partial x} \delta \frac{\partial \varphi_z}{\partial x} \\
& \left. - \kappa_z GA \left(\frac{\partial v}{\partial x} \cos \theta - \frac{\partial h}{\partial x} \sin \theta - \varphi_z \right) \delta \varphi_z + GJ \frac{\partial \alpha}{\partial x} \delta \frac{\partial \alpha}{\partial x} \right] dx dt.
\end{aligned} \tag{B.4}$$

$$\begin{aligned}
\mathcal{K}_h &= (\kappa_y GA + (\kappa_z - \kappa_y) GA \sin^2 \theta) \frac{\partial h}{\partial x} - \frac{(\kappa_z - \kappa_y) GA}{2} \sin 2\theta \frac{\partial v}{\partial x} - \kappa_y GA \cos \theta \varphi_y + \kappa_z GA \sin \theta \varphi_z \\
\mathcal{K}_v &= (\kappa_z GA - (\kappa_z - \kappa_y) GA \sin^2 \theta) \frac{\partial v}{\partial x} - \frac{(\kappa_z - \kappa_y) GA}{2} \sin 2\theta \frac{\partial h}{\partial x} - \kappa_y GA \sin \theta \varphi_y - \kappa_z GA \cos \theta \varphi_z.
\end{aligned} \tag{B.5}$$

$$\begin{aligned}
\int_{t_1}^{t_2} \delta PE dt = \int_{t_1}^{t_2} \int_0^l & \left[\mathcal{K}_h \frac{\partial}{\partial x} (\delta h) + EI_y \frac{\partial \varphi_y}{\partial x} \frac{\partial}{\partial x} (\delta \varphi_y) - \kappa_y GA \left(\frac{\partial h}{\partial x} \cos \theta + \frac{\partial v}{\partial x} \sin \theta - \varphi_y \right) \delta \varphi_y \right. \\
& \mathcal{K}_v \frac{\partial}{\partial x} (\delta v) + EI_z \frac{\partial \varphi_z}{\partial x} \frac{\partial}{\partial x} (\delta \varphi_z) - \kappa_z GA \left(\frac{\partial v}{\partial x} \cos \theta - \frac{\partial h}{\partial x} \sin \theta - \varphi_z \right) \delta \varphi_z \\
& \left. + GJ \frac{\partial \alpha}{\partial x} \frac{\partial}{\partial x} (\delta \alpha) \right] dx dt.
\end{aligned} \tag{B.6}$$

Integration by part,

$$\begin{aligned}
\int_{t_1}^{t_2} \delta P E dt &= \int_{t_1}^{t_2} \left[\mathcal{K}_h \delta h \right]_0^L + \left[EI_y \frac{\partial \varphi_y}{\partial x} \delta \varphi_y \right]_0^L + \left[\mathcal{K}_v \delta v \right]_0^L + \left[EI_z \frac{\partial \varphi_z}{\partial x} \delta \varphi_z \right]_0^L + \left[GJ \frac{\partial \alpha}{\partial x} \delta \alpha \right]_0^L dt \\
&\quad - \int_{t_1}^{t_2} \int_0^l \left[\frac{\partial \mathcal{K}_h}{\partial x} \delta h + \frac{\partial}{\partial x} \left(EI_y \frac{\partial \varphi_y}{\partial x} \right) \delta \varphi_y + \kappa_y GA \left(\frac{\partial h}{\partial x} \cos \theta + \frac{\partial v}{\partial x} \sin \theta - \varphi_y \right) \delta \varphi_y \right. \\
&\quad \quad \quad \left. \frac{\partial \mathcal{K}_v}{\partial x} \delta v + \frac{\partial}{\partial x} \left(EI_z \frac{\partial \varphi_z}{\partial x} \right) \delta \varphi_z + \kappa_z GA \left(\frac{\partial v}{\partial x} \cos \theta - \frac{\partial h}{\partial x} \sin \theta - \varphi_z \right) \delta \varphi_z \right. \\
&\quad \quad \quad \left. + \frac{\partial}{\partial x} \left(GJ \frac{\partial \alpha}{\partial x} \right) \delta \alpha \right] dx dt.
\end{aligned} \tag{B.7}$$

Underlined terms goes to zero according to the boundary conditions,

$$\begin{aligned}
\text{For } \delta h & \quad m \frac{\partial^2 h}{\partial t^2} - S_\alpha \cos \theta \frac{\partial^2 \alpha}{\partial t^2} - \frac{\partial \mathcal{K}_h}{\partial x} = L_h \\
\text{For } \delta \varphi_y & \quad \rho_w I_y \frac{\partial^2 \varphi_y}{\partial t^2} - \frac{\partial}{\partial x} \left(EI_y \frac{\partial \varphi_y}{\partial x} \right) - \kappa_y GA \left(\cos \theta \frac{\partial h}{\partial x} + \sin \theta \frac{\partial v}{\partial x} - \varphi_y \right) = 0 \\
\text{For } \delta v & \quad m \frac{\partial^2 v}{\partial t^2} - S_\alpha \sin \theta \frac{\partial^2 \alpha}{\partial t^2} - \frac{\partial \mathcal{K}_v}{\partial x} = L_v \\
\text{For } \delta \varphi_z & \quad \rho_w I_z \frac{\partial^2 \varphi_z}{\partial t^2} - \frac{\partial}{\partial x} \left(EI_z \frac{\partial \varphi_z}{\partial x} \right) - \kappa_z GA \left(\cos \theta \frac{\partial v}{\partial x} - \sin \theta \frac{\partial h}{\partial x} - \varphi_z \right) = 0 \\
\text{For } \delta \alpha & \quad I_\alpha \frac{\partial^2 \alpha}{\partial t^2} - S_\alpha \cos \theta \frac{\partial^2 h}{\partial t^2} - S_\alpha \sin \theta \frac{\partial^2 v}{\partial t^2} - \frac{\partial}{\partial x} (GJ \frac{\partial \alpha}{\partial x}) = M_\alpha.
\end{aligned} \tag{B.8}$$

Appendix C

Parameter Definition and Validation

Having a NACA0012 shape, a 10mm thickness and flanges located at the 15% and 75% of the chord. The wing cross-section is considered as a box section illustrated as Figure C.1. The cross-sectional properties are calculated based on the hatched box section via NASTRAN beam tool and listed in Table C.1.

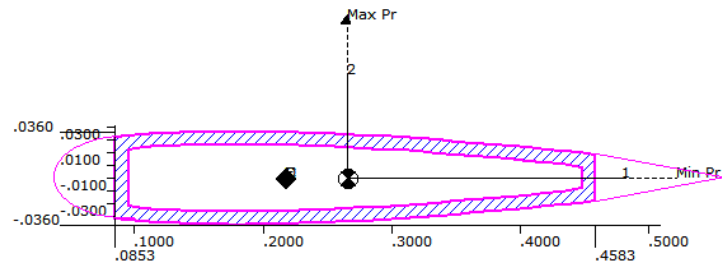


Figure C.1: Wing-box cross-section

Torsion behaviour in a shaft/beam structure can be characterised analytically when knowing the moment applied, beam length and torsional stiffness. Therefore, when applying a unit moment onto a beam of unit length, torsional stiffness can be obtained by measuring torsional displacement at the tip. The described case can be modelled in Abaqus to validate torsional stiffness calculated by NASTRAN.

Modelled with shell elements, boundary constraints are applied to the gravitational centre. As

Table C.1: Cross-sectional properties output from NASTRAN

| | | | |
|---------------------------------------|--------------------------|----------------------------------|--------------------------|
| Shear centre distance to leading edge | 0.217 m | Second moment of area (I_z) | 1.0745e-4 m ⁴ |
| Gravitational centre to leading edge | 0.266 m | Torsional constant (J) | 1.8063e-5 m ⁴ |
| Area (A) | 0.00812 m ² | Shear coefficient (κ_h) | 0.80 |
| Second moment of area (I_y) | 5.2862e-6 m ⁴ | Shear coefficient (κ_v) | 0.05 |

shown in Figure C.2, torsional displacement at the tip can be measured.

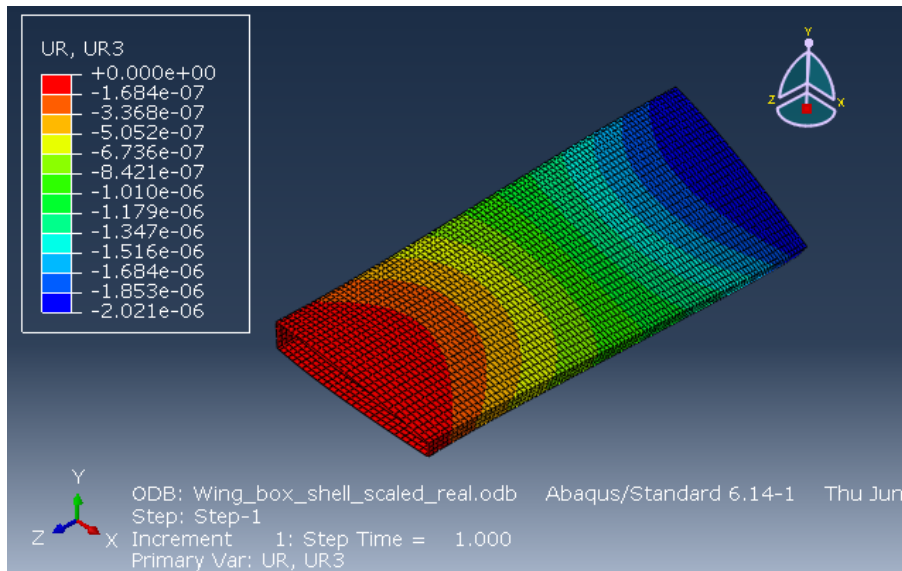


Figure C.2: Abaqus visualisation for rotational displacement in z direction

| | Torsional displacement | | Torsional stiffness | | Torsional constant |
|--------------|------------------------|---|--------------------------|---|--------------------------|
| NASTRAN | 2.086e-6 rad | ⇐ | 4.7936e5 Nm ² | ⇐ | 1.8063e-5 m ⁴ |
| Abaqus | 2.021e-6 rad | ⇒ | 4.9480e5 Nm ² | ⇒ | 1.8645e-5 m ⁴ |
| % Difference | 3.12% | | 3.22% | | 3.22% |

Appendix D

Numerical Modal Analysis Process

D.1 Lead-lag Motion

First of all, simple harmonic motions are assigned to the coordinates of interest. The assumption is written as

$$\begin{Bmatrix} \nu(x, t) \\ \varphi_x(x, t) \end{Bmatrix} = \begin{Bmatrix} \zeta(x) \\ \phi_z(x) \end{Bmatrix} e^{i\omega t} \quad (\text{D.1})$$

Substitute into the lead-lag equation of motions, it writes

$$\begin{aligned} -mb\omega^2\zeta - \kappa_z GA(b\zeta'' - \phi'_z) &= 0 \\ -\rho_w I_z \omega^2 \phi_z - EI_z \phi''_z - \kappa_z GA(b\zeta' - \phi_z) &= 0 \end{aligned} \quad (\text{D.2})$$

Rearrange it into a state-space form, the equation is defined as

$$\mathbf{z}'(x) = \mathbf{A}\mathbf{z}(x) \quad (\text{D.3})$$

In which

$$\mathbf{z} = \begin{Bmatrix} \zeta \\ \zeta' \\ \phi_z \\ \phi'_z \end{Bmatrix} \quad \text{and} \quad \mathbf{A} = \begin{bmatrix} 0 & 1 & 0 & 0 \\ \frac{-m\omega^2}{\kappa_z GA} & 0 & 0 & \frac{1}{b} \\ 0 & 0 & 0 & 1 \\ 0 & \frac{-\kappa_z GA b}{EI_z} & \frac{\kappa_z GA - \rho_w I_z \omega^2}{EI_z} & 0 \end{bmatrix}$$

Hence, the state vector $\mathbf{z}(x)$ at any point of the beam can be obtained by the matrix exponential as

$$\mathbf{z}(x) = e^{\mathbf{A}x}\mathbf{z}(0) \quad (\text{D.4})$$

Since boundary conditions are defined via shear forces, bending moment and torque, the state vector \mathbf{z} can be corrected as

$$\hat{\mathbf{z}}(x) = \mathbf{D}\mathbf{z}(x) \quad (\text{D.5})$$

In which

$$\hat{\mathbf{z}} = \begin{Bmatrix} \zeta \\ S_v \\ \phi_z \\ M_z \end{Bmatrix} \quad \text{and} \quad \mathbf{D} = \begin{bmatrix} 1 & 0 & 0 & 0 \\ 0 & \kappa_z GA b & -\kappa_z GA & 0 \\ 0 & 0 & 1 & 0 \\ 0 & 0 & 0 & -EI_z \end{bmatrix}$$

For a cantilever beam, the clamped end is constrained so that there is zero displacement and zero shear deformation. While for the free end, there is no bending moment or shear force. Hence, the boundary condition can be written as

$$\hat{\mathbf{z}}(0) = \left\{ 0 \quad S_v(0) \quad 0 \quad M_z(0) \right\}^T \quad \hat{\mathbf{z}}(L) = \left\{ \zeta(L) \quad 0 \quad \phi_z(L) \quad 0 \right\}^T \quad (\text{D.6})$$

Combining all above, the governing equations can be written as a homogeneous equation as

$$\begin{Bmatrix} 0 \\ 0 \end{Bmatrix} = \mathbf{T}\mathbf{D}e^{\mathbf{A}L}\mathbf{D}^{-1}\mathbf{R} \begin{Bmatrix} S_v(0) \\ M_z(0) \end{Bmatrix} \quad \text{where} \quad \mathbf{T} = \begin{bmatrix} 0 & 1 & 0 & 0 \\ 0 & 0 & 0 & 1 \end{bmatrix}; \quad \mathbf{R} = \mathbf{T}' \quad (\text{D.7})$$

D.2 Coupled Euler-Bernoulli beam flapping and torsion

First of all, simple harmonic motions are assigned to the coordinates of interest. Since the idea is to derive coupled mode shapes within one harmonic mode, the assumption is written as

$$\begin{Bmatrix} \xi(x, t) \\ \alpha(x, t) \end{Bmatrix} = \begin{Bmatrix} \vartheta(x) \\ \eta(x) \end{Bmatrix} e^{i\omega t} \quad (\text{D.8})$$

$$\begin{aligned}
-mb\omega^2\vartheta + S_\alpha\omega^2\eta + EI_y b\vartheta'''' &= 0 \\
-I_\alpha\omega^2\eta + S_\alpha\omega^2 b\vartheta - GJ\eta'' &= 0
\end{aligned} \tag{D.9}$$

Rearrange it into a state-space form, the equation is defined as

$$\mathbf{z}'(x) = \mathbf{A}\mathbf{z}(x) \tag{D.10}$$

In which

$$\mathbf{z} = \begin{Bmatrix} \vartheta \\ \vartheta' \\ \vartheta'' \\ \vartheta''' \\ \eta \\ \eta' \end{Bmatrix} \quad \text{and} \quad \mathbf{A} = \begin{bmatrix} 0 & 1 & 0 & 0 & 0 & 0 \\ 0 & 0 & 1 & 0 & 0 & 0 \\ 0 & 0 & 0 & 1 & 0 & 0 \\ \frac{m\omega^2}{EI_y} & 0 & 0 & 0 & -\frac{S_\alpha\omega^2}{EI_y b} & 0 \\ 0 & 0 & 0 & 0 & 0 & 1 \\ \frac{S_\alpha b\omega^2}{GJ} & 0 & 0 & 0 & \frac{-I_\alpha\omega^2}{GJ} & 0 \end{bmatrix}$$

Hence, the state vector $\mathbf{z}(x)$ at any point of the beam can be obtained by the matrix exponential as

$$\mathbf{z}(x) = e^{\mathbf{A}x}\mathbf{z}(0) \tag{D.11}$$

The state vector \mathbf{z} can be corrected into $\hat{\mathbf{z}}$ to incorporate boundary conditions.

$$\hat{\mathbf{z}}(x) = \mathbf{D}\mathbf{z}(x) \tag{D.12}$$

In which

$$\hat{\mathbf{z}} = \begin{Bmatrix} \vartheta \\ \vartheta' \\ M_y \\ S_y \\ \eta \\ T \end{Bmatrix} \quad \text{and} \quad \mathbf{D} = \begin{bmatrix} 1 & 0 & 0 & 0 & 0 & 0 \\ 0 & 1 & 0 & 0 & 0 & 0 \\ 0 & 0 & EI_y b & 0 & 0 & 0 \\ 0 & 0 & 0 & EI_y b & 0 & 0 \\ 0 & 0 & 0 & 0 & 1 & 0 \\ 0 & 0 & 0 & 0 & 0 & GJ \end{bmatrix}$$

For a cantilever beam, the clamped end is constrained so that there is zero displacement and zero shear deformation. While for the free end, there is no bending moment, shear force or torque.

Hence, the boundary condition can be written as

$$\widehat{\mathbf{z}}(0) = \left\{ 0 \ 0 \ S_y(0) \ M_y(0) \ 0 \ T(0) \right\}^T ; \widehat{\mathbf{z}}(L) = \left\{ \vartheta(L) \ \vartheta'(L) \ 0 \ 0 \ \eta(L) \ 0 \right\}^T \quad (\text{D.13})$$

Finally, the governing equations can be written as a homogeneous equation below.

$$\begin{Bmatrix} 0 \\ 0 \\ 0 \end{Bmatrix} = \mathbf{T} \mathbf{D} e^{\mathbf{A}L} \mathbf{D}^{-1} \mathbf{R} \begin{Bmatrix} S_y(0) \\ M_y(0) \\ T(0) \end{Bmatrix} \quad \text{where } \mathbf{T} = \begin{bmatrix} 0 & 0 & 1 & 0 & 0 & 0 \\ 0 & 0 & 0 & 1 & 0 & 0 \\ 0 & 0 & 0 & 0 & 0 & 1 \end{bmatrix} ; \mathbf{R} = \mathbf{T}' \quad (\text{D.14})$$

D.3 Coupled Timoshenko beam flapping and torsion

First of all, simple harmonic motions are assigned to the coordinates of interest. Since the idea is to derive coupled mode shapes within one harmonic mode, the assumption is written as

$$\begin{Bmatrix} \xi(x, t) \\ \varphi_y(x, t) \\ \alpha(x, t) \end{Bmatrix} = \begin{Bmatrix} \vartheta(x) \\ \phi_y(x) \\ \eta(x) \end{Bmatrix} e^{i\omega t} \quad (\text{D.15})$$

$$-mb\omega^2\vartheta + S_\alpha\omega^2\eta - \kappa_y GA (b\vartheta'' - \phi_y') = 0$$

$$-\rho_w I_y \omega^2 \phi_y - EI_y \phi_y'' - \kappa_y GA (b\vartheta' - \phi_y) = 0 \quad (\text{D.16})$$

$$-I_\alpha \omega^2 \eta + S_\alpha \omega^2 b \vartheta - GJ \eta'' = 0$$

Rearrange it into a state-space form, the equation is defined as

$$\mathbf{z}'(x) = \mathbf{A} \mathbf{z}(x) \quad (\text{D.17})$$

In which

$$\mathbf{z} = \begin{Bmatrix} \vartheta \\ \vartheta' \\ \phi_y \\ \phi_y' \\ \eta \\ \eta' \end{Bmatrix} \quad \text{and} \quad \mathbf{A} = \begin{bmatrix} 0 & 1 & 0 & 0 & 0 & 0 \\ \frac{-m\omega^2}{\kappa_y GA} & 0 & 0 & \frac{1}{b} & \frac{S_\alpha \omega^2}{\kappa_y GA b} & 0 \\ 0 & 0 & 0 & 1 & 0 & 0 \\ 0 & \frac{-\kappa_y GA b}{EI_y} & \frac{\kappa_y GA - \rho_w I_y \omega^2}{EI_y} & 0 & 0 & 0 \\ 0 & 0 & 0 & 0 & 0 & 1 \\ \frac{S_\alpha b \omega^2}{GJ} & 0 & 0 & 0 & \frac{-I_\alpha \omega^2}{GJ} & 0 \end{bmatrix}$$

Hence, the state vector $\mathbf{z}(x)$ at any point of the beam can be obtained by the matrix exponential as

$$\mathbf{z}(x) = e^{\mathbf{A}x}\mathbf{z}(0) \quad (\text{D.18})$$

The state vector \mathbf{z} can be corrected into $\hat{\mathbf{z}}$ to incorporate boundary conditions.

$$\hat{\mathbf{z}}(x) = \mathbf{D}\mathbf{z}(x) \quad (\text{D.19})$$

In which

$$\hat{\mathbf{z}} = \begin{Bmatrix} \vartheta \\ S_h \\ \phi_y \\ M_y \\ \eta \\ T \end{Bmatrix} \quad \text{and} \quad \mathbf{D} = \begin{bmatrix} 1 & 0 & 0 & 0 & 0 & 0 \\ 0 & \kappa_y GA b & -\kappa_y GA & 0 & 0 & 0 \\ 0 & 0 & 1 & 0 & 0 & 0 \\ 0 & 0 & 0 & EI_y & 0 & 0 \\ 0 & 0 & 0 & 0 & 1 & 0 \\ 0 & 0 & 0 & 0 & 0 & GJ \end{bmatrix}$$

For a cantilever beam, the clamped end is constrained so that there is zero displacement and zero shear deformation. While for the free end, there is no bending moment, shear force or torque.

Hence, the boundary condition can be written as

$$\hat{\mathbf{z}}(0) = \left\{ 0 \quad S_h(0) \quad 0 \quad M_y(0) \quad 0 \quad T(0) \right\}^T; \quad \hat{\mathbf{z}}(L) = \left\{ \vartheta(L) \quad 0 \quad \phi_y(L) \quad 0 \quad \eta(L) \quad 0 \right\}^T \quad (\text{D.20})$$

Finally, the governing equations can be written as a homogeneous equation below.

$$\begin{Bmatrix} 0 \\ 0 \\ 0 \end{Bmatrix} = \mathbf{T}\mathbf{D}e^{\mathbf{A}L}\mathbf{D}^{-1}\mathbf{R} \begin{Bmatrix} S_h(0) \\ M_y(0) \\ T(0) \end{Bmatrix} \quad \text{where} \quad \mathbf{T} = \begin{bmatrix} 0 & 1 & 0 & 0 & 0 & 0 \\ 0 & 0 & 0 & 1 & 0 & 0 \\ 0 & 0 & 0 & 0 & 0 & 1 \end{bmatrix}; \quad \mathbf{R} = \mathbf{T}' \quad (\text{D.21})$$

Appendix E

Matrices Definition

In this chapter, the matrices in Equation (5.3) are expressed in detail.

$$\mathbf{M} = \begin{bmatrix} \mathbf{M}^h & \mathbf{0} & \mathbf{0} & \mathbf{M}^{h\alpha} \\ \mathbf{0} & \mathbf{M}^v & \mathbf{0} & \mathbf{0} \\ \mathbf{0} & \mathbf{0} & \mathbf{M}^z & \mathbf{0} \\ \mathbf{M}^{\alpha h} & \mathbf{0} & \mathbf{0} & \mathbf{M}^\alpha \end{bmatrix} \quad (\text{E.1})$$

$$\mathbf{K} = \begin{bmatrix} \mathbf{K}^h & \mathbf{0} & \mathbf{0} & \mathbf{0} \\ \mathbf{0} & \mathbf{K}^v & \mathbf{K}^{vz} & \mathbf{0} \\ \mathbf{0} & \mathbf{K}^{zv} & \mathbf{K}^z & \mathbf{0} \\ \mathbf{0} & \mathbf{0} & \mathbf{0} & \mathbf{K}^\alpha \end{bmatrix} \quad (\text{E.2})$$

$$\mathbf{M}_{\text{NC}} = \begin{bmatrix} \mathbf{M}_{\text{NC}}^h & \mathbf{0} & \mathbf{0} & \mathbf{M}_{\text{NC}}^{h\alpha} \\ \mathbf{0} & \mathbf{0} & \mathbf{0} & \mathbf{0} \\ \mathbf{0} & \mathbf{0} & \mathbf{0} & \mathbf{0} \\ \mathbf{M}_{\text{NC}}^{\alpha h} & \mathbf{0} & \mathbf{0} & \mathbf{M}_{\text{NC}}^\alpha \end{bmatrix} \quad (\text{E.3})$$

$$\mathbf{K}_{\text{NC}} = \left[\begin{array}{c|c|c|c} \mathbf{0} & \mathbf{0} & \mathbf{0} & \mathbf{K}_{\text{NC}}^{\text{h}\alpha} \\ \hline \mathbf{0} & \mathbf{0} & \mathbf{0} & \mathbf{0} \\ \hline \mathbf{0} & \mathbf{0} & \mathbf{0} & \mathbf{0} \\ \hline \mathbf{0} & \mathbf{0} & \mathbf{0} & \mathbf{K}_{\text{NC}}^{\alpha} \end{array} \right] \quad (\text{E.4})$$

$$\begin{aligned}
\mathbf{M}^h &= \begin{bmatrix} M_{11}^h & M_{12}^h & \cdots & M_{1N_q}^h \\ M_{21}^h & M_{22}^h & \cdots & M_{2N_q}^h \\ \vdots & \vdots & \ddots & \vdots \\ M_{N_q1}^h & M_{N_q2}^h & \cdots & M_{N_qN_q}^h \end{bmatrix} = [M_{ij}^h]_{N_q \times N_q} = \left[m \int_0^L \theta_i \theta_j dx \right]_{N_q \times N_q} \\
\mathbf{M}^{h\alpha} &= \begin{bmatrix} M_{11}^{h\alpha} & M_{12}^{h\alpha} & \cdots & M_{1N_q}^{h\alpha} \\ M_{21}^{h\alpha} & M_{22}^{h\alpha} & \cdots & M_{2N_q}^{h\alpha} \\ \vdots & \vdots & \ddots & \vdots \\ M_{N_q1}^{h\alpha} & M_{N_q2}^{h\alpha} & \cdots & M_{N_qN_q}^{h\alpha} \end{bmatrix} = [M_{ij}^{h\alpha}]_{N_q \times N_q} = \left[-S_\alpha \int_0^L \theta_i \eta_j dx \right]_{N_q \times N_q} \\
\mathbf{M}^v &= \begin{bmatrix} M_{11}^v & M_{12}^v & \cdots & M_{1N_p}^v \\ M_{21}^v & M_{22}^v & \cdots & M_{2N_p}^v \\ \vdots & \vdots & \ddots & \vdots \\ M_{N_p1}^v & M_{N_p2}^v & \cdots & M_{N_pN_p}^v \end{bmatrix} = [M_{ij}^v]_{N_p \times N_p} = \left[m \int_0^L \zeta_i \zeta_j dx \right]_{N_p \times N_p} \\
\mathbf{M}^z &= \begin{bmatrix} M_{11}^z & M_{12}^z & \cdots & M_{1N_p}^z \\ M_{21}^z & M_{22}^z & \cdots & M_{2N_p}^z \\ \vdots & \vdots & \ddots & \vdots \\ M_{N_p1}^z & M_{N_p2}^z & \cdots & M_{N_pN_p}^z \end{bmatrix} = [M_{ij}^z]_{N_p \times N_p} = \left[\rho_w I_z \int_0^L \phi_i^z \phi_j^z dx \right]_{N_p \times N_p} \\
\mathbf{M}^{\alpha h} &= \begin{bmatrix} M_{11}^{\alpha h} & M_{12}^{\alpha h} & \cdots & M_{1N_q}^{\alpha h} \\ M_{21}^{\alpha h} & M_{22}^{\alpha h} & \cdots & M_{2N_q}^{\alpha h} \\ \vdots & \vdots & \ddots & \vdots \\ M_{N_q1}^{\alpha h} & M_{N_q2}^{\alpha h} & \cdots & M_{N_qN_q}^{\alpha h} \end{bmatrix} = [M_{ij}^{\alpha h}]_{N_q \times N_q} = \left[-S_\alpha \int_0^L \eta_i \theta_j dx \right]_{N_q \times N_q} \\
\mathbf{M}^\alpha &= \begin{bmatrix} M_{11}^\alpha & M_{12}^\alpha & \cdots & M_{1N_q}^\alpha \\ M_{21}^\alpha & M_{22}^\alpha & \cdots & M_{2N_q}^\alpha \\ \vdots & \vdots & \ddots & \vdots \\ M_{N_q1}^\alpha & M_{N_q2}^\alpha & \cdots & M_{N_qN_q}^\alpha \end{bmatrix} = [M_{ij}^\alpha]_{N_q \times N_q} = \left[I_\alpha \int_0^L \eta_i \eta_j dx \right]_{N_q \times N_q}
\end{aligned}$$

$$\begin{aligned}
\mathbf{K}^h &= \begin{bmatrix} K_{11}^h & K_{12}^h & \cdots & K_{1N_q}^h \\ K_{21}^h & K_{22}^h & \cdots & K_{2N_q}^h \\ \vdots & \vdots & \ddots & \vdots \\ K_{N_q1}^h & K_{N_q2}^h & \cdots & K_{N_qN_q}^h \end{bmatrix} = [K_{ij}^h]_{N_q \times N_q} = \left[\int_0^L \theta_i (EI_y \theta_j'') dx \right]_{N_q \times N_q} \\
\mathbf{K}^v &= \begin{bmatrix} K_{11}^v & K_{12}^v & \cdots & K_{1N_p}^v \\ K_{21}^v & K_{22}^v & \cdots & K_{2N_p}^v \\ \vdots & \vdots & \ddots & \vdots \\ K_{N_p1}^v & K_{N_p2}^v & \cdots & K_{N_pN_p}^v \end{bmatrix} = [K_{ij}^v]_{N_p \times N_p} = \left[- \int_0^L \zeta_i (\kappa_z G A b \zeta_j') dx \right]_{N_p \times N_p} \\
\mathbf{K}^{vz} &= \begin{bmatrix} K_{11}^{vz} & K_{12}^{vz} & \cdots & K_{1N_p}^{vz} \\ K_{21}^{vz} & K_{22}^{vz} & \cdots & K_{2N_p}^{vz} \\ \vdots & \vdots & \ddots & \vdots \\ K_{N_p1}^{vz} & K_{N_p2}^{vz} & \cdots & K_{N_pN_p}^{vz} \end{bmatrix} = [K_{ij}^{vz}]_{N_p \times N_p} = \left[\int_0^L \zeta_i (\kappa_z G A \phi_j^z)' dx \right]_{N_p \times N_p} \\
\mathbf{K}^{zv} &= \begin{bmatrix} K_{11}^{zv} & K_{12}^{zv} & \cdots & K_{1N_p}^{zv} \\ K_{21}^{zv} & K_{22}^{zv} & \cdots & K_{2N_p}^{zv} \\ \vdots & \vdots & \ddots & \vdots \\ K_{N_p1}^{zv} & K_{N_p2}^{zv} & \cdots & K_{N_pN_p}^{zv} \end{bmatrix} = [K_{ij}^{zv}]_{N_p \times N_p} = \left[- \int_0^L \phi_i^z \kappa_z G A b \zeta_j' dx \right]_{N_p \times N_p} \\
\mathbf{K}^z &= \begin{bmatrix} K_{11}^z & K_{12}^z & \cdots & K_{1N_p}^z \\ K_{21}^z & K_{22}^z & \cdots & K_{2N_p}^z \\ \vdots & \vdots & \ddots & \vdots \\ K_{N_p1}^z & K_{N_p2}^z & \cdots & K_{N_pN_p}^z \end{bmatrix} = [K_{ij}^z]_{N_p \times N_p} = \left[- \int_0^L \phi_i^z ((EI_z \phi_j^z)' + \kappa_z G A (b \zeta_j' - \phi_j^z)) dx \right]_{N_p \times N_p} \\
\mathbf{K}^\alpha &= \begin{bmatrix} K_{11}^\alpha & K_{12}^\alpha & \cdots & K_{1N_q}^\alpha \\ K_{21}^\alpha & K_{22}^\alpha & \cdots & K_{2N_q}^\alpha \\ \vdots & \vdots & \ddots & \vdots \\ K_{N_q1}^\alpha & K_{N_q2}^\alpha & \cdots & K_{N_qN_q}^\alpha \end{bmatrix} = [K_{ij}^\alpha]_{N_q \times N_q} = \left[- \int_0^L \eta_i (G J \eta_j') dx \right]_{N_q \times N_q}
\end{aligned}$$

$$\begin{aligned}
\mathbf{M}_{\text{NC}}^h &= \begin{bmatrix} M_{\text{NC}11}^h & M_{\text{NC}12}^h & \cdots & M_{\text{NC}1N_q}^h \\ M_{\text{NC}21}^h & M_{\text{NC}22}^h & \cdots & M_{\text{NC}2N_q}^h \\ \vdots & \vdots & \ddots & \vdots \\ M_{\text{NC}N_q1}^h & M_{\text{NC}N_q2}^h & \cdots & M_{\text{NC}N_qN_q}^h \end{bmatrix} = \left[M_{\text{NC}ij}^h \right]_{N_q \times N_q} = \left[-\pi \rho b^2 \int_0^L \theta_i \theta_j dx \right]_{N_q \times N_q} \\
\mathbf{M}_{\text{NC}}^{h\alpha} &= \begin{bmatrix} M_{\text{NC}11}^{h\alpha} & M_{\text{NC}12}^{h\alpha} & \cdots & M_{\text{NC}1N_q}^{h\alpha} \\ M_{\text{NC}21}^{h\alpha} & M_{\text{NC}22}^{h\alpha} & \cdots & M_{\text{NC}2N_q}^{h\alpha} \\ \vdots & \vdots & \ddots & \vdots \\ M_{\text{NC}N_q1}^{h\alpha} & M_{\text{NC}N_q2}^{h\alpha} & \cdots & M_{\text{NC}N_qN_q}^{h\alpha} \end{bmatrix} = \left[M_{\text{NC}ij}^{h\alpha} \right]_{N_q \times N_q} = \left[\pi \rho a b^3 \int_0^L \theta_i \eta_j dx \right]_{N_q \times N_q} \\
\mathbf{M}_{\text{NC}}^{\alpha h} &= \begin{bmatrix} M_{\text{NC}11}^{\alpha h} & M_{\text{NC}12}^{\alpha h} & \cdots & M_{\text{NC}1N_q}^{\alpha h} \\ M_{\text{NC}21}^{\alpha h} & M_{\text{NC}22}^{\alpha h} & \cdots & M_{\text{NC}2N_q}^{\alpha h} \\ \vdots & \vdots & \ddots & \vdots \\ M_{\text{NC}N_q1}^{\alpha h} & M_{\text{NC}N_q2}^{\alpha h} & \cdots & M_{\text{NC}N_qN_q}^{\alpha h} \end{bmatrix} = \left[M_{\text{NC}ij}^{\alpha h} \right]_{N_q \times N_q} = \left[\pi \rho a b^3 \int_0^L \eta_i \theta_j dx \right]_{N_q \times N_q} \\
\mathbf{M}_{\text{NC}}^\alpha &= \begin{bmatrix} M_{\text{NC}11}^\alpha & M_{\text{NC}12}^\alpha & \cdots & M_{\text{NC}1N_q}^\alpha \\ M_{\text{NC}21}^\alpha & M_{\text{NC}22}^\alpha & \cdots & M_{\text{NC}2N_q}^\alpha \\ \vdots & \vdots & \ddots & \vdots \\ M_{\text{NC}N_q1}^\alpha & M_{\text{NC}N_q2}^\alpha & \cdots & M_{\text{NC}N_qN_q}^\alpha \end{bmatrix} = \left[M_{\text{NC}ij}^\alpha \right]_{N_q \times N_q} = \left[-\pi \rho b^4 \left(a^2 + \frac{1}{8} \right) \int_0^L \eta_i \eta_j dx \right]_{N_q \times N_q} \\
\mathbf{K}_{\text{NC}}^{h\alpha} &= \begin{bmatrix} K_{\text{NC}11}^{h\alpha} & K_{\text{NC}12}^{h\alpha} & \cdots & K_{\text{NC}1N_q}^{h\alpha} \\ K_{\text{NC}21}^{h\alpha} & K_{\text{NC}22}^{h\alpha} & \cdots & K_{\text{NC}2N_q}^{h\alpha} \\ \vdots & \vdots & \ddots & \vdots \\ K_{\text{NC}N_q1}^{h\alpha} & K_{\text{NC}N_q2}^{h\alpha} & \cdots & K_{\text{NC}N_qN_q}^{h\alpha} \end{bmatrix} = \left[K_{\text{NC}ij}^{h\alpha} \right]_{N_q \times N_q} = \left[-\pi \rho b^2 U_a \int_0^L \eta_i \theta_j dx \right]_{N_q \times N_q} \\
\mathbf{K}_{\text{NC}}^\alpha &= \begin{bmatrix} K_{\text{NC}11}^\alpha & K_{\text{NC}12}^\alpha & \cdots & K_{\text{NC}1N_q}^\alpha \\ K_{\text{NC}21}^\alpha & K_{\text{NC}22}^\alpha & \cdots & K_{\text{NC}2N_q}^\alpha \\ \vdots & \vdots & \ddots & \vdots \\ K_{\text{NC}N_q1}^\alpha & K_{\text{NC}N_q2}^\alpha & \cdots & K_{\text{NC}N_qN_q}^\alpha \end{bmatrix} = \left[K_{\text{NC}ij}^\alpha \right]_{N_q \times N_q} = \left[-\pi \rho b^3 \left(\frac{1}{2} - a \right) \int_0^L \eta_i \eta_j dx \right]_{N_q \times N_q}
\end{aligned}$$

$$\mathbf{u} = \left\{ \begin{array}{c} b \times q_1 \\ \vdots \\ b \times q_{N_q} \\ \hline b \times p_1 \\ \vdots \\ b \times p_{N_p} \\ \hline p_1 \\ \vdots \\ p_{N_p} \\ \hline q_1 \\ \vdots \\ q_{N_q} \end{array} \right\}; \ddot{\mathbf{u}} = \left\{ \begin{array}{c} U_\infty^2/b \times q_1 \\ \vdots \\ U_\infty^2/b \times q_{N_q} \\ \hline U_\infty^2/b \times p_1 \\ \vdots \\ U_\infty^2/b \times p_{N_p} \\ \hline U_\infty^2/b^2 \times p_1 \\ \vdots \\ U_\infty^2/b^2 \times p_{N_p} \\ \hline U_\infty^2/b^2 \times q_1 \\ \vdots \\ U_\infty^2/b^2 \times q_{N_q} \end{array} \right\}; \mathbf{F} = \left\{ \begin{array}{c} \int_0^L \theta_1(L_C + L_g + F_{tip})dx \\ \vdots \\ \int_0^L \theta_{N_q}(L_C + L_g + F_{tip})dx \\ \hline \int_0^L \zeta_1(\frac{1}{10}(L_C + L_g) + F_{thrust})dx \\ \vdots \\ \int_0^L \zeta_{N_p}(\frac{1}{10}(L_C + L_g) + F_{thrust})dx \\ \hline 0 \\ \vdots \\ 0 \\ \hline \int_0^L \eta_1(M_C + M_g + M_{tip})dx \\ \vdots \\ \int_0^L \eta_{N_q}(M_C + M_g + M_{tip})dx \end{array} \right\}$$